Advanced Electrolytes for Calcium Batteries

Antonio Scafuri

THESIS TO OBTAIN THE GRADE OF DOCTOR OF THE UNIVERSITY OF MONTPELLIER

in Chemistry and Physics-chemistry of materials

Doctoral school « Sciences Chimiques Balard »

Research unit « UMR 5253 – Institute Charles Gerhardt of Montpellier »
Team : Aggregates, Interfaces and Materials for Energy

in international partnership with National Institute of Chemistry, Slovenia

Advanced Electrolytes for Calcium Batteries

Presented by Scafuri Antonio
on 29 March 2021

Under the direction of Stievano Lorenzo
and Pirnat Klemen

In front of the jury composed of

Prof. Genorio, Boštjan, UL	Examinateur
Prof. Cerkovnik, Janez, UL	Examinateur
Prof. Stievano, Lorenzo, UM	Directeur de these
Dr. Fontaine, Olivier, UM	Examinateur
Prof. Johansson, Patrik, Chalmers	Rapporteur
Dr. Ponrouch, Alexandre, ICMAB	Examinateur
Prof. Renaud, Bouchet, LEPMI	Rapporteur

UNIVERSITÉ DE MONTPELLIER

UNIVERSITY OF LJUBLJANA

FACULTY OF CHEMISTRY AND CHEMICAL TECHNOLOGY

DOCTORAL DISSERTATION

Antonio Scafuri

Ljubljana, 2021

University *of Ljubljana*
Faculty of *Chemistry and Chemical Technology*

Doctoral programme in CHEMICAL SCIENCES

Field CHEMISTRY

Doctoral dissertation

Advanced Electrolytes for Calcium Batteries

Napredni elektroliti za kalcijeve akumulatorje

Antonio Scafuri

Mentor: viš. znan. sod. dr. Klemen Pirnat

Co-mentor: Prof. Robert Dominko

Ljubljana, 2021

"Millions saw the apple fall, but Newton was the one who wondered why.

Without curiosity, perhaps science would not exist"

Bernard Baruch

To my family

Abstract

Today, Li-ion batteries are the ultimate rechargeable energy storage systems; however, after decades of improvements, the technology might reach its energy-density limits. Ca batteries represent a promising electrochemical systems alternative to Li-ion one. The abundance of Ca, its low redox potential, only slightly higher than that of Li and high volumetric capacity make Ca metal batteries an attractive energy storage for the future. However, the development of Ca batteries is hindered due to the lack of efficient electrolytes able to reversibly strip/deposit calcium at room temperature and with high electrochemical window stability. The objective of this project is to develop and test both new electrolytes and new electrode materials for room temperature batteries by transferring the experience from the Mg systems. Herein, we synthesised at room temperature high purity fluorinated alkoxyborate salt $Ca[B(hfip)_4]_2 \times 4DME$ and use it in calcium electrolyte. Reversible Ca plating/stripping at room temperature and a wide electrochemical stability up to 4 V vs. Ca/Ca^{2+} were evidenced. Further, we demonstrated that anthraquinone-based polymer could be used as cathode material to develop high energy density Ca-organic batteries. Electrochemical mechanism investigation confirms the reversible reduction of the carbonyl bond of anthraquinone backbone and coordination with Ca^{2+} cations in the discharged state. Finally, we combined calcium anode and appropriate sulfur-based cathode to report a reversible electrochemical activity at room temperature of Ca/S battery proof-of-concept. This innovative system is characterized by a medium-term cycling stability with high specific capacity. Insights into the electrochemical mechanism governing the chemistry of the Ca/S system were obtained for the first time by combining XPS and XAS spectroscopy. The reversible electrochemical activity implies the formation of different types of soluble polysulfide species during both charge and discharge. These promising results open the way to the comprehension of emerging Ca/S systems.

Résumé

Aujourd'hui, les batteries Li-ion sont les meilleurs systèmes de stockage d'énergie rechargeable; cependant, après des décennies d'améliorations, la technologie pourrait atteindre ses limites. Les batteries au calcium représentent une alternative prometteuse aux systèmes électrochimiques au Li-ion. L'abondance du calcium, son faible potentiel redox et sa grande capacité volumétrique sont attractifs. Cependant, le développement de ces systèmes est entravé en raison du manque d'électrolytes efficaces et du manque de matériaux d'électrode positive. L'objectif de ce projet est de développer et de tester à la fois de nouveaux électrolytes et de nouveaux matériaux d'électrode pour batteries à température ambiante en transférant l'expérience des systèmes Mg.

Nous avons synthétisé à température ambiante le sel $Ca[B(hfip)_4]_2 \times 4DME$ et l'avons utilisé dans l'électrolyte. Le phénomène de déposition/dissolution électrochimique du calcium a été observé, à température ambiante et de manière réversible, ainsi qu'une grande stabilité électrochimique jusqu'à 4 V. En outre, nous avons démontré qu'un polymère à base d'anthraquinone pouvait être utilisé comme matériau de cathode pour développer des batteries Ca-organiques à haute densité d'énergie. L'étude du mécanisme électrochimique confirme la réduction réversible de la liaison carbonyle du squelette anthraquinone et la coordination avec les cations Ca^{2+} à l'état déchargé. Enfin, nous avons combiné une anode de calcium et une cathode à base de soufre pour créer une preuve de concept d'une batterie Ca/S fonctionnant à température ambiante. Ce système innovant se caractérise par une stabilité cyclique à moyen terme avec une capacité spécifique élevée. Des informations sur le mécanisme électrochimique ont été obtenues pour la première fois en combinant les spectroscopies XPS et XAS. L'activité électrochimique réversible implique la formation de différents types d'espèces de polysulfures solubles pendant la charge et la décharge. Ces résultats prometteurs ouvrent la voie au développement des systèmes Ca/S émergents.

Povzetek

Danes so Li-ion akumulatorji vrhunski sistemi za shranjevanje energije, ki jih je mogoče ponovno napolnit. Po desetletjih izboljšav pa ta tehnologija dosega teoretične zmogljivosti z vidika energetske gostote. Kalcijevi akumulatorji predstavljajo obetaven elektrokemijski sistem, ki je alternativa Li-ionskemu. Zaradi razširjenosti Ca v zemeljski skorji, nizkega redoks potenciala in velike volumetrične energijske gostote so Ca akumulatorji privlačni za shranjevanje energije v prihodnosti. Razvoj Ca akumulatorjev je oviran zaradi pomanjkanja ustreznih elektrolitov, ki bi omogočali reverzibilno odlaganje kalcija pri sobni temperaturi in bi hkrati imeli široko elektrokemijsko okno. Cilj tega projekta je na podlagi izkušenj iz Mg akumulatorskih sistemov razviti in preizkusiti nove elektrolite kot nove elektrodne materiale za Ca akumulatorje, ki bi delovali pri sobni temperaturi. Tako smo pri sobni temperaturi sintetizirali fluorirano alkoksiboratno sol $Ca[B(hfip)_4]_2 \times 4DME$ z visoko čistostjo in jo uporabili v kalcijevem elektrolitu. Dokazali smo reverzibilno odlaganje Ca pri sobni temperaturi in široko elektrokemijsko stabilnost do 4 V vs. Ca/Ca^{2+}. Nadalje smo pokazali delovanje polimera na osnovi antrakinona kot katodnega materiala v Ca akumulatorju. S pomočjo IR spektroskopije smo potrdili elektrokemijski mehanizem, kjer se karbonilna vez pri praznjenju reverzibilno reducira in koordinara s Ca^{2+} kationi. Na koncu smo sestavili Ca/S akumulator na osnovi kalcijeve anode in katode na osnovi žvepla ter pokazali reverzibilno elektrokemijsko aktivnost. Na ta način smo dobili Ca/S akumulator s srednjo stabilnostjo delovanje ampak visoko specifično kapaciteto. Vpogled v elektrokemijski mehanizem tega sistema smo kot prvi dobili s kombinacijo XPS in XAS spektroskopije. Pokazali smo, da med polnjenjem/praznjenjem akulumatorja nastajajo različni topni polisulfidi kot intermediati med začetnim S in končnim CaS. Ti obetavni rezultati odpirajo pot do razumevanja in razvoja novih Ca/S akumulatorjev

Acknowledgments

A research doctorate is not just a work experience, but also a deep personal journey of changing and discovering of new introspective features, in which in the end in our path, we find ourselves as more mature and responsible people. We learn what the strength of a group means with respect to the will of individuals, what it means to be able to assume responsibilities, to react against adversities and to know how to rejoice in a goal achieved together all the people have always supported you. During these intense 3 years, I had the lucky to approach and to live two different realities, the France and Slovenia, which gave me the incredible environments to let me grow up as person and scientist, to put myself always in discussion and feel so enthusiastic to live day by day this new experience. If I realize what I have in my hands now, there is something more than this manuscript; there is the remind of all wonderful moments spent with everybody taught me something, a suggestion, an advice, simply a word to let me feel happy to push myself always above my capacities. As every time that a new path begins, we have to face with many challenges, which we are called to transform in opportunities to become wiser; and since nobody can rise up alone in the life, I want to be thankful and express my gratitude to all people mentioned below.

First, I want to be thankful with the opportunity to have worked in the laboratories of ICGM-AIME in Montpellier and National Institute of Chemistry in Ljubljana. This framework of co-sharing experience can represent the metaphor of how it is so essential the power of the group above all, acts to create a good and homogeneous working environment between different physical places. How the union of different knowledges can let us to track a common road devoted to a final shared result.

I would like to thank the ALISTORE group, not only for having founded our project, but also for having had the opportunity to know and meet wonderful people who share our results time by time. Every professional talk and funny moment during our meetings helped me to find enthusiasm in my work.

I want to acknowledge all the jury members that accepted to examine this PhD thesis. Your interesting questions, positive comments and remarks led to an increased the overall quality of the final manuscript.

A special acknowledgment is devoted to my supervisors: Prof. Lorenzo Stievano, Prof. Robert Dominko, Dr. Klemen Pirnat and Dr. Romain Berthelot. They have been the perfect expression of the word “leader”, since the true leader is not the strongest or the best, but the one who helps others to be stronger and better. I feel so lucky to have had these wonderful people during not only working environment, but also a deep and beautiful friendship outside the laboratory. Since the first months of PhD, they always taught me how to approach at this new topic, all the methodologies of work and how to push ourselves as to be never satisfied about what we have, but to reach the best of our capacities. Simply, they have instilled in me the conception in knowing how to always think and reason, in life as well as at work. That everything has logical dynamics, which we have the task of investigating and then being able to use to better understand the science around us. They were able to stimulate and support me when my weaknesses took over my abilities, madding me feel like a nice person more than I believed, when my unconvincing results could take away my smile. Because there is nothing better than going to work every day with a smile, knowing that I can make them happy and proud of me with good results, but above all with the spirit of sacrifice, the commitment, dedication and enthusiasm of every single day. On the other hand, when they knew how to cheer me up every time I was lost (many times!). All you have been the deep engine of my brain and my heart each day of this PhD, because I will never forget all your attentions, your every single word that has given me the desire and the courage to do always more than I can give. Thank you very much because you have simply always been here for me and every time, since if I have to see even just a battery on this thesis, the credit is simply even yours. Because the results can also come, good or bad, but the first step in life is always the most difficult, when you start a long journey. Thank you for giving me strength and courage to take this first step.

Many thanks to the people that, although working in different places as Montpellier and Ljubljana, has been always bringing their experience, knowledge, support and important advices during my path. They have been always interested since beginning in all my work progresses and my growth in becoming more critical of the data to be analyzed. I will always remember all our scientific exchanges, but also all the times they helped me when I was in trouble. For the AIME team: thanks to the chief Prof. Laure Monconduit, Dr. Nicolas Louvain, the research engineers Bernard Fraisse, Julien Fullenwarth and Moulay Tahar Srougati. For the NIC team: thanks to Dr. Jan Bitenc, Dr. Alen Vižintin, Prof. Dr. Ivo Jerman, Dr. Jože Moškon,

Dr. Marjan Bele, Prof. Dr. Miran Gaberšček, Prof. Dr. Jože Grdadolnik. Thanks to Ivana Maver for all the help every time I needed.

Thanks to Prof. Iztok Arčon, Dr. Giuliana Aquilanti and Dr. Luca Olivi for their precious work at ELETTRA synchrotron for XAS analysis. Thanks also to Prof. Rémi Dedryvère and ingenieur de recherché Dominique Foix for the important work at IPREM for XPS analysis.

A special thanks to the people with I shared this life experience: my friends. For me now, it is difficult to be able to mention all the friends I have been lucky to know, from the beginning of this adventure until today. Each of them brought something new to me and taught me something special. They made me grow as a person and bring that joy that is needed always to start a path together. Sharing one's happiness, but also difficult moments in which we felt much more united and going beyond any troubles together. Friends are the family that we ourselves choose and they are able to put you in front of the mirror, even when you do not want. In addition, in the mirror I have always found a special way to complain and to be in discussion with myself, since if we decide to start a journey to grow up, we should be able to accept even the bad sides of us. I would like to thank all my friends for this adventure, with whom we shared everything, from funny to difficult moments, to carefree moments or simply when one of us needed and could always count on the other. Thanks to all my friends of BAT group in Montpellier and D10 in Ljubljana; your constant presence has always made me feel like the happiest person. Thanks to all my friends of BAT-15 and BAT-17 in Montpellier, to all my friends of NIC in Ljubljana, being able to exchange a single word with you (and many coffees togheter too!) and moments of lightheartedness meant that my days could pass much light-hearted. Thanks to all my friends I had opportunity to meet in Montpellier and Ljubljana, who taught me to live and know how to be part of these two new realities. Thanks to my friends in Italy, because despite the distance, we know that we will always be there for each other and each time far away, we cannot wait to hug each other again. All you simply have been and always will be my second family.

Thank you to my family, to my brother Nicola and my mother Maria. Because without the strong and deep roots of the family, no man is capable of doing something good in the life, let alone knowing how to share the love. If I am now lucky enough to have learned certain values, in knowing how to improve every day in my behavior and education, it is because I am fortunate to have a family that is always present and attentive. Thanks, because without you, I

would have fallen many times, but you have always taught me that sharing love and kindness is the best way to live happily.

Everybody of you has always taught me something new and special to know how to grow and improve every day, as guy and professionist. Without all you, I probably would not be the person I am now.

Table of abbreviations

ACN	Acetonitrile
CE	Counter electrode
CV	Cyclic voltammetry
DGM	Dimethylglyoxime
DMA	*N*,*N*-Dimethylacetamide
DME	1,2-dimethoxyethane
EC	Ethylene carbonate
EDS	Energy dispersive X-ray spectroscopy
EVs	Electric vehicles
ESW	Electrochemical stability window
GBL	Gamma-butyrolactone
GCPL	Galvanostatic cycling with potential limitation
HCF	Hexacyanoferrate
HEVs	Hybrid electric vehicles
HOMO	Highest occupied molecular orbital
IL	Ionic liquid
LIBs	Lithium-ion batteries
PANI/CC	Polyaniline/carbon clothes
PC	Propylene carbonate
PLiBs	Post-lithium batteries
RE	Reference electrode
SEI	Solid electrolyte interphase
SEM	Scanning electron microscopy
TBA	Tetrabutylammonium
THF	Tetrahydrofuran
TM	Transition metal
WCAs	Weakly coordinating anions
WE	Working electrode

Index of figures

Index of tables

Statement of authorship of the doctoral dissertation

I, Antonio Scafuri, confirm the authorship of the doctoral dissertation entitled:

Advanced Electrolytes for Calcium Batteries

With my signature I declare that:

- the doctoral dissertation is the result of my individual work under the mentorship of Dr. Klemen Pirnat,
- I have consistently cited all scientific literature used in the work,
- the electronic form of the doctoral dissertation is identical to the printed form.

Ljubljana, date: 28/12/2020 Author's signature

Summary

I. Introduction

1. The importance in society of battery storage for sustainable energy

The world's population keeps increasing, industry is growing, so too is the demand for energy. Yet fossil fuels such as coal and oil are finite. The initial local energy systems developed by enterprises around 1900 evolved into the present fossil-fuel based, networked form due to various technological and societal developments, such as increasing demand and economies of scale.[1] The world needs alternative forms of energy that are naturally replenishing and in infinite supply. They include hydropower, solar and wind energy, biomass and geothermal heating. The plants and systems do not emit greenhouse gases or pollutants and so produce energy in a way that is not harmful to the environment and health. Energy storage is arguably the next big thing in the cleantech industry, with the potential of bringing constructive disruptions to the renewable energy and electric vehicle markets. Today, storing electricity is expensive, but the cost of storage is falling rapidly. Cheaper energy storage opens up a plethora of opportunities to accelerate the transition to sustainable energy systems, including electric vehicles, urban power consumption, rural energy access, electricity distribution, grid-integration and the complete replacement of coal power plants. Renewable energy is not yet a fully reliable alternative to fossil-powered generation; the sun does not always shine and the wind does not always blow, meaning renewable energy systems are dependent on supplemental generation through other means. Access to energy is a key pillar for human wellbeing, economic development and poverty alleviation. Ensuring everyone has sufficient access is an

ongoing and pressing challenge for global development. However, our energy systems also have important environmental impacts. Historical and current energy systems are dominated by fossil fuels (coal, oil and gas) which produce carbon dioxide (CO_2) and other greenhouse gases, the fundamental driver of global climate change. To meet our global climate targets and avoid a dangerous climate change, we need to implement a significant and concerted transition in its energy sources. Balancing the challenge between development and environment therefore provides us with an ultimate goal of ensuring that everyone has access to enough sustainable energy to maintain a high standard of living.[2]

In Figure 1 is shown the trends in per capita energy use; this is inclusive of all dimensions of energy (electricity plus transport and heating), not exclusively electricity (with energy normalized kilowatt-hour equivalents per year).[4] It is important to note that the global average per capita energy consumption has been consistently increasing; between 1970-2014, average consumption has increased by approximately 45 %.

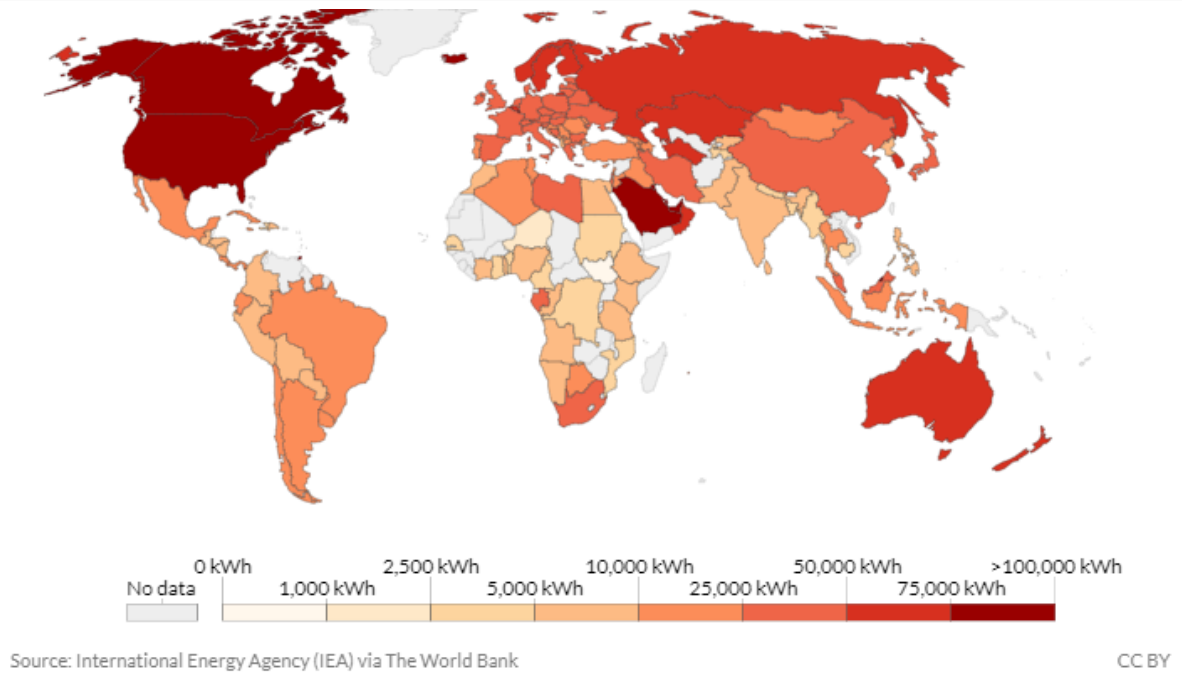

Figure 1: Annual average per capita energy consumption is measured in kilowatt-hours per person per year.[2]

This growth in per capita energy consumption does however vary significantly between countries and regions. Most of the growth in per capita energy consumption over the last few decades has been driven by increased consumption in transitioning middle-income (and to a lesser extent, low-income countries). In the chart we see a significant increase in consumption in transitioning BRICS economies (China, India and Brazil in particular); China's per capita use has grown by nearly 250 % since 2000; India by more than 50 %; and Brazil by 38 %.

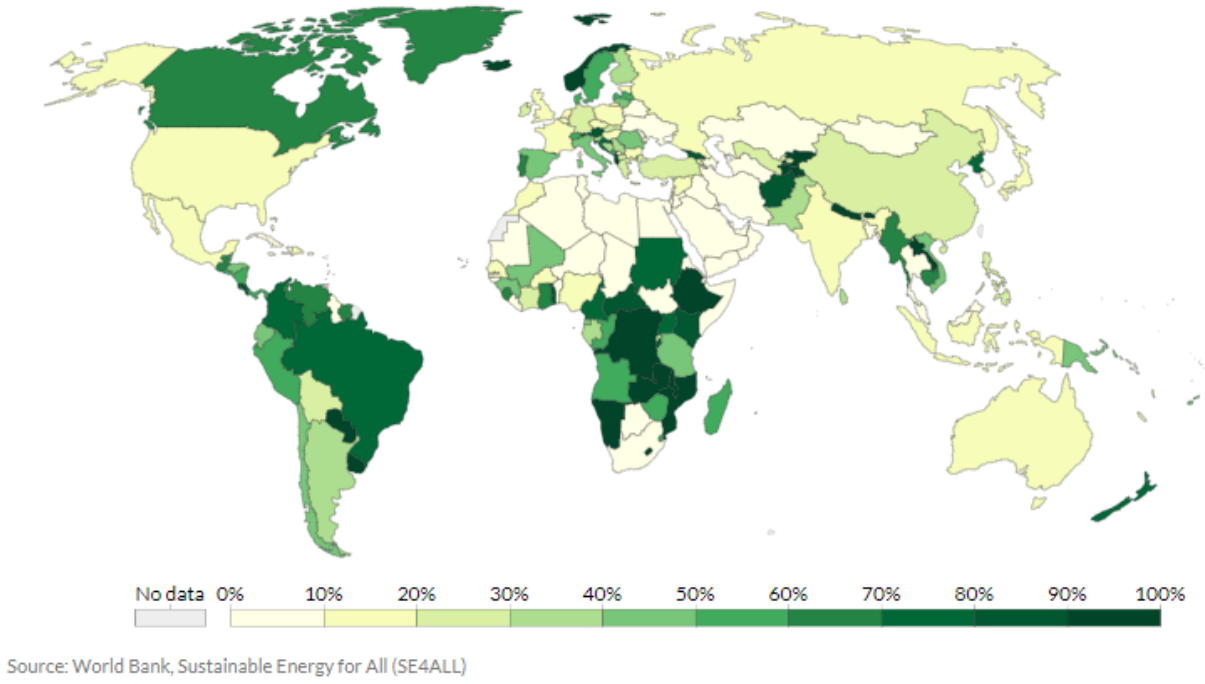

Figure 2: Percentage of electricity produced through renewable sources. This includes biomass, hydropower, solar, wind, geothermal and marine energy. Electricity produced by nuclear sources is not included.[2]

Over the last decade (2005-2015) the share of renewables in our electricity mix has increased by approximately 5-6 %. The total share of low-carbon electricity production is almost exactly the same as a decade ago (as shown in Figure 2). Since 2005, natural gas and coal have increased their share by one and two percent, respectively whereas the contribution from oil

has declined by two percent. Nonetheless, overall, the relative mix of electricity sources has changed very little over the last few decades. Global primary energy grew by 2.9% in 2018, the fastest growth since 2010. At carbon emissions from energy use grew by 2.0%, again the fastest expansion for many years, with emissions increasing by around 0.6 gigatonnes. This growth was largely driven by China, US and India which together accounted for around two thirds of the growth.[3] Relative to recent historical averages, the most striking growth was in the US, where energy consumption increased by a whopping 3.5%, the fastest growth seen for 30 years and in sharp contrast to the trend decline seen over the previous 10 years (Figure 3).

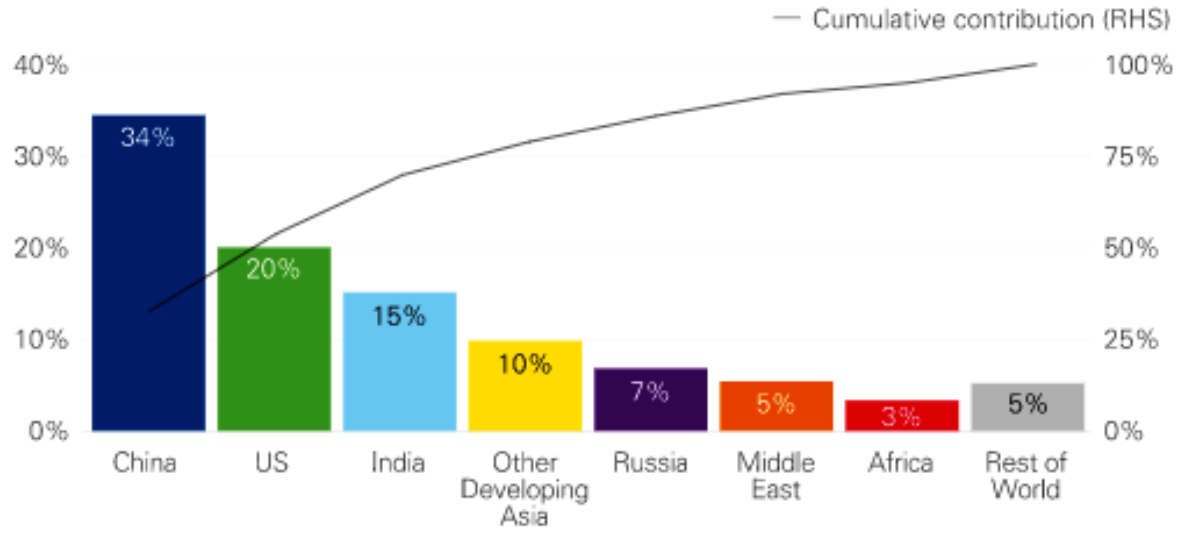

Figure 3: Contribution to primary energy growth in 2018.[3]

The increase in energy consumption was pretty much reflected across all the fuels, most of which grew more strongly than their historical averages. This acceleration was particularly pronounced in natural gas demand, which increased 5.3%, one of its strongest growth rates for over 30 years, accounting for almost 45% of the entire growth in global energy consumption. Coal demand (1.4%) also increased for the second consecutive year, following three years of declines. Growth in renewable energy (14.5%) eased back slightly relative to past trends although remained by far

the world's fastest growing energy source. The context is able to explain much of the broad contours in energy demand over the past 20 years or so. This framework predicts that the growth in energy demand should have slowed until 2018, reflecting the slightly weaker economic backdrop and the strengthening in energy prices. Instead, energy demand picked up quite markedly.[4] Digging into the Figure 4, it seems that much of the surprising increase in energy consumption in 2018 may be related to weather effects, so ascribed to the climate change phenomena. In particular, there was an unusually large number of hot and cold days across many of the world's major demand centers last year, particularly in the US, China and Russia, with the increased demand for cooling and heating services helping to explain the strong growth in energy consumption in each of these countries.

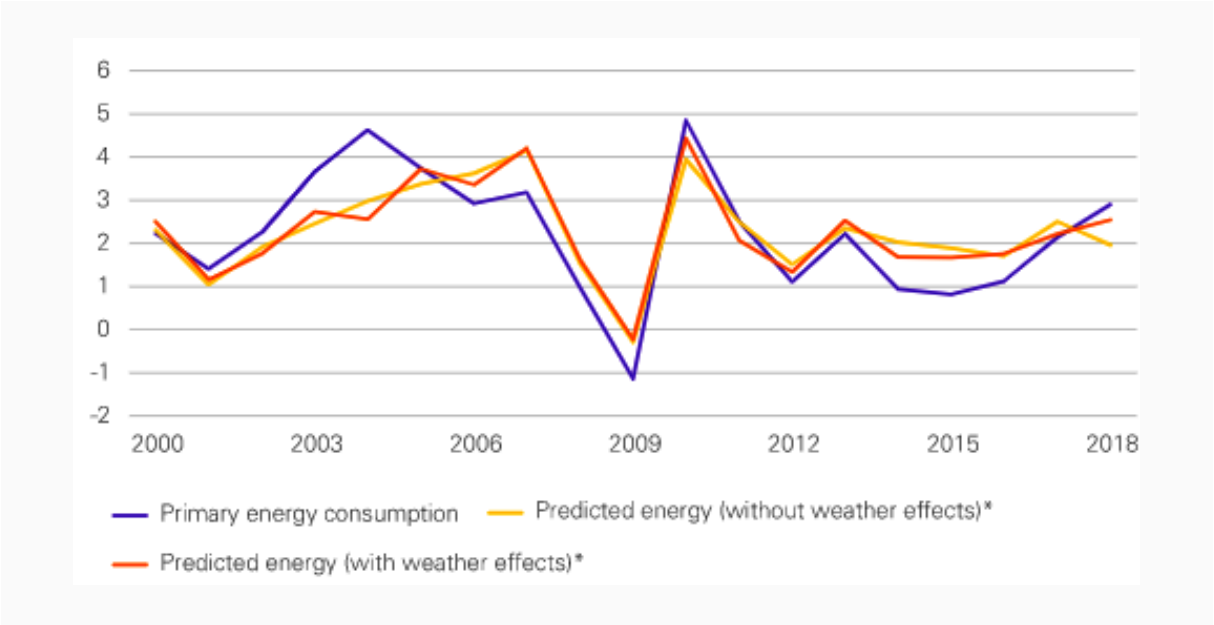

Figure 4: Global energy consumption growth (annual change, %).[4]

The growth in carbon emissions is simply a direct consequence of the increase in energy growth. Relative to the average of the previous five years, growth in energy demand was 1.5 percentage points higher in 2018 and the growth in carbon emissions was 1.4 percentage points higher. One

led to the other as the improvement in the carbon intensity of the fuel mix was similar to its recent average.[5]

Two of the planet's main environmental problems, climate change and air pollution, are closely linked. While the sources of air pollution and climate change are indeed generally similar, *i.e.*, current methods of transport, the production and consumption of goods and energy, etc., there are slight nuances that differentiate the two. Climate change is the global variation of the Earth's climate due to natural causes and human activity; it is accelerated by greenhouse gases caused by human activity. The main greenhouse gases are carbon dioxide (CO_2), methane (CH_4) and nitrous oxide (N_2O). Although CO_2 is the main gas contributing to climate change, it is not harmful to human health. The air pollution given by CO_2 and hydrocarbons, and climate change tend to get worse over time. The impacts mentioned above will be felt with increasing severity as time goes on if we do not change the energy model. The effects will be more devastating for both the planet and for people's health. CO_2 accumulates and can last at least 100 years in the atmosphere. The global level of air pollution could increase fivefold over the next half-century if the situation is not remedied.[6]

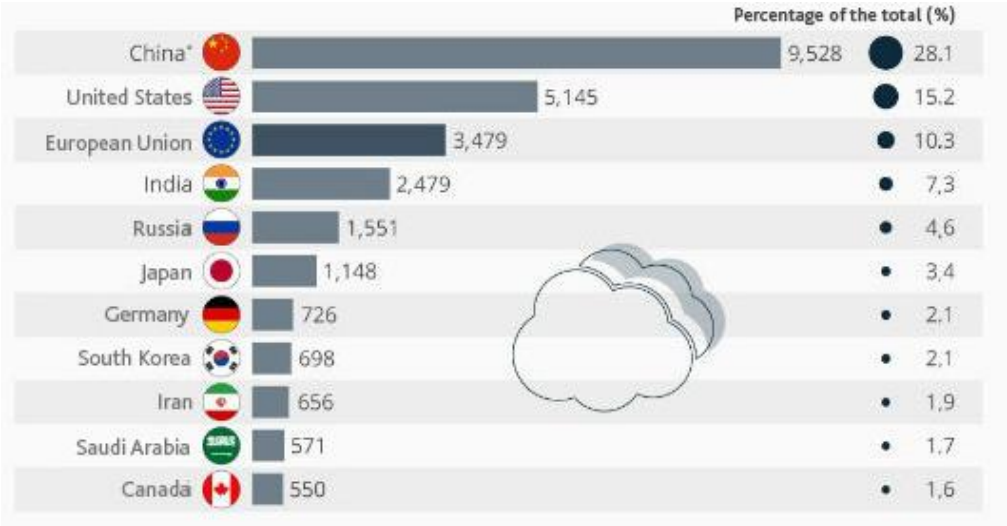

Figure 5: Countries that emit the most air pollution.[6]

Climate change is one of the world's most pressing challenges. Human emissions of greenhouse gases, carbon dioxide (CO_2), nitrous oxide, methane, and others, have increased global temperatures by around 1℃ since pre-industrial times. A changing climate has a range of potential ecological, physical and health impacts, including extreme weather events (such as floods, droughts, storms, and heatwaves); sea-level rise; altered crop growth; and disrupted water systems.

Energy storage is one of the key blocks for the flexible energy system, intended as increased storage capacity as to contribute the long-term carbonization, can enable integrated and synergized operation of these several flexibility options as well as different sectors such as heat, electricity and transport.[5] There are many different types of energy storage technologies being used and developed which can be classified based on materials used, form of energy stored, their functions, response times and storage durations. Broadly, energy storage technologies can be categorized into mechanical, electrochemical, electrical, thermochemical, chemical and thermal energy storage. According to the United States Department of Energy, Global Energy Storage database (2018)[1], pumped-hydro is the most deployed stationary energy storage technology worldwide followed by electrochemical and thermal energy storage, as summarized in Table 1:

Technology	Rated power (GW)
Pumped hydro	185.2
Electro-chemical	4.7
Thermal	4.03
Electro-mechanical	2.65
Hydrogen	0.022

Table 1: Global status of energy storage deployment.[1]

The development of affordable battery storage is increasingly being looked at as an indispensable component of sustainability. Clean, renewable energy sources are needed to help create a sustainable society: they must displace our current dependence on more problematic sources of power such as oil, natural gas and uranium. The trouble with such renewable power sources is that they might not be produced at the time when most needed, during periods of peak energy demand. The creation of energy from such sources depends on environmental conditions. Wind energy is harnessed when it is windy, and solar energy creation is dependent on sunlight. Such challenges require a storage solution such as lithium-ion batteries.[7] They enable renewable energy generation to be stored until required. Batteries offer a viable solution for storing intermittent energy supplies associated with renewable energy. Cost is lowering as production increases, and they provide hope for a future that is tied to clean renewable energy. The advancements in energy storage are encouraging, with batteries becoming cheaper and more efficient, and with longer life. Between 2011 and 2017, the cost of LIBs fell by 74%. Experience rates suggest that this cost may reduce by another 50% by 2025. Similarly, the cost is also falling for other battery technologies. Cheaper, more efficient electricity storage has the potential of bringing constructive disruptions in four distinct areas: urban power consumption, rural energy access, electric vehicles, and grid integration with the complete phasing out of coal power plants.[8] Today's price for LIB packs is roughly USD 150–120/kWh. The expected cost will decline to well below USD 100/kWh by 2024, a cost level that all future batteries must reach to be competitive.[9]

As indicated in Figure 6, there are several energy storage technologies. In general, electrochemical energy storage possesses a number of desirable features, including pollution-free operation, high round-trip efficiency, flexible power and energy characteristics to meet different grid functions, long cycle life, and low maintenance. Batteries represent an excellent

energy storage technology for the integration of renewable resources. Their compact size makes them well suited for use at distributed locations, and they can provide frequency control to reduce variations in local solar output and to mitigate output fluctuations at wind farms. Although high-cost limits market penetration, the modularity and scalability of different battery systems provide the promise of drop in costs in the coming years.[10]

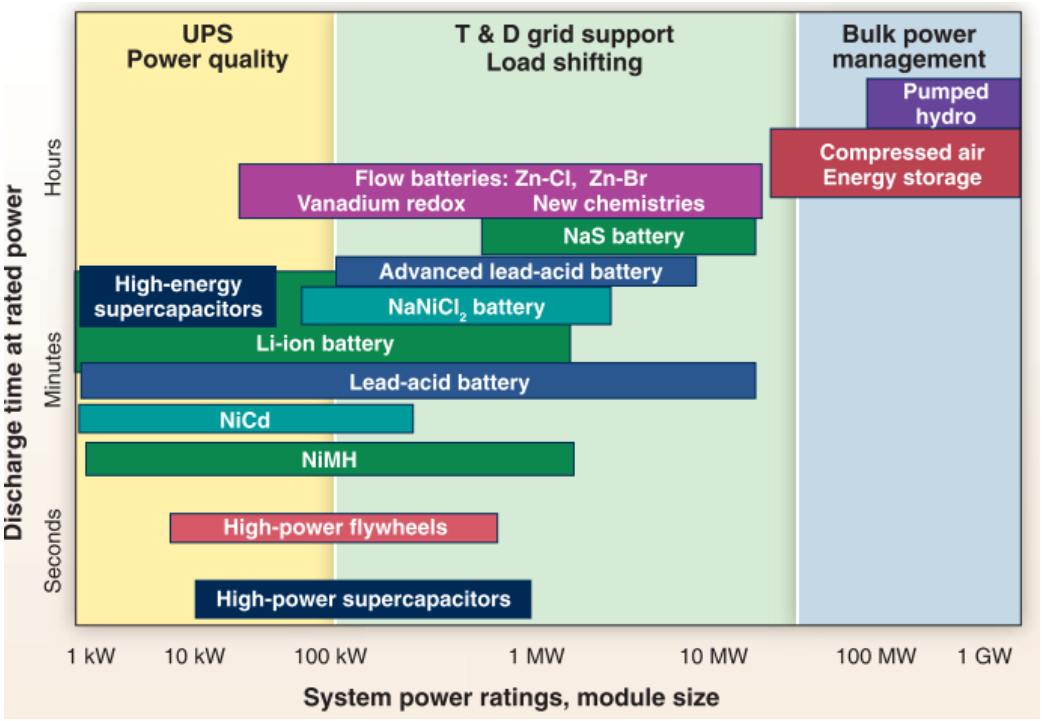

Figure 6: Comparison of discharge time and power rating for various EES technologies. The comparisons are of a general nature because several of the technologies have broader power ratings and longer discharge times than illustrated.[10]

The amount of electrical energy, expressed either per unit of weight (W h kg^{-1}) or per unit of volume (W h L^{-1}), that a battery is able to deliver is a function of cell potential (V) and capacity (A h kg^{-1}), both of which are linked directly to the chemistry of the system. LIBs are used in applications ranging from consumer electronics to electric vehicles, but also in large-scale energy storage. Lead-acid batteries are still being developed for several of these markets due

to their robust performance over a wide temperature range and low cost. Advanced lead-acid batteries are expected to gain an increased market share over the next ten years. They cannot compete, however, for use in EVs due to their considerably lower energy density.[11] The status of current commercial batteries and possible future chemistries is summarised in Figure 7, which depicts the energy performance characteristics of the major rechargeable battery types.[12]

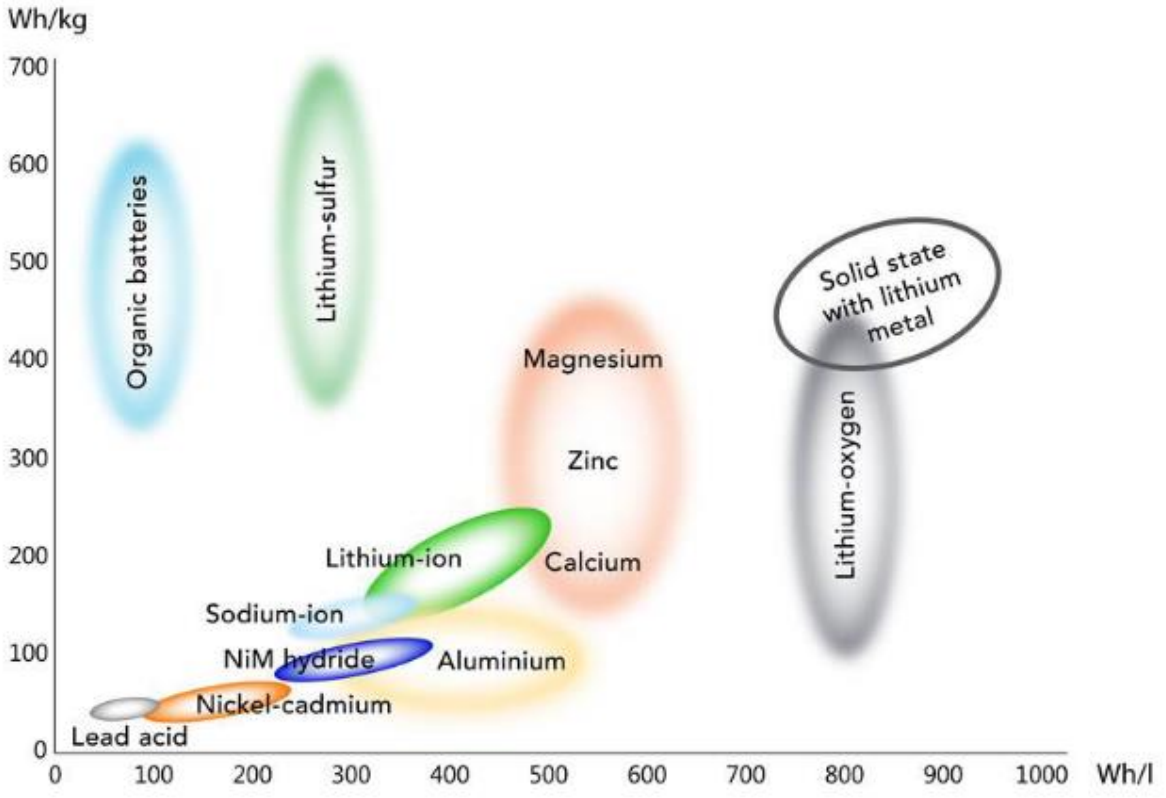

Figure 7: Current commercial batteries and targeted performance of future possible chemistries. The PLBs chemistries are given as names indicating all kinds of metal-type batteries in respective category. NiM hydride refers to nickel metal hydride.[11]

Figure 8 shows the recent decline in cost of both lithium storage batteries and renewable energy sources - costs that are forecasted to continue to fall. Battery storage projects with four-hour duration cost $186/MWh in the second half of 2019, a 35% decrease since the beginning of 2018, and a 76% drop since 2012. Onshore and offshore wind prices have also dropped by

about 57% since 2009, and utility scale PV system costs have fallen by 86% over the last decade. Large-scale battery-plus-solar system prices are becoming more competitive with traditional generation, especially in areas with abundant solar energy output, like the South America. With more extreme weather, they may be seen as economically viable, particularly when potential financial losses from grid outages are considered.[13]

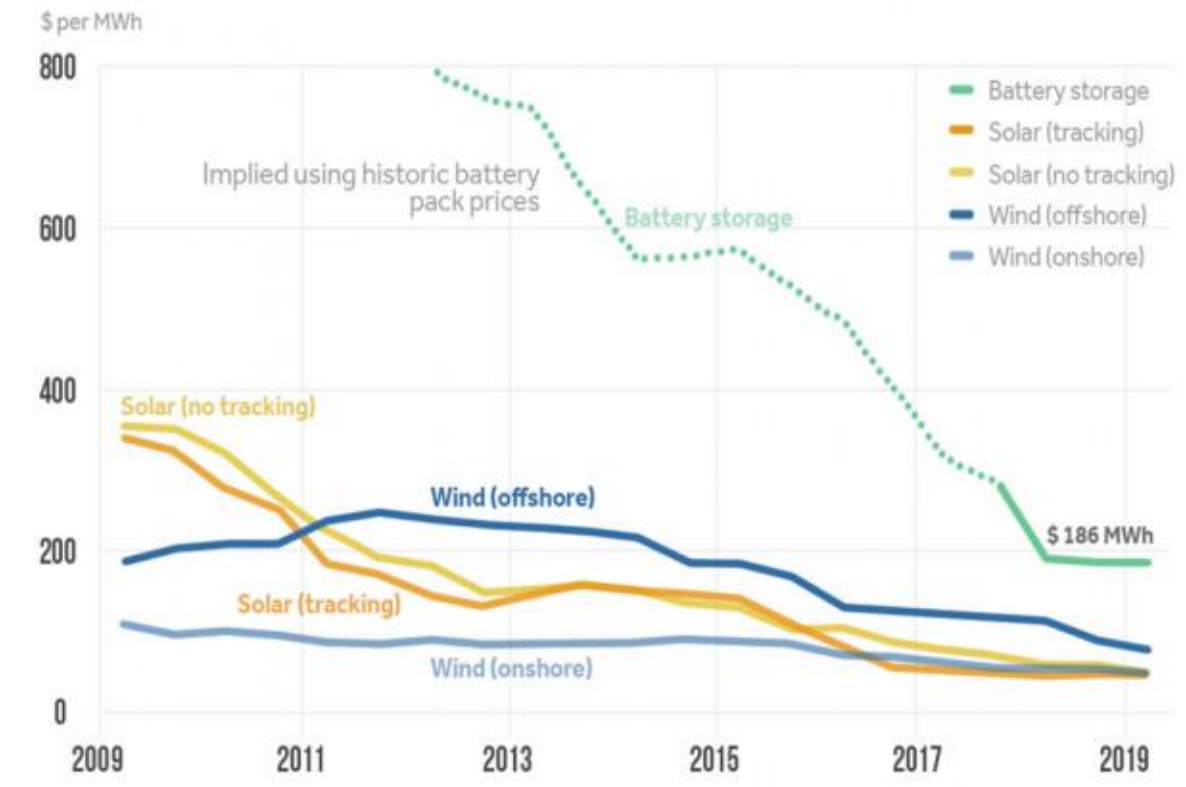

Figure 8: Solar, wind and batteries price falling.[14]

2. How do batteries work? An overview of an electrochemical cell

An electrochemical cell is a device that allows converting chemical energy into electrical energy. It consists of a negative and a positive electrode (that are also improperly called anode and cathode, respectively) and an electrolyte. Each electrode exhibits its own electrochemical potential that depends on its physicochemical nature.[14] If the two electrodes are allowed to exchange electrons through an external circuit, the system reacts spontaneously to reach the equilibrium, *i.e.*, to minimize its free energy. The redox (half) reactions occurring at the electrodes produce a spontaneous electrons flow from the negative side to the positive one. This electric current is confined in the external circuit by the presence of the electrolyte, which acts as an electron insulator. In order to ensure the electro neutrality of the system, however, the electron's flow must correspond to an ion transfer in the electrolyte, which has to be therefore an ionic conductor. When the reactants at both sides are completely consumed by the electrochemical reactions, the electrons' flow stops, *i.e.*, the system has reached the equilibrium and the cell is discharged. Such electrochemical devices can be considered as power supplies that end their activity after the first discharge and should be therefore replaced by new charged cells. In some cases, depending on the chemistry of the system, the reactions leading to the discharge of the cell can be reversed by applying an opposite current from the exterior, and the cell can be thus brought back to its initial state. The first irreversible devices are also called primary cells, whilst the rechargeable ones are named secondary cells (Figure 9); this storage system can be used as power supplies, portable consumer devices and battery storage power station. Unlike primary cells, they can be in principle built in their discharged state.[15]

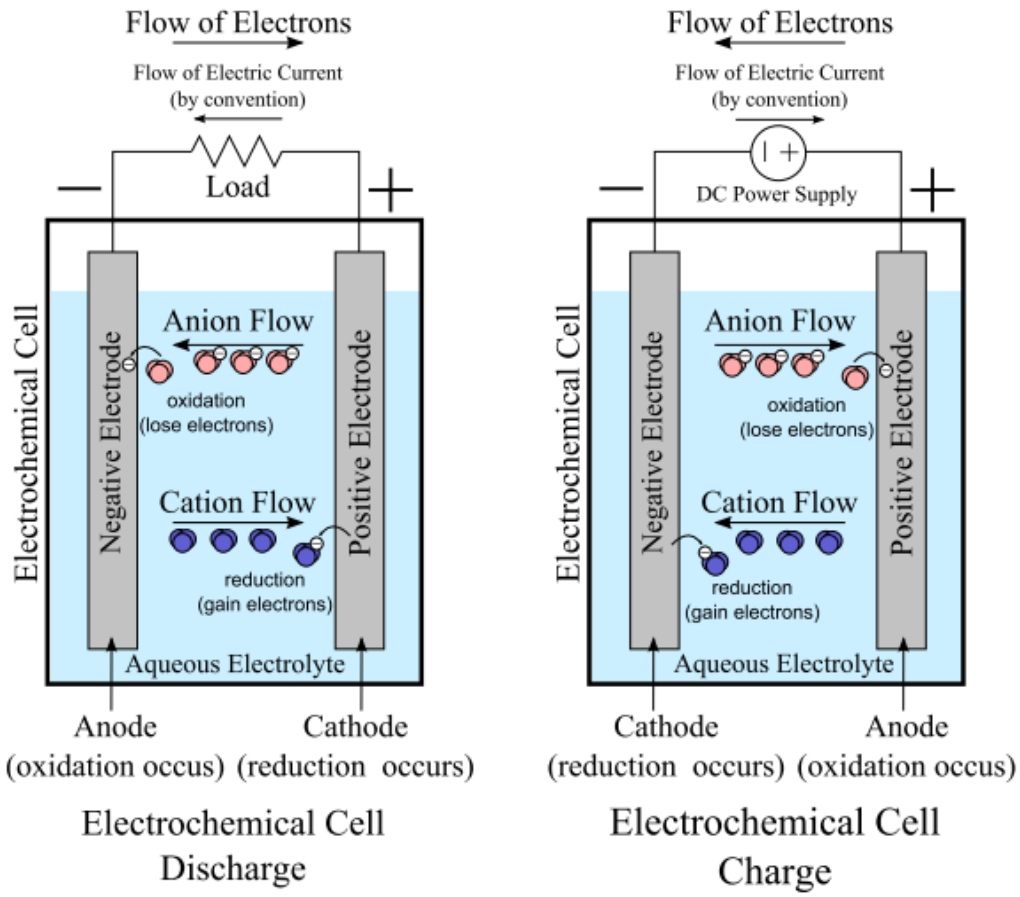

Figure 9: Schematic representation of the discharge and charge process in a secondary cell.[14]

The Daniell cell is an improvement of the Volta's cell, which was invented by the British John Daniell in 1836.[16] It exploits the two electrodes made of zinc and copper in order to produce a difference in potential of 1.1 V (see Figure 10). For this, the zinc anode is immersed in a solution of zinc sulfate ($ZnSO_4/H_2O$) and the copper cathode is immersed in a copper sulfate solution ($CuSO_4/H_2O$). Reactions at the level of the two semi-cells are thus the following:

1) Anode: $Zn \rightarrow Zn^{2+} + 2e^-$

2) Cathode: $Cu^{2+} + 2e^- \rightarrow Cu$

The electrons produced at the anode and received at the cathode circulate within the circuit charged by the cell. The terminal marked negative is the source of electrons that will flow

through an external electric circuit to the positive terminal with the help of an electrolytic bridge (a saline bridge) containing potassium nitrate (a solution containing the ions K^+ and NO_3^-). When power is provided by the cell, the ions NO_3^- and K^+ derive towards zinc and copper sulfates solutions:

- For each ion produced Zn^{2+}, two ions NO_3^- are levied from the electrolytic bridge towards the zinc sulfate solution.
- At the same time, an ion Cu^{2+} is transformed in a copper atom Cu on the cathode: two ions K^+ are then levied from the electrolytic bridge towards the zinc sulfate solution.

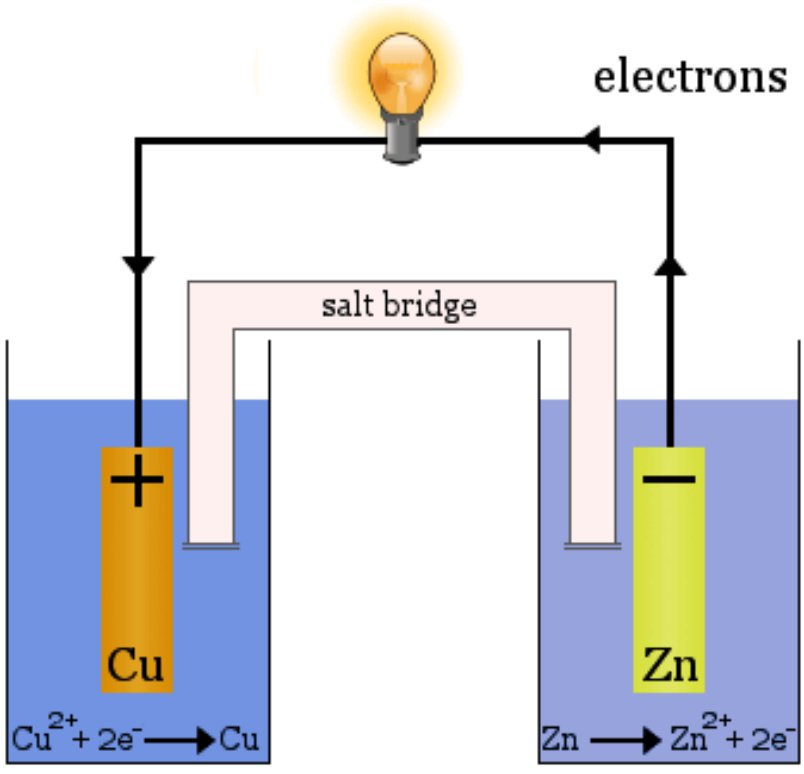

Figure 10: Scheme of Daniell cell.[15]

By stacking, in series or in parallel two or more electrochemical cells, it is possible to increase either the voltage or the capacity, respectively, of the resulting system, which should be called

"battery". It is worth mentioning that nowadays the words "electrochemical cell" and "battery" can both be referred to a closed electrochemical power source, with no distinction between one or several connected electrochemical cells. The energy ε that can be stored in a battery can be calculated according to the next equation:

$$\varepsilon_{cell} = E \cdot C$$

Where E is the cell potential and C is the capacity ($mA{\cdot}h{\cdot}g^{-1}$ or $A{\cdot}h{\cdot}kg^{-1}$). The whole potential of the cell can be obtained by the following expression:

$$E = E_{red} - E_{ox}$$

Here E_{red} and E_{ox} are the potentials where, respectively, the reduction and oxidation reactions take place. In a general fashion, the electrode potential can be calculated using the Nernst equation:

$$E_{el.} = E^0_{el.} + \frac{RT}{nF} ln \prod_i a_i^{\nu_i}$$

Where R is the gas constant (8.31 $J{\cdot}mol^{-1}{\cdot}K^{-1}$), T the absolute temperature (K), n the number of transferred electrons, F is the Faraday constant (96485 $As{\cdot}mol^{-1}{\cdot}K^{-1}$), a is the activity of the species (/), ν is its stoichiometric coefficient (/) and E_0 is the standard electrode potential (V vs. reference).[17] If the electrode is coupled to a hydrogen standard electrode, the standard electrode potential E_0 can be related to the Gibbs free energy of the cell reaction via the following equation:

$$E^0_{el.} = -\frac{\Delta G^0}{nF}$$

The capacity, C ($mA{\cdot}h{\cdot}g^{-1}$), represents the quantity of charge stored into the battery; and is defined according to the following equation:

$$C = \int_0^t I(t)dt$$

Where I (mA) is the current intensity flow over the time the time t (h).

Capacity of the whole battery can be also calculated using this equation, when capacities of both electrodes are known:

$$C = \frac{C_+ C_-}{C_+ + C_-}$$

According to the Faraday's law, electrode capacity can be expressed as follow:

$$Cx = \frac{mzF}{M}$$

Where m is the mass of the electrochemical active material (g) and M is its molecular weight ($g \cdot mol^{-1}$), z is number of transferred electrons per ion (/), F is the Faraday constant (26800 $mA \cdot h \cdot mol^{-1}$ derived from 96485 $A \cdot s \cdot mol^{-1}$). In order to compare the capacities of different materials, it is common to adopt the gravimetric specific capacity, thus dividing last equation with the mass m. The gravimetric specific capacity, commonly expressed in $mA \cdot h \cdot g^{-1}$, is therefore one of the crucial parameter when considering the choice of a potential electrode material. Another key factor is the operating voltage, which should be the lowest for a negative electrode and the highest for the positive one, in order to maximize the overall energy of the cell. It is worth noting that this is an ideal approach that does not take into account neither the non-active materials and cell components that reduce the capacity nor the limitation on the voltage window imposed by the electrolyte stability.

Coulombic efficiency (/) is the ratio between the discharge and charge capacities ($A \cdot h$ or $mA \cdot h$) of the battery:

$$q_{Ah} = \frac{Q_{discharge}}{Q_{charge}}$$

This parameter is extremely important because it shows us the level of side reactions that are taking place during operation of the battery. If we want to make a battery that can be discharged and charged many times, then the Coulombic efficiency should be as close to unity as possible. Because all side reactions mean to some degree decomposition of the electrolyte and degradation of electrode materials, they lead to shortening of the battery life and loss of capacity.

3. Li-ion technology roadmap: advantages and limitations

3.1. How LIBs revolutionized our society

A modern "energy revolution" was provided by the discovery and the subsequent commercialization of LIBs, which dramatically changed communications, work, mobility and lifestyle of western society in last 25 years. They stem from the pioneering studies on the reversible intercalation of Li^+ into host materials. The motivation for using a battery technology based on Li metal as anode relied initially on the fact that Li has the lowest standard electrode potential (–3.04 V versus standard hydrogen electrode) as well as the lightest (equivalent weight 6.94 $g \cdot mol^{-1}$) metal, thus facilitating the design of storage systems with high energy density. The overwhelming appeal of Li-electrochemistry lies in its low molecular weight and small ionic radius, which is beneficial for diffusion. The lowest standard potential enables high-output voltages and therefore high-energy densities. Such attractive properties, as low self-discharge rate and no memory effect, coupled with its long cycle life and rate capability, have enabled Li-ion technology to capture the portable electronics market and make in-roads in the power tools equipment field. During the 70's, layered TiS_2 was found to reversibly insert Li^+ and hence was proposed as a possible positive electrode in lithium batteries in a working prototype by Whittingham.[18] Beside this pioneering work, more studies were performed in order to get insight into their mechanism. One of the most important contributions was provided by Peled and co-workers, who demonstrated the *in situ* formation of a SEI, due to parasite reactions between Li metal and the electrolyte.[19] Unfortunately, SEI on the surface of the Li metal negative electrode hinders uniform Li plating during charge, thus leading to the

formation of dendrites. Along subsequent cycles, dendrites may grow and create internal short circuits in the battery, with consequent risk of overheating and explosions.[20] The way to circumvent this major issue was the replacement of the metallic Li negative electrode with another material able to insert Li ions at relatively low potential. Yazami and Touzain observed that Li ions can be reversibly inserted into graphite (0.2 V vs. Li^+/Li) without forming dendrites. In parallel, Mizushima and co-workers tried to reversibly remove Li from several layered $LiMO_2$ (M = Cr, Co, Ni). In particular, $LiCoO_2$ allows reversible Li extraction at 4 V vs. Li^+/Li, opening the gates for high potential positive electrodes.[21] These two major findings paved the way for the further realization and commercialization by Sony in 1991 of the so-called LIBs. A general scheme of a typical LIB is presented in Figure 11. The negative electrode consists of graphitic carbon that holds Li in the interlayer between graphene layers, whereas the positive electrode is a Li-intercalation compound, usually an oxide because of its higher potential. $LiCoO_2$ is characterized by 2D layered structure, while $LiMn_2O_4$ is characterized by a 3D spinel. Both electrodes are able to reversibly insert and remove Li ions from their respective structures. On charging, Li ions are removed or deintercalated from the layered oxide compound and intercalated into graphite. The process is reversed on discharge. The electrodes are separated by a non-aqueous electrolyte that transports Li ions between the electrodes.[22]

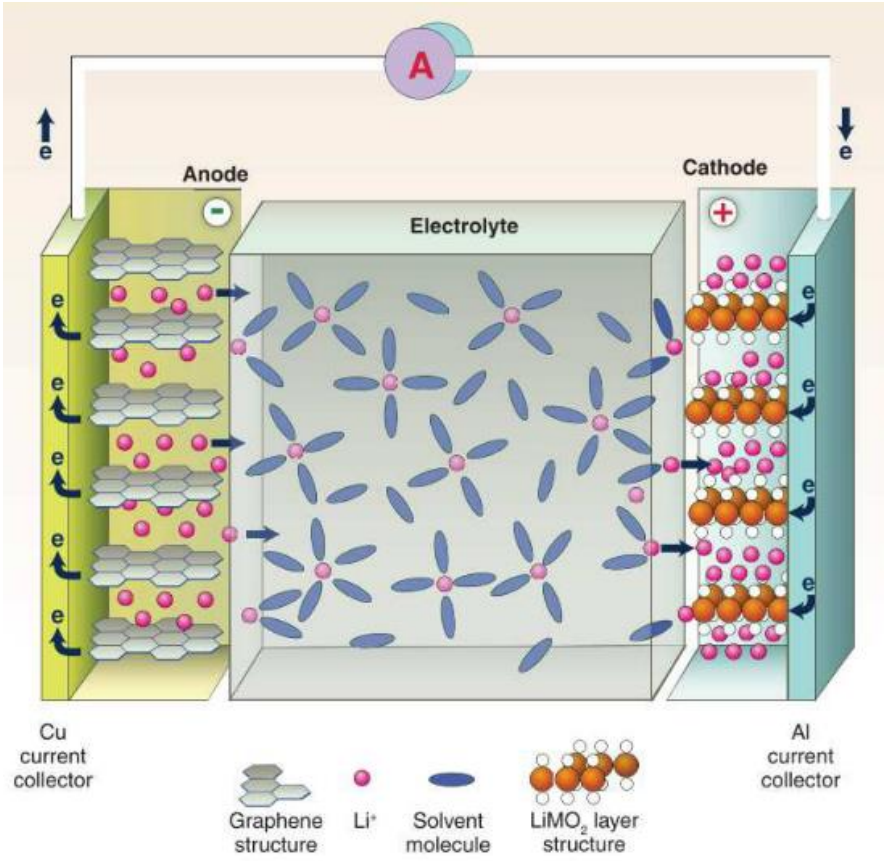

Figure 11: *Scheme of a LIB.*[22]

The graphite-based negative electrode undergoes Li^+ de-intercalation, according to the following equation:

$$Li_xC \rightleftarrows C + {}_xLi^+ + {}_xe^-$$

Li^+ migrates toward the positive $Li_{1-x}CoO_2$ in order to obtain the reduced $LiCoO_2$:

$$Li_{1-x}CoO_2 + {}_xLi^+ + {}_xe^- \rightleftarrows LiCoO_2$$

Electrolyte features a lithium salt (*e.g.*, $LiPF_6$) dissolved in a mixture of liquid carbonates (ethylene carbonate, propylene carbonate, etc.).

LIBs are also regarded as the battery of choice for powering the next generation HEVs as well as plug-in EVs, provided that improvements can be achieved in terms of performance, cost, and safety. EVs are the technology of choice for eco-friendly car buyers because they have no

emissions tied to their operation; they can be powered with clean, renewable energy; and even when charged with power from non-renewable sources, the inherent fuel efficiency of electric motors versus internal combustion engines means they release less carbon per mile (when similar vehicles are compared). Even though they're technically more efficient, how much cheaper electric vehicles are to drive depends on the local cost of electricity and gasoline (or diesel). For example, The LIB packs that power some EVs have to be plugged into 240 volts by special hardware which represent additional cost. Clearly, renters and those without garages are at a disadvantage.[23]

Because long-term stability, high-energy density, safety, and low cost are common to batteries for both automotive and grid applications, considerable synergy should exist between the two areas, although there will be certain differences. In fact, nowadays, the greatest challenge for battery researchers is to make price-competitive batteries that could power EVs and HEVs, which would be able to compete with traditional vehicles with internal combustion engines in all aspects (vehicle price, driving range, recharging time). The most important characteristics of batteries for electric propulsion are their price, gravimetric and volumetric energy density (driving range), power (recharging time), operational safety and last but not least important the lifetime of the battery. Because the price of the battery pack is estimated to be around 25% of the price of the EVs ($140 per kWh) future advances in battery technology should help with lowering the price of EVs and HEVs.[24] In the light of these facts, the research is focused on driving down the cost of batteries, increase the capacity utilization of existing battery technologies and developing new technologies that could offer similar or even higher energy densities and at the same time be significantly cheaper. Transitioning to EV mobility is a critical component of the larger transition to sustainable energy systems.[25] There are two major factors that will determine the mass adoption of electric vehicles. First, the charging infrastructure, and second, the cost of battery storage. The government needs to support the former,

particularly in developing countries, while the market will drive the latter. Taking into account the cost of electricity and the cost of petrol, the on-road energy consumption of a EVs car is 70% cheaper than that of a petrol-based car. However, the cost of a EVs-car is up to 50% higher (Figure 12). Thus savings from the cost of fuel can take 2-4 years to compensate for the higher upfront cost.

Figure 12: *Tesla "Model 3", a fully- electric four-door automobile with a range of 345 km at a cost of 35000 US$ (2017).*[22]

3.2. Growth in energy demand and price forecast

Lithium is the 25th most abundant element on Earth; LIBs has proven crucial for the advancement of portable electronics and is also finding new uses as economies look for cleaner automotive and energy solutions. Most notable though, they have contributed to the huge growth in the smartphone industry over the past few years.[26] The resulting battery offers a number of benefits over competing materials. Lithium-ion batteries have the highest output of energy for its weight and therefore last longer than similar sized rival cells, due to their higher energy density, which can be up to three times greater than other materials. LIBs have a longer runtime from a single charge and also don't suffer from decreased charge capacity over time, unlike nickel-cadmium and nickel-metal hydride batteries. A demand forecast up to 2020 is given in four different scenarios, including the increasing demand in electric mobility, forced by political driven influence.[27]

Lithium is an essential metal with widespread applications in next generation technologies, such as LIBs. Because lithium cannot be substituted in most applications, a steady increase of 8–11% in annual demand is anticipated. Furthermore, the increasing production of electric cars has been predicted to be a major driver in growing lithium demand. Since 2000 the global lithium production for use in batteries has increased by approx. 20% per annum, amounting to 35% of the overall lithium consumption in 2015. According to USGS (United States Geological Survey), estimated reserves of more than 14 mill. t are available. Resources are considerably greater and are reported to amount to approx. 34 mill. t. In 2014, the global lithium production reached roughly 32,000 t, corresponding to 170,000 t LCE (lithium carbonate equivalents).[28] Figure 13 shows the geographical distribution of global lithium resources; almost 60% are found in South America, especially Chile, Bolivia and Argentina.

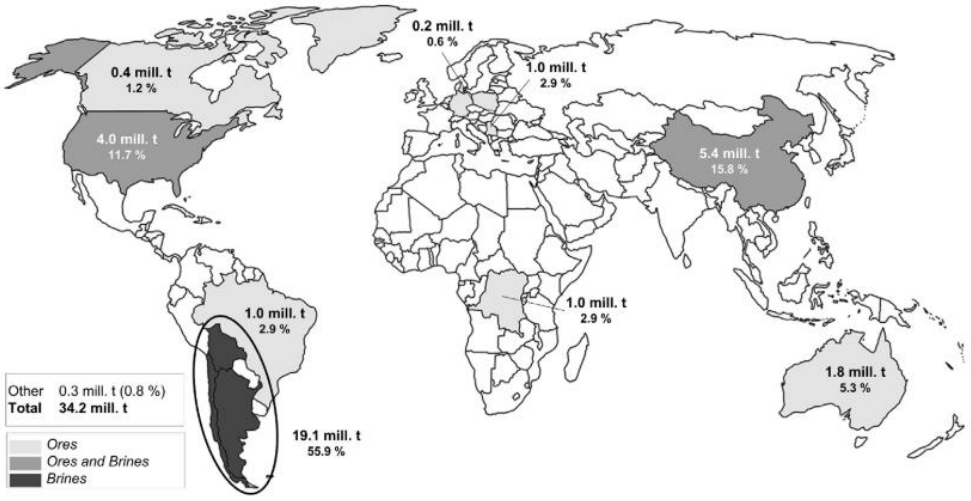

Figure 13: Geographical distribution of global lithium resources.[24]

The production volume is shown in Figure 14, which includes Global annual production of lithium, represented in lithium carbonate equivalents (LCE).

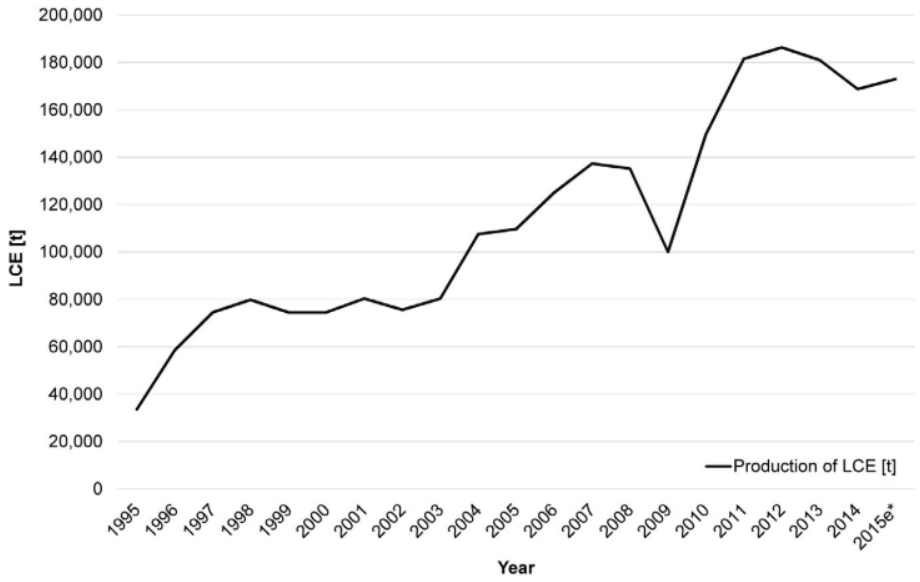

Figure 14: *Global annual production of lithium.*[24]

The global production of lithium rose steadily from 1995 starting at around 30,000 t LCE and reaching close to 140,000 t LCE in 2007, whereby the first significant quantitative decrease

happened in 2009, the year of the economic crisis. Subsequently, for the following five years the production volume increased by 70%. Metal production begins with either primary or secondary resources. Primary resources, or ores, contain relatively high concentrations of metals and are generally found at depths up to 1 kilometer beneath the surface. Secondary sources include all metals that have entered but no longer serve a purpose in the economy. Due to huge lithium primary reserves and resources, which can be exploited at rather low cost, lithium from secondary sources had no significant impact on the total supply so far. Currently, the proportion of recycled lithium is less than 1%. Indeed, some scenarios agree on the importance of lithium recycling, predicted to attain relevance in about 2030 and are forecasted to substitute up to 25% of the supply in 2050.[24]

Lithium has a wide range of applications. The majority of the annually extracted lithium (35%) is consumed in batteries, followed by glass and ceramic applications (32%). Other important applications include lubricants with a share of 9%, continuous casting as well as air treatment with 5% each, polymer production with 4% and aluminum production with 1%. Further industrial applications (9%) are among others, sanitization, organic synthesis, construction, pharmaceuticals, alloys and alkyd resins such as other minor end uses. (Figure 16).

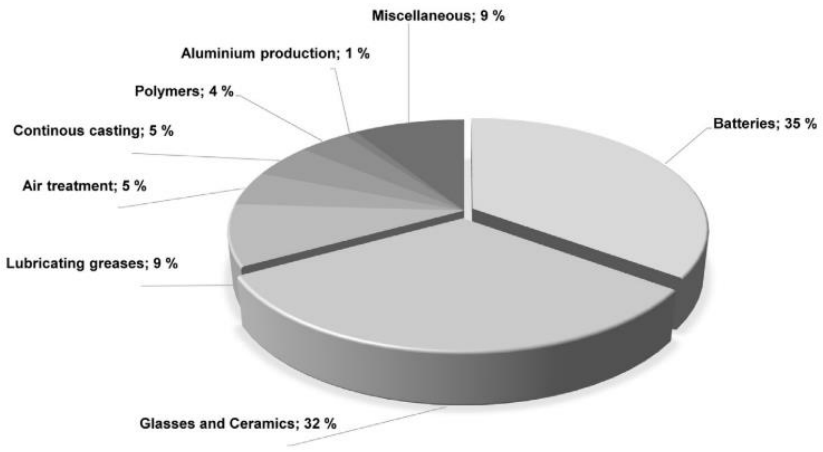

Figure 15: *Application areas of lithium.*[24]

In secondary batteries, lithium compounds are used inside electrodes and in electrolytes. For production, typically lithium hydroxide (LiOH), lithium carbonate (Li_2CO_3) and several salts are employed. According to the Basic-scenario forecast, lithium demand for batteries is significantly rising by approx. 34% into 2020, which corresponds to an annual average growth rate of about 7%. The demand is likely to increase due to the growing number of electrified drives. Beside Tesla, other major vehicle manufacturers have promoted the production of electric and hybrid vehicles. According to Financial Times Tesla's Gigafactory will require 24,000 t $LiOH \cdot H_2O$ (~21,000 t LCE) per annum. Lithium consumption (in Tesla) is increasing by 42 % between 2017 and 2020, driven by increased battery production. Price increases in the near term are expected to be followed by decreases from 2019 onward as lithium production increases. Battery production is also highly reliant on cobalt and nickel; they both have a stabilizing effect and prevents cathode corrosion that can lead to a battery fire. Cobalt prices doubled between 2016 and 2017, with LIB production fueling 49 % of Co demand in 2017. The price is predicted to grow to 61 % by 2022. The cost of LIB production continues to fall. Elon Musk of Tesla believes that LIB costs will fall to 100 $/kWh by 2020, down from a price of 1,000 $/kWh only as recently as 2010. Bloomberg projects battery storage costs to drop below 50 $/kWh by 2030.[29] Current cost is in the 100 $/kWh range. As the cost drops, alternative energy sources will become increasingly competitive with non-renewables conventional energy projects.[28] LIBs exceeding 8 grams but no more than 25 grams may be carried in carry-on baggage if individually protected to prevent short circuits and are limited to two spare batteries per person. From a theoretical perspective, there is no metallic lithium in a typical LIB; there is, however, equivalent lithium content that must be considered. For a Li-ion cell, this is calculated at 0.3 times the rated capacity (in ampere-hours). A 2 Ah 18650 Li-ion cell contains 0.6 grams of lithium. On a typical 60 Wh laptop battery with 8 cells (4 in series and 2 in parallel), this adds up to 4.8 g.

LIBs demand is set to increase about 10 fold between 2018 and 2030 (see Figure 16). The forecast demand increase is due mostly to the electric vehicle boom, as experts predict electric cars going from ~2.0% market share in 2018, to ~25-35% by 2030. This is a 15 fold increase in electric car demand to 2030. Added to this will be consumer electronics, other non-car EVs (including e-bikes, e-3 wheelers, e-trucks, e-buses, e-ships, e-trains, & e-planes etc.), and energy storage.[30]

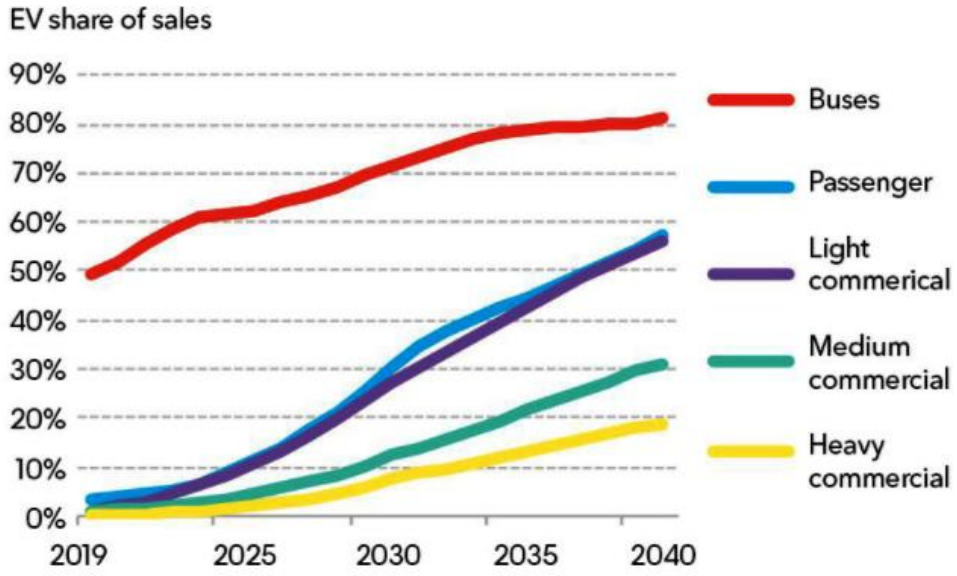

Figure 16: *EVs share of annual vehicle sales by segment.*[31]

One of the main obstacle that hinders the large-scale applications of LIBs in EVs concerns the safety. The most catastrophic failure mode of a LIB is the thermal runaway; it describes a process which increase in temperature changes the conditions in a way that causes a further increase in temperature of the battery, inducing smoke, fire, and even explosion.[32] It can be caused by several conditions, as overcharging, internal short circuiting and vehicle collision (in the case of EVs). The abuse conditions can lead to the decline of battery performance and

they are categorized in into mechanical, electrical and thermal abuse. Regarding electrical abuse, the decline of electrochemical performance is related to the increase of internal resistance and the formation of non-electrochemically active lithium dendrites on the anode surface during the low-temperature cycling. When a LIB charges, lithium ions travel from the cathode to the anode; the ions flow the other way during discharge. At a lithium metal anode, lithium ions leave and return to the surface unevenly. This means that after several charging cycles, spiny projections called dendrites begin to grow from the electrode's surface (Figure 17). As these lithium dendrites grow, they can pierce the separator, touch the cathode and short circuit the cell, and this can result in thermal runaway and starts fires. Successful commercialization of rechargeable batteries containing lithium metal anodes has been hampered by the inherent instability of lithium metal, especially during the charge.[33]

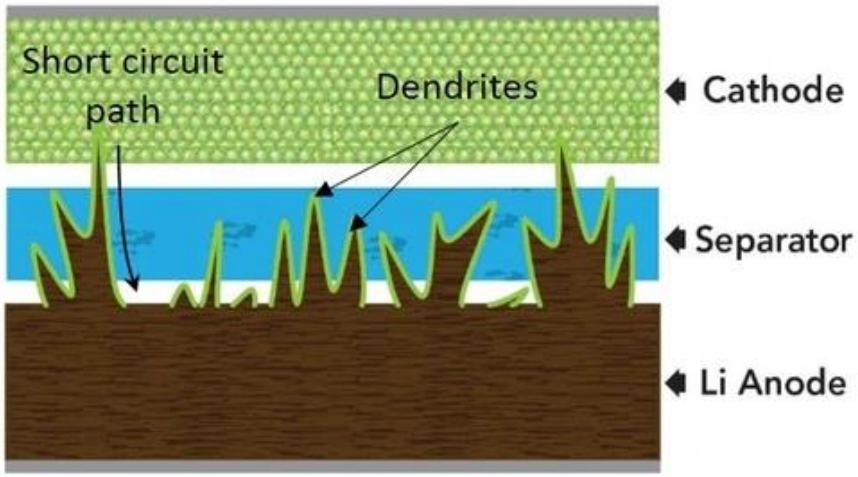

Figure 17: *Dendrite growth in lithium battery leads to failure.*[34]

Electrolyte reacts with these lithium dendrites at elevated temperatures to produce gases, which makes the internal pressure of the batteries increase continuously, causing safety problems such as battery explosion and electrolyte leakage.[35] They compromise even the thermal stability of

SEI, accelerating the decomposition of it and leading to a series of thermal runaway chain reactions (Figure 18).

Figure 18: *Scheme of phenomena responsible for LIBs failure.*[35]

Wang et al.[36] studied the relation between the formation the lithium dendrites and thermal runway of LIBs, giving the conclusion that dendrites grown is favored in LIBs of 10 years calendar life, due to increase of internal resistance during low-temperature cycling. Lithium dendrites reduces the temperature of self-heating (from 80° to 50°C) and temperature of thermal runway (from 170° to 100°C), so the time for the battery to reach thermal runway temperature is shorter.

Numerous LIB explosions were reported in the worldwide on the internet (Table 2), especially for the cell phones and laptops LIBs.

No.	Date	Accidents replay	Fire causes
1	18 July, 2011	EV bus catch fire, Shanghai, China	Caused by overheated $LiFePO_4$ batteries
2	11 April, 2011	EV taxi catch fire, Hangzhou, China	Caused by 16 Ah $LiFePO_4$ battery
3	3 September, 2010	A Boeing B747-400F cargo plane catch fire, Dubai	Caused by overheated lithium batteries
4	26 April, 2010	Acer recalled 2700 laptop batteries, as Dell, Apple, Toshiba, Lenovo and Sony done in 2006	Potential overheating and fire hazards
5	March, 2010	Two iPod Nano music player overheating and catching fire, Japan	Caused by overheated lithium batteries
6	January, 2010	Two EV buses catch fire, Urumqi, China	Caused by overheated $LiFePO_4$ batteries
7	July, 2009	Cargo plane catch fire before fly to USA, Shenzhen, China	Caused by spontaneous combustion of lithium ion batteries
8	21 June, 2008	Laptop catch fire in a conference, fire burning 5 min, Japan	Caused by overheated battery
9	June, 2008	Honda HEV catch fire, Japan	Caused by overheated $LiFePO_4$ batteries
10	2006–now	Tens of thousands of mobile phone fires or explosions	Caused by short-circuit, overheating, etc.

Table 2: *Some LIB accidents in the past few years.*[20]

In recent years, significant attention has been directed to the development of Li/S and Li/O_2 battery systems. These systems are both extremely interesting due to significantly higher capacities of their cathodes than the inorganic cathodes from LIBs; in fact, the sulfur cathode theoretically offers 1672 mAh/g and the O_2 cathode 3350 mAh/g. Practical capacities are significantly lower because cathode material needs to be properly structured to allow efficient transport of ions and electrons and active material utilization. The Li/S system suffers from problems connected with the insulating nature of sulfur and Li_2S produced at the end of the discharge; moreover, dissolution of Li polysulfides species and the polysulfide-shuttle effect decreases dramatically the cyclability and performance of these systems.[37] All these issues are being addressed and it seems that Li/S batteries are close to commercialization. On the other hand, Li/O_2 batteries are much more complicated and less understood, so their investigation is only in its early stages.[38]

In conclusion, mass-market EV adoption and broader storage applications remain constrained by current limitations of LIBs. These include limited capacities of oxide intercalation cathodes (~150 – 280 mAh/g practical) and, secondarily, of graphite (372 mAh/g theoretical); which results in limited commercial cell-level energy densities (~305 Wh/kg and 700 Wh/L). Although the replacement of graphite with Li metal would significantly increase gravimetric and volumetric energy, development of metallic lithium batteries is impeded by the tendency

of Li to form dendridets during cycling, an unacceptable safety hazard. Development of innovative batteries, using different metal anodes, with improved energy density and cost vs. existing commercially available LIBs is essential.

4. Which strategies to go beyond Li-ion batteries?

The development of post-lithium-ion technologies is considered to be a promising pathway to achieving the keys to increase the market acceptance of the EVs technologies; the goal is to reduce cost and increase range of EVs which will require further advances in battery technology. The worldwide rechargeable battery market is continuously growing and the cost of the state-of-the-art LiBs has been reduced by 8% annually in the last decade at the pack level. It is now reaching its fundamental limits in terms of energy density.[39] Moreover, the risks of limited lithium supply and/or significantly increased prices cannot be ignored. Consequently, sustainable battery chemistries based on other elements and higher energy densities must be developed, in line with recent ranking of next-generation batteries. The quest for next-generation batteries must be based on a rational approach targeting long-term sustainable solutions by using abundant materials and eco-efficient production protocols. It is highly expected to meet the demand by new huge energy-consuming applications. Thus, development of PLIB's may require the substitution of lithiated graphite or alloy-based anodes with pure metal anodes. Despite its propension to form dendridets, lithium metal is considered to be a strong candidate due its high volumetric capacity of 2062 mAh/mL and highly negative reduction potential of −3.04 V vs SHE (Figure 19). The aim of increasing the energy density of batteries is a long-lasting game with rather simple rules. One needs to (1) increase the cell voltage (difference in working potentials between the positive and the negative electrode active materials), (2) increase the specific capacity of the positive and negative electrode active materials, and/or (3) decrease the dead weight of the cell (separator, electrolyte, cell packaging, etc.) While significant progress has been made over the last decades in order to improve the

cell engineering, the quest for new battery chemistries (negative and positive electrode materials) is still in progress.[40]

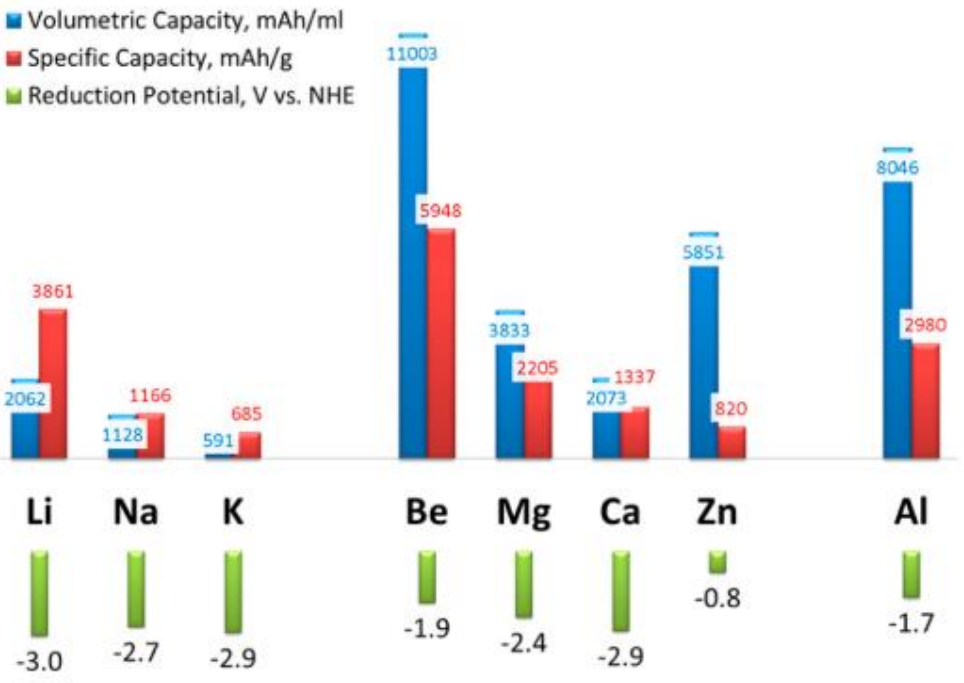

Figure 19: *Capacities and reductive potentials for various metal anodes employed in PLiBs (Be is not employed).*[32]

Research in lithium-ion cathodes has evolved toward attempts to achieve two-electron reduction at a single metal redox center. This offers the promise of doubling the capacity of current cathode materials but has to overcome the challenge of inserting two lithium cations for every transition metal center in the cathode material. This is not trivial due to the volume expansion resulting from insertion of two lithium cations. Interestingly, two-electron reduction can be achieved by insertion of a single divalent cation, such as magnesium, which has a similar radius to that of monovalent lithium cation (ionic radius of Li^+ is 0.9 Å and of Mg^{2+} 0.86 Å) as shown in Figure 20, thus circumventing the excessive volume expansion problem. However, the higher charge density of magnesium cations poses solid-state diffusion challenges. A battery containing a calcium anode may have some advantages over a battery containing a

magnesium anode due to the more negative reductive potential of calcium (~500 mV more negative). In addition, the ionic radius of the calcium cation (Ca^{2+}) is 33% (1.00 Å) larger than that of Mg^{2+} while carrying the same charge (Figure 21). This lower charge density may allow faster solid-state diffusion in cathodes. Interestingly, volumetric capacities higher than magnesium or calcium can be achieved by denser multivalent metals such as aluminum and zinc. Unfortunately, their reduction potentials are significantly less negative. The reduction potential of zinc is 2.2 V vs. SHE more positive than lithium. It has been demonstrated that Zn can be reversibly electroplated and stripped in a safe aqueous electrolyte. However, a low Coulombic efficiency has been obtained in acidic and neutral electrolytes due to unavoidable side reactions. In alkaline electrolytes, battery operation is hindered by the dendritic deposition morphology. While the reduction potential of aluminum is −1.7 V vs SHE, its volumetric capacity (8045 mAh/mL) is nearly four times higher than that of lithium. Unlike calcium, electrodeposition of aluminum has a rich history due to the well-established aluminum electroplating industry. While offering impressive Coulombic efficiencies close to 100%, aluminum electrolyte baths are often corrosive, this hinders the use of high-voltage cathodes for rechargeable Al batteries. There are however several reports of rechargeable aluminum batteries operating below 1 V.[30]

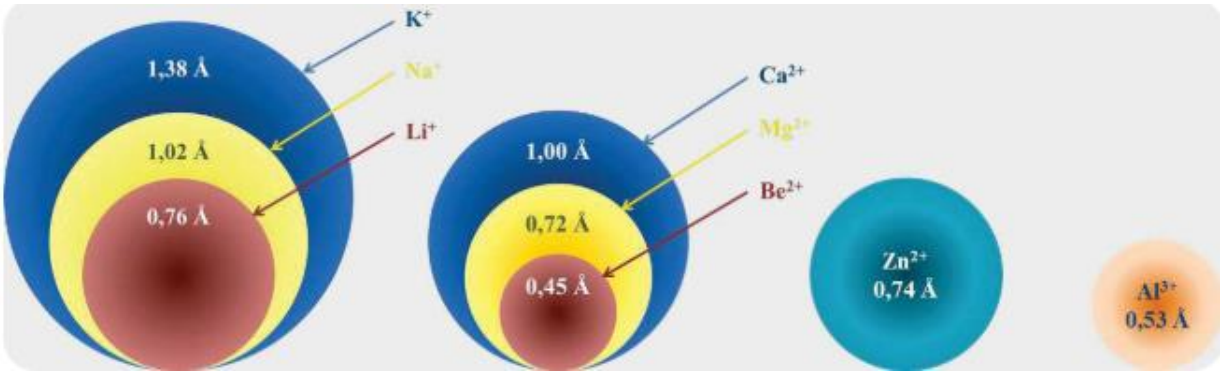

Figure 20: *Comparison between Shannon's ionic radii for mono- and multivalent ions.*[30]

The density and redox potential of the metal are the keys to promising theoretical electrochemical performance and therefore the largest figures of merit clearly correspond to the very light and electronegative lithium metal. However, other metals such as the here considered magnesium, calcium, and aluminum are also of interest despite their larger atomic weight as they are able to exchange two and three electrons per M-ion as compared with only one electron for lithium (Table 3).[41]

Metal	Abundance Earth's crust (ppm) [2]	Density (g/cm^3)	-E° vs SHE (V) [3]	Gravimetric Capacity (Ah/g)	Volumetric Capacity (Ah/cm^3)	Ionic Radius (Å) [4i]	Cost ($/ton) [5ii]	LC_{50} (µg/L) [6iii]
Li	18	0.53	3.04	3.86	2.05	0.76	20745	650
Na	22700	0.97	2.71	1.17	1.13	1.02	419	-
Mg	*27640*	*1.74*	*2.37*	*2.21*	*3.85*	*0.72*	*4740*	-
Ca	*46600*	*1.54*	*2.87*	*1.34*	*2.06*	*1.00*	*177*	-
Al	*83000*	*2.7*	*1.66*	*2.98*	*8.05*	*0.53*	*2160*	*182*
Fe	62000	7.86	0.45	0.96	7.55	0.61	75	>1000
Zn	76	7.14	0.76	0.82	5.85	0.74	2950	70
Cd	0.16	8.64	0.4	0.48	4.15	0.95	1700	0.57

Table 3: *Properties for some metals of interest as PLiBs anodes.*[32]

Magnesium and calcium seem to be less prone to dendrite formation, potentially due to the different adsorption energies and lower self-diffusion barriers during plating.[42] In particular, magnesium and calcium exhibit a tendency towards the growth of smooth surfaces as they exhibit lower diffusion barriers than lithium and sodium.[43] Although Davidson et al.[44] demonstrated the growth of crystal dendritic magnesium deposits upon the galvanostatic electrodeposition of metallic Mg from Grignard reagents in symmetric Mg/Mg cells. Concern the research into Ca-ion batteries, a depth understanding of the Ca plating and stripping behavior and the mechanisms by which adverse dendritic growth may occur remains underdeveloped; Pu et al.[45] demonstrated the critical role of current density and the solid-electrolyte interphase layer in controlling the plating morphology. By using *in situ* TEM, it is

shown the real-time Ca plating processes with different current density regimes and 1 M $Ca(BH_4)_2$ in THF as electrolyte. A transition from globular to dendritic growth was observed as the plating current density was increased and formation of electrochemically isolated dead Ca deposits during stripping. The inhomogeneous nature of the CaH_2-based SEI led to the presence of localized high current density regions that promoted dendritic deposition. On basis of that, even if challenges remain in understanding their chemistry before they can beconsidered viable, the use of these light metals couples the advantages of high theoretical volumetric capacity with natural abundance, low cost and safety. Furthermore, the use of divalent charge carriers accounts for a twofold increase in achievable energy density with respect to Li^+ for equal amounts of reacted ions.[46] Performance wise, the low cost alternatives of Na, Mg, and Ca technologies would also benefit from high standard reduction potentials, ca. −2.71, −2.37, and −2.87 V vs. SHE for Na, Mg, and electrochemical capacities, both gravimetric and volumetric, for the Ca, respectively, as compared to −3.04 V for Li, and large theoretical metal electrodes (Figure 21).

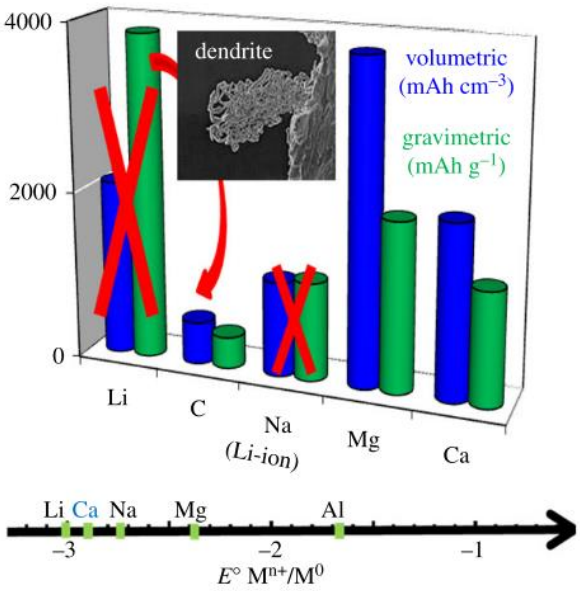

Figure 21: Gravimetric/volumetric capacities and standard reduction potential of metal anodes compared to conventional LIBs. The energy density is the product of both measures.[35]

5. Move from mono- to polyvalent cations

5.1. Magnesium

Mg batteries are one of the natural candidates for the future beyond LIBs. Magnesium is an alkaline earth metal which has nearly double the volumetric capacity (3832 mAh/mL) of lithium with a very negative reduction potential of −2.4 V vs SHE. The volumetric energy density of a battery pack becomes important when there is a limited volume for mounting it. A high volumetric energy density is more desirable for mobile devices (such as vehicles or assistive robots) than for stationary energy storage. The more portable the device (such as personal electronics), the less space is available for its battery and the volumetric energy density plays a crucial role. Magnesium is also far more abundant in the earth's crust, resulting in wider availability and much lower cost.[47]

Reports of effective magnesium electrodeposition from Grignard reagents in ethereal solutions date back to the early part of the 20th century and have periodically appeared in the literature ever since. In an attempt to enhance the stability of the electroplating baths based on Grignards, in 1957, Connor et al.[39] investigated the electro-deposition of magnesium from $Mg(BH_4)_2$ generated in situ by reaction of $MgBr_2$ and $LiBH_4$. Rather, boron and magnesium co-deposit in a 1:9 ratio. Use of $Mg(BH_4)_2$ as an electrolyte for magnesium batteries has been recently demonstrated by Mohtadi et al.[48] The electro-chemical performance of $Mg(BH_4)_2$ in glyme is superior to that in THF, and surprisingly, addition of $LiBH_4$ dramatically enhances the current densities of magnesium deposition. One of the obstacles in developing high-voltage rechargeable magnesium batteries is moving beyond the oxidative stability of Grignards such as ethyl magnesium bromide (EtMgBr) and butyl magnesium chloride (BuMgCl) which has an

oxidative stability of 1.3 V vs Mg. The low oxidative stability of Grignard solutions limits the choice of available cathodes. In the same year, Mayer et al.[49] investigated the electrodeposition of magnesium from organo-metallic electrolytes. Mayer's initial attempt at formulating magnesium plating electrolytes was to evaluate complexes of dialkylmagnesium (R_2Mg) and metal fluorides such as sodium fluoride with 2 equivalent of dibutylmagnesium (Bu_2Mg). Following on this observation, Aurbach et al.[50] investigated the Coulombic efficiency and oxidative stability of electrolytes as a function of different combinations and ratios of organomagnesium compounds (R_2Mg) to Lewis acids. Surprisingly, no magnesium deposition was obtained from THF solutions of dialkylmagnesium Lewis bases in combination with a wide variety of Lewis acids (BPh_2Cl, $BPhCl_2$, $B[(CH_3)_2N]_3$, BEt_3, BBr_3, BF_3, $SbCl_3$, $SbCl_5$, PPh_3, PEt_2Cl, $AsPh_3$, $FeCl_3$, and TeF_3). However, reaction of 1 equivalent of dibutylmagnesium and 2 equivalent of ethyl aluminum dichloride in-situ generated magnesium organo-halo aluminate with a given formula of $Mg(AlCl_2BuEt)_2$ (DCC). This electrolyte exhibited an ESW of 2.4 V and 98% Coulombic efficiency for reversible deposition of magnesium. In particular, a magnesium organo-halo aluminate, called APC, generated in situ via reaction of 1 equivalent of $AlCl_3$ with 2 equivalent of PhMgCl displayed a significantly broader ESW of 3.3 V vs Mg on a Pt WE. (Figure 22).

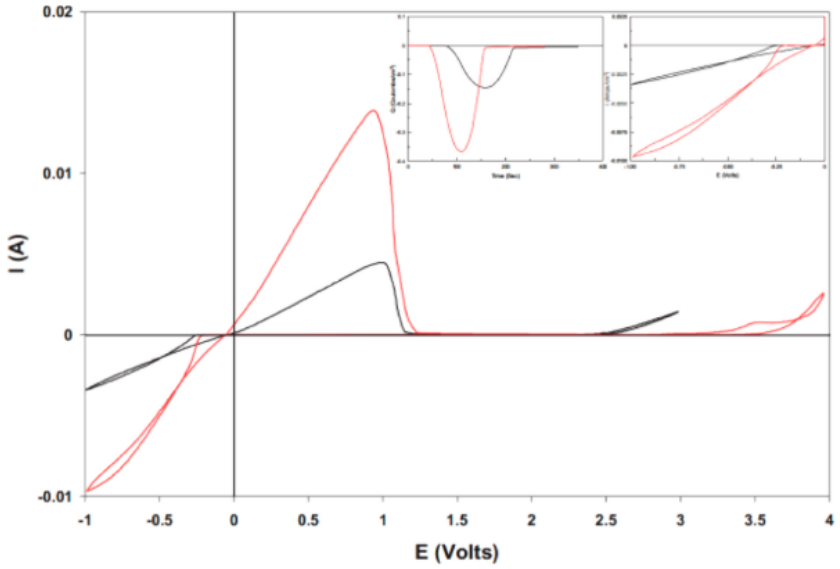

Figure 22: Comparison between the voltammetric behavior (vs. Mg^{2+}/Mg_0) of THF solutions containing 0.25 M of the reaction product between 1:2 $MgBu_2$ and $AlCl_2Et$ (DCC, black profile) and 0.4 M of the reaction product between 1:2 $AlCl_3$ and PhMgCl (designated APC, red profile) as indicated.[50]

Kim et al. utilized non-nucleophilic HMDSMgCl (HMDS = hexamethyldisilazide) salt combined with $AlCl_3$.[51] HMDSMgCl has been previously reported as being capable of reversible Mg deposition, but the Coulombic efficiency and ESW were not satisfactory.[52] Kim et al. also reported that crystallized $[Mg_2(\mu Cl)_3 \bullet 6THF][HMDSAlCl_3]$ from the solution of HMDSMgCl:$AlCl_3$ (3:1) in THF had an increased voltage stability compared with in situ generated electrolyte (Figure 23).

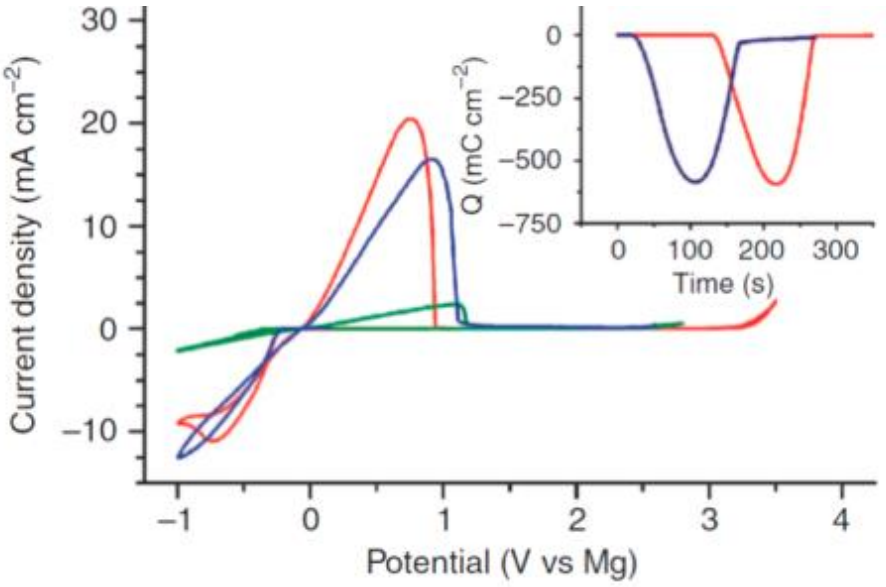

Figure 23: Cyclic voltammetry of different electrolyte solutions: HMDSMgCl (green), in situ generated HMDSMgCl:AlCl3 = 3:1 (blue), electrolyte from dissolved [Mg2(μCl)3•6THF][HMDSAlCl3] complex (red). Inset shows the charge density during the stripping and deposition.[52]

Zhao et al.[53] reported a dependence of the oxidative stability of Grignard reagents on the type of WEs used. A plausible explanation for the metal corrosion observed using magnesium organo-halo aluminates is the presence of halides in the cation and anion components of the electrolyte. The magnesium organoborate electrolyte $(Mg_2(\mu\text{-}Cl)_3\cdot 6THF)\cdot(BPh_4)$ with a halogen-free anion BPh_4^- exhibits reduced corrosivity as evidenced by the same measured oxidative stability (2.6 V vs Mg) on both SS and Pt electrodes, which represents a 400 mV improvement vs crystallized APC and $(Mg_2(\mu\text{-}Cl)_3\cdot 6THF)\cdot(HMDS_nAlCl_{4-n})$ on stainless steel. In addition, cyclic voltammograms of $(Mg_2(\mu\text{-}Cl)_3\cdot 6THF)\cdot(BPh_4)$ using a stainless steel working electrode do not exhibit hysteresis (Figure 25a). In order to enhance the oxidative stability of $(Mg_2(\mu\text{-}Cl)_3\cdot 6THF)\cdot(BPh_4)$ use of fluorinated Lewis acids such as $B(C_6F_5)_3$ was considered. As previously noted, reaction of $B(C_6F_5)_3$ with PhMgCl results in formation of

$(Mg_2(\mu\text{-}Cl)_3 \cdot 6THF)[B(C_6F_5)_3Ph]$, which has an oxidative stability of 3.7 V vs Mg on Pt as determined by a linear scan voltammogram between OCV and 4.5 V vs Mg. (Figure 24b)

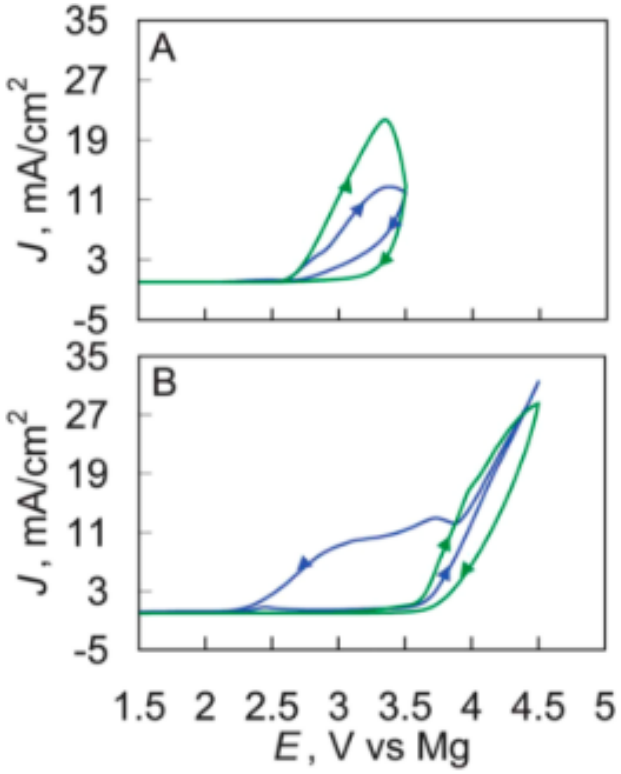

Figure 24: Cyclic voltammograms of $(Mg_2(\mu\text{-}Cl)_3 \cdot 6THF)(BPh_4)$ (a) and $(Mg_2(\mu\text{-}Cl)_3 \cdot 6THF)[B(C_6F_5)_3Ph]$ (b) on platinum (green) and stainless steel (blue) WEs.[53]

Magnesium organoborates based on a naked magnesium cation $(Mg \cdot 6THF)^{2+}$ partnered with a halide-free anion may eliminate the corrosive nature previously observed with magnesium organohaloaluminates and magnesium organoborates containing the magnesium dimer $(Mg_2(\mu\text{-}Cl)_3 \cdot 6THF)^{+}$ cation.

5.2. Zinc

Zinc is the 23th most abundant element on Earth's crust. It is a moderately reactive metal, which combines with oxygen and other non-metals; it reacts with diluted acids to generate hydrogen and has similar characteristics to calcium, but a lower reactivity. Zn batteries are particularly advantageous among rechargeable multivalent-ion systems, owing to the following properties of Zn anode: high volumetric energy density of 5851 $Ah{\cdot}L^{-1}$, non-toxicity, high tolerance toward oxygen and moisture, as well as scalability.[54] In addition, the Zn^{2+}/Zn redox chemistry usually exhibits low polarization with fast kinetics in a wide variety of liquid electrolytes, potentially rendering high rate capabilities. Great progress has been made in developing transition metal oxide cathodes including α-MnO_2 nanofibers, cation-deficient $ZnMn_2O_4$, $Zn_{0.25}V_2O_5{\cdot}nH_2O$ nanobelts, $ZnAl_xCo_{2-x}O_4$ spinels and $Na_2V_6O_{16}$ nanowires for building Zn batteries with high energy density. An obstacle that has held back the widespread application of rechargeable Zn batteries lies in its poor cycle life that has been traced to the dendritic growth of Zn deposit and H_2 evolution commonly observed in routine aqueous electrolytes. Graphite is a kind of redox-amphoteric intercalation host which can be intercalated by anions such as $AlCl_4^-$, PF_6^-, BF_4^- and $TFSI^-$ upon charging. Very recently, Feng et al. found that both PF_6^- and $AlCl_4^-$ intercalation into graphite are fast pseudo capacitive processes, which dramatically differ from slow diffusion-controlled cation migration in metal oxide hosts. In this context, coupling anion intercalating graphite cathode with Zn anode in the presence of suitable electrolytes could have a transformative effect on charging/discharging rate limits. In addition, compared with transition metal oxide cathodes, graphite exhibits much higher electrical conductivity and superior electrochemical stability, which are also favorable for enhancing rate capability as well as cycling performance of Zn batteries. Inspired by the above points, it is

reported a high rate capability up to 200C (to be fully charged in 18 s) on a rechargeable Zn battery with a new configuration comprising Zn anode, graphite cathode and $Zn(TFSI)_2$/acetonitrile electrolyte (abbreviated as Zn/graphite battery). The battery reaction involves reversible Zn plating/stripping at anode side and $TFSI^-$ (de)intercalation into graphite cathode (Figure 25). This is in contrast to the conventional rechargeable Zn batteries in which the Zn^{2+} cation, serving as the only charge carrier, is shuttled between cathode and anode.[55]

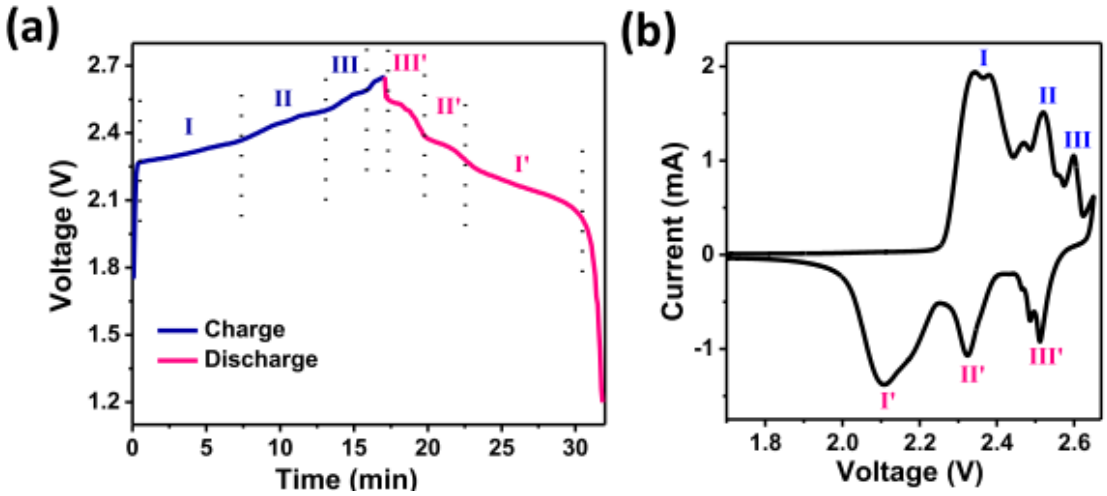

Figure 25: (a) Galvanostatic charge/discharge curve of Zn/ graphite battery at 4C within a voltage window of 2.65–1.20 V. (b) A typical CV curve of graphite electrode within a voltage window of 2.65–1.20 V using a two-electrode cell with Zn metal foil as the counter and reference electrode.[55]

5.3. Aluminum

Aluminum is the third most abundant element on Earth's crust, after oxygen and silicon. An aluminum metal anode is a superior multivalent candidate in terms of volumetric capacity (8040 mAh/cm^3). Its multivalent nature (it can provide three electrons per cation for reduction of a cathode), low atomic weight (26.98 g/mol), and high density compared to other candidates

(2.7 g/cm^3) endow aluminum with a volumetric capacity twice as large as that offered by magnesium. Aluminum batteries could deliver energy at a much more economically feasible rate (*i.e.*, cost per kW h) due to the reduced cost of aluminum metal. However, aluminum suffers from a standard reduction potential 0.7 V more positive (−1.67 V vs SHE) than magnesium. As a result, given cathodes with similar discharge voltages and similar anodic polarization, a battery with an aluminum anode would operate 0.7 V lower than one with a magnesium anode.[56]

The first attempts at using aluminum as a battery electrode by Hulot et al. in 1855 do not describe the use of aluminum as the anode but as a cathode in combination with a zinc (mercury) anode and dilute sulfuric acid as the electrolyte. Aluminum was first utilized as an anode in the Buff cell in 1857. A century later, Sargent and Ruben[57] considered aqueous electrolytes for use in Leclanche battery cells with an aluminum anode and a MnO_2 cathode. These batteries are plagued by the intrinsic formation of an oxide layer which passivates the aluminum metal anode and decreases the battery voltage and efficiency. Therefore, in order to develop a rechargeable aluminum battery where both aluminum deposition and dissolution is required, it is essential to develop electrolytes based on aprotic solvents stable against reduction by aluminum. Reports of positive electrode materials which operate by reversible electrochemical intercalation of Al^{3+} have been scarce. Interestingly, many of the cathode materials demonstrated in secondary aluminum batteries, including Chevrel-phase Mo_6Se_8, V_2O_5, Ag halides, and various manganese oxides, have also been demonstrated as cathodes for magnesium batteries.[58] Unfortunately, aluminum batteries containing these cathodes are plagued by low open-circuit potentials when compared to their magnesium counterparts and the operating potential was below 0.5 V. Improvements in terms of voltage and capacity were reported by Archer *et al.*, who observed a capacity of 273 mAh/g for V_2O_5 nanowire cathodes

at an average discharge voltage of 0.5 V with good cyclability (Figure 26). The battery electrolyte consisted of $AlCl_3$ dissolved in 1-ethyl-3-methylimidazolium chloride.[59]

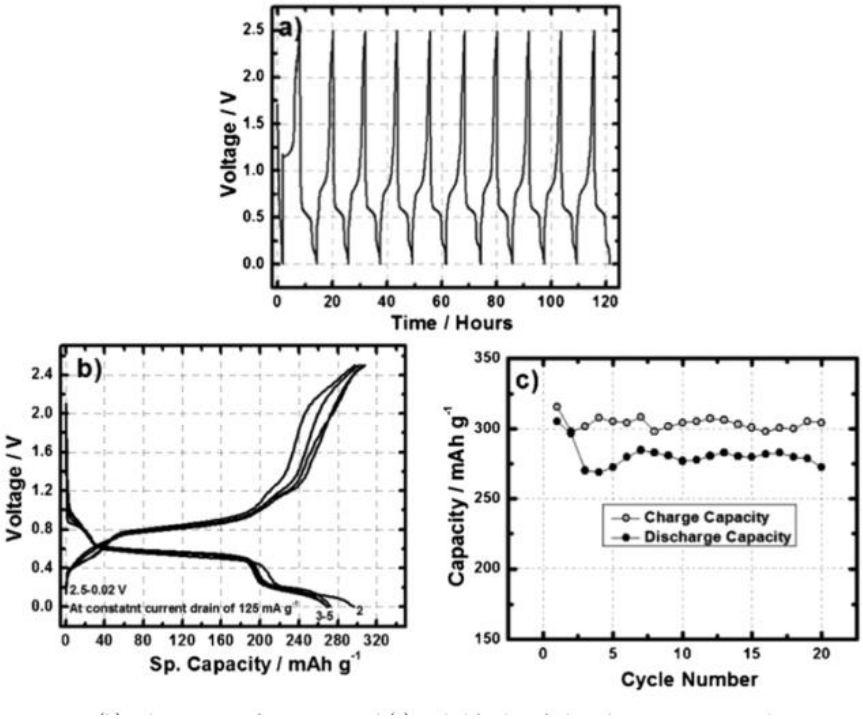

Figure 26: (a) Voltage vs time, (b) voltage vs specific capacity, and (c) cycle life plot of Al-ion battery containing aluminum anode, V_2O_5 nanowire cathode in ionic liquid under the potential window 2.5−0.02 V and at a constant current drain of 125 mA/g.[59]

Other cathodes reported for aluminum batteries are conversion materials such as metal halides (Hg_2Cl_2, AgBr, $NiCl_2$, CuF_2, and $FeCl_3$). These cathodes offer voltages slightly below 1 V with Al, but their solubility in the electrolyte results in direct reaction with the aluminum anode which limits cell cyclability.[57]

6. Challenge and prospects of Ca batteries

Calcium is the 5th most abundant element on Earth's crust (41,500 ppm, 2000 times the abundance of Li). The Earth's crust is the outermost layer of the Earth: its thickness varies from 5 km to 80 km and takes less than 1 % volume of the whole planet. It formed billions of years ago because of the cooling of the Earth. Elemental composition of Earth's crust is mentioned in Figure 27. Oxygen and silicon make more than 70% of the crust; they are followed by aluminum, iron, calcium, sodium, potassium and magnesium.[60]

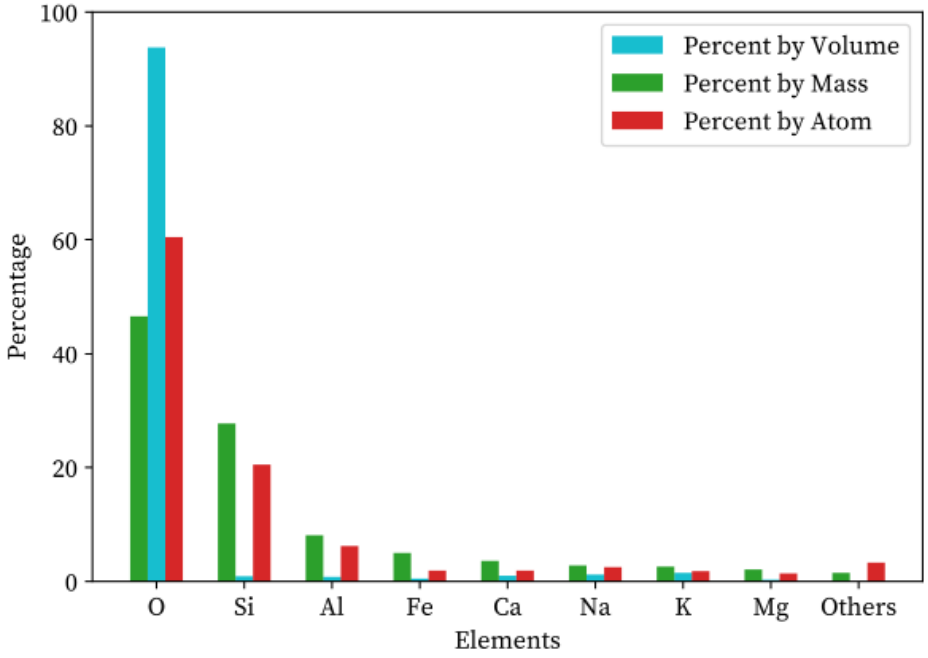

Figure 27: The most abundant elements in the Earth's crust.[60]

It is a nontoxic element: calcium plays a vital role in physiology and biochemistry of the human body and cell. The most common compound of calcium is calcium carbonate, found in limestone and fossils dating back to ancestral marine life, as well as gypsum ($CaSO_4 \cdot 2H_2O$), anhydrite, fluorite, apatite and aragonite ($CaCO_3$). Calcium is less reactive towards H_2O and O_2 than Li, K and Mg, allowing the slow formation of $CaCO_3$ and CaO, without phenomena of

explosions and burning. Furthermore, Ca has a significantly higher melting temperature than Li (842 °C vs. 181 °C) and thus potentially improves safety. Concern electrochemical properties, Ca^{2+}/Ca standard reduction potential is −2.87 vs SHE (only 0.17 V higher than that of the Li^{+}/Li couple), which combined with its density of 1.54 g/cm^3 and charge capacity of 1.34 Ah/g, results in a theoretical energy density of 2.06 Ah/cm^3. In comparison, the graphite of today's LIBs is at a mere 0.97 Ah/cm^3 hence a 2-fold increase in this measure is achievable, which is only 0.17 V higher than that of the Li^{+}/Li couple. Moreover, its ionic radius is 1.0 Å, only 24% larger than that of Li^{+}. As stated above, elevated charge density could lead to sluggish insertion/de-insertion kinetics and Ca^{2+} represents a good compromise between size and carried charge. Unlike magnesium, aluminum or zinc, calcium did not benefit from basic studies on electroplating, since the first electrochemical studies showed that reversible Ca plating/stripping was very complicated, and therefore it was abandoned. In addition, the Ca^{2+} ion should be more mobile in liquid electrolytes and in the solid-state because of its less polarizing character (charge/ radius ratio) than both Mg^{2+} and Al^{3+} ions.[61]

Despite all these interesting features, the electrochemistry of Ca includes some important lacks, as the stable character of calcium oxides. The Ellingham−Richarson diagram (Figure 28) shows the temperature dependence of the stability of compounds by plotting the Gibbs free energy (ΔG) change for each oxidation reaction as a function of temperature.[63] ΔG of a reaction is a measure of the thermodynamic driving force that makes a reaction occur; a negative value for ΔG indicates that a reaction can proceed spontaneously and this value is more negative for the more stable oxide.

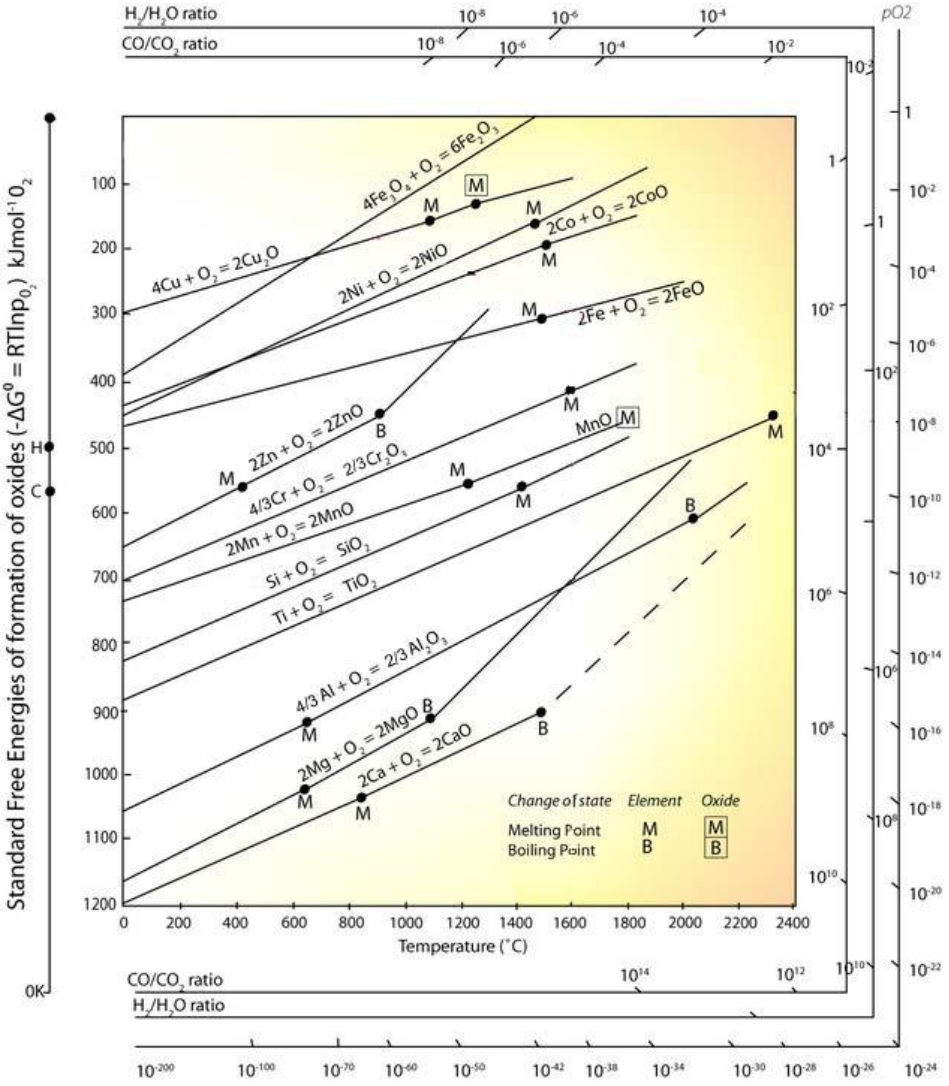

Figure 28: *Ellingham−Richardson diagram of the standard free energy of formation for oxides vs temperature.*[62]

The position of the line for a given reaction on the Ellingham diagram shows the stability of the oxide as a function of temperature. As we move down toward the bottom of the diagram, the metals become progressively more reactive and their oxides become harder to reduce; a given metal can reduce the oxides of all other metals whose lines lie above theirs on the diagram. Hence, we can deduce that CaO is clearly more stable than MgO and Al_2O_3. It has a great impact on the electrochemistry of Ca, since the formation of passivation layers consisting mostly of CaO can be favored thermodynamically with a low ΔG.

The first application of calcium in batteries was in 1935, where it was applied as an additive for alloy strengthening the lead grids for Pb−acid battery cells; the authors[63] presented their findings on the comparative electrochemical behavior of lead, lead-antimony, and lead-calcium alloys in sulfuric acid. It was shown that the substitution of about 1% calcium for the antimony, usually employed for hardening lead grid alloys, produced a storage cell having a greatly reduced rate of self-discharge. It was indicated that such a lead-calcium alloy would be expected to be much more resistant to anodic corrosion than lead-antimony alloys.

The first report of calcium as an electroactive element appeared in 1964, and is related to primary thermal batteries, a technology mostly used in military and aerospace applications.[64] These Ca batteries contained electrolytes with high melting points (such as mixtures of metal chlorides), kept at ambient temperature during storage periods to avoid self-discharge and thermally activated to deliver power. The Ca/KCl−LiCl−AgCl−K_2CrO_4/Ag cells were reported to discharge at 450 °C for 11 min, despite issues related to the formation of a Li−Ca alloy at the anode; this type of cell was used in military applications since World War II.[65] The timeline of Ca battery technology is shown in Figure 29:

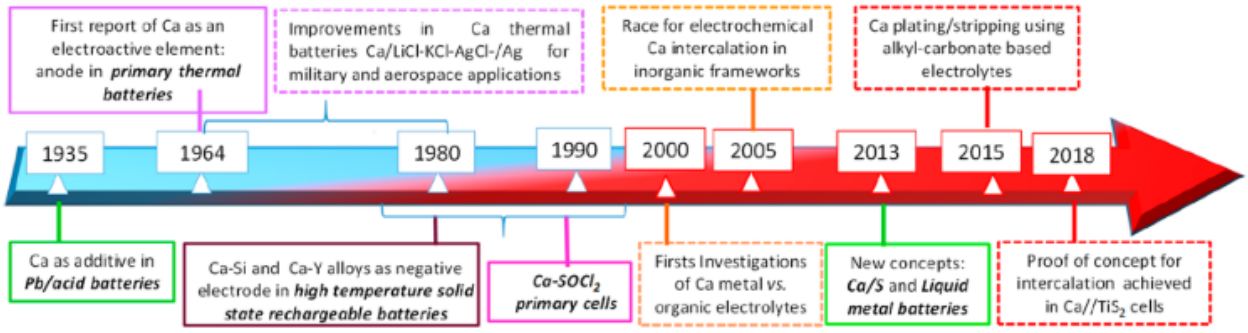

Figure 29: Timeline of Ca use in battery technologies.[66]

Other high-temperature concepts investigated in these years involved the use of a Ca−Si alloy anode coupled to a Ca^{2+} conducting β″-alumina solid electrolyte for rechargeable cells operating at 580 °C. Moreover, a Ca−Y alloy anode coupled to a fluoride conducting solid

electrolyte and even a Ca−O_2 cell also using a Ca−Si alloy anode complement with a zirconia-based electrolyte.[67] Despite a few charge−discharge cycles being reported for the above systems, the redox mechanism was not unambiguously ascertained, and no further studies were published. Staniewicz et al.[67] was the first to report on the electrochemistry of Ca−$SOCl_2$ as an alternative to the Li−$SOCl_2$ primary cells used for military applications; this system presented the impossibility of calcium plating upon cell reversal as a safety advantage. Further studies by Peled *et al.* attributed this feature to the formation of a passivation layer consisting mainly of $CaCl_2$, impermeable to the Ca^{2+} ions. The Ca−$SOCl_2$ cells lost ca. 10% of their capacity after only 2 weeks of storage. The strategy to avoid corrosion and self-discharge was to use different additives such as $Ca(AlCl_4)_2$, formed by reacting Ca with $AlCl_3$, $Sr(AlCl_4)_2$ or $Ba(AlCl_4)_2$, changing the composition of the passivation layer.[68]

Studies related to the behavior of calcium metal anodes, using organic electrolytes similar to those used at the time of emerging LIB technology, were made by Aurbach et al.[69] Their studies included solvents such as ACN, THF, GBL, and PC as well as $Ca(ClO_4)_2$ and $Ca(BF_4)_2$ salts together with no calcium containing salts. The conclusion of this pioneering work was that the passivation layer formed on calcium metal does not enable transport of calcium ions. This is in full agreement with the results for the $SOCl_2$ battery technology, with the major consequence being the impossibility to develop any secondary Ca batteries using these electrolytes, as even if calcium stripping would be feasible, plating upon charge would not. Yet, no similar electrolytes were available for Ca, and hence, the study of Ca^{2+} intercalation and the quest for cathodes was not straightforward. The basics of calcium-ion intercalation in transition-metal compounds were studied in the 1960s−1970s as part of early intercalation chemistry research. Metal sulfides WS_2, TaS_2, TiS_2, and some metal oxides, e.g., MoO_3, and V_2O_5, in which intercalation of a wide range of neutral or charged species was possible, the latter concomitant to reduction of the transition metal of the host.[70]

Only in current era, by the end of 2016, the feasibility of reversible calcium metal plating and stripping was assessed by Ponrouch et al.[71] at moderate temperatures using conventional alkyl-carbonate organic-solvent-based electrolytes. Despite issues associated with these electrolytes this research opened a more extensive electrode materials screening. Ca plating has also been recently reported by Bruce et al.[72] at room temperature, using $Ca(BH_4)_2$ in THF with an SEI layer mostly consisting of CaH_2. This electrolyte showed a severe limitation in terms of ESW until 2.5 V vs Ca. The new frontier of a breakthrough in room-temperature Ca^{2+} deposition/stripping was made recently by the Zhao-Karger[73] and Nazar[74] research groups simultaneously. Both groups reported calcium bis-tetrakis(hexafluoroisopropyloxy)borate, $Ca[B(hfip)_4]_2$, an electrolyte capable of the reversible plating/stripping of Ca at room temperature, with a ESW up to 4 V vs Ca and open a new reality for the Ca battery technologies, paving the way for their practical applications.

6.1. Electrolytes

The development of Ca batteries is impeded by the lack of suitable electrolytes. One of the fundamental problems identified in the early study of non-aqueous Ca electrolytes is the incompatibility of Ca metal with the conventional salts in aprotic solvents due to the formation of passivation surface films preventing Ca-ion transport. Therefore, rational design of ion-conductive Ca compounds, compatible with the metallic Ca anode, capable of plating and stripping Ca at room temperature and having wide electrochemical window is needed. The chemical bonding in anion is one the main factors that determines the anodic stability of an electrolyte.[75]

6.1.1. Ca/$SOCl_2$ as the first primary cell

The first interest in non-aqueous Ca electrochemistry began in 1980 with Staniewicz's study of the Ca-thionyl chloride (Ca/$SOCl_2$) primary battery.[48] The attraction of a Ca analogue to the successful Li/$SOCl_2$ system was safety, due to Ca's higher melting temperature and apparent lack of electrodeposition upon accidental cell reversal, a safety issue with Li/$SOCl_2$ systems. The Ca anode was found to corrode through continuous reaction of Ca and/or the $CaCl_2$ SEI with the electrolyte. As a result, the CE during full cell discharge was only ~50%. In 1982, Binder et al.[76] reported the Ca/SO_2Cl_2 primary battery as a potential improvement to Li/SO_2Cl_2. Ca/SO_2Cl_2 cells showed discharge voltages ~0.4 V higher than Ca/$SOCl_2$ (~3.2 vs. 2.8 V, 0.1 mA/cm^2) but ionic conductivities were significantly lower. The interface in Ca primary batteries containing $SOCl_2$ or SO_2Cl_2 consisted primarily of $CaCl_2$. Unlike the Li SEI, which is Li^+ conducting, (Figure 31), $CaCl_2$ is mostly an anion (Cl^-)-conductor (anion transference number of ~ 0.9).

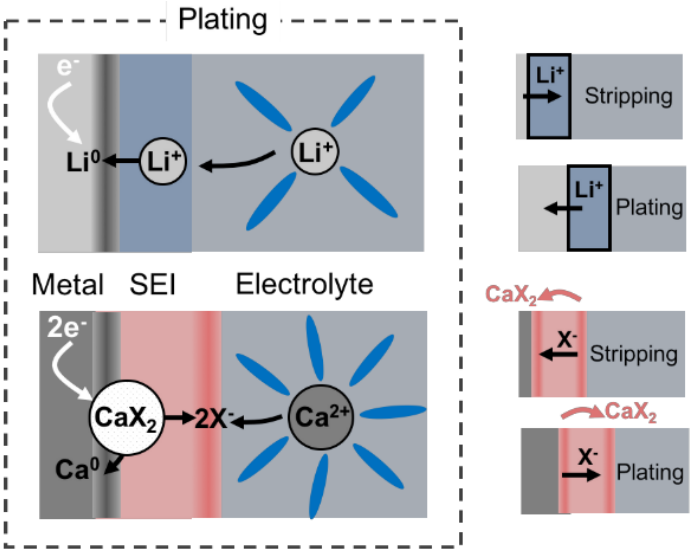

Figure 30: SEI behavior with a cation (Li^+) vs. anion (X^-) conductor. (Left) Li^+ plating with a cation-conductive SEI and Ca^{2+} plating (hypothetical) with an anion-conductive SEI. (Right) Nominal stripping and plating processes. A cation- conductive Li^+ SEI is nominally displaced during cycling, whereas an anion conductor requires active dissolution/precipitation of the SEI at interfaces.[77]

The electrolyte-facing redox step involves precipitation of $CaCl_2$; thus, a dynamic chemical precipitation/dissolution occurs. Given that several SEI-relevant phases observed include CaF_2 and CaH_2 (discussed further below), which are reported to be anion-conductors, there is much yet to be learned about the fundamental physical behaviors of Ca interfaces. Subsequent Ca-based research shifted away from oxyhalides and towards common organic battery solvents.[77]

6.1.2. First investigations of Ca metal vs. organic electrolytes

In 2016, the first reversible Ca deposition was demonstrated by Ponrouch et al.[71] at elevated temperatures (75-100 °C). The electrolyte was $Ca(BF_4)_2$ salt dissolved in EC:PC 1:1 (v-v). The concentration of $Ca(BF_4)_2$ was a critical parameter: reduction currents were maximized at 0.45 M (Figure 31). The ionic conductivity (measured at room temperature) was also found to be a maximum (5.4 mS/cm) at this concentration.

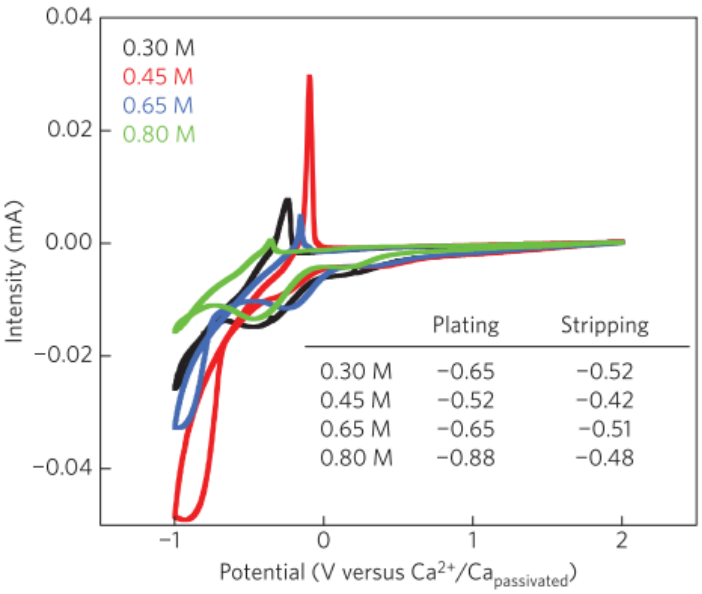

Figure 31: CVs showing Ca plating/stripping with $Ca(BF_4)_2$ in EC:PC as a function of concentrations at 100 °C and 0.5 mV/s.[71]

The SEI formed on deposited Ca from $Ca(BF_4)_2$ contained CaF_2 as determined from X-ray diffraction (XRD), as well as solvent-derived organic phases identified by FT-IR. The origin of CaF_2, whether from fully-dissociated BF_4^- or Ca^{2+}-solvating BF_4^-, is not currently known. CaF_2 plays a functional role and is thus a desirable phase within the SEI as being an anion conductor.[78]

6.1.3. Ca plating/stripping using ethereal-based electrolytes

The investigation of ether-based Ca^{2+} electrolytes began in 2018 when Bruce et al.[72] reported highly reversible Ca plating in 1.5 M $Ca(BH_4)_2$ in THF, using a gold WE. Under CV conditions at 25 mV/s, high areal current densities of ~10 mA/cm^2 were achievable with high plating capacities (~1mA h cm^{-2}) and a Coulombic efficiency of 95% (Figure 32).

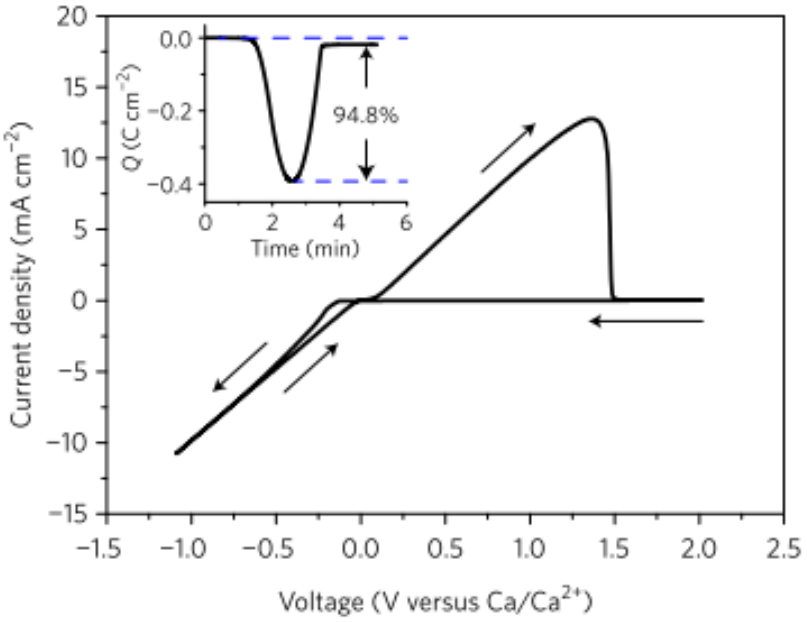

Figure 32: CV with 1.5 M $Ca(BH_4)_2$ in THF (Au as WE) at 25 mV/s.[72]

The electrolyte was reported to react quickly with freshly-deposited Ca to form exclusively CaH_2 in the SEI. It was indicated that the reactive electrolyte component forming CaH_2 was likely THF rather than BH_4^-. This was based on gas chromatography-mass spectrometry measurements of THF-soaked Ca, where dehydrogenated THF byproduct was reported. Recently, Ta et al.[79] proposed an explanation for the functional role of BH_4^- in the successful $Ca(BH_4)_2$/THF system. The authors found that Ca deposition occurs through a chemical-electrochemical mechanism, in which chemical H abstraction from BH_4^- in the bulk electrolyte (and not THF) and surface H adsorption precedes subsequent reduction of Ca^{2+}. It is important to note that, so far, Ca deposition from $Ca(BH_4)_2$ in THF has only been reported on precious metal surfaces (Au or Pt), which may be necessary for the initial H surface adsorption. Thus, the authors concluded that Ca^{2+} is predominantly solvated by THF via the ethereal oxygen and is coordinated with two BH_4^- anions. Understanding the origins of these distinct CV features, whether related to differences in surface film composition and SEI transport, different Ca^{2+} desolvation and redox mechanisms for ether- vs. carbonate-based electrolytes, etc., will be valuable in future experimental efforts.

6.1.4. Development of alkoxyborate based Ca salts

Two independent studies by Nazar et al.[74] and Fichtner et al.[73] recently reported a new Ca^{2+} salt that allows Ca plating and stripping in DME (Figure 36), $Ca[B(hfip)_4]_2 \times 4DME$, which contains four electron-withdrawing hexafluoroisopropoxy groups ($hfip^-$), prepared by solution synthesis. The salt is analogous to a recent Mg-battery electrolyte which allows reversible Mg plating/stripping thanks to the limited ion pairing from charge delocalization in the bulky anion. CV measurements by Nazar et al. with 0.5 M $Ca(B(Ohfip)_4)_2$/DME, using Au working

electrode, at 25 mV/s, exhibited high ESW at 4 V vs. Ca, roughly twice as that of $Ca(BH_4)_2$/THF at the same scan rate, and a Coulombic efficiency of 92% (Figure 33).

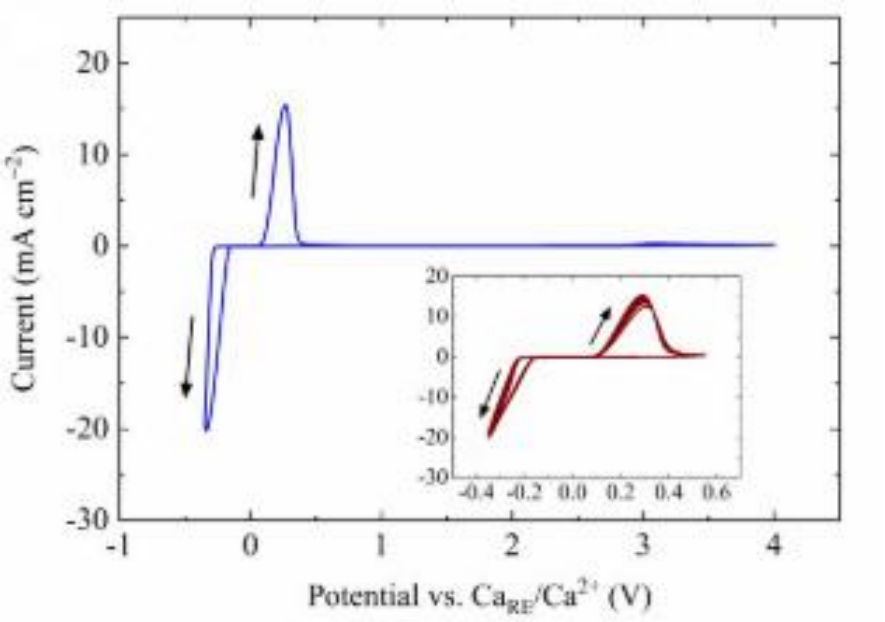

Figure 33: Cyclic voltammetry of 0.25 M $Ca(B(Ohfip)_4)_2$ in DME at 80 mV/s using Pt as WE.[74]

A common point invoked in the context of both carbonate and ether studies so far is the preliminary observation that minimizing Ca^{2+} anion pairing may facilitate good electrochemical performance as well as increase current density and Coulumbic efficiency.[80]

6.2. Positive electrodes

Due to the lack of stable electrolytes allowing the reversible plating/stripping at the negative electrode, only a few Ca battery cathodes have been successfully tested electrochemically until now. For Ca^{2+}, its divalent charge suggests similarities with Mg^{2+} intercalation chemistry, but its resemblance to Na^{+} in terms of ionic radius in metal oxides ($r(Ca^{2+})$ = 1.0 Å and $r(Na^{+})$ = 0.99 Å) may also result in similar site preference. DFT investigations of virtual spinels $Ca_T[M_2]O_4$ (Ca in tetrahedral coordination) predicted some promising cathode properties, but yet, the preference of Ca^{2+} for larger sites indicates that the synthesis of such compounds could be very tricky. Indeed, the $CaMn_2O_4$ stable polymorph, 0.9 eV more stable than the spinel, is the marokite with Ca in 8-fold coordination sites. A good ionic diffusion coefficient ($D \approx 10^{-12}$ $cm^2\ s^{-1}$) is a prerequisite for battery electrode materials. There are no direct measurements of Ca diffusion coefficients reported, and estimates from electrochemistry are hampered by the poor reliability of testing protocols and problems with the stabilities of electrolytes and interfaces. In Figure 35, reported calculated energy barriers for Ca migration in various TM compounds are depicted, and notably, <0.650 eV has been predicted for some virtual spinel-$Ca_T[M_2]\,O_4$ with Ca occupying the tetrahedral sites.[61]

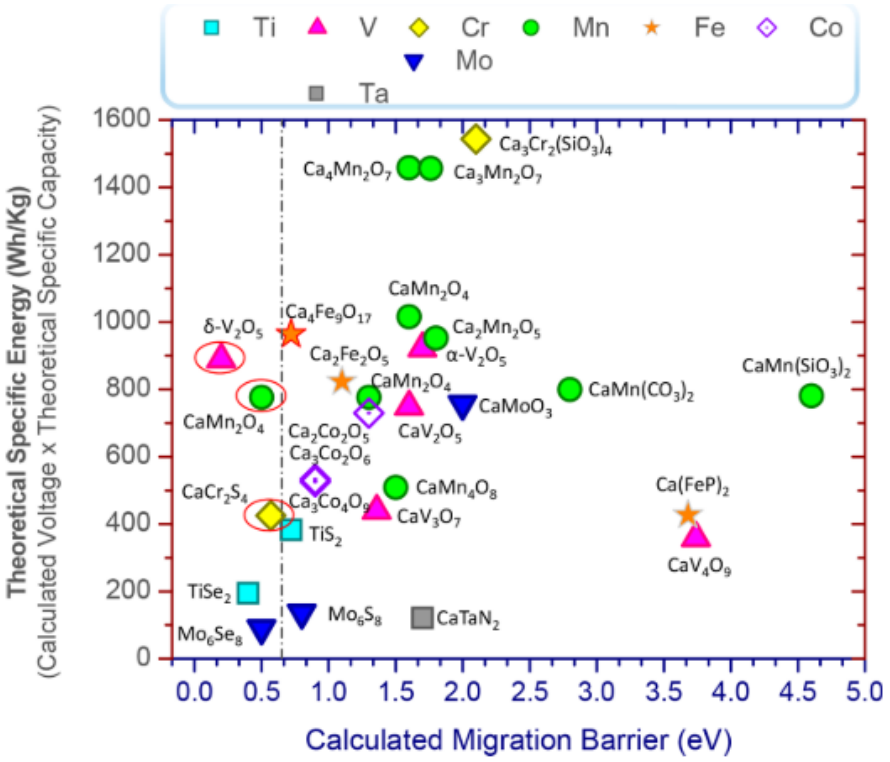

Figure 34: Theoretical specific energy vs calculated energy barriers (eV) for proposed Ca hosting TM compounds. The specific energy is estimated from the calculated average voltage for a particular redox couple and the corresponding theoretical specific capacity. The vertical line denotes the criterion for good cathode performance (<0.650 eV, see text). The red circles indicate virtual compounds.[53]

A good mobility was predicted in spinel-$Ca_T[M_2]_OO_4$, since the Ca ion would diffuse from an unfavorable site (tetrahedral) to a preferred site (octahedral). Similarly, a barrier as low as 0.2 eV is predicted for the virtual δ-CaV_2O_5, where Ca ions occupy an unfavorable site (bicapped-tetrahedral).

Another family of potential positive electrode is represented by the Prussian blue analogues $K_xMFe(CN)_6 \cdot nH_2O$ (KMFe-PBA), which allow reversible insertion/extraction of Ca^{2+}, giving a discharge capacity of 50 mAh/g with Coulombic efficiencies of 92%, at room temperature. Ca^{2+} ions are inserted and extracted into and from the interstitial sites of KNiFe-PBA without destruction of the open framework structure.[81] For reversible electrochemical Ca^{2+} intercalation in TiS_2, the first phase formed upon reduction is found to be the result of an ion-solvated

intercalation mechanism, with solvent molecule(s) being cointercalated with the Ca^{2+} cation. Upon further reduction, new non-cointercalated calcium containing species seem to form at the expenses of unreacted TiS_2. From the combination of experimental and computational techniques, it was concluded that the cation-solvated intercalation mechanism improves Ca^{2+} diffusion, by both expanding the interlayer space (the DFT barrier lowers to 0.5 eV with a more stable transition state) and screening the cationic charge.[82]

Chalcogenide networks may also provide better screening of electrostatic interactions and consequently lower the migration barriers; those calculated for Mo_6S_8 (0.8 eV), Mo_6Se_8 (0.5 eV), TiS_2 (0.72 eV), and $TiSe_2$ (0.4 eV) are so far the lowest reported for existing compounds.

Reversible calcium extraction from electrodes containing $Ca_3Co_2O_6$ as active material was attempted electrochemically in 2012 by Palacin et al.; The 1D framework of $Ca_3Co_2O_6$ is maintained upon oxidation and the new phase formed exhibits a modulated structure, using $Ca(BF_4)_2$ in EC:PC (1:1) as electrolyte.[83]

6.2.1. Primary Ca/S cells

With the rapid progress in the development of Li/S batteries and the non-aqueous sulfur chemistries during the last 10 years, it is natural for the electrochemical energy storage research community to attempt at coupling high-capacity sulfur cathodes with the other alkali– and alkali-earth-metal systems. While the electrochemical mechanisms of Li/S and Na/S batteries are relatively well established, the fundamental properties of Mg/S, Ca/S, and Al/S batteries are not yet clearly understood. With suitable non-aqueous electrolytes, the Mg/S and Al/S systems have been successfully demonstrated as rechargeable batteries.[84] However, the discharge of a Ca/S battery is believed as an irreversible process. In particular, the

electrochemical mechanism of Ca/S cell has not yet been understood. With the electrolytes tested in the literature, the discharge of the Ca/S chemistry was indeed an irreversible process (Figure 35).

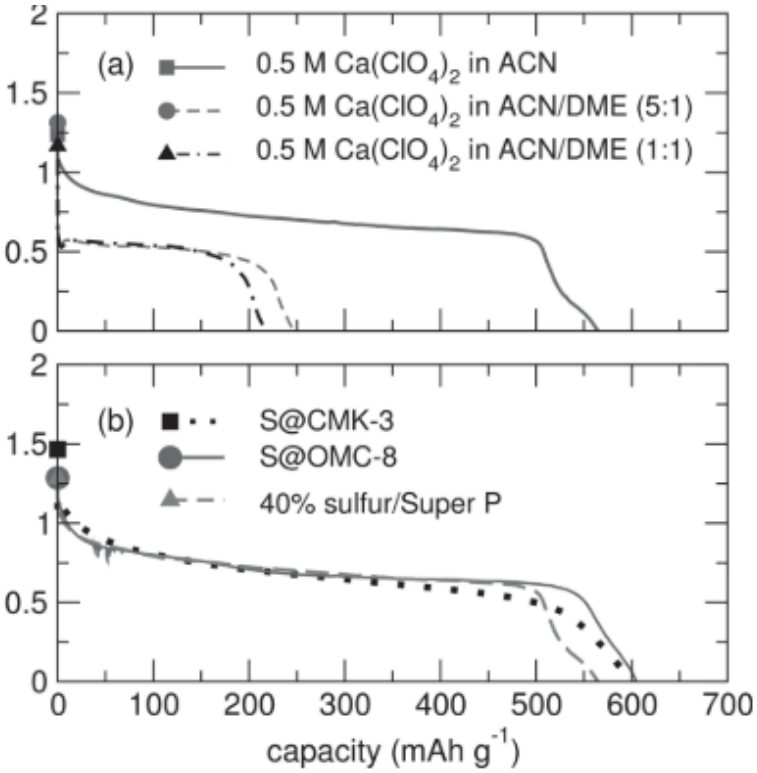

Figure 35: Galvanostatic discharge profiles a rate of C/3.5. (a) Illustrates the dependence of sulfur utilization (capacity) on the electrolyte composition with a S@CMK-3 cathode.(b) Illustrates the independence of the capacity on the structure of the S host in 0.5 M $Ca(ClO_4)_2$ in ACN electrolyte.[74]

6.3. Calcium-based negative electrodes

Calcium is a silvery-white metal when freshly cut, which tarnishes to a blue-gray color in air. It can also be found as a powder. In this work, two different types of Ca anodes have been electrochemically tested, either in three- or two-electrode cell configuration. The use of Ca metal anodes requires reversible stripping (at discharge) and plating (at charge).

During the first part of the project, during development of the alkoxy borate based electrolyte (treated in 2° chapter) done in Ljubljana, Ca shots (Alfa Aesar, 99.5% metal basis) have been used as CE and RE strip metal for three- or two-electrode cell configuration. As it is shown in Figure 36 shot is characterized by irregular shape, covered by a dark native layer constituted by product of oxidation of Ca with air, as carbonates and oxides. Before to be used as metal anode, the shot must be hammered in order to obtain a flat metal disc, then its surface must be scratched to remove the oxidation-based layer.

Figure 36: Picture of Ca shot.[85]

During the second and last part of the project, during development of the organic based batteries (treated in 3° chapter) and the Ca/S batteries (treated in 4° chapter) done both in Ljubljana and Montpellier, Ca foils (ACI Alloy, 99.8% metal basis) have been used as CE and RE strip metal for three- or two-electrode cell configuration. The foil as received shown a dark cover, constituted by product of oxidation of Ca with air (Figure 37a); before using, surface must be scratched, onto Ar-filled glovebox, in order to remove this cover, obtaining a shining surface of fresh Ca (Figure 37b).

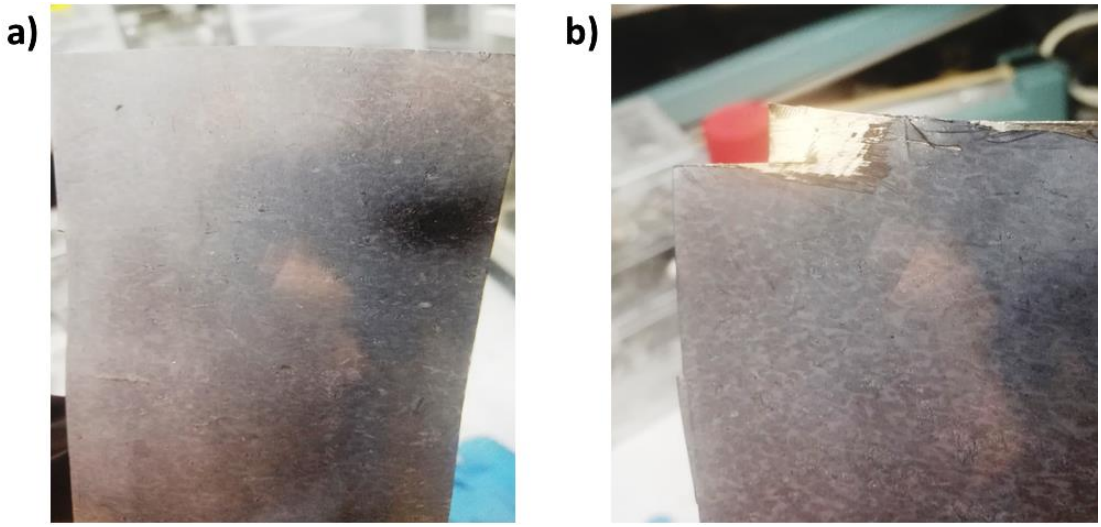

Figure 37: a) Ca foil not scratched. b) Ca foil scratched

6.3.1. Intercalation materials

Graphite is by far the most representative and studied insertion anode material for the LIBs technology. Calcium-ion intercalation can be remarkably fast and reversible in natural graphite, constituting the first step toward the realization of high-power calcium electrodes. The reversible intercalation was obtained at room temperature with the aid of a co-intercalating DMA solvent. The graphite electrode delivered a reversible capacity of 85 mAh g^{-1} over 200 cycles with negligible degradation of the graphite.[86]

Adil et al.[87] have presented an aqueous Ca^{2+} full-cell comprising of a PANI/CC anode and a Ca_xCuHCF cathode in a $Ca(NO_3)_2$ aqueous electrolyte. Polyaniline is investigated for the first time as an anode in aqueous rechargeable Ca-ion battery. The charge/discharge mechanism of this battery includes doping/dedoping of NO_3^- anion at the anode, and intercalation and deintercalation of Ca-ion at the cathode. The fabricated full-cell delivers not only good cycling

performance but also excellent rate capability. It provides an average specific capacity of 130 $mA{\cdot}h{\cdot}g^{-1}$ at a current rate of 0·8 $A{\cdot}g^{-1}$ in addition to a capacity retention of 95% over 200 cycles.

6.3.2. Ca alloys

Alloys are considered a viable alternative to Ca metal anodes, as they often have both high specific capacity and low potential. As expected from the divalent nature of Ca and Mg cations, a similar volume expansion can be calculated for the formation of A_xM (with A= Ca or Mg and M= Sn, Si, etc.) as for the formation of Li_2xM, and a similar amount of charge is stored.[88] The most promising alloy candidates were selected considering calcination voltage, volume expansion, and specific capacity. These criteria resulted in a wide range of metals being considered worthy of further investigation; M = Sn, Si, Sb, Ge, Al, Pb, Cu, Cd, $CdCu_2$, Ga, Bi, In, Tl, Hg, Ag, Au, Pt, and Pd. The operation temperature of such cells could be lower by using Ca alloys such as Ca−Bi, Ca−Sb, Ca−Ge, and Ca− Mg.[89]

Kang et al. demonstrated that calcium-ion intercalation can be remarkably fast and reversible in natural graphite. The capacity stably maintains over 200 cycles without notable cycle degradation. It was found that the calcium ions are intercalated into graphite galleries with a staging process using a suite of techniques including synchrotron in situ X-ray diffraction. They used electrolyte, composed of $Ca(BH_4)_2$ salt dissolved in different solvents as DMA, DME, EC/DMC, and THF.[90]

7. Aim of the thesis

The objective of this project is to develop and test both new electrolytes and new positive electrode materials for room temperature calcium batteries, employing calcium metal as the negative electrode.

The whole project was carried out between the laboratories of universities of Ljubljana and Montpellier, in which we can reach our goals by combination of material chemistry's knowledge by Montpellier team, while Ljubljana team gives us knowledge about organic chemistry field, electrolyte developing and organic cathodes. The thesis is organized in chapters, ordered in chronologic way, following my work experience. The first prior goal is to develop a suitable electrolyte, then using it to build up a working innovative Ca battery, employing organic and sulfur positive electrodes. Organic based cathodes were already studied by Ljubljana team for Mg-, Li- and Al- based organic batteries and sulphur based cathodes by Montpellier team for Li/S and Mg/S batteries.

The first goal of this thesis, discussed in 2° chapter, concerns the development and full characterization of a new Ca salt, and the subsequent electrolyte preparation, going above the issues concerning Ca based electrolytes previously discussed in state-of-art of Ca batteries in 1° chapter. Ca deposition is surface-film controlled, which means that fresh deposits readily react with the electrolyte and block subsequent ion flow. The formation of passivation layer on Ca metal anode prevents the reversible Ca plating/stripping with a good Coulumbic efficiency. Just after the beginning of this PhD work, in 2017, the first example of Ca stripping/deposition at room temperature appeared in the literature from the work of Peter G. Bruce et al[72], using $Ca(BH_4)_2$ in THF as an electrolyte. This system showed important lacks, as electrolyte's low anodic stability at 2.5 V vs. Ca, which prevents further application for high-voltage cathodes.

Moreover, the nucleophilic nature of borohydride anion and its reductive character does not allow it to be employed with organic-based cathodes, in which carbonyl groups are highly reactive toward electronegative species. Our idea was to approach the rational design of a new innovative Ca based salt to improve the ESW of electrolyte, allowing it to be suitable for practical application in batteries. While we were performing the successful electrochemical tests of this electrolyte, two papers appeared in the literature about fluorinated alkoxyborate salts and their potential use as novel electrolytes for Ca batteries. They were published by research groups of Fichtner[73] and Nazar[74]. Our idea was to improve the synthetic procedure of calcium tetrakis(hexafluoroisopropyloxy) borate $Ca[B(hfip)_4]_2$ salt, previously developed by Fichtner, which synthetic procedure involves the derivatization of $Ca(BH_4)_2$ by reflux conditions. We thus concentrated on the synthesis of high purity $Ca[B(hfip)_4]_2$, belonging to the class of WCAs. Its magnesium counterpart was already used for Mg-batteries[91], via the reaction of $Mg(BH_4)_2$ with hexafluoroisopropanol at room temperature. On other hand, In recent years, lithium bis(oxalato)borate, $LiB(C_2O_4)_2$ (LiBOB) has been proposed as an alternative salt to the commonly used electrolyte $LiPF_6$.[92] Then, we got a detailed characterization of the fluorinated alkoxyborate Ca based salt, as to understand better the chemical-physical proprieties of it and to study how all the chemical interactions between electrodes/electrolytes moieties can affect drastically the cell's cyclability and performances.

Once set the preparation of a working electrolyte, the second goal of this thesis, discussed in 3° chapter, is centered on the application of this electrolyte to develop high energy density Ca organic batteries. The soft chemical nature of redox active organic materials, based on PAQ (polyanthraquinone) and PAQS (polyanthraquinonyl-sulfide) based polymers, allow the reversible reduction/oxidation of the organic backbone, at room temperature, towards insertion of divalent cation into polymer matrix. The proof of electrochemical activity and the non-

nucleophilic nature of Ca based salt toward carbonyl-based groups of cathode is given by applying FTIR spectrometry.

In the third and last goal of the thesis, we present the reversible activity of an innovative Ca/S battery at room temperature. It showed a good cycling stability, promoted by the use of a simple positive electrode, made of sulfur supported on an activated carbon cloth scaffold, and the fluorinated alkoxyborate-based electrolyte. Insights on the electrochemical mechanism governing the chemistry of the Ca/S system were obtained by combining XPS and XAS spectroscopies. The electrochemical activity is proven by the formation of different types of soluble polysulfides species during both charge and discharge at room temperature, and the formation of solid CaS at the end of discharge. The reformation of elemental sulfur at the end of the following charge ensures the reversible activity. These promising results open the way to the comprehension of emerging Ca/S systems that may represent a valid alternative to Mg/S and Li/S batteries. This last part of the work is given in 4° chapter.

II. The design of the electrolyte

1. Rational design of Ca conducting electrolyte

Electrolyte must fulfill the requirements of ionic mobility and chemical stability. Two main approaches are employed: i) electrolytes that permit reversible deposition of calcium on Ca metal anodes, with the main issue being the Ca^{2+} mobility through SEI covering its surface, and ii) electrolytes that do not form any SEI, employing non-metallic anodes. Figure 38 displays the most employed salts and solvents for Ca battery electrolytes.[66]

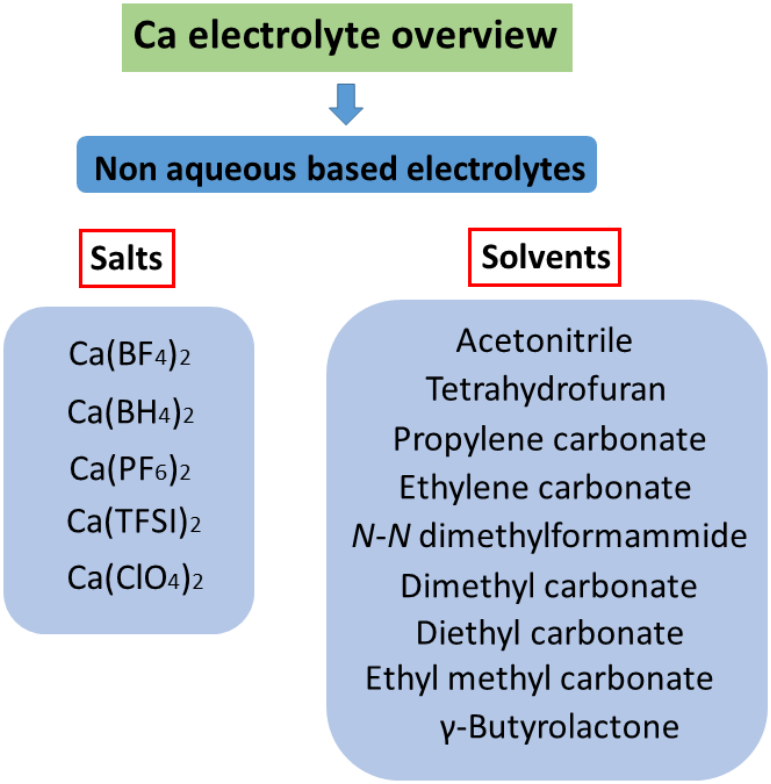

Figure 38: Summary of the most employed salts and solvents for Ca-batteries.

Overall, there is a lack of commercially available calcium salts: most of the investigations have employed calcium perchlorate $Ca(ClO_4)_2$, calcium tetrafluoroborate $Ca(BF_4)_2$, calcium bis(trifluoromethane)sulfonimide $Ca(TFSI)_2$ and calcium borohydride $Ca(BH_4)_2$, dissolved in organic solvents. Recently, Lipson et al.[93] synthesized calcium hexafluorophosphate $Ca(PF_6)_2$ and used this salt in 3:7 EC:PC electrolyte to study Ca insertion in manganese hexacyanoferrate. To the best of our knowledge, no tests in Ca cells of this salt have been reported. A detailed study on the passivation layers formed from $Ca(BF_4)_2$ or $Ca(TFSI)_2$ in EC:PC electrolytes identified calcium carbonates, fluorides, and borates, with the latter only being observed for BF_4^--based electrolytes. Nevertheless, no reversible plating/stripping is observed for the electrolytes containing TFSI.[94] Only in 2021, Ponrocuh et al.[95] reported that the addition of borontrifluoride diethyletherate to a $Ca(TFSI)_2$ EC:PC electrolyte allows for calcium plating and stripping; these study confirms the crucial role of boron containing species in the electrolyte, as the salt or an additive.

BF_4^- anion is a tetrahedral species, isoelectronic with many stable and important species, including perchlorate anion ClO_4^-, tetrafluoromethane CF_4 and tetrafluoroammonium NF_4^+. In recent years, BH_4^- become popular for organic reactions as reducing reagent for organic carbonyls, leading to decrease use of ClO_4^-, that it is more dangerous, because it could give potentially explosive derivatives. One disadvantage to BH_4^- is its sensitivity to hydrolysis, whereas ClO_4^- does not suffer from this problem. BF_4^- anion is characterized by high solubility in organic-type solvents, more than related halide or nitrate salts.[96] Moreover, it is less nucleophilic and basic than nitrates, halides and borohydride-derivatives, so it can be assumed that this tetrahedral anion is practically inert regarding nucleophilic attack against electropositive substrates. BF_4^- owes its inertness to two factors: it contains four highly electronegative fluorine atoms, which lower the basicity of the anion, and it is symmetrical so that the negative charge is equally distributed over them (Figure 39):

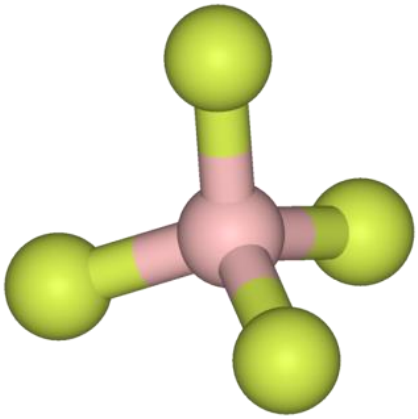

Figure 39: The structure of the tetrafluoroborate anion, BF_4^-.[97]

One of most common application of tetrafluoroborate salts is electrochemistry; in particular, lithium tetrafluoroborate has been extensively tested and used as electrolyte in commercial rechargeable batteries. Reasons of its popularity as electrolyte are to find in its moderate ion conductivity in non-aqueous solvents and in its greater thermal stability[98] and moisture tolerance compared to $LiPF_6$. Despite this, it was out of favor in the early days of lithium battery research because in ether-based electrolytes it resulted in poor lithium cycling efficiency, rapidly decaying with cycle number.[99] Moreover, it does not form a stable SEI on graphite electrodes. However, $LiBF_4$ has been widely studied to find correlations between the evolution of electrolyte viscosity and ionic conductivity with salt concentration and working temperature. In particular, Ding et al.[99] demonstrated that, at room temperature, the viscosity of the electrolyte increases with salt concentration, while ionic conductivity first increases but then fades with increasing salt concentration. This behavior depends on the amount of dissociated ions which decline at high conentrations due to the rise of viscosity and ion pairing.

These results did not stimulate the research effort in calcium-based batteries in the following years. Only in 2015, Ponrouch[71] revisited these electrolyte formulations; inspired by the studies carried out by Ding et al.[99] on $LiBF_4$ and obtained the best electrochemical performance for

$Ca(BF_4)_2$. The ionic conductivities of 0.3M $Ca(ClO_4)_2$ and $Ca(BF_4)_2$ salt in EC: PC solvent at room temperature are similar (6 and 4 mS/cm respectively) as well as their viscosity. For $Ca(BF_4)_2$, at room temperature, the viscosity was found to significantly increase with concentration up to 23 cP for 1M electrolyte. In contrast, the ionic conductivity increases with concentration from 0.3M to 0.45M but decreases above this value. Ion pairing is known to be temperature dependent and takes place to a larger extent in solutions containing divalent ions due to the strong columbic interactions with the anions. The choice of the solvent is critical for electrochemical performance: EC is known to build very stable passivation layers, but melts at 36°C, while PC melts at −49°C. Their mixture exhibits a wide liquids state in a temperature range between -90°C and 240°C. Typical reversible metal plating/stripping are observed in the case of $Ca(BF_4)_2$, whereas $Ca(ClO_4)_2$ showed low reversibility. The onset potential (potential at which the sharp increase in reduction current is observed) depends on both the temperature and salt concentration, with the smallest differences between oxidation and reduction peaks being found for 0.45 M $Ca(BF_4)_2$ at 100°C.

In 2020, Ponrouch[100] combined experimental and theoretical approaches to unveil the SEI components enabling Ca plating/stripping, as well as to study the interface between the calcium metal anode and the electrolyte. It was demonstrated that linked boron polymer-based passivation layer is produced by anion decomposition upon reduction in $Ca(BF_4)_2$/EC:PC electrolyte. This SEI allows reversible calcium plating/stripping and also limits further electrolyte decomposition.

Nowadays, the challenge is to move beyond the chemistry of borofluoride-based compounds at room temperature. The isosteric substitution of the C-F bond with C-H bond, allow us to entry into chemistry of borohydride-based compounds.

The tetrahydroborate anion BH_4^- represents the smallest anionic boron hydride; it stabilizes hydrogen-rich environments and can be the hydrogen source in metal-hydrogen interactions of significant commercial, synthetic and biochemical applications.[101] Tetrahydroborate complexes are used as selective reducing agents, starting compounds in the synthesis of organometallic derivatives, precursors for the production of borides, hydrides and other inorganic materials, and as catalysts of hydrogenation, isomerization and polymerization processes. BH_4^- ligands also present very interesting properties from the perspectives of structure and bonding and it is a very effective polyhapto ligand for which up to six coordination modes have been reported. The ligation invariably occurs through bridging hydrogen atoms. Borohydride anion is much stronger nucleophile than the tetrafluoroborate anion due to decreased electronegativity of hydrogen atom with respect to fluorine. It is a reducing agent and can reduce a wide spectrum of organic carbonyls and also releases hydrogen when exposed to many metal catalysts.[102,103] Borohydride salts are soluble in most protic solvents but slowly react with them producing hydrogen gas. Metal borohydrides generally undergo decomposition in acidic and aqueous media but not in basic media.

Mohtadi et al.[101] demonstrated that electrolytes based on $Mg(BH_4)_2$ in both THF (0.5 M) and DGM (0.1 M) allow reversible Mg plating and stripping at room temperature, achieving up to 94% Coulombic efficiency with the addition of $LiBH_4$. Using diglyme, the efficiency of an $Mg(BH_4)_2/LiBH_4$ electrolyte was shown to increase to approximately 100%, with the increase attributed to enhanced chelation of Mg^{2+} (compared to DME and THF) and synergistic effects arising from $LiBH_4$ addition. The presence of $LiBH_4$ in $Mg(BH_4)_2$ based electrolytes may facilitate dissociation of the $Mg(BH_4)_2$ salt, or equivalently, retard the recombination of Mg^{2+} and BH_4^- ions into ion pairs or larger agglomerates. This could improve the solubility of the salt and increase conductivity. On the contrary, electrolytes based on simple $Mg(BH_4)_2$ salts suffer from poor salt solubility and/or low conductivity. There is only a limited number of

electrolytes that show reversible Mg plating/stripping, such as volatile solvents such as THF, or DME. Electrolytes based on less volatile or nonvolatile solvents are desired, such as long-chain glyme-based solvent systems. The performance of the electrolyte is closely related to the solvated structure of Mg^{2+}; The better performance of the $Mg(BH_4)_2$-$LiBH_4$ in DGM electrolyte could be explained by the coordination chemistry in the electrolytes. In terms of density and donor strength, these coordinating solvent molecules (DGM, DME and THF) could impose different kinetic and thermodynamic influences on the Mg electrochemical process, which is essentially related to Coulombic efficiency. DGM, as a tridentate solvent ligand, is thermodynamically more favorable than DME (and THF) in the complexation of stripped Mg^{2+}. This is consistent with the better stability of these complexes in long-chain glymes.[104] Glymes-based solvents possess unique characteristics, as they show both hydrophilic and hydrophobic character, differently from common organic solvents.[105] Moreover, they are thermally and chemically stable, can coordinate cations and are characterized by high-permittivity and low-viscosity. For these reasons, glymes have been extensively investigated in electrochemistry as electrolyte solvents. Their relatively higher boiling point than ethereal-based solvents, allow glymes to be used with improved safety and efficiency in battery systems.[106]

Inspired by the excellent results of Mohtadi[101] about $Mg(BH_4)_2$ based electrolyte, $Ca(BH_4)_2$/THF electrolyte was developed by Bruce et al.[72] and showed a calcium stripping/ deposition at room temperature. As explained in the 1° chapter, many issues limit the practical application of this electrolyte formulation for batteries, as the low oxidative stability and the strong nucleophilic character of borohydride anion. In next paragraph, it will be carefully described how a rational molecular approach can lead us to develop new classes of boron derivatives, with interesting physical-chemical properties.

The report of Ca electrolytes, including the relative salt and solvents used with ESW, is briefly summarized in Table 4 below.

Salt	Solvent	ESW (V vs. Ca^{2+}/Ca)	*Reference*
$Ca(ClO_4)_2$	ACN, PC, DME	+2	*69*
$Ca(BF_4)_2$	EC:PC (1:1)	+2 (100°C)	*71*
$Ca(BH_4)_2$	THF	+2.5	*72*
$Ca(TFSI)_2$	EC:PC (1:1) + BF_3·DE	Ox: −3.12 vs. AgRE	*100*
$Ca[B(hfip)_4]_2$	DME	+4	*73,74*
$Ca(PF_6)_2$	EC:PC (3:7)	+2.9	*93*

Table 4: Summary of progress in the field of Ca electrolytes.

2. The chemistry of WCAs

Non-coordinating anions, more accurately termed as WCAs, interact only weakly with cations. They are commonly found as counter ions in metal complex compounds, and are unlikely to bind directly to the metal center of a complex.[107] These anions are larger and even more weakly coordinating than those classic 'noncoordinating" (as tetrafluoroborate BF_4^-, hexafluorophosphate PF_6^-, perchlorate ClO_4^-);[108] These include BPh_4^- and its derivatives, $CB_{11}H_{12}^-$ and related carborane anions.[109]

About state of art of WCAs, a revolution in this area occurred in the 1990s, signing the "BARF" era, with the introduction of tetrakis[3,5-bis(trifluoromethyl)phenyl]borate ion, $B[3,5\text{-}(CF_3)_2C_6H_3]_4^-$, abbreviated as $[BAr^F{}_4]^-$ commonly known as "BARF" (Figure 40).[110]

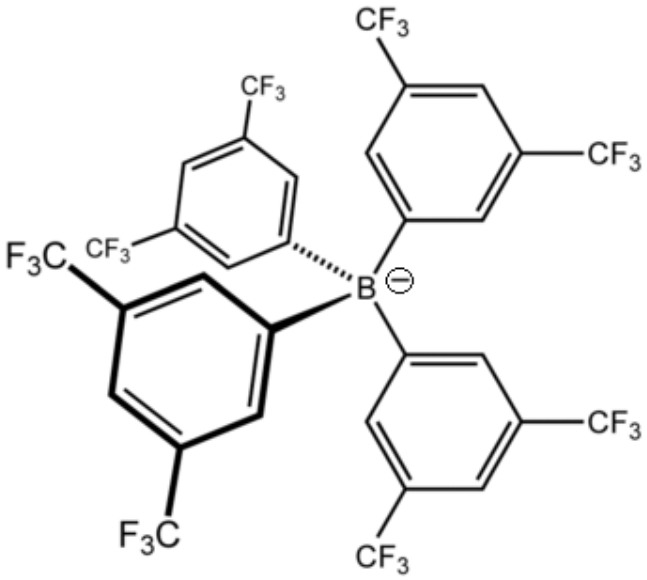

Figure 40: The $[BAr^F{}_4]^-$ anion with four fluorinated aryl groups distributed tetrahedrally around a central boron atom.[111]

This anion is far less coordinating than tetrafluoroborate, hexafluorophosphate and perchlorate, and consequently has enabled the study of very electrophilic cations. In bulky borates and aluminates, the negative charge is symmetrically distributed over many electronegative atoms. Tetraphenylborate anion has an unique structure in which four phenil groups are tetrahedally bonded to the central boron atom by dative covalent bonds. We have to consider the pre-"BARF" era, in which, prior to the 1990th, BF_4, PF_6^-, and ClO_4^- anions were considered weakly coordinating anions. These species are now known to bind strongly to electrophilic metal centers. Tetrafluoroborate and hexafluorophosphate anions are coordinating highly electrophilic metal ions, such as Zr(IV) centers, which can extract fluoride ions from these anions. Other anions, such as triflate ($CF_3SO_3^-$), are considered to be low-coordinating with some cations.[112] Very prominent amongst alternative anions are sulfonyl substituted bis-imides, such as bis(trifluorome-thanesulfonyl)imide (TFSI) and its smaller analogue bis(-fluorosulfonyl)imide (FSI), which have relatively good ionic conductivities and stabilities. These are also the anions of choice to stabilise metallic Li anodes during extensive charge discharge cycling, which is an important requisite to enable high energy density LIBs.[109]

Another advantage of these anions is that their salts are more soluble in non-polar organic solvents such as dichloromethane, toluene, and, in some cases, even alkanes. Polar solvents, such as acetonitrile, THF and water tend to bind to electrophilic cation centers, in which cases, the use of a non-coordinating anion is pointless.

The prime role of WCAs is to suppress strong cation-anion interactions and to replace the few strong electrostatic interactions in classical salts by a multitude of weak interactions.[113] To achieve this goal, the majority of more recent WCAs are rather large and exhibit diameters in the nanometer range. Moreover, their "surfaces" are often covered by poorly polarizable fluorine atoms that produce a "Teflon"-type coating additionally dampening the efficiency of

ion pairing and increasing the (kinetic) inertness and (thermodynamic) stability of these anions against ligand coordination or abstraction as well as oxidation. Overall, this leads to improved solubility of WCA salts in less or even non polar solvents, reducing ion pairing, and ultimately also leading to high ionic conductivity (Figure 41). In the last two decades, several research groups synthesized new WCAs using sterically bulky anions with the negative charge dispersed over a large surface.[114]

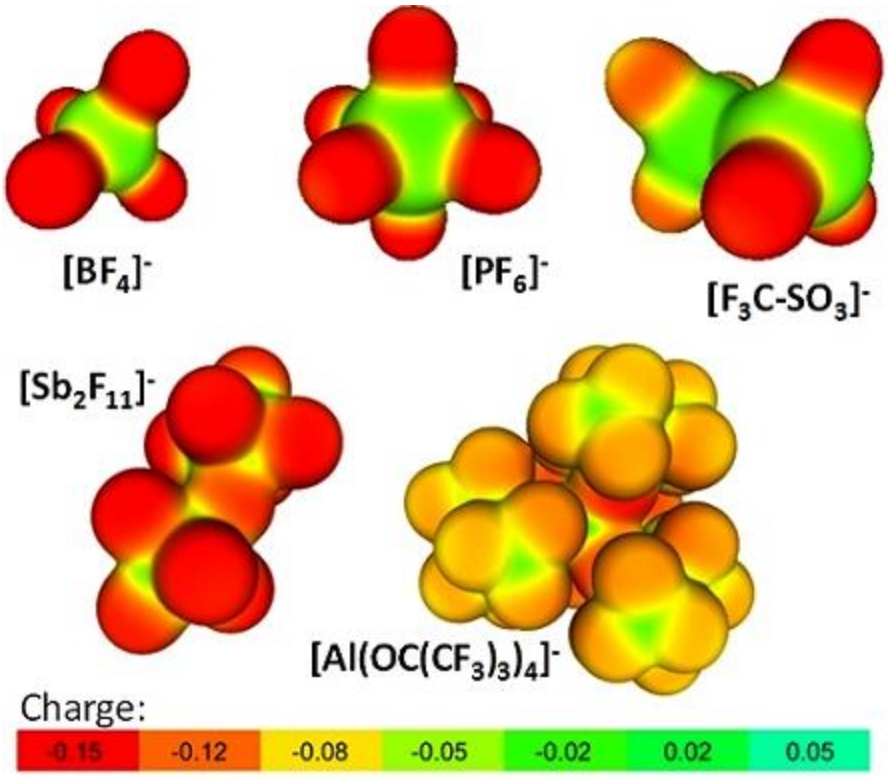

Figure 41: Density maps of some WCAs; red coloration indicates high accumulation of negative charge.[114]

In the last years, most of research was done on alkoxy- and alkoxyaluminates with general formula $[M(OR^F)_n]^-$ (R^F = poly- or perfluorinated alkyl or aryl group; M = Al^{III}, Nb^V, Ta^V, Y^{III}, La^{III}).[115] They found applications in homogenous catalysis, polymerizations, electrochemistry

and supercapacitors. Salts of $[M(OR^F)_n]^-$ are easily accessible even in larger scales. Some of these anions have successfully been tested, e.g., as counter ions in cationic polymerization reactions. In particular, the introduction of sterically bulky ligands like $-OC(CF_3)_3$, $-OC(CH_3)(CF_3)_2$ or $-OCH(CF_3)_2$ has led to alkoxyaluminate anions that are well suited for many purposes. $[Al(OC(CF_3)_3)_4]^-$ is among the most weakly coordinating anions currently known, due to the high number of peripheral C-F bonds. This high stability arises from the steric shielding of the basic oxygen atoms by the bulky ligands with perfectly interlocking $-CF_3$ groups and the electronic stabilization resulting from perfluorination. Fluorine is a strong electron acceptor which stabilizes the negative charge of the oxygen.[116]

2.1 Towards the functionalization of B-H bond

Starting from the classical BF_4^- anion, substitution of fluorine is an illustrative example for the first approach of functionalization, leading to polyfluorinated tetraaryl- or tetraalkylborates $[B(R^F)_4]^-$ (R^F = CF_3, C_6F_5, $C_6H_3(CF_3)_2$, and others), a class of anions nowadays mainly used in homogenous catalysis. These borates are simple to prepare and are surprisingly thermodynamically stable.[117]

Similarly to the alkyl borates, the substitution of the fluorine atoms in BF_4^- or hydrogen atoms in BH_4^- with alkoxy groups, lead us to a new class of anions: the alkoxyborate $[B(OR^F)_4]^-$ Figure 42).[118] The extraordinary physico-chemical properties of these WCAs are given by the B-O bond. Boron is almost exclusively found in the environment in the form of boron-oxygen compounds, which are often referred to as oxyborates. The high strength of the B-O bond (536

kJ/mol) relative to those between boron and other elements (B-C 356 kj/mol for example) makes boron oxide compounds more stable compared to nearly all non-oxide boron materials. Indeed, the B-O bond is among the strongest found in the chemistry of naturally occurring substances.[119]

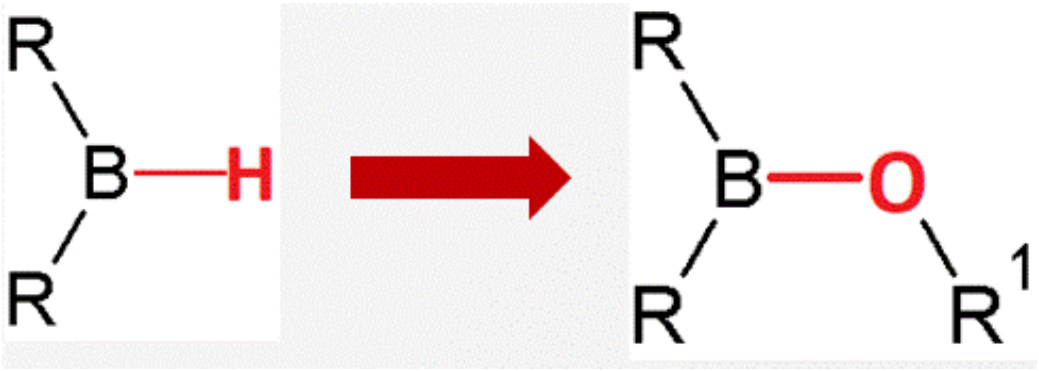

Figure 42: *Scheme of derivatization from borohydride to alkoxyborate compounds.*

A rational design of ion-conductive Ca compounds is of primary importance to develop an innovative electrolyte, which is capable of plating and stripping Ca at room temperature. It needs to have the essential properties including compatibility with the metallic Ca anode, a wide ESW and efficient ion transport. An anion that lacks donor atoms with electron lone pairs leads to more favored ion association, higher cation mobility and ionic conductivity. The anion oxidation stability can be predicted by theoretical calculation: the lower the HOMO energy level of the anion, the greater oxidative stability can be expected.[120] The fluorinated alkoxyaluminate and alkoxyborate anions such as $[B(hfip)_4]^-$ or $[Al(hfip)_4]^-$ (hfip = -$OCH(CF_3)_2$) have been proven to be promising candidates for the formulation of salts with high ionic conductivity and high anodic stability.[121] Owing to the high electronegativity of fluorine, the charge in bulky alkoxyaluminate and alkoxyborate anions is extensively delocalized resulting in weak cation-anion interactions and thus a high ionic conductivity. Moreover, the stable C-F bonds account for the high electrochemical stability: for example,

$Li[Al(hfip)_4]$) exhibits a high anodic stability > 5.0 V vs. Li^+/Li. More recently, research on magnesium batteries has tended towards the preparation of halide free, anodically stable and low-ion pairing compounds, for the realization of an efficient non-corrosive Mg ion-conductive electrolyte. Such Mg salts have favorable electrolytic characteristics and are compatible with the Mg electrode. Arnold et al.[122] demonstrated that magnesium hexafluoroisopropylaluminate $Mg[Al(hfip)_4]_2$ in ethereal solvents can reversibly deposit magnesium with high oxidative stability (> 3.5 V vs Mg^{2+}/Mg) and conductivity (> 6 mS cm^{-1}). Robust synthetic routes for Mg fluorinated alkoxyborate and Mg alkoxyaluminate have been recently established. In particular, magnesium tetrakis(hexafluoroisopropyloxy) borate $Mg[B(hfip)_4]_2$ can be straightforwardly synthesized by the dehydrogenation reaction of $Mg(BH_4)_2$ with hexafluoro-2-propanol (hfip) in DME with high yield, by refluxing conditions.[91] The DME solution of $Mg[B(hfip)_4]_2$ is capable of reversible Mg plating/stripping, with a Coulumbic efficiency close to 100% and possesses an extremely high anodic stability (> 4.3 V vs Mg/Mg^{2+}). Moreover, $Mg[B(hfip)_4]_2 \times 3DME$ is thermally stable up to 150 °C and also air and hydrolysis stable, which makes it safe in storage and convenient in handling for practical applications. $Mg[B(hfip)_4]_2$ is basically compatible with any type of cathode and anode materials and can serve as an universal electrolyte for Mg batteries. The high stability of this WCA depends on the strong electron acceptor character of perfluorinated alkoxy chain, which contributes to the stabilization of the boron atom, by delocalization the negative charge, making it a very poor nucleophile.[123]

The first goal of our project is to design an effective Ca based electrolyte, which enables Ca stripping/deposition at room temperature with relatively high ESW. Inspired by the promising results in Mg electrolytes, calcium tetrakis(hexafluoroisopropyloxy) borate, $Ca[B(hfip)_4]_2$ salt in glyme-based solvents was proposed as a potential electrolyte for room-temperature rechargeable Ca batteries. It signed an important step into state-of-the-art non-aqueous Ca electrolyte, since, with the outstanding stability, $Ca[B(hfip)_4]_2$ based electrolytes may open the

pathway to explore high-voltage cathodes for Ca batteries. In their pioneering work, Zhao-Karger and al.[73] synthesized $Ca[B(hfip)_4]_2$ salt by combining calcium borohydride and hexafluoro-2-propanol in DME solvent at reflux conditions. In parallel, Nazar and al.[124] demonstrated the reversible Ca plating/stripping activity at room temperature using $Ca[B(hfip)_4]_2$/DME electrolyte. In this case, $Ca[B(hfip)_4]_2$ was prepared from Calcium hexafluoroisopropoxide ($Ca(hfip)_2 \times XTHF$) and tris-hexafluoroisopropoxy borate ($B(hfip)_3$) in DME solvent at 65°C.

Both (Zhao-Karger and Nazar) synthetic procedures use elevated temperatures for the preparation of the salt. In this work, we wanted to improve the synthetic pathway, using no reflux or even no heating. Several attempts brought us to understand that the derivatization of B-H bond of starting borohydride with hexafluoropropanol is allowed also at room temperature.

3. Synthesis of the $Ca[B(hfip)_4]_2 \times 4DME$ salt

All operations of synthesis and work-up were carried out into Ar-filled glovebox (H_2O and O_2 contents <0.1 ppm).

Hexafluoropropan-2-ol ($HOC(H)(CF_3)_2$) (further denoted "H-hfip") was purchased from Apollo Scientific, bubbled with Ar to remove air, transferred inside an Ar-filled glovebox and dried twice with activated 4Å molecular sieves for a period of 10 days, giving a final value of H_2O lower than 0.1 ppm by Karl-Fisher titration.

Calcium borohydride bis(tetrahydrofuran) ($Ca(BH_4)_2 \times 2THF$) was purchased from Sigma-Aldrich; the powder flask was opened inside the anti-chamber of Ar-filled glovebox and stored inside it after degassing under vacuum.

DME was purchased from Sigma-Aldrich; it was bubbled with Ar, transferred inside Ar-filled glovebox, dried first with 4Å molecular sieves for 3 days, then refluxed with K/Na (3/1 wt.) for one day and finally distilled. Karl-Fisher titration analysis gave a value of 3.1 ppm of H_2O.

$Ca[B(hfip)_4]_2 \times 4DME$ salt was synthetized by dissolving of $Ca(BH_4)_2 \times 2THF$ powder (1.07 g, 5 mmol) into 10 ml of anhydrous DME. Then, 42.5 mmol of anhydrous H-hfip (4.5 mL, 7.14 g) was added dropwise over 30 minutes onto a stirred solution of $Ca(BH_4)_2 \times 2THF$/DME. The clear solution was stirred at room temperature for 20 hours. Then, the solvent was evaporated at reduced pressure and the solid product, a white powder (8.32 g, 94%), was dried in vacuo at 50°C for 1 day (Figure 43).[125]

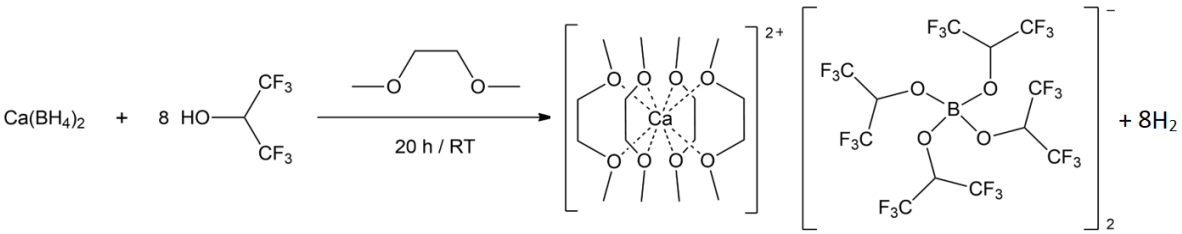

Figure 43: *Scheme of synthesis of Ca[B(hfip)$_4$]$_2$×4DME.*[125]

The reaction is characterized by the absence of byproducts at the end of synthetic process, since only elemental hydrogen is formed and its evolution represents the driving-force of the whole conversion. As DME and excess of H-hfip are both low-boiling point solvents, they can be easily removed by drying in vacuo, resulting in pure Ca salt. Moreover, owing to the stronger basicity of $Ca(BH_4)_2$, the substitution of its four hydride ions with fluorinated alcohol is easier and it can be promoted even at room temperature, compared to $NaBH_4$, in which basicity degree results lower than Ca- and Mg- derivatives and higher temperature is needed for the reaction.[126]

4. Characterization of $Ca[B(hfip)_4]_2$ ×4DME salt

The conversion from the $Ca(BH_4)_2$ to the $Ca[B(hfip)_4]_2$×4DME salt was verified through various complementary characterization techniques: ^{1}H, ^{11}B, ^{13}C and ^{19}F NMR, powder and single crystal X-ray diffraction (XRD), FTIR and Raman spectroscopy, high resolution mass spectroscopy (HRMS) and inductively coupled plasma atomic emission spectroscopy (ICP-AES). Our goal was to confirm the complete reaction conversion without starting borohydride and byproducts at the end of synthetic process.

4.1. Nuclear magnetic resonance (NMR) spectroscopy

The conversion from hexafluoropropan-2-ol (H-hfip) to $Ca[B(hfip)_4]_2$×4DME was confirmed by means of NMR spectroscopy. NMR spectra were obtained with a Bruker AVANCE NEO 600 MHz NMR spectrometer using MeCN-*d3* solvent in all cases except ^{11}B NMR. To correct the chemical shift, MeCN residual peak was used for ^{1}H (1.94 ppm) and ^{13}C (1.32 ppm) NMR spectra.[127]

^{1}H NMR (600 MHz, MeCN–*d3*)**:** δ 4.72 (br m, 8H, –CH–$(CF_3)_2$), 3.49 (s, 16H, –OCH_2–), 3.32 (s, 24H, OMe) ppm.

The singlet peaks at 3.49 and 3.32 ppm belong to the protons resonance of H_3C- and –CH_2-groups of DME molecules linked to the complex. Septet peaks at 4.72 ppm belong to resonance of H-F heteronuclear coupling between H of complex and F. The integration of singlet peaks of DME and septet of salt gives us the information that 4 DME molecules are linked for each molecule of alkoxyborate salt (Figure 44).

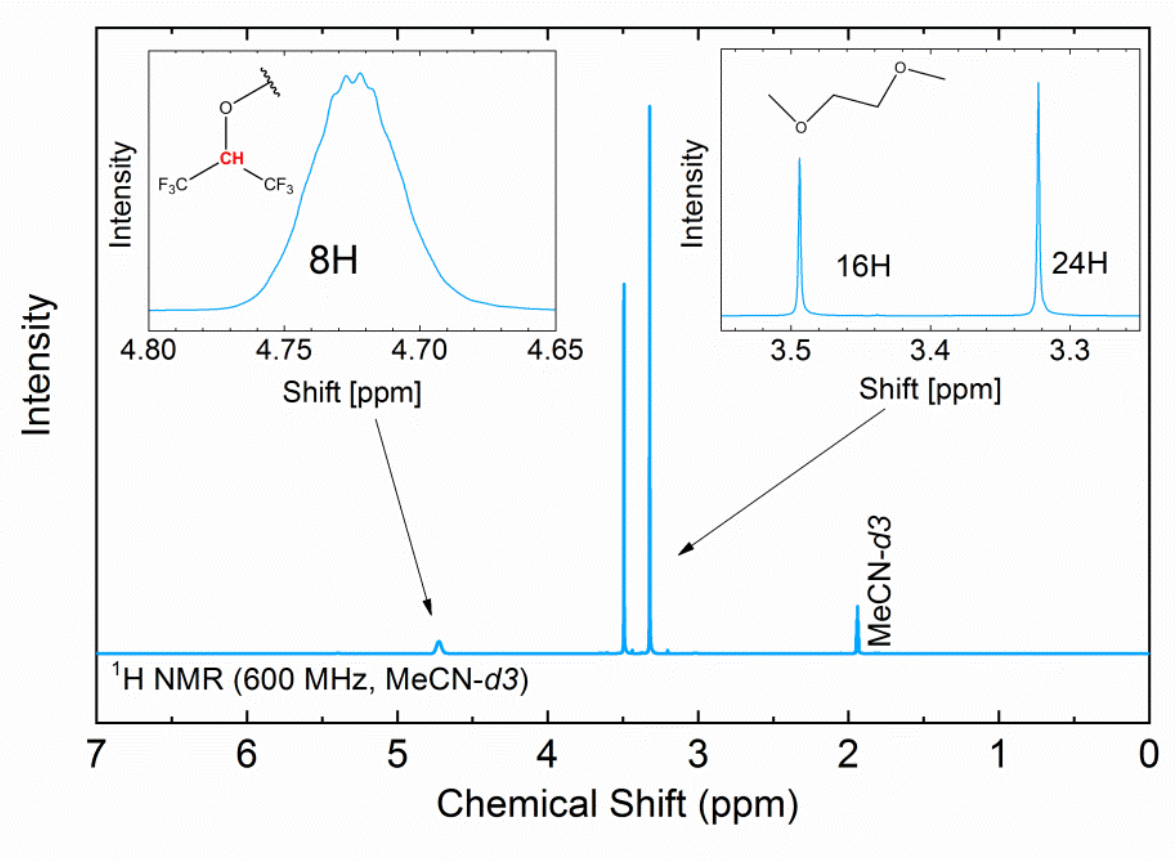

Figure 44: *^{1}H NMR spectrum of $Ca[B(hfip)_4]_2 \times 4DME$ in MeCN-d3.*[125]

^{19}F NMR (565 MHz, MeCN–*d3*)**:** -75.7 (d, $^{3}J_{HF}$ = 6.5 Hz) ppm.

For ^{19}F NMR spectra (Figure 45), trifluoroacetic acid was used as internal standard with reported chemical shift of -76.72 ppm. NMR spectra were also not decoupled from ^{1}H, which resulted in dublet $^{3}J_{HF}$ = 6.5 Hz.[128]

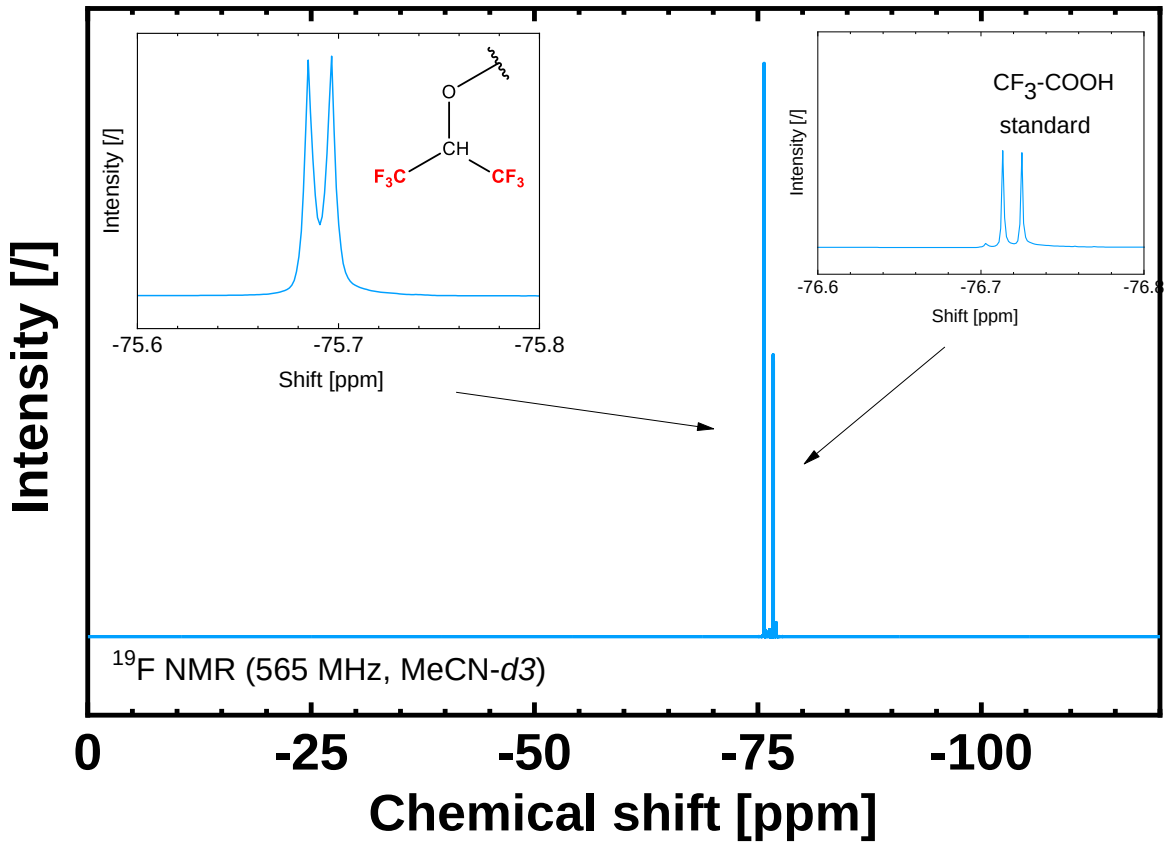

Figure 45: *^{19}F NMR spectrum of Ca[B(hfip)$_4$]$_2$ ×4DME in MeCN-d3.*[125]

^{11}B NMR (160 MHz, THF–d_8): δ -55 (s, 1B, BH_4^-), δ -17.8 (s, 1B, $Ca[B(hfip)_4]_2$).

The conversion from calcium borohydride to $Ca[B(hfip)_4]_2 \times 4D$ ME was confirmed even by shifting of signal from -55 ppm of $Ca(BH_4)_2$, that was completely consumed during reaction, to -17 ppm of final fluorinated alkoxyborate based salt (Figure 46). The sharp peaks in the spectra are given by contribution of glass probes.

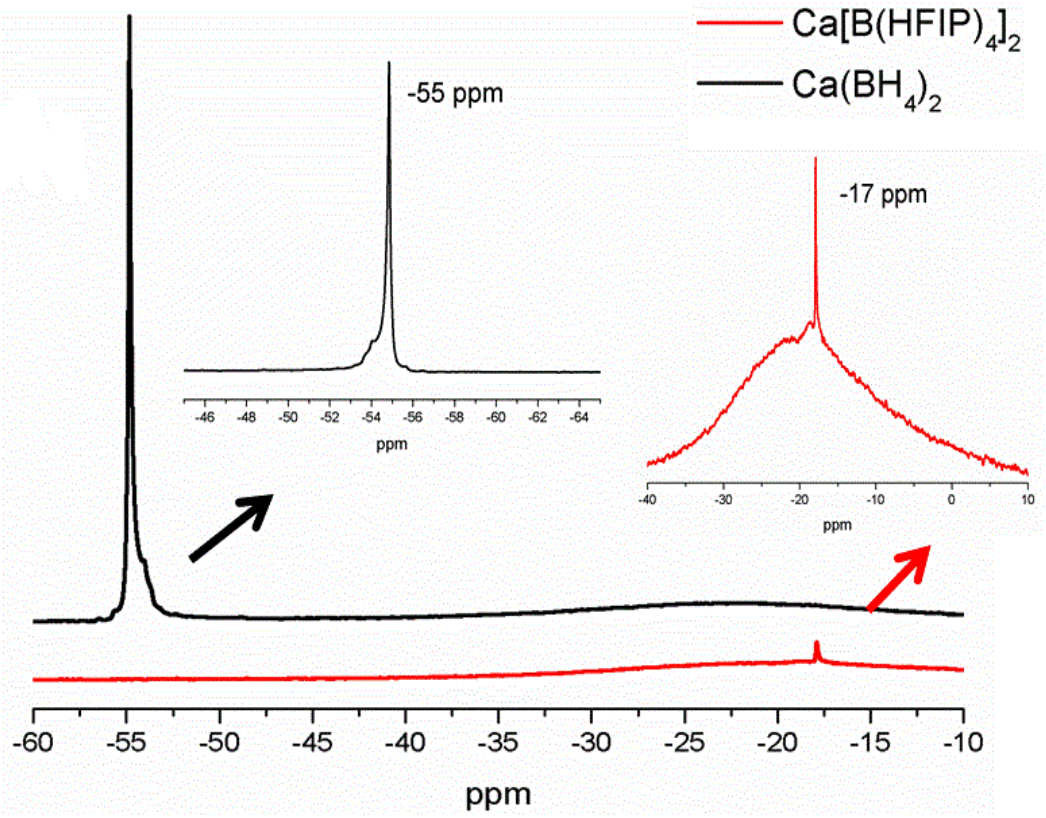

Figure 46: *Comparison of ^{11}B NMR spectra of $Ca[B(hfip)_4]_2 \times 4DME$ and $Ca(BH_4)_2$ in THF–d_8.*

^{13}C NMR (151 MHz, MeCN–*d3*)**:** 123.9 (q, $^{1}J_{CF}$ = 285 Hz), 72.3, 70.5 (s, $^{2}J_{CF}$ = 32 Hz), 59.2 ppm.

The ^{13}C NMR spectra were decoupled from ^{1}H but not from ^{19}F. Due to this –CF_3 carbon is visible as a quartet ($^{1}J_{CF}$ = 285 Hz) and CF_3–CH(–O–)–CF_3 as a septet ($^{2}J_{CF}$ = 32 Hz) (Figure 47)

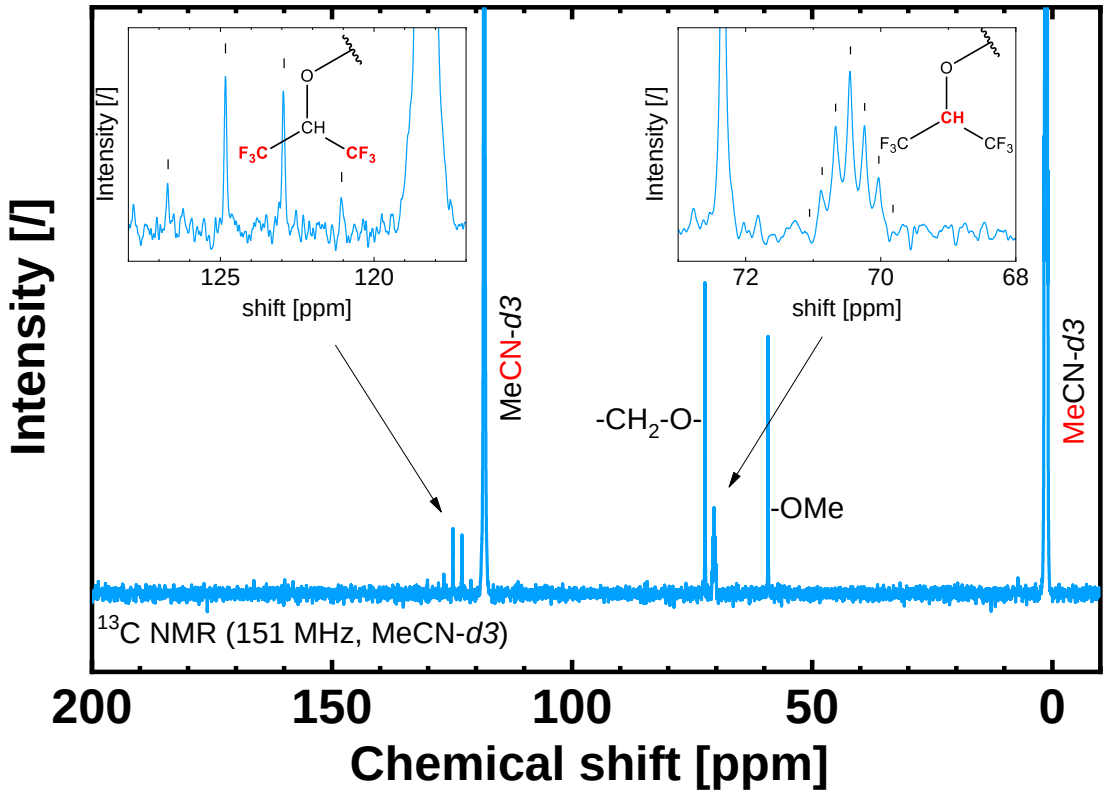

Figure 47: *^{13}C NMR spectrum of $Ca[B(hfip)_4]_2$ ×4DME in MeCN-d3.*[125]

4.2. Fourier-trasform infrared spectroscopy (FTIR)

FTIR measurements were performed on the Bruker Alpha II ATR with the Ge crystal operating inside the Ar-filled glovebox. FTIR spectra were collected and averaged over 64 scans with the resolution of 4 cm^{-1} in the range between 4000 cm^{-1} and 600 cm^{-1}. All spectra presented were recorded at the room temperature.

$Ca[B(hfip)_4]_2 \times 4DME$ FTIR spectrum (Figure 48) has a central band at 1187 cm^{-1} that can be attributed to the B−O−C stretching vibrations and CF_3 symmetric and antisymmetric stretching vibrations. Another new band is at 1381 cm^{-1}, due to the vibration of C−CF_3 groups.[129] The presence of the CF_3 group is further verified by the sharp and intense band at 686 cm^{-1} due to the deformation mode of the CF_3 group. [130] Two bands at 1097 cm^{-1} and 1058 cm^{-1} correspond to two C−O stretching vibrations from dme solvent and boron complex.[131]

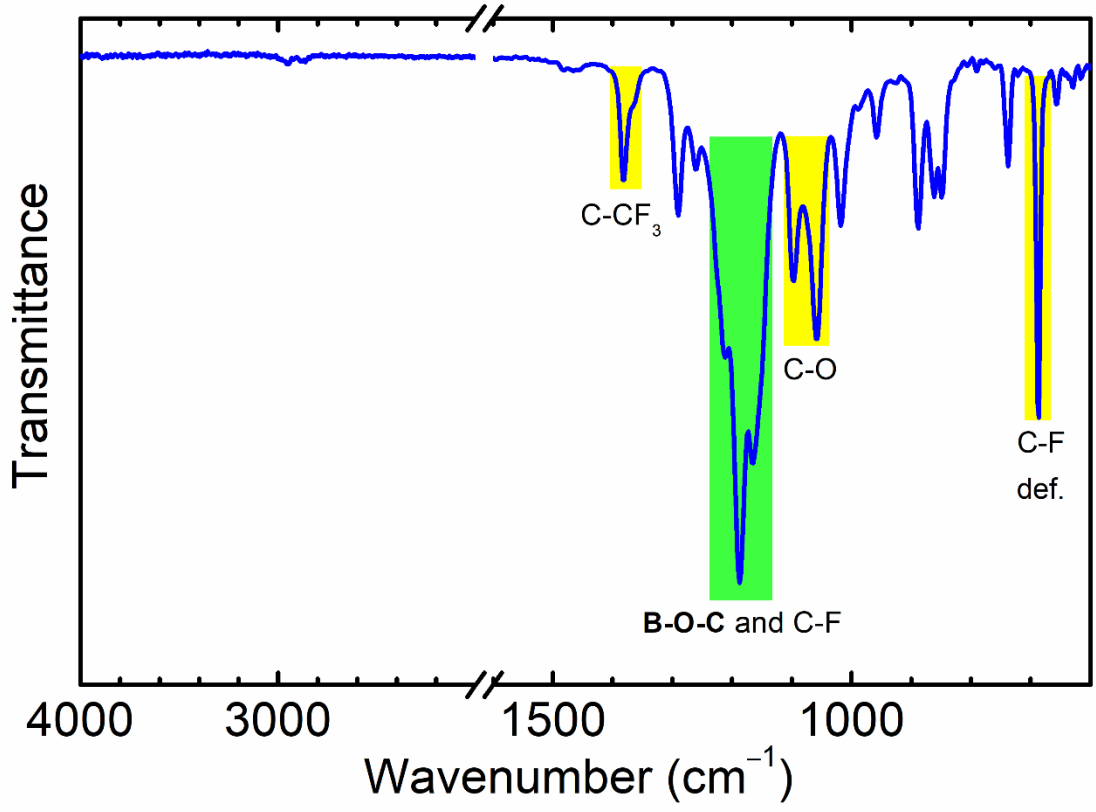

Figure 48: *FTIR spectrum of* $Ca[B(hfip)_4]_2 \times 4DME$.[125]

The disappearance of B-H bond stretching peaks (Figure 49) at 2394 cm^{-1} and 2256 cm^{-1} from $Ca(BH_4)_2 \times 2THF$ leads to confirmation that starting borohydride is completely converted to final fluorinated alkoxyborate based salt.[132]

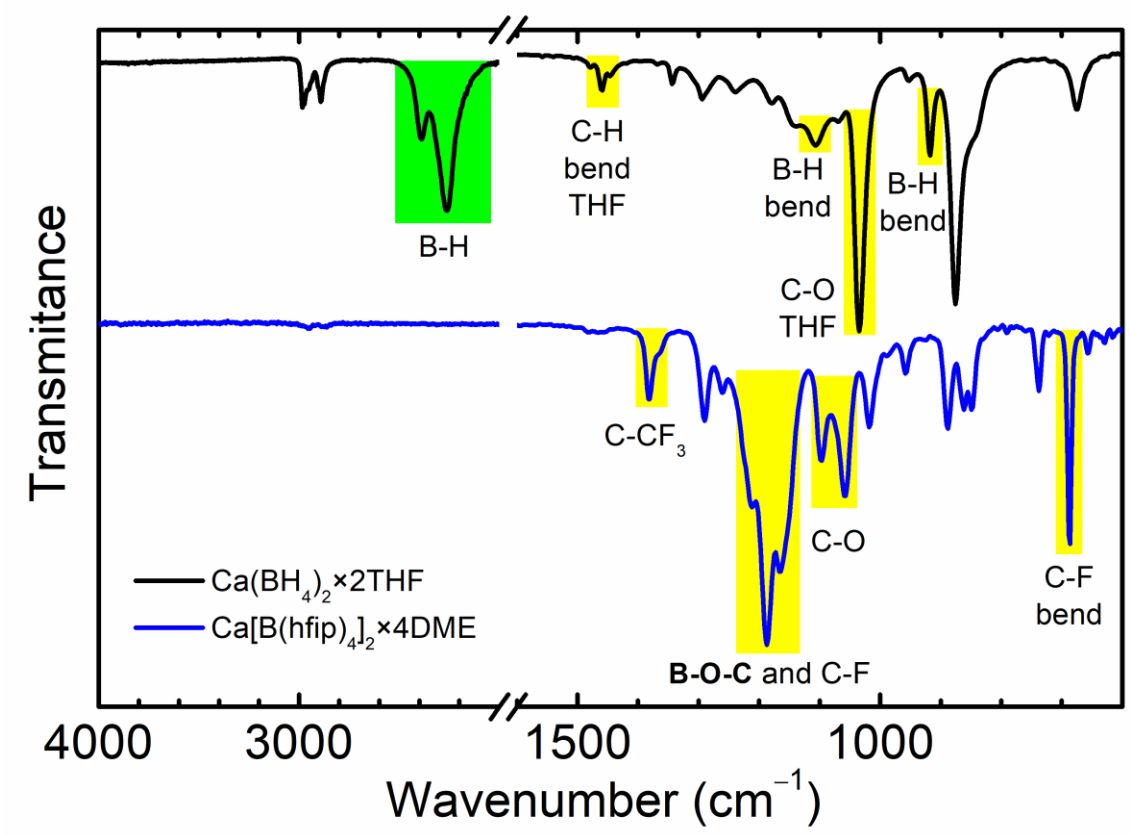

Figure 49: *Comparison of FTIR spectra of $Ca(BH_4)_2 \times 2THF$ and $Ca[B(hfip)_4]_2 \times 4DME$.*[114]

The $Ca[B(hfip)_4]_2 \times 4DME$ salt was dried at different temperatures, from 70°C to 120°C, under vacuum overnight into Ar-filled glovebox. The corresponding FTIR spectra in Figure 50 show the retention of main FTIR absorbance peaks of the salt with the increasing drying temperature. The C-F bond bending at 686 cm^{-1} is observed until 120°C proving the high thermal stability of this chemical group; in fact, the carbon–fluorine bond is one of the strongest in organic chemistry (an average bond energy around 480 kJ/mol).[133] Moreover, by comparing the spectra to that of DME, as C-O bond stretching at 1106 cm^{-1} and bending at 847 cm^{-1}, and C-H bond bending at 1362 cm^{-1}, it is possible to observe how the intensities of these peaks decrease with

the increase of drying temperature. This indicates that DME molecules contained in the solid alkoxyborate salt are gradually released along the drying process although from this results we can see that 120 °C is not enough to fully remove all DME from complex.

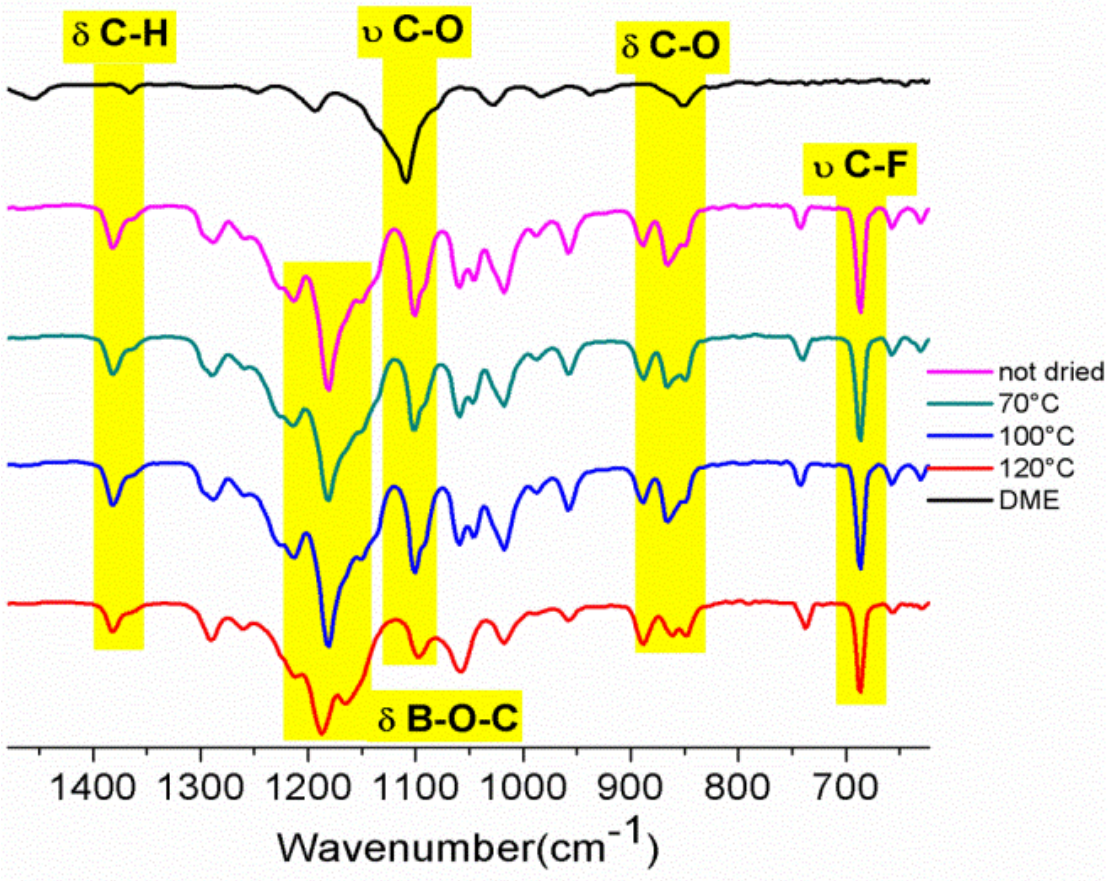

Figure 50: *FTIR spectra of Ca[B(hfip)$_4$]$_2$×4DME salt, dried in vacuum at different temperatures, comparing with FTIR spectrum of DME.*[114]

4.3. Raman spectroscopy

The Raman spectrum of $Ca[B(hfip)_4]_2 \times 4DME$ was recorded in the spectral range from 3700 cm^{-1} to 70 cm^{-1} with a Witec Alpha 300 confocal microscope using a green laser with the excitation wavelength of 532 nm. The resolution of the recorded spectra was 4 cm^{-1} and the laser power was adjusted to 10 mW. The spectrum of the synthesized complex was measured in a closed glass vial to avoid contamination with oxygen and water. The spectra were recorded by 100 accumulations with an integration time of 0.6 s.

The Raman spectrum of the $Ca[B(hfip)_4]_2 \times 4DME$ (Figure 51) is more complex and less informative than the corresponding FTIR spectrum, due to low intensity of the CF_3 and B–O–C bands. However, there is clear evidence of the presence of DME molecules in the fluorinated salt, for the presence of asymmetric and symmetric bands of CH_3, CH_2 from 3000 cm^{-1} to 2800 cm^{-1} and deformation modes at 1483 and 1455 cm^{-1}.[134] There are two strong strain modes, C−O at 879 cm^{-1} and C−C at 722 cm^{-1}.[135] The most prominent and at the same time characteristic anion band is located at 805 cm^{-1} and is attributed to the symmetric type of B−O−C stretching..[136]

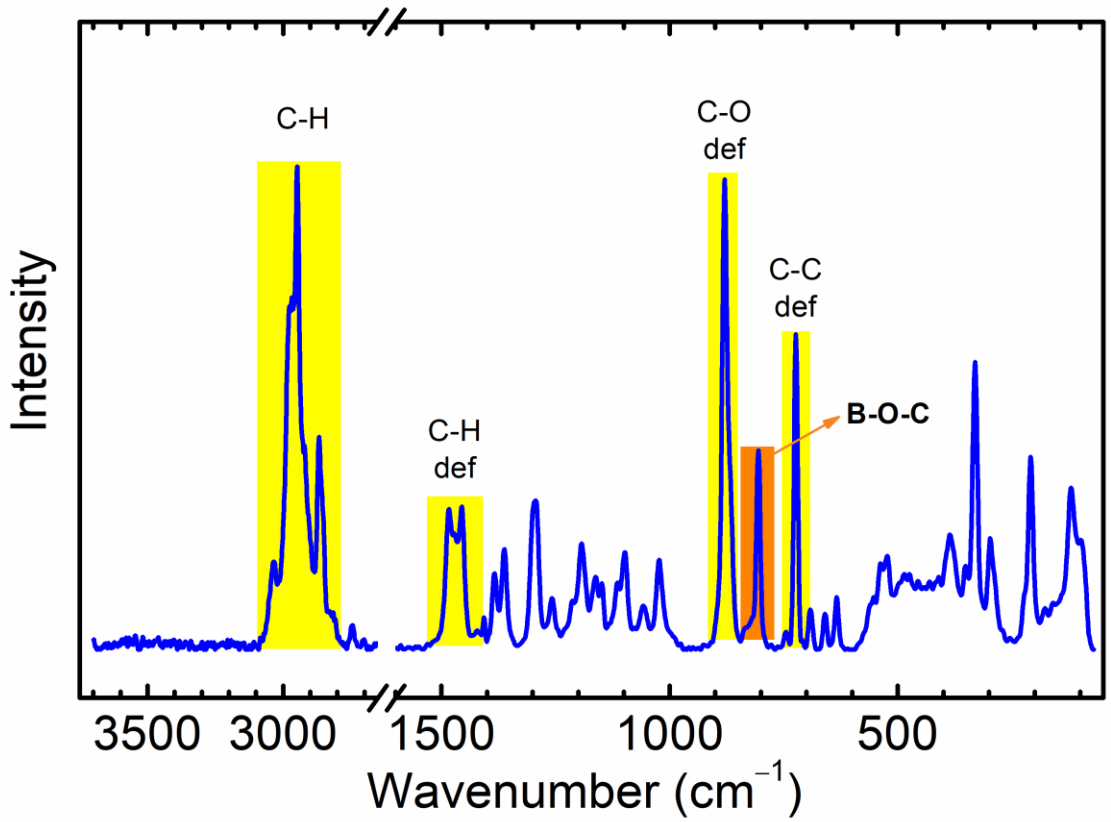

Figure 51: *Raman spectrum of $Ca[B(hfip)_4]_2 \times 4DME$.*[125]

4.4. Elemental analysis by inductive coupled plasma (ICP-OES)

The ICP-OES used for the measurements was sequential radial Optical Emission Spectrometer 715-ES, Varian. For quantitative determination of Boron and Ca inductively coupled plasma optical emission spectroscopy (ICP-OES) was used. The sample was dissolved in deionized milli-Q water: 50 mg of sample were transferred into a 50 mL measurement flask and dissolved with milli-Q water to which 0.5 mL of HNO_3 was added. Before the measurements, the solution was diluted 10-fold with milli-Q water and acidified with nitric acid. To correct for possible matrix effect, Y and Sc were used as internal standards. Calibration solutions contain Ca and B in a concentration range between 0–30 mmol/L were prepared. Calcium was measured at 396.8 and 317.9 nm and boron at 249.8 nm, respectively. As shown in Table 5, it has been got a good matching between measured ICP and theoretical value for $Ca[B(hfip)_4]_2 \times 4DME$; a small differences about Ca and B % mass values are due to samples preparation and measurement errors.

Element (% mass)	ICP	$Ca[B(hfip)_4]_2 \times 4DME$ theoretical
Ca	2.30	2.28
B	1.30	1.23

Table 5: Results of ICP-OES elemental analysis of our salt and theoretical calculated values for $Ca[B(hfip)_4]_2$ and $Ca[B(hfip)_4]_2 \times 4DME$.[125]

4.5. SEM and EDS analysis

SEM was performed with a field emission Supra 35 VP Carl Zeiss microscope coupled with EDS at 20 kV of accelerating voltage. The $Ca[B(hfip)_4]_2 \times 4DME$ powder consisted of particles with irregular shape and sizes lower than 600 µm (Figure 52).

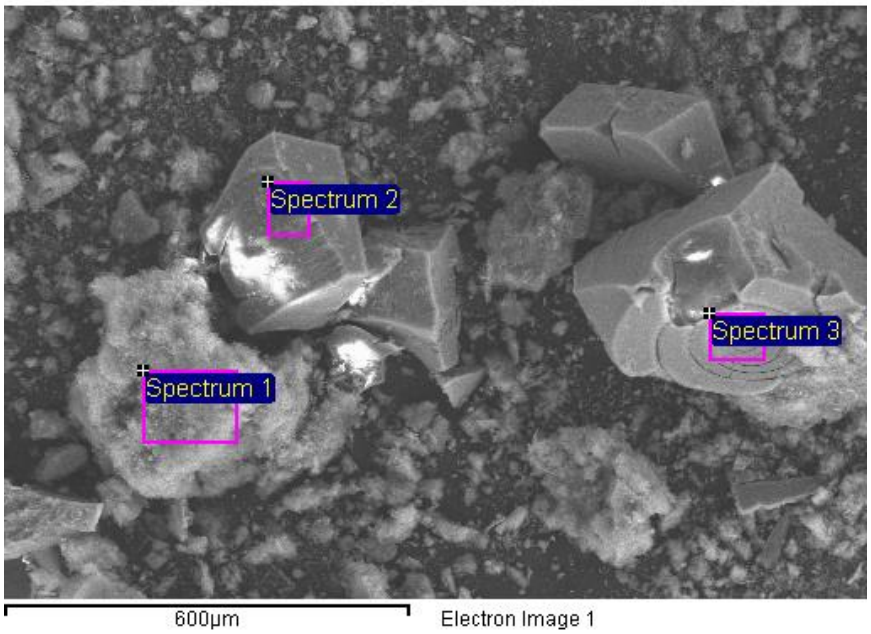

Figure 52: *Scanning electron micrographs of* $Ca[B(hfip)_4]_2 \times 4DME$ *powder*.

The homogeneous distribution of fluorine (purple) and calcium (green) on the surface of these particles was confirmed by EDS analysis. (Figure 53).

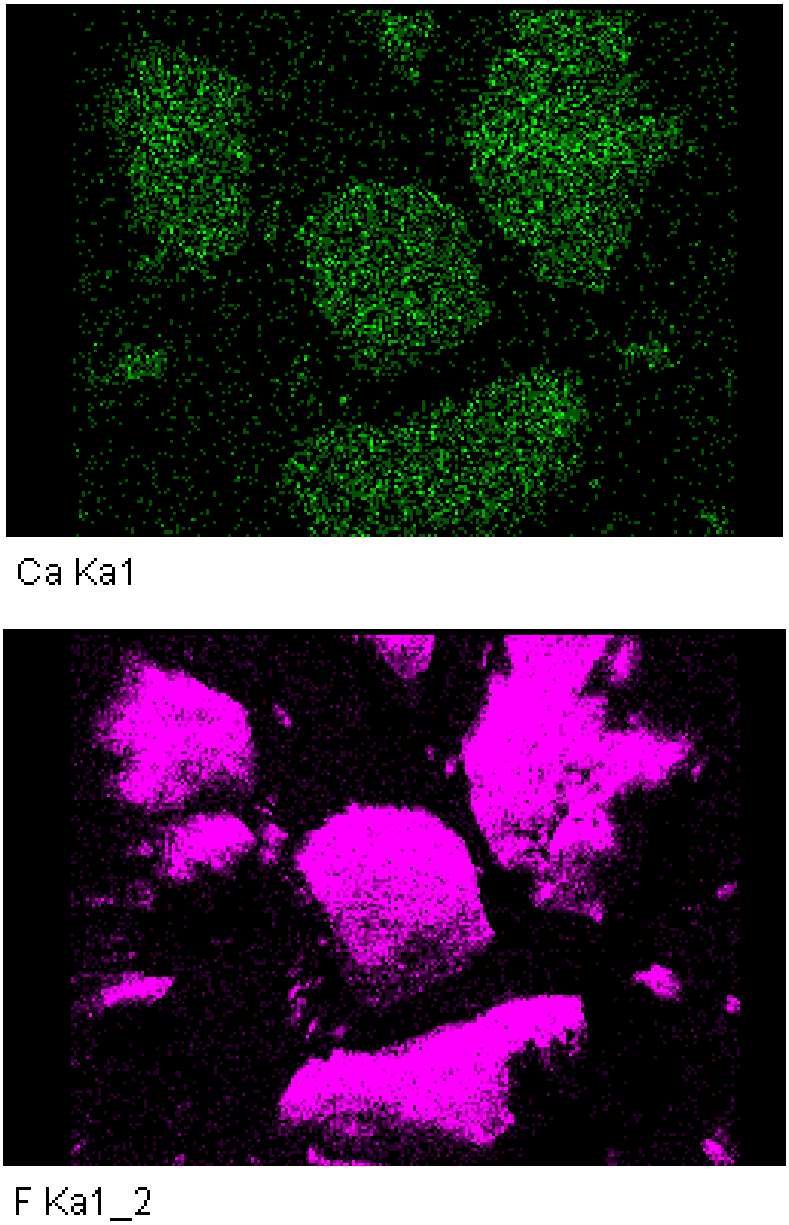

Figure 53: *EDS analysis of Ca[B(hfip)$_4$]$_2$×4DME particles, with evidence of uniform fluorine (purple) and calcium (green) distribution on the surface.*

4.6. High resolution mass spectrometry (HRMS)

The $Ca[B(hfip)_4]_2$ salt was analyzed by high resolution mass spectrometry (HRMS) coupled with negative electrospray ionization (Figure 54). The sample was dissolved in 2 ml of dried acetonitrile (1.4 ppm of H_2O, mobile phase of spectrometer), into a glass flask sealed onto Ar-filled glovebox, to have a final concentration of 36 µM. Then, 10 µL sample solution was directly injected in the high-resolution mass spectrometer with electrospray ionization in a positive and negative mode at 3kV capillary voltage at source temperature 1000°C and desolvation nitrogen gas of flow 550 L/h. Mass measurements were run on a hybrid quadrupole orthogonal acceleration time-of-flight mass spectrometer (Q-ToF Premier, Waters, Milford, Massachusetts, USA) equipped with an electrospray ionisation interface operating in positive ion mode. The capillary voltage was set to 3.0 kV, the source and desolvation temperatures were set to 100 and 230 °C, respectively. The nitrogen desolvation gas flow rate was set to 600 L/h. HRMS data were collected in the m/z range 100-1500 at 10000 mass resolution. Data were collected in a centroid mode, with a scan accumulation time set to 0.25 s and interscan delay of 0.02 s. Data station operating software was MassLynx v4.1.

EI-HRMS: Calc. for $C_{12}H_4O_4BF_{24}$: m/z = 678.9304 (M^-). Found: *m/z* = 678.9306

Calc. for $C_{24}H_8O_8B_2F_{48}Ca$: m/z = 1397.93 (M^-). Found: *m/z* = 1397.9402

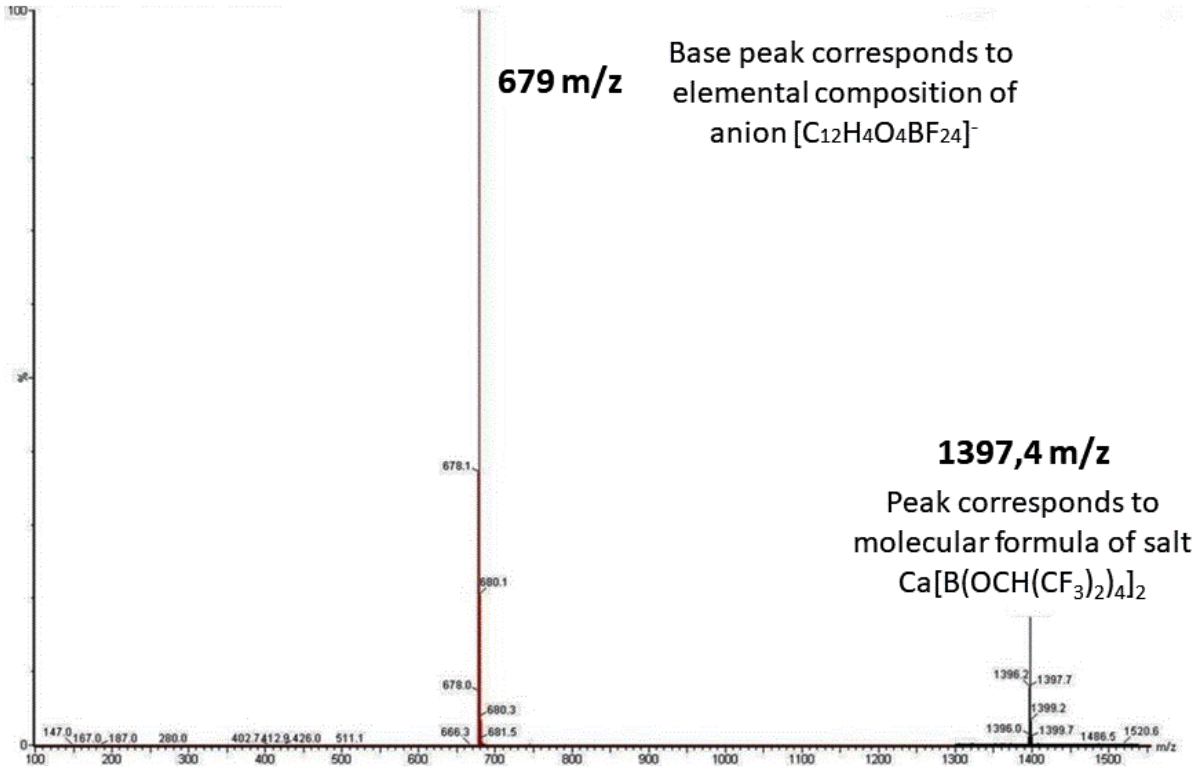

Figure 54: *HRMS spectrum of $Ca[B(hfip)_4]_2 \times 4DME$.*

4.7. X-ray diffraction

The X-ray diffraction pattern of the $Ca[B(hfip)_4]_2 \times 4DME$ salt (Figure 55), previously sealed into a quartz capillary, was measured on X'Pert MPD diffractometer (PANalytical) with Cu $K_{\alpha 1}$ wavelength, 7–80° in the 2theta range from 7 to 80° with steps of 0.034 °, with a counting time of 100 seconds. Detector was totally opened 2,122. Soller slit 0.04 rad, mask 5mm, divergence and ant scatter slit 5mm, no rotation.

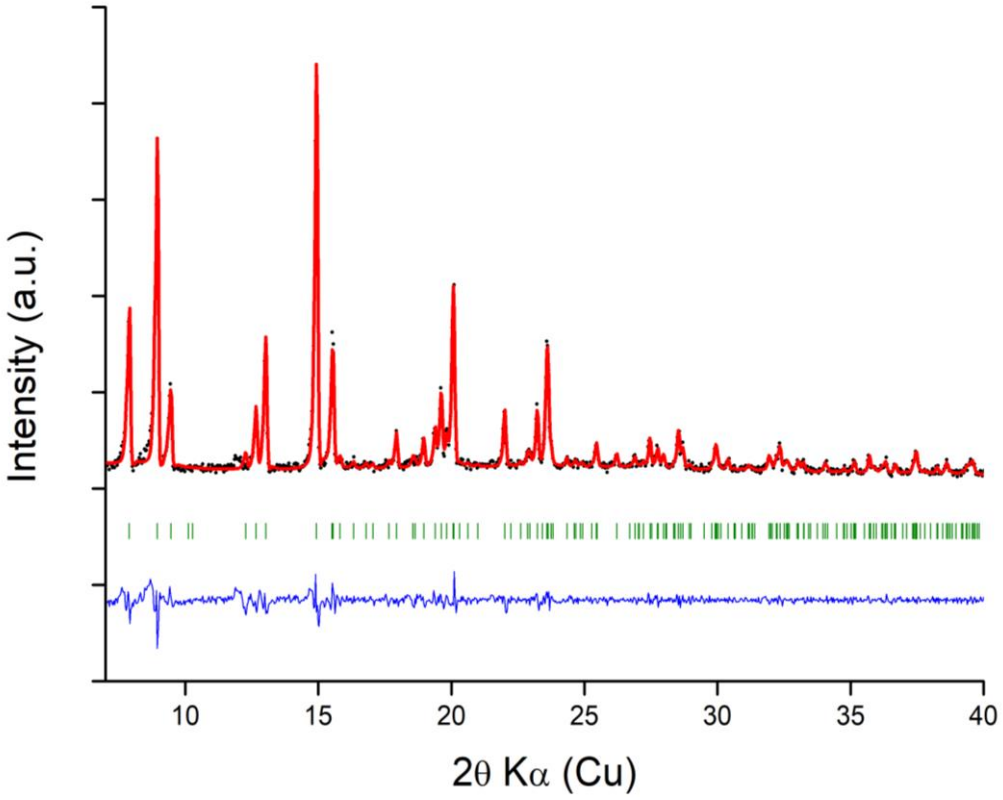

Figure 55: *Profile matching refinement of our calcium alkoxyborate salt, with the observed (black points) and calculated (red line), relative difference (blue line) and Bragg position (vertical green bars).*[125]

The XRD pattern of the $Ca[B(hfip)_4]_2 \times 4DME$ salt is compared (Figure 56) with a theoretical pattern simulated from the crystallographic information file provided by Zhao-Karger and Fichtner.[73] There is an evident matching of the diffraction peaks, with however a significant

shift towards lower angles. A profile matching refinement was performed using the tetragonal space group $I4_1/a$ and gives cell parameters a = b = 19.766 Å and c = 37.412 Å. The values are in fairly good agreement with the two previously cited works of Zhao-Karger and Fichtner, with a tiny mismatch that could be explained by a small variation of number of the solvent molecules in the cell. In that sense, the strong asymmetry of the diffraction peaks could be related to a distribution of cell sizes, probably related to an inhomogeneous repartition of the solvent molecules between the salt grains. This difference can come from the different synthetic routes between our salt (at room temperature) and the one of Zhao-Karger and Fichtner (heating up the reaction batch).

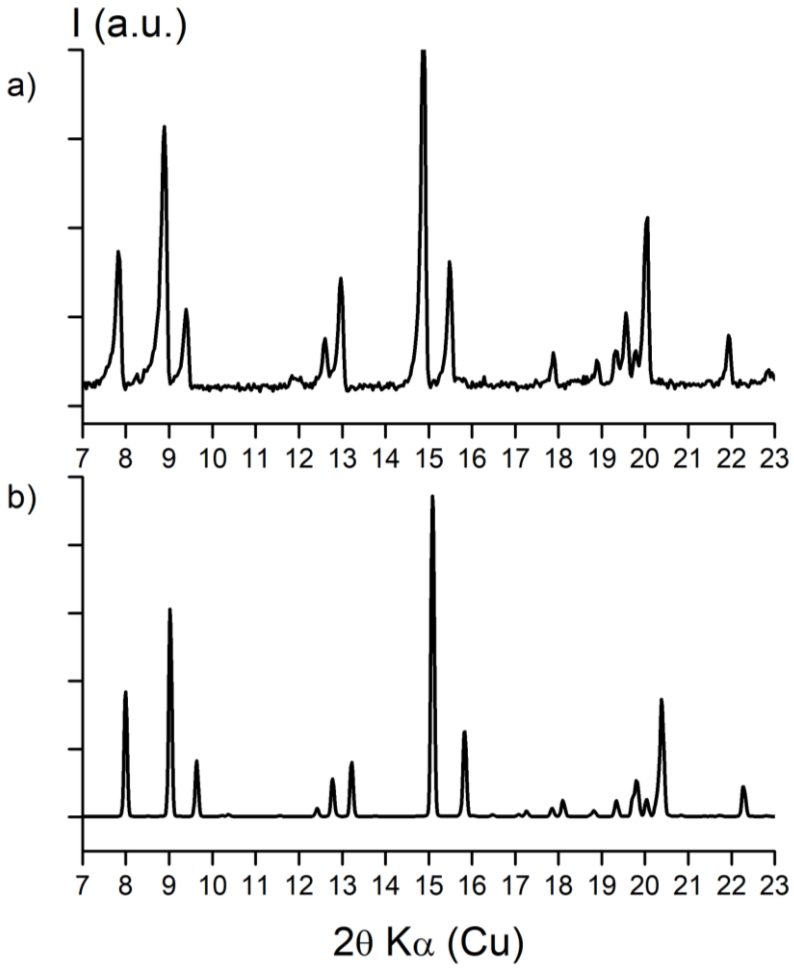

Figure 56: *Comparison between (a) our raw diffraction pattern of the calcium alkoxyborate salt and (b) a theoretical pattern simulated from the crystallographic information file provided by Zhao-Karger and Fichtner.*[125]

4.8. $Ca[B(hfip)_4]_2 \times 4DME$ single crystal analysis

Single crystals were grown from solutions of $Ca[B(hfip)_4] \times 4DME$ salt in DME by vapor diffusion or solvent layering employing cyclohexane as antisolvent. Crystallization experiments were performed in an Ar-filled glove box. Both crystallization procedures yielded low-quality crystals with exact structure $[Ca(DME)_4][B(hfip)_4]_2$, which showed that four DME is molecules are coordinated around Ca^{2+} cation. Selected crystals were attached to a glass fiber or a MiTeGen MicroLoop LD™ with silicone grease (Merck or Bayer). Single crystals were screened and measured either on Agilent New Gemini Dual, diffractometer using fine-focus sealed X-ray tube with graphite monochromator or on Agilent SuperNova Dual diffractometer using micro-focus sealed X-ray tube with mirror monochromator. Both four-circle kappa-goniometer diffractometers were equipped with an Atlas CCD area detector. Crystals were measured with Cu *K*α radiation in cold nitrogen stream at 150 K (Cryojet). Data collection and processing was performed with *CrysAlis*^{Pro} software (version 1.171.40.67a), including an empirical absorption correction using spherical harmonics, implemented in *SCALE3 ABSPACK* scaling algorithm, and an analytical numeric absorption correction using a multifaceted crystal model.[137] Crystal structures were solved by the computer program *Superflip*[138] and refined by full-matrix least-squares minimization with *SHELXL*[139] (v. 2018/3) within *Olex2*[140](v. 1.3) software. The unit cell dimensions of $[Ca(DME)_4][B(hfip)_4]_2$ single crystals analyzed in this work are in good agreement with the previous cell parameters reported by profile matching refinement of our Ca salt (Table 6).[124,141] Different measurement temperatures (150, 180,[141] and 200 K[124]) applied in the cited studies may account for the observed differences in unit-cell lengths and volumes. The reported crystal structures were refined in $I4_1/a$[141]or in $I4_1/acd$[124] space group. In this work, the crystal structure of could be

solved and refined in $I4_1/a$ space group. Furthermore, the same twin law (matrix 0 1 0 1 0 0 0 0 −1 2) was observed as reported previously.[141]

The Ca^{2+} ion is solvated by four DME molecules organized with an hexacoordinated geometry, exhibiting a slightly distorted square antiprismatic coordination.[142] Due to the larger size of Ca^{2+} ion, compared to Mg^{2+} ion, the solvated Ca^{2+} ion has eight-coordination (4 DME), with an average O-Ca bonding length of approximately 2.43 Å, which is longer than that of O-Mg bonds in $Mg[B(hfip)_4]_2$×3DME (2.06 Å). This result indicates that the desolvation energy for the solvated Ca^{2+} ion can be estimated to be lower than that of solvated Mg^{2+} ion; this is crucial about intercalation of Ca^{2+} ion into a solid electrode, since the whole energy of desolvation and intercalation results lower than Mg^{2+}.[143]

	This work	Zhao Karger et al.[73]	Nazar et al.[74]
Formula	$C_{40}H_{48}B_2CaF_{48}O_{16}$	$C_{40}H_{48}B_2CaF_{48}O_{16}$	$C_{40}H_{48}B_2CaF_{48}O_{16}$
F_w	1758.48	1758.48	1758.48
Crystal system	Tetragonal	Tetragonal	Tetragonal
Space group	$I4_1/a$	$I4_1/a$	$I4_1/acd$
***a* [Å]**	19.6213(2)	19.5970(6)	19.6322(8)
***b* [Å]**	19.6213(2)	19.5970(6)	19.6322(8)
***c* [Å]**	36.3693(4)	36.7108(15)	36.8549(15)
***α* [°]**	90	90	90
***β* [°]**	90	90	90
***γ* [°]**	90	90	90
***V* [Å^3]**	14002.0(3)	14098.5(10)	14204.7(13)
Z	8	8	8
ρ_{calc} [g/cm^3]	1.666	1.657	1.645
***T* [K]**	150.0(1)	180.15	200(2)
Radiation type	Cu *K*α	Cu *K*α	Mo *K*α
***λ* [Å]**	1.54184	1.54184	0.71073

Table 6: Summary of the crystal data and comparison with the literature for the crystal structure of [Ca(DME)$_4$][B(hfip)$_4$]$_2$.[125]

4.9. $Ca[B(hfip)_4]_2$×4DME air/H_2O instability

The H_2O and air stability of $Ca[B(hfip)_4]$×4DME salt was investigated by tools of XRD diffractometry, SEM/EDS analysis and FTIR spectroscopy. The experiments were carried out by processing two samples of salt: one was aged in the glovebox, while a second one was left in ambient atmosphere for 1 day, then both were studied by XRD. As shown in Figure 57, the crystallinity of salt exposed to air is completely lost. By this analysis, we can deduce that the salt (black pattern) reacts irreversibly with ambient moisture, leading to an ill-defined amorphous decomposition represented by an amorphous flat pattern (red pattern).

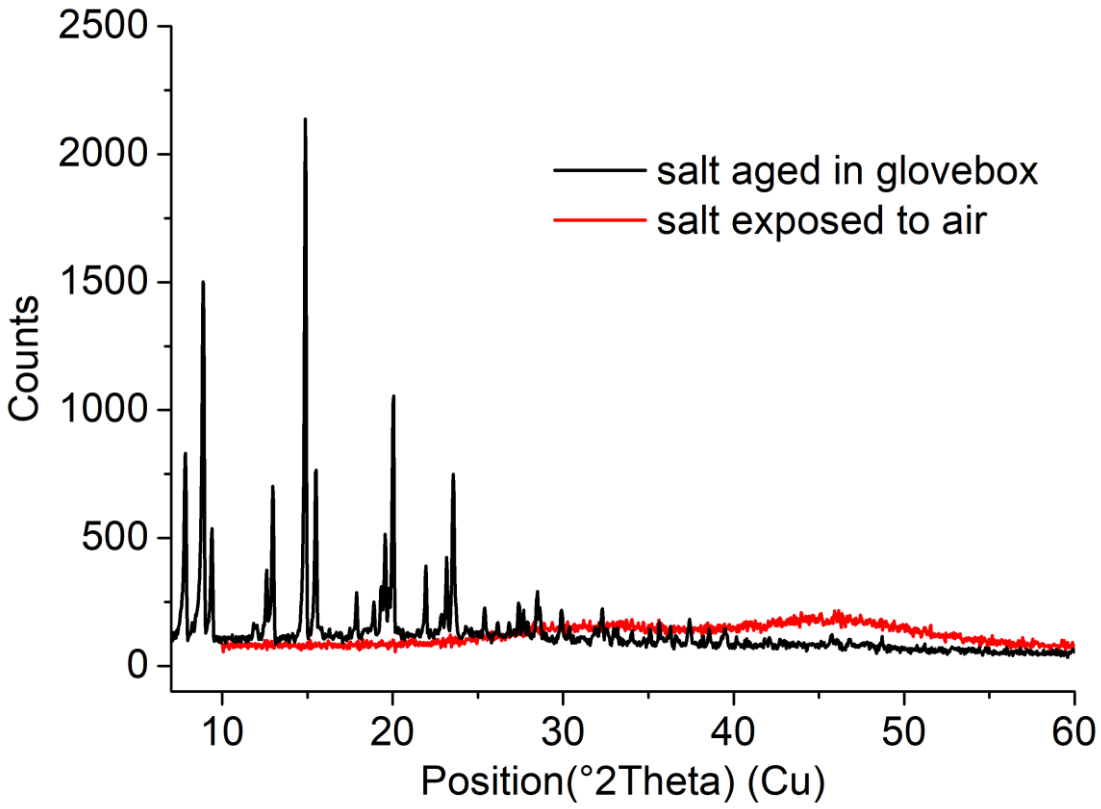

Figure 57: *XRD patterns comparison of $Ca[B(hfip)_4]_2$×4DME after exposition in air and aged in glovebox.*

Since XRD does not provide chemical information about the nature of the amorphous decomposition product, the latter was investigated also by FTIR spectroscopy and compared to the sample stored in the glovebox. As it is shown in Figure 58, while the spectrum of salt aged in glovebox shows the typical absorption peaks of $Ca[B(hfip)_4]\times4DME$, the spectrum of salt, exposed to ambient air for 1 day, shows some important differences: a broad peak appears in the range 3000-3600 cm^{-1}, ascribable to the O-H stretching modes of water molecules. The disappearing of the B-O-C stretching mode at 1214 cm^{-1} suggests that this bond is not stable in air. As reported in the literature[144] and shown in Figure 59, the salt left in air shows the typical adsorption peaks of the calcium borate CaB_4O_7: the broad peak appearing in the 850-1000 cm^{-1} range is probably due to the B–O stretching modes of tetrahedral BO_4^- units. The B-O stretching mode of trigonal BO_3 units is detected at around 1400 cm^{-1}.

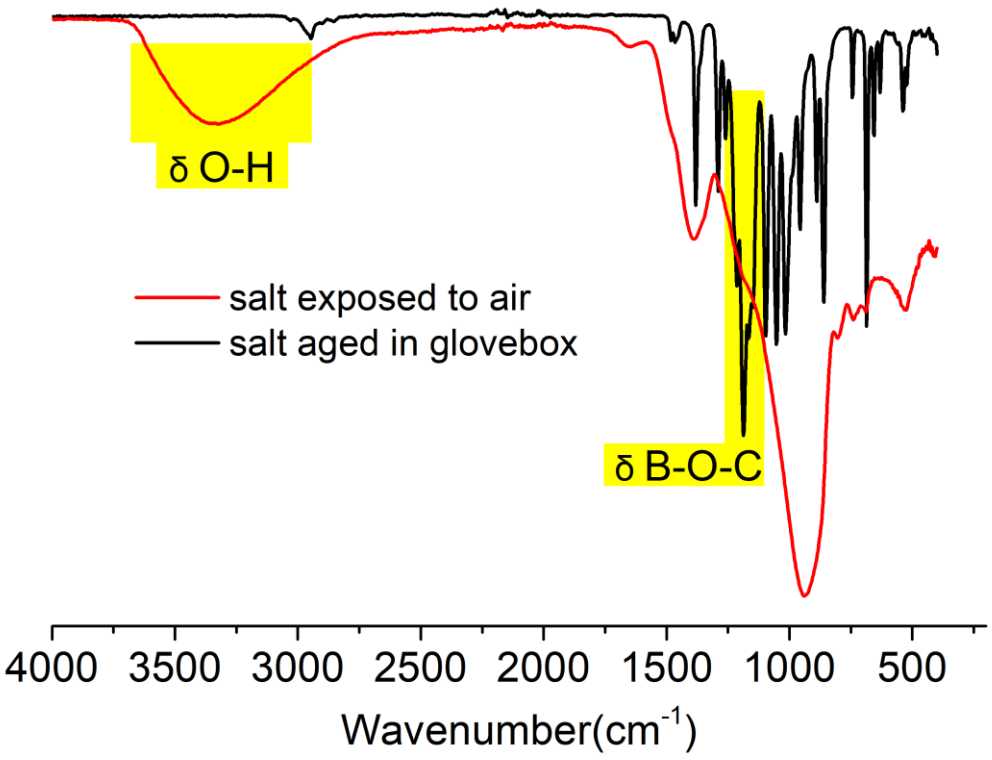

Figure 58: *FTIR spectra comparison of $Ca[B(hfip)_4]\times4DME$ after exposition in air and aged in glovebox.*

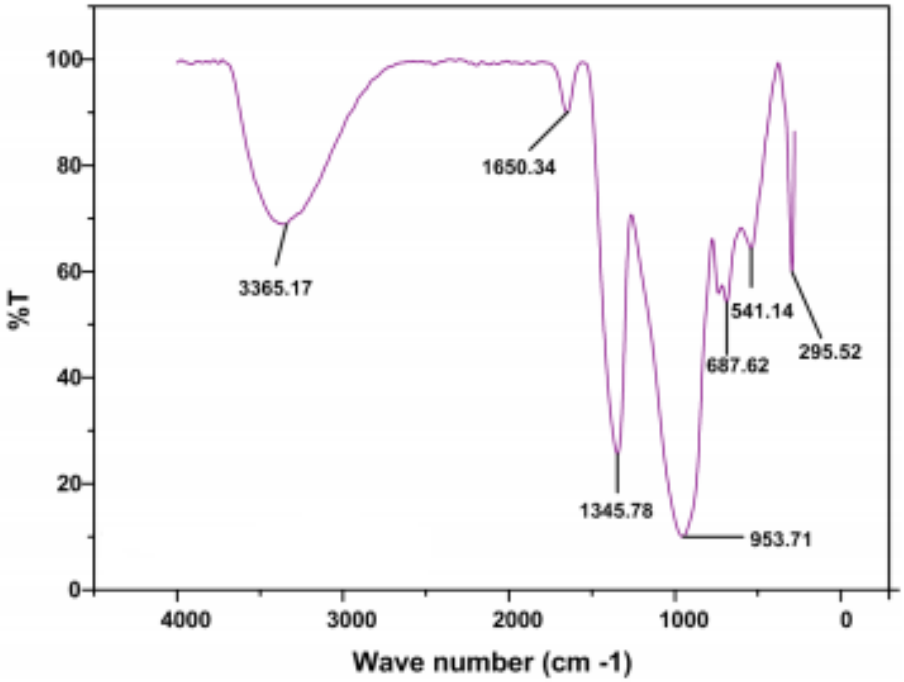

Figure 59: *FTIR spectrum of calcium borate* CaB_4O_7[144]

A SEM/EDS analysis was also performed on the salt after exposition to air for 1 day, as shown in Figure 60.

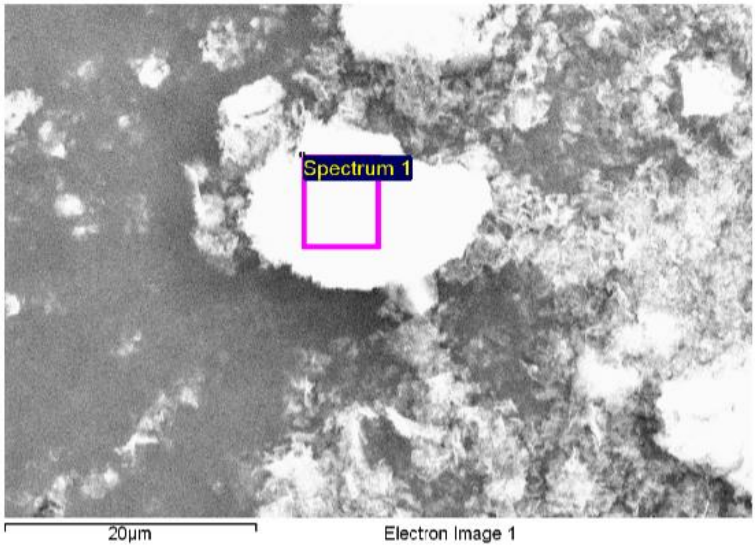

Figure 60: *SEM photo of* $Ca[B(hfip)_4]\times 4DME$ *particles after air exposition.*

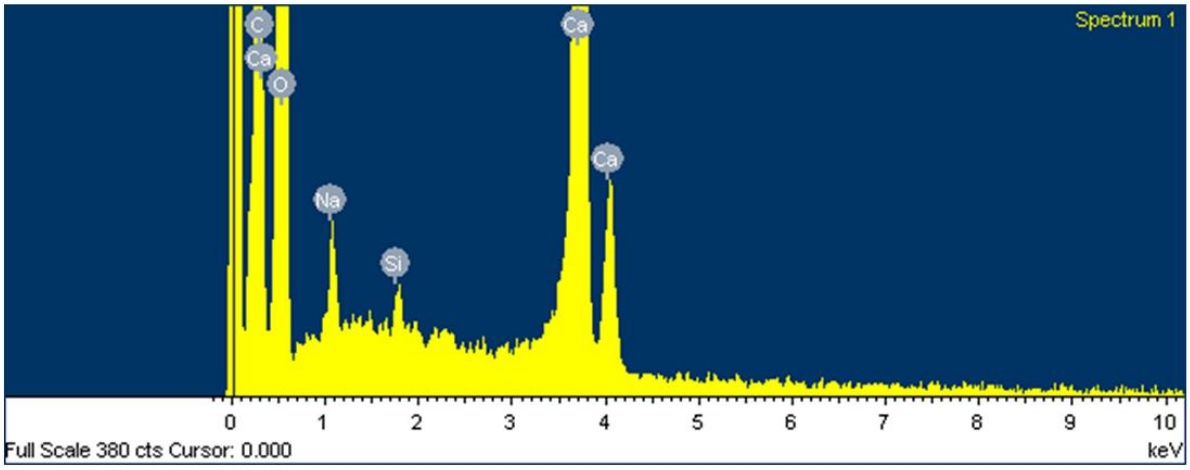

Figure 61: *EDS analysis of Ca[B(hfip)$_4$]×4DME particles after air exposition.*

These analyses show that total amount of the fluorine is lost, proving that air exposure enhances the salt decomposition. Boron is not visible by EDS (Figure 61), since the carbon signal can hide it if the boron content is low. Here, the carbon signal is artificially enhanced by the use of a carbon tape for supporting the sample. The Ca/O atomic ratio is around 1/10, much lower than for Ca borate or $CaCO_3$ (5/2), showing that salt decomposition gives other unknown byproducts besides the Ca borate detected by FTIR.

5. Electrochemistry

5.1. Materials and methods

Electrolyte solutions were prepared by dissolving the suitable amount of $Ca[B(hfip)_4]_2 \times 4DME$ salt in anhydrous DME to obtain a final concentration of 0.3 M; DME was purchased from Sigma-Aldrich. It was degassed with Ar and transferred inside an Ar-filled glovebox. Drying was performed with 4Å molecular sieves for 3 days, refluxed with K/Na (3/1 wt.) for one day and finally distilled. Karl-Fisher titration analysis gave a value of 0.4 ppm of H_2O. Electrochemical studies were performed in Swagelok type cells. The assembly of the Swagelok cells was carried out in an Ar-filled glovebox. CV and linear sweep voltammetry analyses were obtained using a Bio Logic SP200 potentiostat with a two-electrode cell, with a scan rate of 25 mV s^{-1} and 5 mV s^{-1}, respectively. Ca shot (99.5%, Alfa Aesar) was used as RE and CE. One borosilicate glass fiber sheet and one Celgard sheet were used as separators and wetted with 80 µl of electrolyte.

5.2. Results and discussions

5.2.1. Electrochemical Ca plating/stripping by CV

Reversible Ca stripping/deposition at room temperature was proven using a SS (stainless steel) disc as the WE. As can be seen from the CV curve (Figure 62), there is an activation in the initial cycles, which is probably connected with an overpotential contribution from Ca as CE that has to be taken into account, with Ca plating starting at -0.2 V and Ca stripping at +0.2 V. The latter cannot be discriminated from other effects at the SS electrode given that a 2-electrode cell setup is used. The lack of additional anodic peaks shows that the electrolyte has good oxidative stability until 4 V. It should enable the testing of cathode materials in the whole voltage window up to this value of potential 4 V vs. Ca metal. Coulumbic efficiency of the Ca stripping increases from an initial 53% up to 67%, where it stabilizes. Coulombic efficiency of the Ca plating/stripping process is calculated on basis on the charge balance in each CV scan. Increase in Coulumbic efficiency, as even reported from literature, could be attributed to specificity of SS as WE, decomposition of the electrolyte and/or to detachment of the small sized Ca deposits from the working electrode surface.[73] The changing of cell set-up with an Au disc as WE, the decrease of Coulombic efficiency can be attributed to a not homogeneous deposition of Ca on Au surface.[124] Current Coulumbic efficiency is suitable for proof-of-concept testing on lab scale, but in real cells efficiency higher than 99.9 % are targeted.

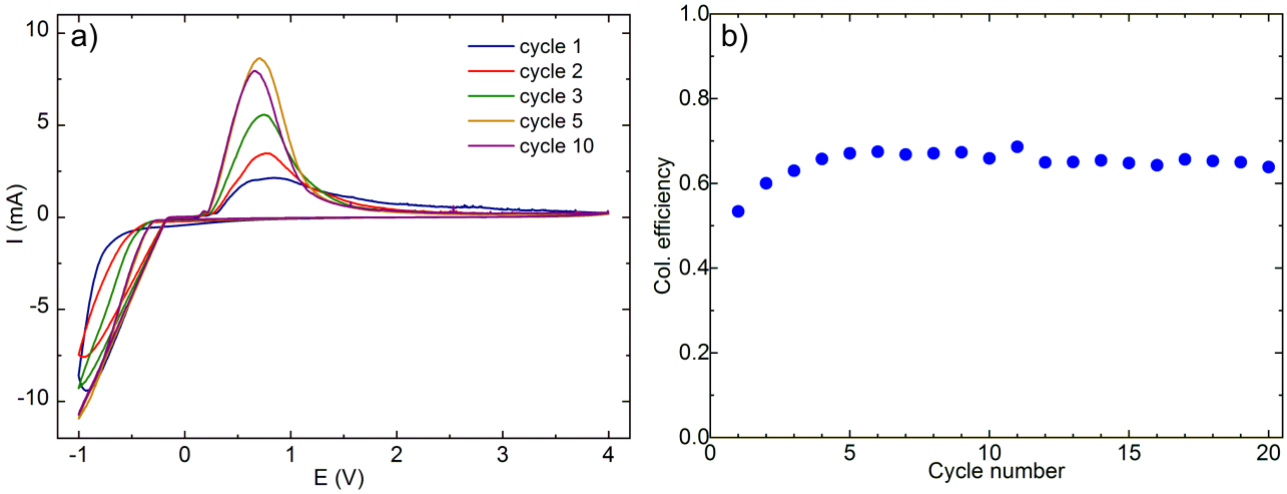

Figure 62: a) CV of Ca stripping/deposition on SS electrode using 0.3 M $Ca[B(hfip)_4]_2$ in DME, in the voltage window from -1.0 to 4.0 V with a sweep rate of 25 mV/s, at room temperature. b) Coulumbic efficiency of Ca stripping/deposition during corresponding CV test.[125]

5.2.2. Linear sweep voltammetry (LSV)

Linear sweep voltammetry is performed to check the anodic stability of the electrolyte with several WEs as SS, Pt, Al and Cu. Analysis is carried out at sweep rate 5 mV/s (Figure 63). The LSV profile indicates that the electrolyte has an oxidative stability up to 4 V vs Ca on all of them, demonstrating the $Ca[B(hfip)_4]_2$/DME electrolyte is well suited for conventional current collectors. On Pt it can catalyze the oxidation of DME[145], so the current generated is higher than with others. Some spikes are detected on Al and SS curves, probably due to phenomena of corrosion on disc surface during oxidation.

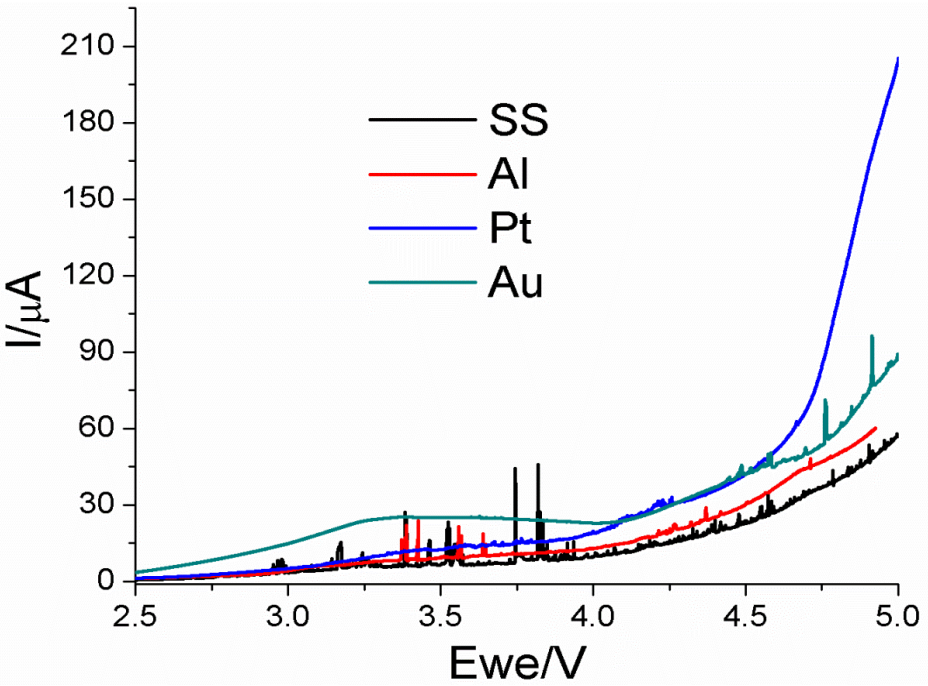

Figure 63: Linear sweep voltammogram on various electrodes at a scan rate of 5 mV s^{-1}, at room temperature.

The analogous $Mg[B(hfip)_4]_2$/DME electrolyte, developed by Fichtner et al., shown the same anodic stability on several working electrodes. [91] The $Ca[B(hfip)_4]_2$ salt developed by Fichtner et. al. shows an anodic stability of 3.9 V for Pt.[73]

5.2.3. Electrochemical Ca plating/stripping by GCPL

The galvanostatic reversible Ca stripping/deposition was determined by using a Swagelok 2-electrodes cell, with Ca metal as the CE and SS disc as the WE. A constant cathodic current of 100 $mA \cdot cm^{-2}$ was initially passed through the cell until for a time of 20 minutes. Figure 64 indicates that the electrolyte retained a reversible Ca deposition/dissolution for 3 hours.

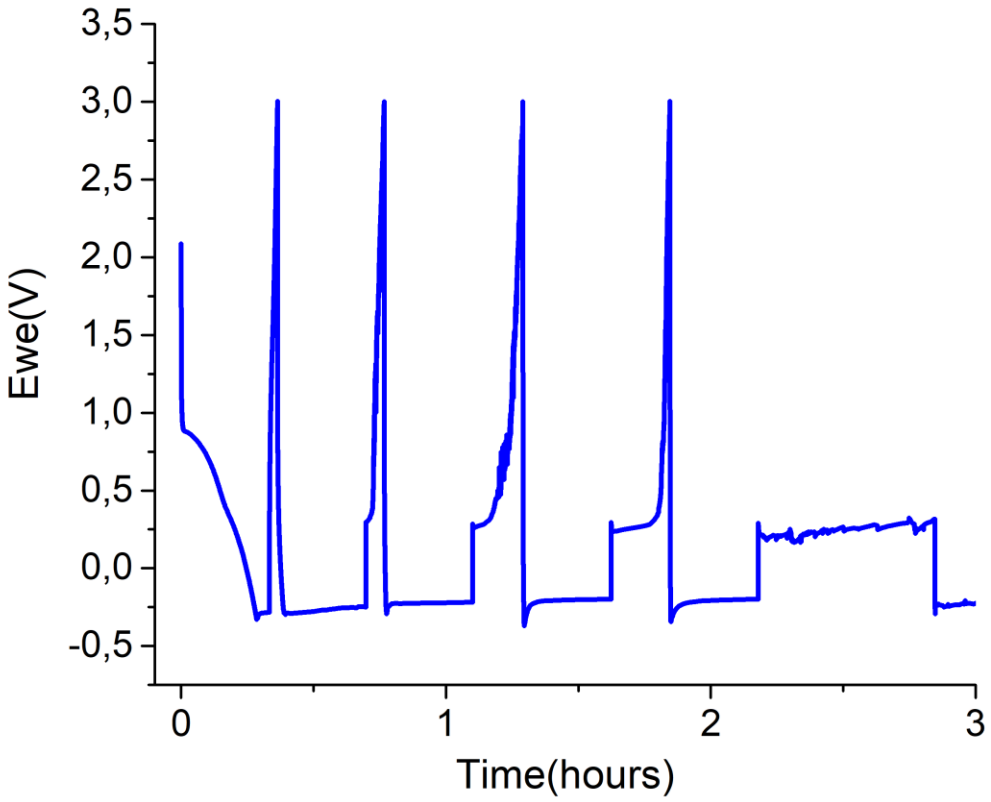

Figure 64: Long-term Ca stripping/plating in $Ca[B(hfip)_4]_2$ in DME (0,3M) on SS disc as WE, at a current density of 100 mA cm^{-2} at room temperature.

The Coulombic efficiency of GCPL Ca reversible stripping/deposition (Figure 65) indicates that the reversible GCPL Ca electrochemistry is limited at 66% after 4 cycles, probably for the side reactions of fresh deposits with electrolyte and problems with shortcuts after the 5° cycle. It must be noticed that shortcuts have been often present in our GCPL Ca stripping/deposition tests, since a plenty of Ca deposited on SS disc is not stripped away in good efficiency for the time limitation (t charge = t discharge).

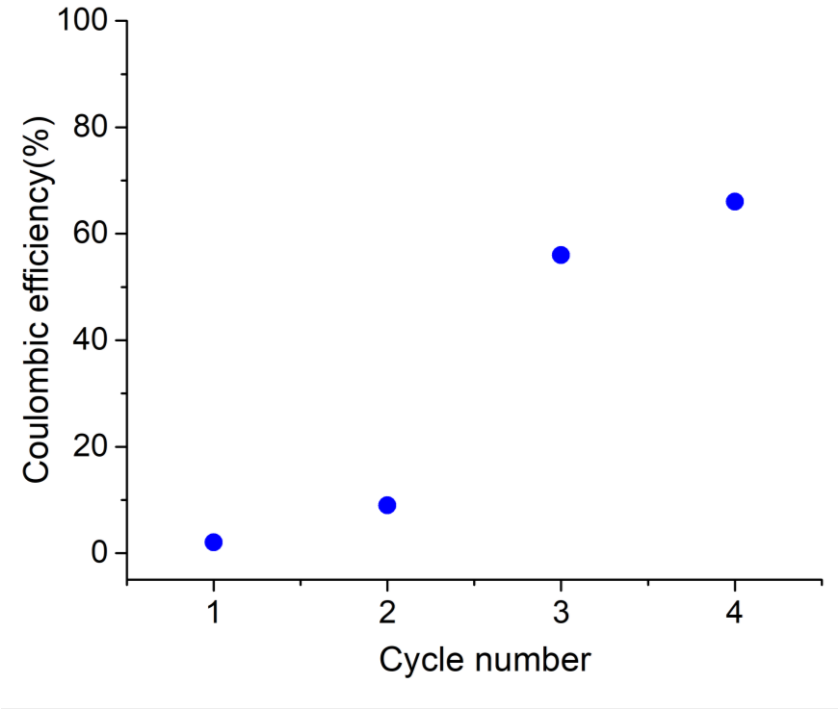

Figure 65: *Coulumbic efficiency of Ca stripping/deposition during corresponding galvanostatic test.*

To investigate the cyclability of the $Ca[B(hfip)_4]_2$/DME electrolyte, symmetric Ca//Ca cell was assembled to carry out the galvanostatic measurements at constant current density of 616 $\mu A \cdot cm^{-2}$ for 10 minutes. The over-potential 200 mV was observed (Figure 66), which could be caused by the native surface passivation of the Ca electrodes. A typical voltage profile exhibits flat plateaus, suggesting a long-term smooth Ca deposition/dissolution process.

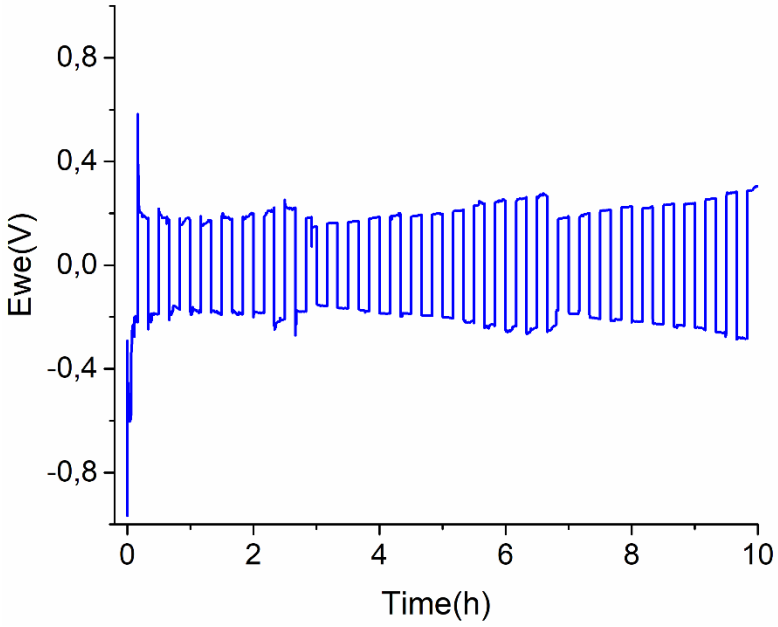

Figure 66: *Long-term Ca stripping/plating in $Ca[B(hfip)_4]_2$ in DME (0,3M) in symmetric Ca//Ca cell, at room temperature and a current density of 616 $\mu A \cdot cm^{-2}$.*

5.2.4. Determination of nature of deposit after cycling

The nature of deposit on working electrode, resulting from the electrolyte after a reduction at a current of 100 $mA \cdot cm^{-2}$ (Figure 67) was investigated by XRD. The SS disc was taken out from the Swagelok cell after Ca plating and stored into a coffee bag, equipped with a Kapton window, as shown in Figure 68; all these operations were performed into an Ar-filled glovebox.

Figure 67: *Ar-filled coffee bag with kapton foil window, used to analyze the SS disc after cycling.*

The pattern refinement performed using the Maud software starting from the cubic "Fm-3m" structure of Ca metal. The collected pattern is identical to that of crystalline Ca metal, as shown in Figure 68. The refinement of the cell parameters gives a cell length (a=b=c) of 5.576 ± 0.005 A°, in very good agreement with the published value for Ca metal.[146]

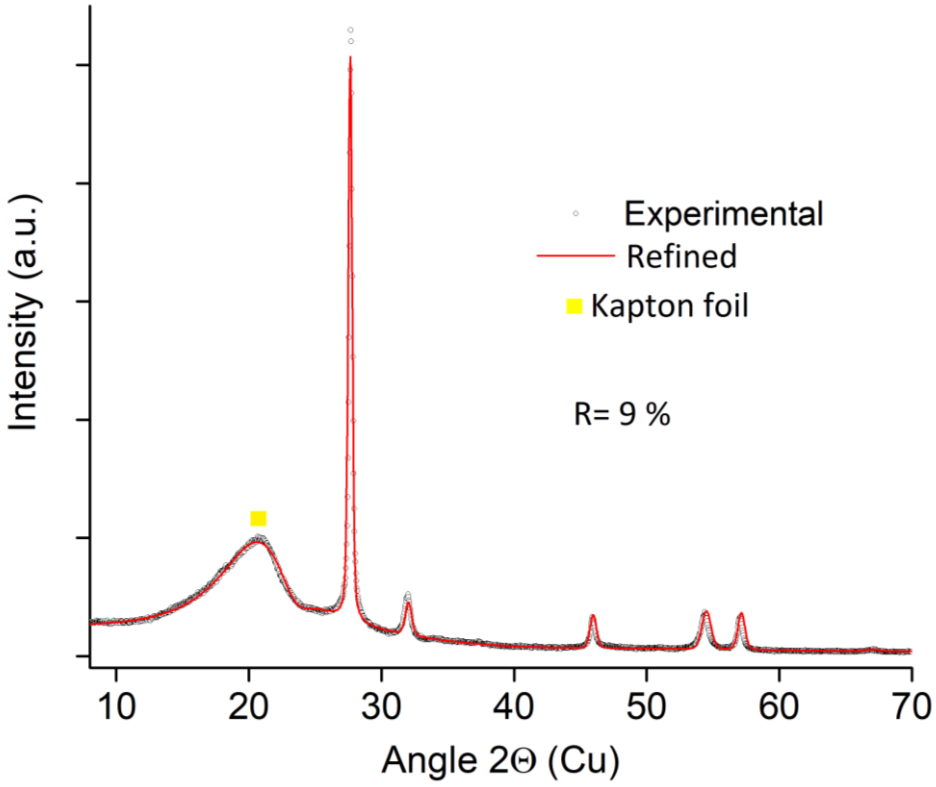

Figure 68: *XRD pattern matching refinement of Ca deposit on SS surface.*

SEM/EDS analysis was carried out taking into account the both contribution of SS disc surface and the deposit after cycling as shown in Figure 69:

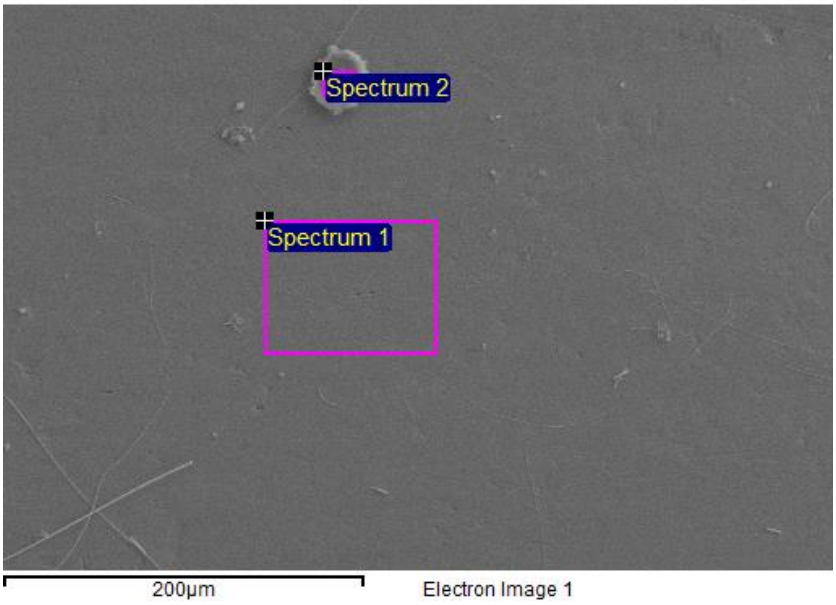

Figure 69: *SEM analysis of SS surface after cycling (spectrum 1 indicates SS surface and spectrum 2 is Ca deposit).*

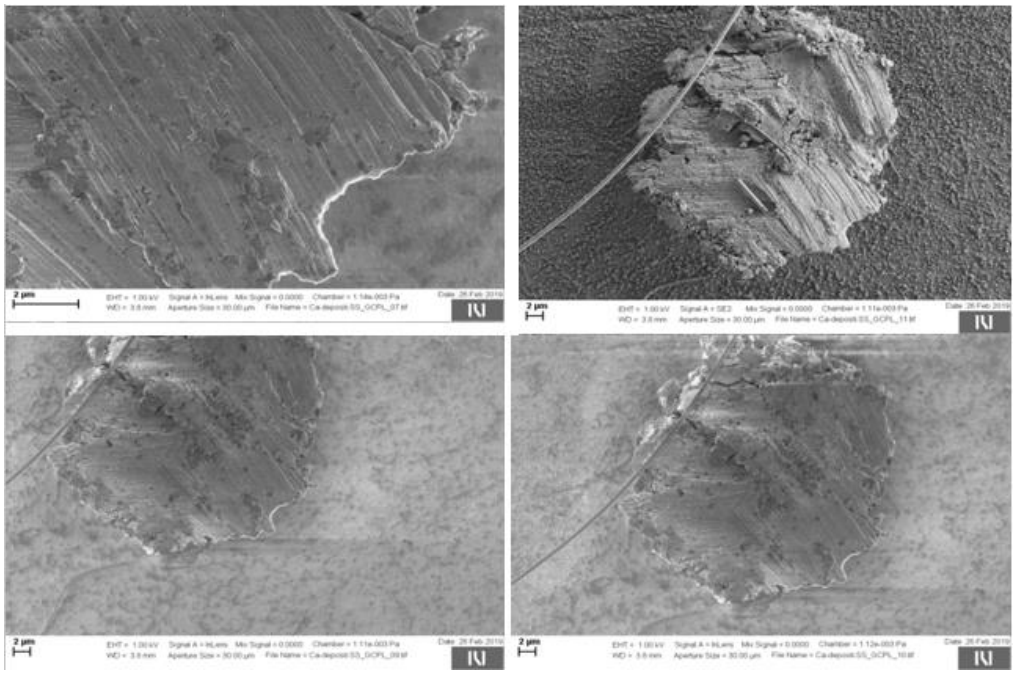

Figure 70: *SEM analysis of Ca deposits on SS disc (zoom of Ca deposit of figure 69).*

EDS analysis (atomic %) was performed on both spectrum 1 and 2:

	C	O	Na	Si	Ca	Cr	Fe	Ni
1	-	4	-	-	-	17	2	9
2	3	26	3	1	**69**	-	-	-

Table 7: *EDS analysis of SS surface after cycling.*

- **Spectrum 1** = Cr / Ni / Fe: contribution of atomic composition of the SS disc.
- **Spectrum 2** = O / Si / Na: contribution from glassy fibers as a separator.

The deposits are mainly composed of Ca and O with trace amounts of carbon, while a small amount of impurities is detected (Na, Si) due to the intertwining of glassy fibres from the separator with Ca deposits.

The contamination from oxygen and carbon probably originates from the short period of air-exposure of the electrode containing highly reactive fresh Ca deposits to air, during its transfer from the glove box to the microscope for the EDS measurement.

6. Conclusions

We have presented a new scalable synthetic method and the structural characterization of a new fluorinated alkoxyborate calcium salt, $Ca[B(hfip)_4]_2$, based on a weakly coordinating hexafluoroisopropoxy borate anion. Further, we have confirmed the promising electrochemical properties of the salt-based electrolyte, which represents the current state-of-the-art Ca electrolytes in terms of high oxidative stability, high conductivity, excellent Coulombic efficiency of Ca plating/stripping and good capability of long-term reversible Ca cycling. These electrochemical properties make this glyme-based electrolyte promising for potential high-energy Ca batteries at room temperature. Furthermore, the feasibility of such synthetic routes for Ca salts also provides strategic direction for the research on the multivalent ion based batteries, such as Ca.

The complete derivatization of the boron-hydrogen bond of $Ca(BH_4)_2$, the starting reagent, in the new boron-oxygen bond of final Ca salt is proved by tools of NMR, Raman and FTIR spectroscopy. This chemical conversion occurs even at room temperature, and the alkoxyborate salt can be easily isolated by drying of the solvent. By comparison with the recent literature, especially with the works of the groups of Zhao-Karger[73] and Nazar[124], we showed for the first time that calcium borohydride can be derivatized at room temperature, allowing an easier synthetic method and manipulation of final salt.

Despite its promising physical-chemical properties, our fluorinated alkoxyborate Ca salt suffers from air/water instability, characterized by breaking down of C-O bond after air/water exposition, causing the loss of the fluorinated based chains and the formation calcium borate as the main decomposition product. This might be a limit for a future scalable production of the salt and the electrolyte, since all the operation of synthesis, work-up and manipulation of

the salt and electrolyte must be carried out in Ar-protective atmosphere. These results are in sharp contrast to the homologous anion $Mg[B(hfip)_4]_2$ and $Na[B(hfip)_4]$ salts, which are air stable[147]. The homologous $[Al(hfip)_4]^-$ anion also shows the same issues of air instability as our Ca salt.[148] To understand the reasons for stability differences between these salts, we have to take in account the Ellingham diagram[62]. The formation of Ca oxide is thermodynamically more favored, at same conditions of temperature, then Mg and Na oxides. So the ease of decomposition of Ca salt by reaction with atmospheric O_2 is due to the higher reactivity of Ca than Mg and Na, allowing at formation of more stable Ca oxide and more difficult to reduce.[149]

7. Perspectives

The easy synthetic pathway and the interesting electrochemical properties of this innovative Ca based electrolyte make this class of Ca salts very promising from an application perspective. The feasibility of such synthetic routes for Ca salts also provides strategic direction for the research on the multivalent ion based batteries. The reaction is scalable, even if, on other hand, the air/water instability of salt makes its manipulation possible only in inert atmosphere. The first objective is to make such fluorinated alkoxyborate based Ca salts more stable in air/water, similarly to the homologous $Mg[B(hfip)_4]_2$ and $Na[B(hfip)_4]$ salts. A possible strategy to obtain air-stable salts could be the use of organic substituents with different fluorinated chains. The design of new Ca salts based on WCAs by incorporation of various fluorinated alkoxyborate anions will serve as a useful tool for further optimization of the electrolyte properties. The rational design drives us to improve the electron-drawing character of the chains, to stabilize the C-O bond and make it less susceptible to decomposition with water or O_2. By taking inspiration from the literature, the chemistry of fluorinated alcohols as environmentally benign solvents has attracted extensive interest in recent years due to their favorable properties such as lower boiling points and higher melting points than their non-fluorinated counterparts, high polarity, strong hydrogen bond donation properties and the ability to solvate protic solvents[150]. Since 1999, WCAs with different types of fluorinated alkoxy residues $OR^F = OC(CH_3)(CF_3)_2$ or $OC(H)(CF_3)_2$ have been used to successfully stabilize reactive and other cations. In addition, they can be easily separated from the reaction mixture, are available on a commercial scale and have relatively low toxicity.[108]

Another strategy to improve the electrochemical properties of the electrolyte is the possible use of ILs, where cations and anions are coordinate weakly with each other.[151] They have recently

attracted attention due to their benefits in contrast to conventional solvent. They have extremely low vapor pressures, interesting transport and electrochemical properties. In 2011, Gao et al.[152] prepared several mixtures of Ca salts and ILs as electrolytes for Ca-batteries. Quantitative analysis reveals that the alkoxy-functionalized ammonium cation (N_{07}^{+}), bearing seven ether oxygen atoms, can displace the $TFSI^{-}$ anion from the Ca^{2+} ion coordination sphere. The ($[Ca(BH_4)_2]_{0.05}[N_{07}TFSI]_{0.95}$) based electrolyte shown to facilitate the reversible Ca deposition/stripping process (figure 71).

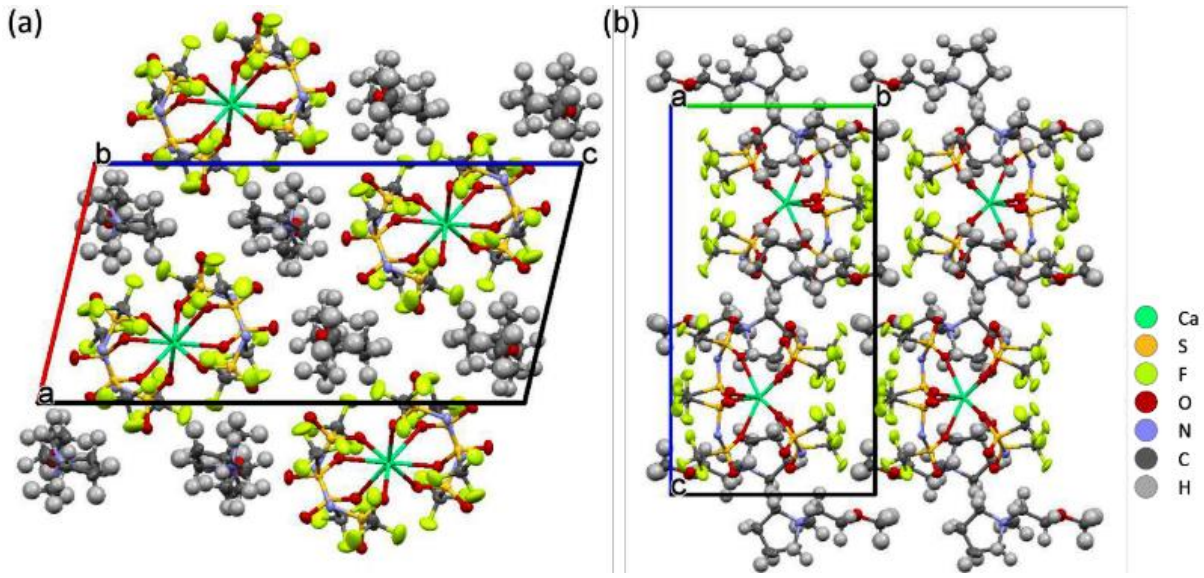

Figure 71: *Projection of the crystal structure of $[Pyr1201]_2[Ca(TFSI)_4]$ along the crystallographic (a) b- and (b) a-axes.*[152]

These interesting results highlight the excellent potential of alkoxy-functionalized IL-based electrolyte as an attractive model system to control speciation of metal ions and ionic interaction in the electrolyte.[153]. The future goal is synthesis of ILs based electrolyte on our fluorinated alkoxyborate calcium salt as the anion counterpart.

The next goal is to investigate the physico-chemical properties of this new $Ca[B(hfip)_4]_2$/DME electrolyte. The ion conductivity is a key parameter to quantifies the ion mobility within the electrolyte as to determines the rate capability of a battery. In the paper of Zhao-Karger et al.[154],

The 0.3 M $Mg[B(hfip)_4]_2$/DME electrolyte has a high conductivity of approximately 11 $mS \cdot cm^{-1}$ (measured at 23 °C). When the concentration increases to 0.3 M, the conductivity increases linearly and then decreases at higher concentrations, due to the formation of ion pairs and then reduced ion mobility within electrolyte bulk. On other hand, for the 0.25 M $Ca[B(hfip)_4]_2$/DME electrolyte, the conductivity was found as approximately 8.3 $mS \cdot cm^{-1}$ (measured at 23 °C).[73]

III. Towards a calcium metal-organic battery

1. State of the art of organic based batteries

Batteries based on organic electrode materials are also increasing attention in recent years due to their promising electrochemical performance and distinct advantages in sustainability and environmental friendliness.[155] Organic based materials have been considered as one of the most sustainable alternatives as they are composed of abundant and light-weight elements, which also puts their price tag lower than in the case of inorganic materials. They generally deliver high capacity because of the considerable number of active sites per weight. Moreover, they are composed of light elements such as C, H, O, N, and S, that can be obtained from biomass resources or through mild synthesis processes. Furthermore, the structure of organic molecules can be designed flexibly, which contributes to easy tailoring of their electrochemical performance. Their gravimetric capacity is high thanks to the light elements, and they can be cycled at very high rates.[156] The organic compounds are non-ion-specific, so these materials normally show high versatility with reversible redox behaviors toward different ionic species. It means that the progress made with the LIBs chemistry would benefit the Na^+-ion battery chemistry, and even Mg^{2+} works in a similar fashion with the organic materials. They have several advantages, such as high specific capacities, which is ascribed to the efficient swelling due to flexible nature of the organic latter. In addition, most of them are environmentally. The

replacement of inorganic electrodes with abundant organic materials is desirable, not only for reducing the price of LIBs, but also for reducing the CO_2 footprint.

However, several difficulties are limiting the development of organic electrodes, despite the advantages mentioned above.

First, organic molecules have a tendency to dissolve into the electrolytes, which results in a poor cycle and battery life.[157] A strategy to avoid this issue is to increase the molecular weight by polymerization. Redox polymers can be divided into conducting, nitroxyl radical, carbonyl and sulfur containing polymers. They have many advantages, such as film forming ability, flexibility, abundant resources, versatile chemical structures, tunable redox properties, and recyclability. Among them, carbonyl-containing polymers, such as polyimides and polyquinones, are the most promising as electrodes for the next generation of rechargeable batteries, because they have the best electrochemical properties. For instance, quinone-based polymers were constructed by linking the monomeric units with various organic groups, such as methylene ($–CH_2–$), as we will see later.

A second difficulty with organic materials is their poor conductivity although recent publication shows they are comparable to commercial inorganic materials, such as Li cobalt oxide (LCO), Li iron phosphate (LFP), Li titanate (LTO), Li mangan oxide (LMO).[158] Therefore, the active organic material is mixed with some form of conductive carbon, which is usually in large amounts, up to 60 wt.%. However, high loading of carbon additives limits the overall capacity of the battery. The best performance can be obtained using a low amount of carbon nanotubes.[159]

The third limitation is the operational voltage, commonly being lower than 4 V for organic cathodes, thus limiting the energy density. Carbonly based organic compounds are often electrophilic, which urges the use of non-nucleophilic based electrolytes. This disadvantage

was one of the reasons for slow development of Ca-organic batteries. Until recently, only $Ca(BF_4)_2$ and $Ca(BH_4)_2$ based electrolytes allowed reversible Ca stripping/plating.[160] Since both are strong nucleophiles, their employment with electrophilic-based materials was completely precluded.[161] Different classes of organic molecules have been proposed as electrode materials through the years: quinones, imides, nitroxides, disulfides, carboxylates, carbonyl compounds, as well as trioxotriangulene, antiaromatic corroles, triazines, and tetracyano quino-di-methane.[162] In Figure 72, properties of different types of organic electrode materials are compared according to: capacity, solubility, preparation complexity, thermal stability, kinetics, voltage, conductivity, and self-discharge in the form of radar plots.

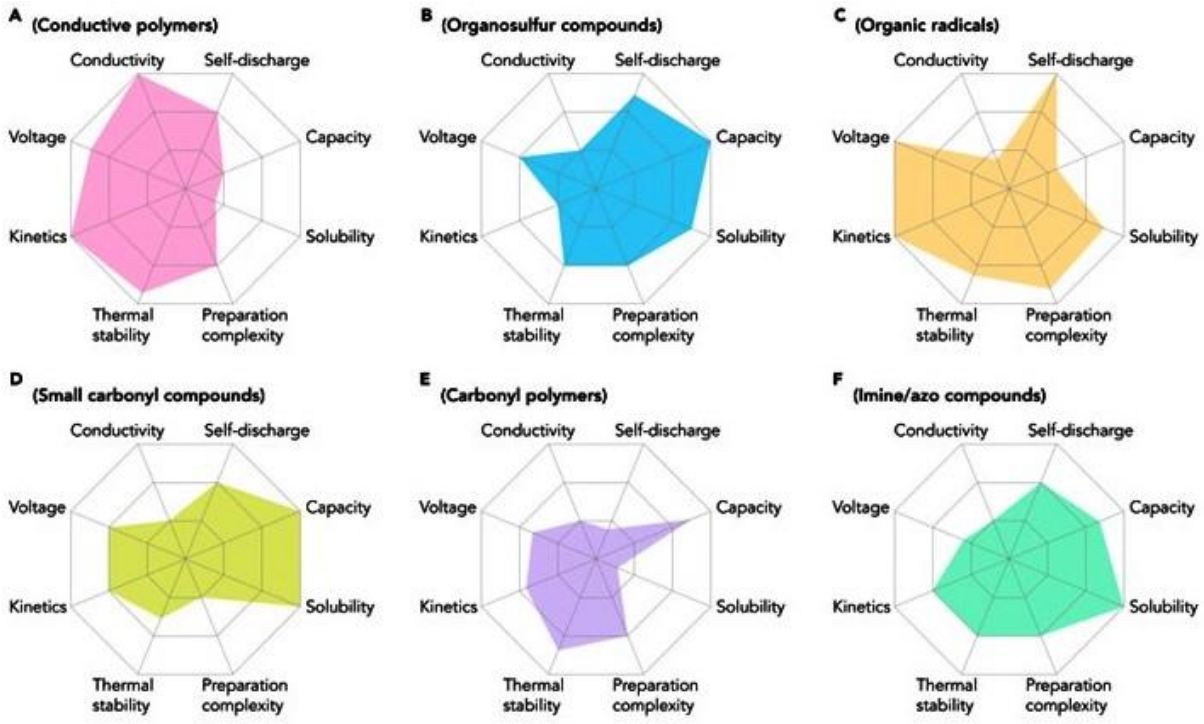

Figure 72: Overview of fundamental properties of different types of organic electrode materials.[162]

There is a plethora of different organic electrode materials that can operate in different ways. Organic electrode materials are commonly grouped based on the role they perform in the redox

reaction: P-type materials contribute to the redox reaction by donating electrons, N-type materials by accepting electrons, while bipolar (B-type) materials may be either oxidized (P-type reaction) or reduced (N-type), depending on the applied voltage (Figure 73).[161]

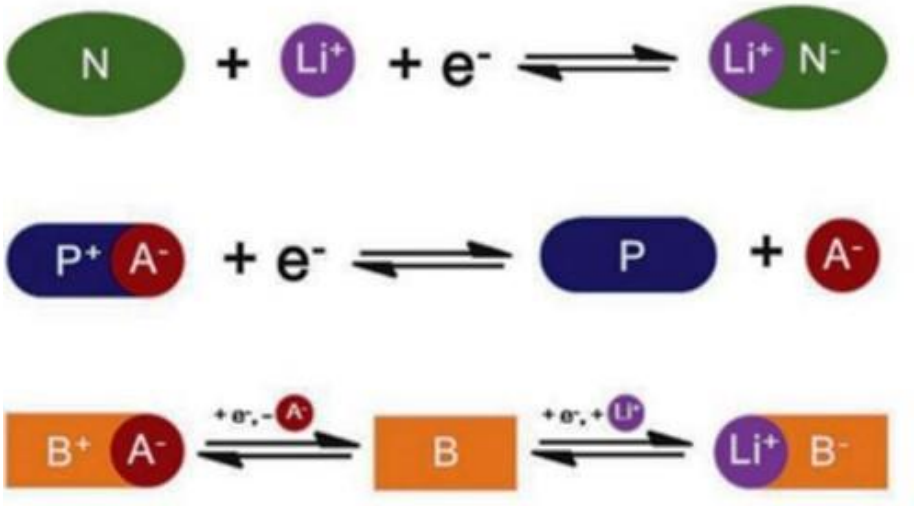

Figure 73: *Classification of electroactive organic molecules according to their electrochemical activity: n-type, p-type and bipolar.*[161]

N-type organics are neutral molecules that undergo reduction and become negatively charged (N) and a cation is included to balance the charge ($N^{-}Li^{+}$). P-type organic materials undergo oxidation and become positively charged (P) and an anion is included in the new state of the molecule ($P^{+}A^{-}$). In the case of bipolar organics, they can undergo both reduction and oxidation. N-type organic compounds are the most practical cathode material for metal anodes, because they store only metal cations from anode and allow operating in lean electrolyte conditions inside real battery cells. Among the classical redox active organics, nitrogen radicals, amines and thioethers are usually of the P-type. Carbonyls, quinoxalines, phenazines, cyanides, azocompounds, and disulfides are N-type. Hydrocarbons and conjugated nitrogen systems can be classified as B-type materials. Representative example molecules for each type and their redox mechanisms are presented in Figure 74:

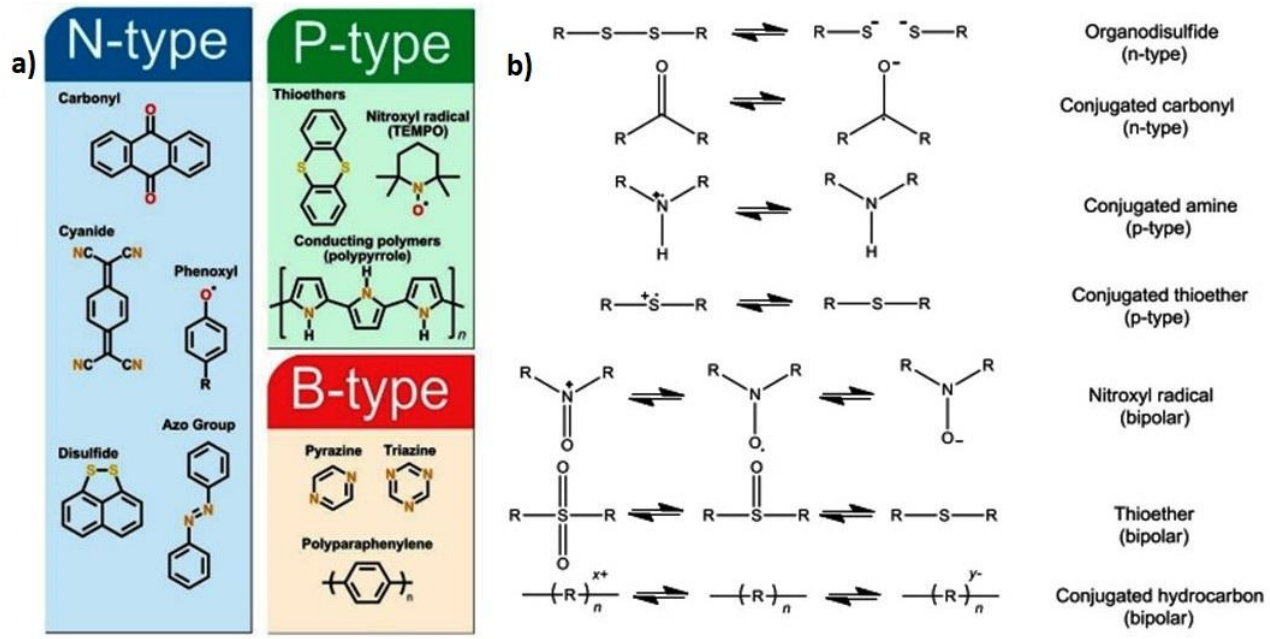

Figure 74: *(a) Division between representative and model examples of organic electrode materials and (b) classification about their redox mechanism.*[162]

In the 1980s, conductive polymers were extolled as promising materials for the next generation of environmentally benign and efficient batteries.[163] Their interesting electronic properties originate in the overlap of adjacent π-orbitals, resulting in a band structure analogous to inorganic semiconductors. Their conductivity is greatly affected by doping, which occurs upon charging and creates cations and anions that are delocalized along the polymer backbone. Since the charged centers are not separated electronically and strongly affect each other, the redox potentials of conjugated polymers depend on the doping level and gradually change upon charging/discharging. This results in a sloping cell voltage, which limits the range of application. Since conjugated polymers possess these significant disadvantages, the research shifted to other classes of redox-active polymers during the past decade. These materials are, in general, based on a nonconductive backbone bearing electroactive pendant groups, which determine the redox behavior of the material and lead to a distinct redox potential due to the localized redox sites.[164]

Antraquinones (AQ) are a class of organic compounds that are derived from aromatic compounds by the conversion of an even number of –CH= groups into –C(=O)– groups, resulting in a fully conjugated cyclic dione structure. In nature, quinones play a vital role in numerous electrochemical reactions for energy transduction and storage, including respiration and photosynthesis.[165] Organic materials based on the carbonyl group have been widely studied as promising electrode materials for actual energy storage applications because of their many desirable characteristics, such as high theoretical capacity and fast reaction kinetics. The carbonyl-based compounds shows high kinetic of redox reaction that allow a high rate of capability even at fast current rates.[166] The number of feasible carbonyl compounds is enormous, as previously well documented in an extensive review.[155] Carbonyl compounds are in general N-type materials, since upon reduction electron is added to the C=O group LUMO resulting in a negative anion (Figure 75) which is then balanced by a cation provided by the electrolyte. AQ are structurally constructed from an anthracene ring (a tricyclic aromatic ring) with carbonyl groups at positions 9 and 10. Recent studies suggest the use of AQ in energy applications in the form of quinone molecules hybridized with various organic and inorganic materials.[167] The redox mechanism of AQ, basically includes the redox process of the quinonyl group.[168]

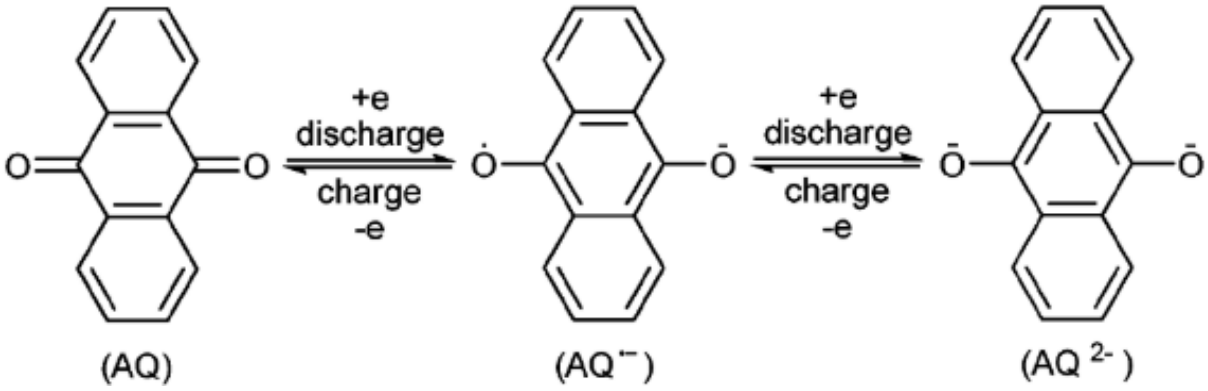

Figure 75: *Redox mechanism of AQ.*[168]

AQ-based materials often serve as model compounds due to their availability, relatively straightforward polymerization and the fact that their redox potential fits well within the voltage stability window of most battery electrolytes. Hence, electrochemical performance and electrochemical mechanism of anthraquinone-based compounds have already been studied in Li-, Mg- and Al- battery systems.[169]

AQs are characterized by a low working potential, which can affect the energy density of battery. The first approach towards increasing the working potential of anthraquinone consisted of adding a functional group to the anthracene molecule. Capacity retention is of AQs is achieved by polymerization and the most promising redox polymers belong to the class of carbonyl-containing polymers. Among them, polyanthraquinone (PAQ) and poly(anthraquinonyl sulfide) (PAQS) are the most popular (Figure 76), which combine the good reversibility of the anthraquinone moiety with the stability and poor solubility of polymers.[170]

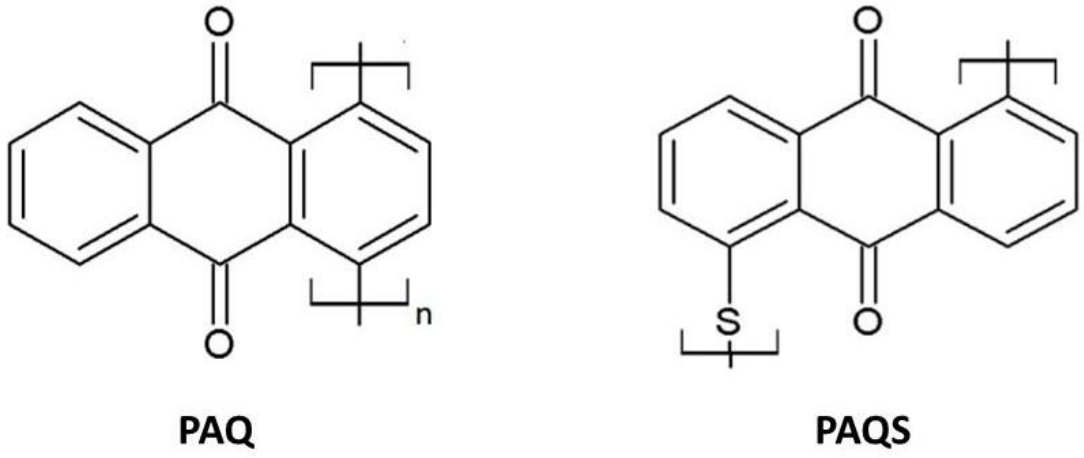

Figure 76: *Chemical structures of PAQ and PAQS.*

PAQ is synthesized from the 1,4-dibromoanthraquinone monomer through cross-coupling polymerization, while PAQS (in particular, the 1,5-PAQS isomer) can be synthesized by a

simple polycondensation called the Phillips method.[168] Among them, PAQS is the most promising redox polymer, which has shown a high performance cathode for lithium, sodium and magnesium batteries. Although cathodes based on PAQS show high cycling stability, it has a relatively low theoretical specific capacity of 225 mAh/g.

In 2015, the group of Dominko et al.[171] carried out an initial electrochemical characterization of PAQS in a Mg battery, using a Mg powder anode, a cathode composite containing PAQS, and two 0.2M electrolyte solutions of $MgCl_2$–$AlCl_3$ in THF (MACC) and $MgCl_2$–$Mg(TFSI)_2$ in a mixture of THF and glyme (MTCC) (Figure 77).

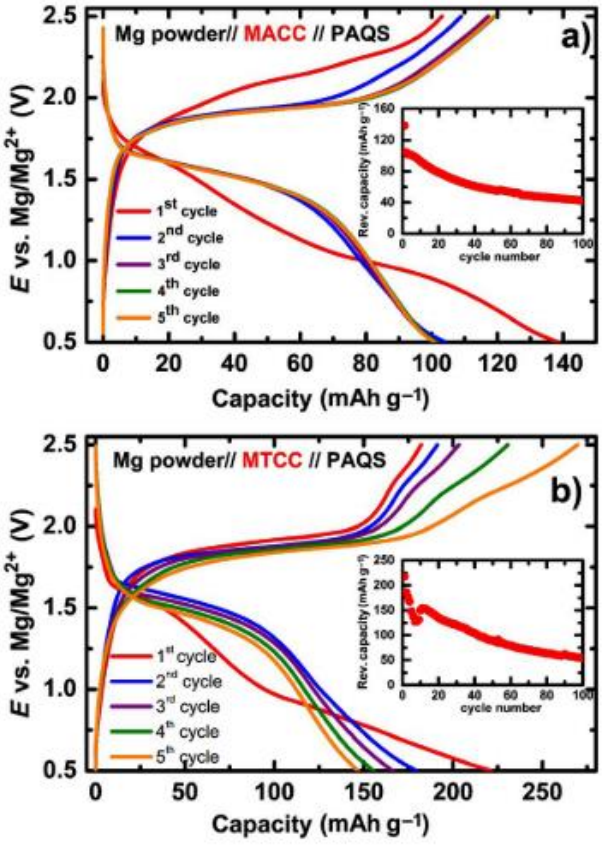

Figure 77: *Galvanostatic curves for cycling of PAQS in a) MACC and b) MTC with a current density of 50 mAh/g*$^{-1}$.[150]

Importantly, the profile of the first discharge half cycle is different with respect to the subsequent profiles. The first cycle is called "formation cycle" and many different processes

are happening at the same time (beside main redox reaction): formation of cathode SEI, activation of material, structural changes, swelling, etc. The latter is then able to accommodate the cations in the following cycles that proceed though single-step plateau. Therefore, we can deduce that PAQS system requires a preliminary activation phase to enhance the further cyclability.

In 2019, the group of Dominko et al.[172] also investigated the electrochemical performance of PAQ in Li- and Mg-organic batteries. They exhibit both good capacity retention and rate capability in both Mg and Li systems, employing as electrolytes 1M LiTFSI in DME:DOL (1:1 vol %) and 0.4M $Mg(TFSI)_2$/0.4M $MgCl_2$ in TEG:DOL (1:1 vol %) (Figure 78).

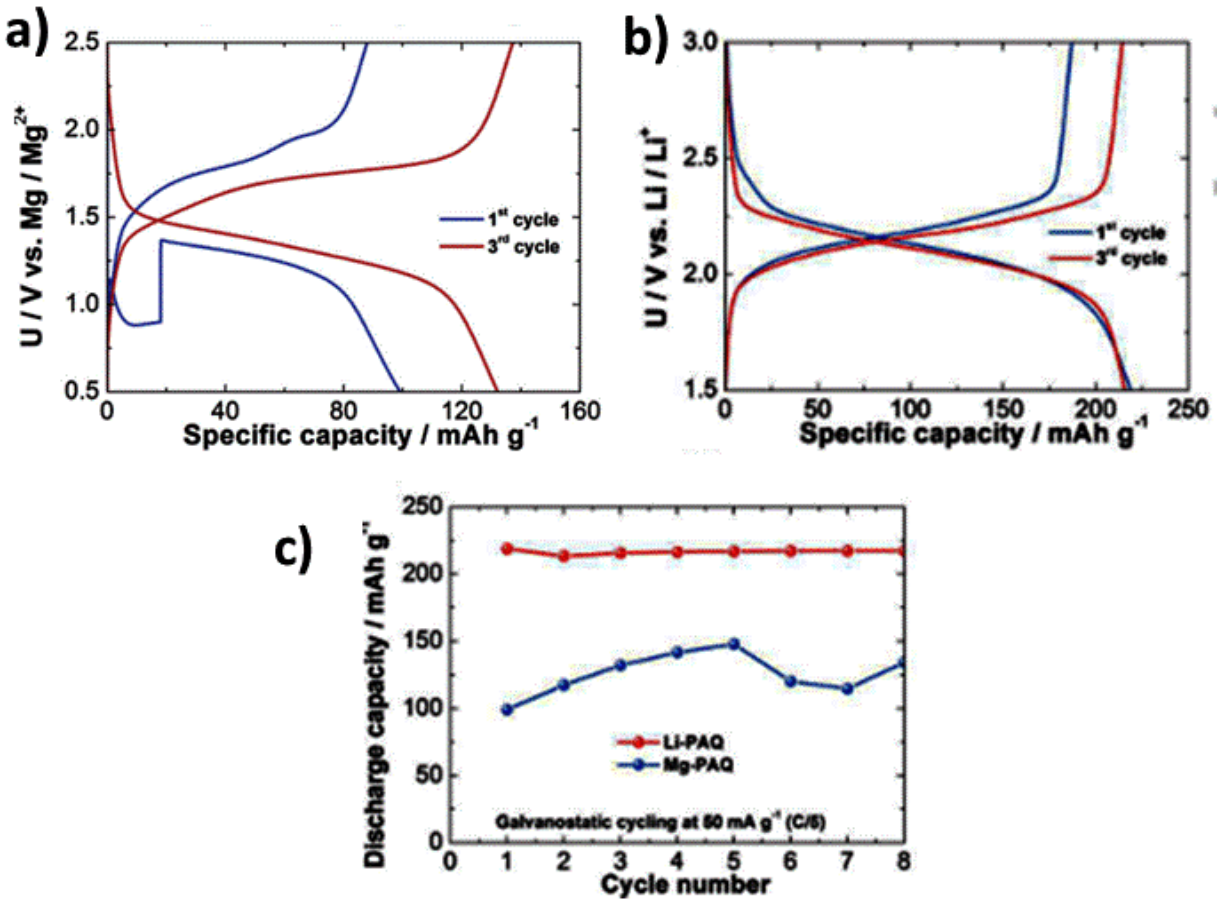

Figure 78: a) Galvanostatic discharge/charge cycles for the Mg-PAQ battery at a current density of C/5. b) Galvanostatic discharge/charge cycles for the Li-PAQ battery at a current density of C/5, and c) Discharge capacity for PAQ in Li (red) and Mg (blue) battery at a current density of C/5.[151]

While both systems exhibit a single slightly sloped voltage plateau, maximum practical capacity in Li batteries is close to the theoretical value (260 mA h g^{-1}), while the maximum capacity in Mg is considerably lower, only slightly above 50% of the theoretical one (133 mA h g^{-1}). This suggests that the electrochemical mechanism might change from Li to Mg batteries or that the performance of PAQ is worse in Mg electrolyte.[173]

In the work of Vizintin et al[174], in 2018, the polymeric structure of PAQS was modeled by tool of DFT, as to understand how the organic molecules are arranged to decrease the steric stress. Each PAQS backbone is organized with geometry orthogonal to the other.

These interesting results pave the way for the further use of other organic active materials with other multivalent metals, such as calcium. So far organic materials based on conjugated organic carbonyl compounds have been tested exclusively in aqueous Ca electrolytes.[175] In this chapter, PAQ and PAQS are tested against a Ca metal anode using $Ca[B(hfip)_4]_2$/DME electrolyte. This work is divided into two practical parts: the first one is focused on the investigation of the electrochemical performance of PAQ and PAQS based cathodes in calcium cells with an alkoxyborate Ca/DME based-electrolyte. Self-standing electrodes were prepared as explained in Section 2.1. In the second part of the work, with the help of Dr. Jan Bitenc, we prepared PAQS-based cathodes with carbon nanotubes in oder to improve conductivity and cycling performance of this Ca-organic system.

2. Results and discussions

2.1. Materials and methods

PAQ and PAQS were prepared as described in the literature.[168] The purity of the final polymers was checked by AT-IR spectroscopy. For the preparation of PAQS/MWCTN, 0.30 g of multi-walled carbon nanotubes (MWCNTs) (NTL, C-grade) were put into 50 mL of *N*-methyl pyrrolidone (NMP) and sonicated with an ultrasound tip (Sonics Vibra Cell CV 334) for 20 minutes, 2 times. Then, 3.41 g (14 mmol) of 1,5-dichloroanthraquinone were added and the mixture was again sonicated for 20 min. Subsequently, the mixture was cooled down to 8°C and 0.93 g (11.91 mmol) of anhydrous Na_2S, dehydrated by azeotropic distillation with toluene, was added. At this point, the reaction flask was closed and sonicated using an ultrasound bath for 30 min. The mixture was then heated at 200 °C overnight (14 hours) to complete the reaction. After that, the reaction mixture was filtered and washed with hot water (2x) and acetone (2x). Final product was purified with Soxhlet extraction in EtOH. Yield of reaction was 95% (Figure 79).

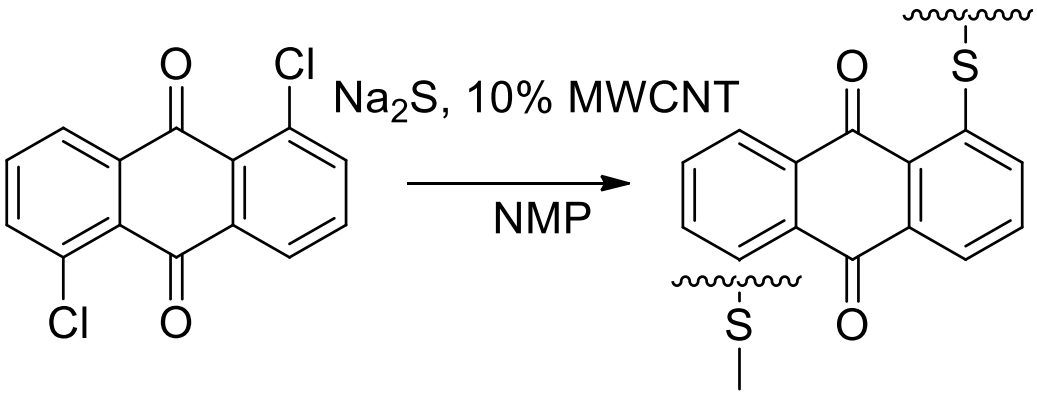

Figure 79: *Synthetic route of PAQS/MWCNT.*[149]

Self-standing electrodes were prepared from the active material, Printex XE2 carbon black and PTFE binder in the ratio of 60:30:10. The mixture was ball milled with isopropanol using a Retsch PM100 mill at 300 rpm. The composite was then put in agate mortar and ground until a viscous sticky composite was obtained. The latter was rolled on a glass plate to obtain self-standing electrodes with loadings of active material of 2–3 mg/cm^2. The prepared electrodes were dried at 50 °C overnight and transferred inside an Ar-filled glove box.

Electrochemical characterizations were performed in 2- and 3-electrode Swagelok cells assembled inside an Ar-filled glove box. Ca shots (99.5 % Alfa Aesar) were shaped into 12 mm round discs and used as CE. A Ca disc was also used as the RE in a 3-electrode cell. Glassy fibre Whatman GF/A sheets were used as separators. Organic material performance was tested by galvanostatic cycling at C/5 (122.5 mA/g) in the potential window from 1.3 to 3.3 V vs. Ca/Ca^{2+}. All the electrochemical tests were performed on WMP3 and MPG2 potentiostats from Bio Logic S. A.

Cells for the *ex situ* characterisation of the electrodes were disassembled inside the glove box after cycling. Electrodes were carefully removed from the cells and washed 3 times successively with the 2 ml of DME. Three types of separate electrodes (soaked with electrolyte, discharged, and charged electrode) were prepared for ATR-IR analysis. ATR-IR spectra were measured using the Bruker Alpha II spectrometer equipped with the Ge crystal (several spots were measured, giving equivalent spectra) placed inside the glove box to prevent the degradation of samples (especially discharged one). *ex situ* electrodes were transferred to the SEM chamber using specially designed sample holder in vacuum to prevent their decomposition in air. EDS characterization was performed on several electrode areas of at least 1 mm^2 with an Oxford Instruments INCA EDS detector. The presented composition values represent the average of at least three different areas.

2.2. Investigation of non-nucleophilic nature of electrolyte by FTIR

The compatibility of the PAQS based electrode with the fluorinated alkoxyborate Ca/DME based electrolyte was first assessed by putting them in contact. This test is crucial to verify whether the Ca based salt has nucheophilic character towards the carbonyl group in the polymer. The analysis was carried out by FTIR spectroscopy.[174] The comparison between the FTIR spectrum of pristine PAQS and of PAQS after contact with the Ca electrolyte for 1 day is shown in Figure 80. The typical stratching mode of –C=C– bond and –C=O bond, as highlighted, are retained after aging of PAQS electrode in electrolyte solution, indicating that the Ca based electrolyte doesn't react with carbonyl groups of the polymer, and that they are thus compatible. It must be noted that we have marked the chemical stability only of –C=O and –C=C– groups of the polymer, responsible for the redox activity, before and after contact with electrolyte; on other hand, the whole polymer system undergo important changes in structure, as shown in spectral region between 800 and 1300 cm^{-1}. It can be justified by interaction of other componts of the polymer matrix with the electrolyte.

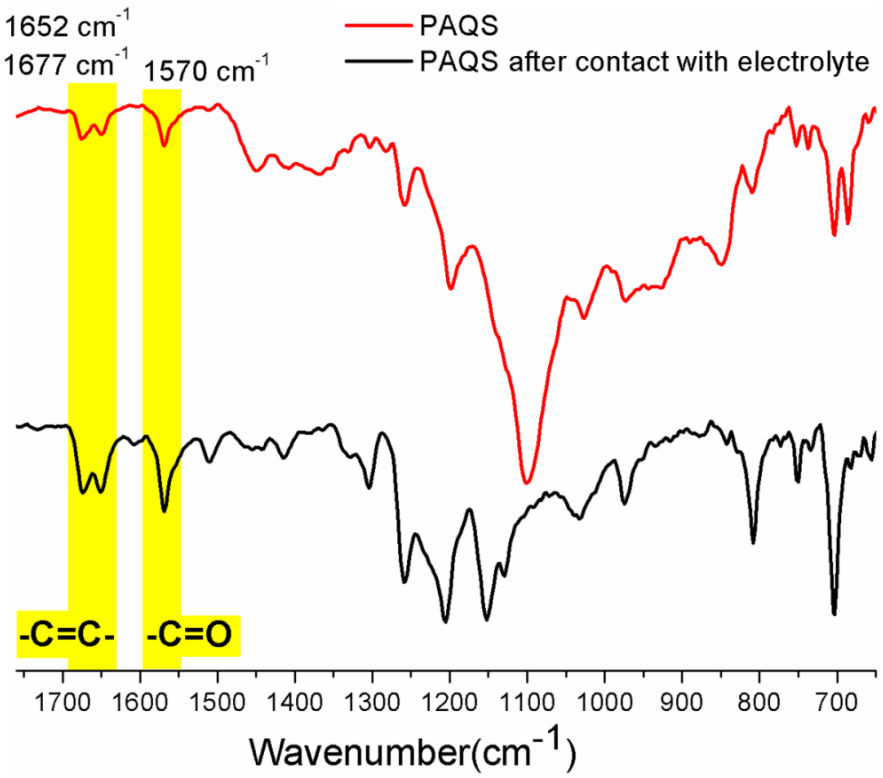

Figure 80: *FTIR spectra of fresh PAQS electrode and PAQS electrode after contact with electrolyte.*

2.3. Electrochemical performance

First tests with the PAQ and PAQS based polymers displayed both low electrochemical activity, as shown in Figure 81. The galvanostatic profiles at current density of C/5 are characterized by only approximately 20% - 40% of the theoretical capacity and with a relatively high polarization. In particular, in both PAQ and PAQS systems, discharge/charge profiles proceed thought a single-step sloped plateau, whereas the initial activation profile previously observed in the first discharge for PAQS-Mg systems cycled with MHCC and MTC electrolytes is absent for both materials.[171] This indicates that the preliminary swelling of polymer matrix and further activation of the organic moieties to accommodate calcium ions does not seem to occur, justifying the low activity and high degree of polarization.

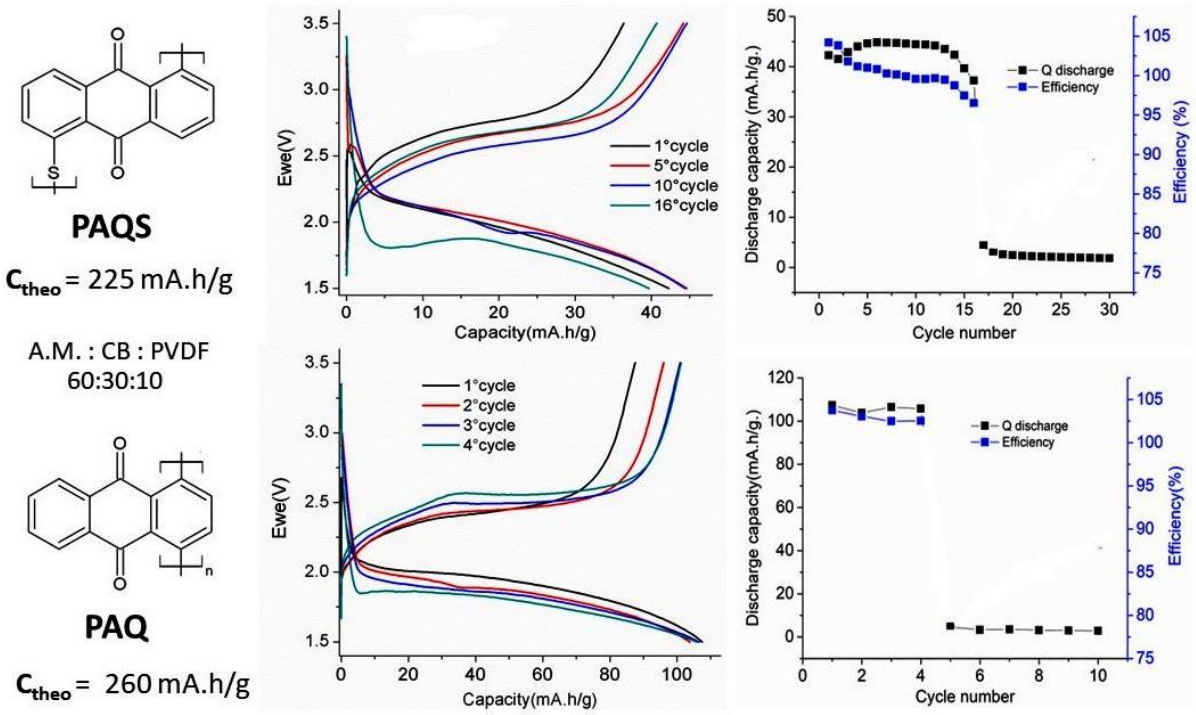

Figure 81: top) Galvanostatic discharge/charge cycles for the Ca-PAQS battery at a current density of C/5. down) Galvanostatic discharge/charge cycles for the Ca-PAQ battery at a current density of C/5.[125]

For PAQS, the cycle life is limited to the 16th cycle, while, for PAQ, the reversible capacity fades after 4 cycles, with the discharge capacity only 40% of theoretical one. To explain the electrochemical performance of these materials, beside the possibility of shortcuts, their solubility in the electrolyte was investigated. As shown in Figure 82, the PAQS-based electrodes presents a low solubility in the electrolyte, both in the pristine and in the discharged form (C/5, +1.5V), producing a clear transparent solution. On other hand, the PAQ-based cathode is more soluble in electrolyte, producing a red solution, in both pristine and discharged states. For this reason, only the PAQS-based polymer was employed for further electrochemical experiments as a cathode in Ca-organic system.

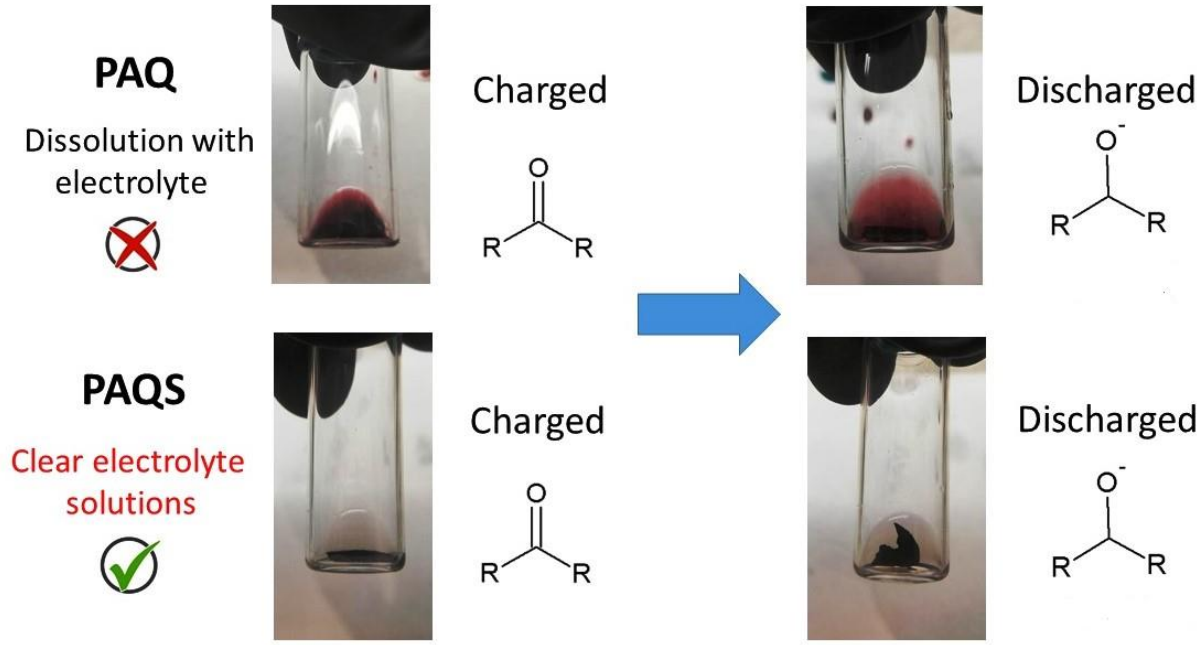

Figure 82: *ex situ pictures of electrolyte solutions after contact with both fresh electrodes and their discharged state.*

To improve its performance, PAQS was polymerized in a suspension of multi-walled carbon nanotubes(CNTs), giving a nanostructured PAQS/CNTs composite that was used as the active material.[125] 2-electrode cell, the nanostructured cathode with the new electrode formulation delivered a first discharge capacity of 169 mAh/g (Figure 83a), corresponding to 75% of the theoretical one (225 mAh/g). This result confirms a significant improvement of the capacity due to the improved electronic wiring or more porous structure of the material induced by the incorporation of CNTs. The discharge in the first half-cycle is different from the subsequent cycles, which is less inclined and single-voltage plateau less pronunced. It is a feature previously observed even in electrolytes for Mg-organic batteries, as MAC and MTC in mixture of glyme-based solvents and THF. The process is still not well understood yet in term of mechamism, but it can be refered to an initial "formation cycle". Such an increase in the overpotential results in a significant decrease of the cathode capacity, from 169 mAh/g in the first cycle down to 112 mAh/g in the 6th cycle (Figure 83b). In the following cycles, the

overpotential at the beginning of the discharge increased further and eventually led to the blocking behavior of the cell.

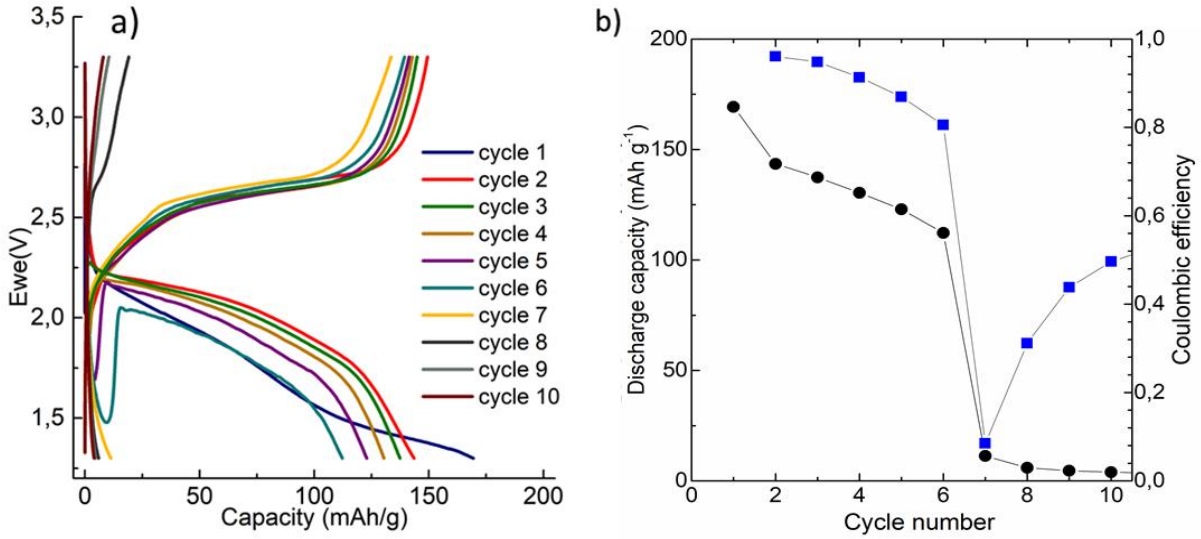

Figure 83: *a) Galvanostatic cycles in 2-electrodes cell of Ca metal–PAQS/CNTs battery at 0.2 C (122.5 mA/g) in the voltage range between 1.3 and 3.3 V. b) Discharge capacity and Coulombic efficiency for the Ca metal–PAQS/CNTs cell.*[125]

There are several possible reasons for the observed capacity fading:(1) decreased oxidation stability of the electrolyte in the presence of the active material, (2) continuous passivation of the freshly formed Ca surface obtained during deposition, and (3) partial dissolution of oligomers. With the purpose to move inside the mechanistic insight of the processes that govern the capacity fade, electrochemical tests are carried out in three-electrode cell, holding the same cell set-up of 2-electrode-cell.

Tests in three-electrode cell setup with a Ca metal strip as a reference electrode, were performed to confirm the hypothesis that the increased overpotential on the calcium anode led to the fast degradation of Ca metal-organic battery in the previously two-electrode cell setup. Figure 84a shows the electrochemical characterization of Ca metal–organic battery in the three-electrode cell, at 0.2 C current density. The shape of the galvanostatic cycle displays a single discharge

plateau, which is better seen as a derivative of the galvanostatic curve (Figure 84b). This means that reduction of anthraquinone group proceeds as a one-step two electron reduction or two step one-electron reduction occurring at similar potentials.[172] A big increase of the overpotential with cycling is observed between reference and counter electrode during the Ca stripping process, in a good agreement with results obtained in a two-electrode cell. The increase of the overpotential at the Ca anode is connected with the accumulation of the degradation species from the electrolyte and deposition of the CaF_2 on the Ca metal anode. The formation of the CaF_2 along with the plating of Ca metal was already observed in the previous reports on the use of $Ca[B(hfip)_4]_2$ electrolyte.[176] After 10 cycles, a capacity of 114 mAh/g is obtained, confirming that both the capacity fade at the cathode and the increase of the overpotential at the Ca anode are responsible for the fast capacity decay in the previous 2-electrode cell, with a larger contribution of the latter (Figure 84c).

In the paper of Bitenc et al.[125], it is explained the organization of the PAQS polymer with Ca ions in the discharged state. Although most of the charge is compensated by Ca^{2+} cations, a non-negligible fraction of the $Ca[B(hfip)_4]^+$ ion-paired cations takes part in the electrochemical reaction. SEM EDS was used to check the possible presence of $[B(hfip)_4]^-$ anion in the discharged compound, giving an assestment of $PAQS^{2-}$-Ca^{2+} as most predominant species, with lower fraction of $PAQS^{2-}$-$2Ca[B(hfip)_4]^+$ and undischarged PAQS.

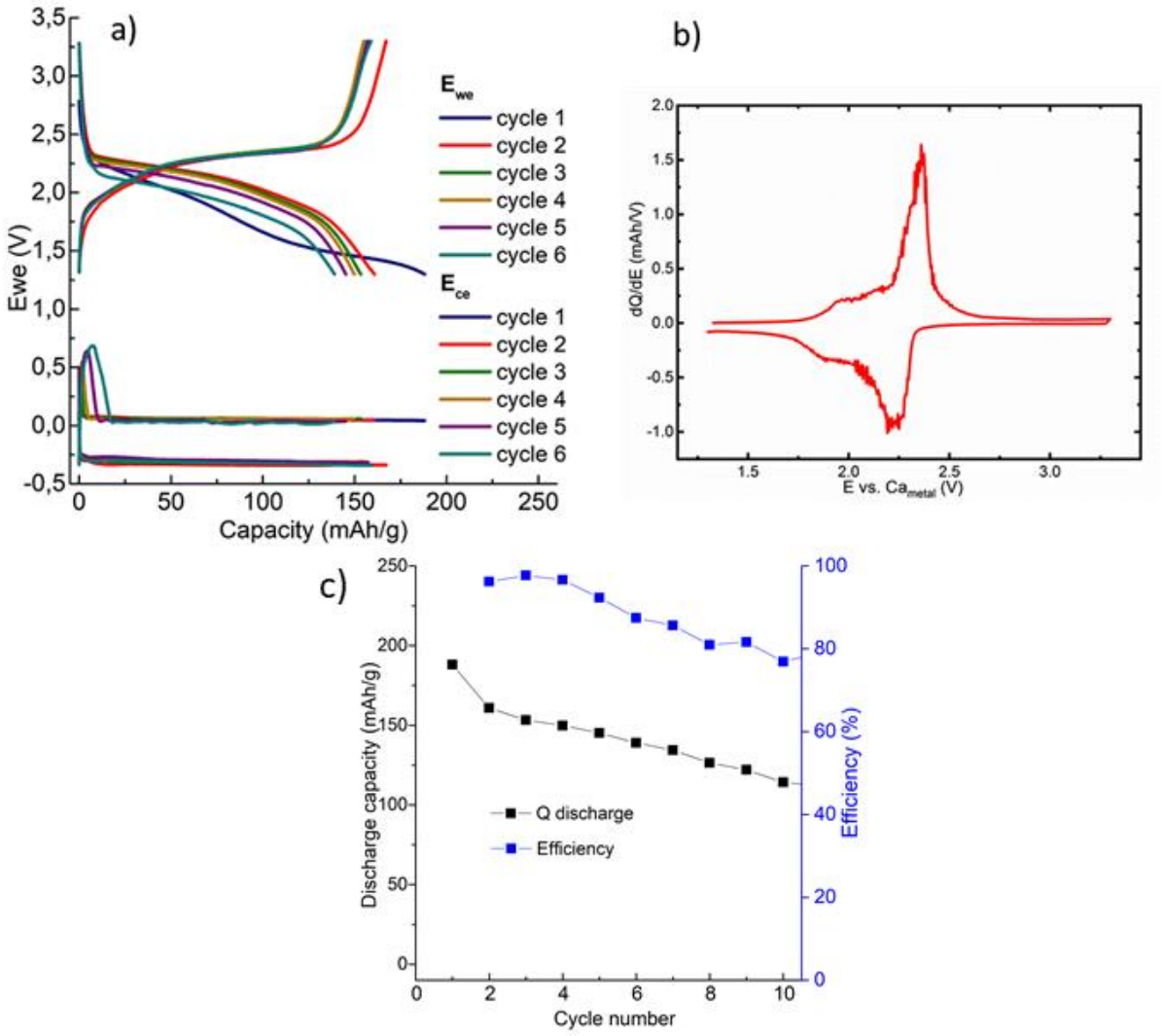

Figure 84: *a) Galvanostatic cycling of Ca metal–PAQS/CNTs cell with Ca reference electrode at 0.5 C (122.5 mA/g). The top curves show the potential of PAQS/CNTs cathode, whereas the bottom curves show the potential of Ca metal anode. Part of Ca metal anode potential over 0 V corresponds to the Ca stripping process and part below 0 V to the Ca plating process. b) Derivative curve dQ/dE vs. E Ca_{metal} in 3-electrode cell. Derivative is provided for the third galvanostatic cycle. c) Discharge capacity and Coulombic efficiency during cycling.*[125]

3. *ex situ* FTIR characterization

In order to investigate reversible electrochemical reaction of PAQS in Ca battery, pristine and cycled PAQS electrodes were studied by FTIR spectroscopy. In the case of conjugated carbonyl compounds, the reversible reduction of the carbonyl group to phenolate with the addition of one electron per carbonyl group is expected (Figure 85a). Three *ex situ* electrodes were analyzed to study the electrochemical mechanism of PAQS and compared to the pristine material: one electrode simply soaked in the electrolyte and washed, one fully discharged and one fully charged electrode. Simple soaking of the electrode in the electrolyte does not cause any major changes, as shown in Figure 85b. Very low-intensity bands were observed in the region between 1100 and 1000 cm^{-1}, which could be attributed to traces of the electrolyte and could be assigned to C−O stretching modes.

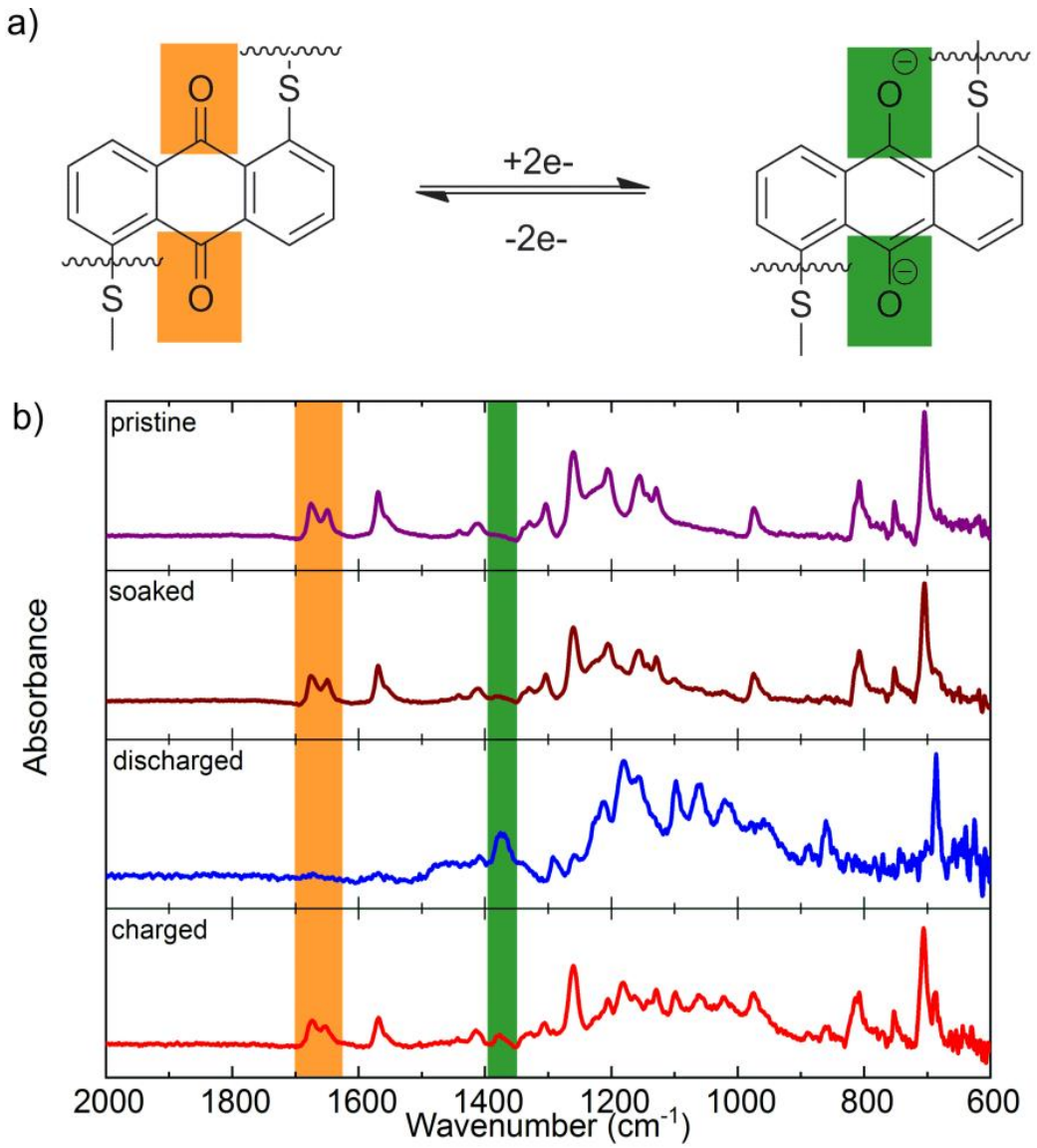

Figure 85: *a) Electrochemical reaction of PAQS electrochemical group upon cell discharge and charge. b) ATR-IR spectra of ex situ PAQS/CNTs electrodes. Pristine electrode (purple), electrode soaked in the electrolyte and washed (brown), discharged electrode (blue) and charged electrode (red).*[125]

The spectrum of the discharged electrode displays a completely different set of bands. The C=O double band at 1674 and 1650 cm^{-1}, the –C=C– stretching at 1570 cm^{-1} and the C−H out of plane bending at 704 cm^{-1}, which are characteristic of the PAQS polymer, disappeared. On the other hand, a new band at 1374 cm^{-1} is observed, which can be assigned to the phenolate group in agreement with previous observations in the reduced monovalent (Li)[174] and bivalent

(Mg)[177] anthraquinone salts. Even though this band is relatively broad and is close to the C−CF_3 stretching band belonging to the salt anion, its observed red shift indicates that both vibrational modes contribute to it. Several additional bands in the region between 1200 and 1000 cm^{-1} are observed, together with a very intense C−F vibration band at 686 cm^{-1} that can be confused with a shifted C−H out of the plane vibration. The charged cathode again displays well-defined C=O and C=C stretching bands together with the C−H out of plane vibration, indicating good reversibility of the electroactive carbonyl groups. The remainder of the stretching bands between 1200 and 1000 cm^{-1} and C−F vibration band in the charged cathode indicate incomplete charging (88% according to the capacity difference between discharge and charge) and/or the possible presence of decomposition products.

4. Conclusions

A proof of concept Ca metal–organic battery was obtained through the application of PAQ and PAQS organic polymer cathodes with the fluorinated alkoxyborate Ca based electrolyte. At the start of the experimental work reported in this chapter, inspired by the pioneering works of Prof. Dominko research group in Ljubljana on the development of PAQ and PAQS based cathodes in Li- and Mg- systems, there were no reports on the use of organic materials in Ca battery systems. The non-nucleophilic $Ca[B(hfip)_4]_2$/DME based electrolyte, investigated by FTIR spectroscopy, enables the use of organic compounds in Ca batteries with voltages within the expected voltage range, in analogy with sister Mg organic batteries. Preliminary attempts by using an electrode formulation with active material, carbon black and binder have shown the occurring of reversible Ca^{2+} insertion in both PAQ and PAQS cathode, but after a few cycles, a sudden drop of the cell capacity was observed for PAQ, which one of possible reasons could be related to its high solubility in the electrolyte. PAQS was thus chosen for further studies of the mechanism, less soluble in the electrolyte. The electrode formulation was improved by incorporating carbon nanotubes (MWCTN) within the active material, which allowed an improved discharge capacity by enhancing the electronic conductivity and enhanced porosity. The use of a 3-electrode cell setup allowed us to pinpoint the overpotential to Ca metal anode during the Ca stripping process. Reversibility of PAQS-based cathode confirmed through *ex situ* FTIR showed a reversible reduction of carbonyl bond upon discharge. These results demonstrate the practical applicability of Ca metal-organic batteries and provide a very good starting point for the future development of organic electrodes for Ca batteries.

These pioneering results demonstrate the feasibility of a Ca metal–organic battery as a sustainable alternative solution for energy storage. Theoretically, Ca metal–PAQS battery could offer an energy density of around 400 Wh/kg[125] according to mass of both PAQS cathode and Ca anode, while substitution of the relatively large anthraquinone group with the smaller and higher redox potential benzoquinone group could raise energy density of such cells up to 940 Wh/kg. The gravimetric energy density of these cells is comparable to the state-of-the-art Li-ion cells.[178]

5. Perspectives

For developing sustainable Ca-organic systems, many issues concerning the improvement of discharge voltage, cycle life and practical capacity remain to be addressed. N-type organic materials results to be viable candidates for the next generation polymer-based electrodes. Conventional organic electrode materials include small organic molecules, polymers and other organic materials. Although polymerization of small organic molecules could enhance the cycling stability of the electrodes, as observed for PAQ and PAQS, the obtained polymers generally exhibit low practical capacity and cycle life due to a low use of the active groups.

Porous organic frameworks (COFs) show outstanding advantages because their robust networks can enhance the stability and provide open pores that facilitate the diffusion of electrolyte ions.[179] COFs are a class of crystalline porous polymers with an atomically precise integration of building blocks into two- or three-dimensional topologies, characterized by lightweight elements and strong covalent bonds. These materials show excellent electrochemical performance in rechargeable batteries by taking advantage of featured porous networks and tunable redox properties. Several examples of COFs-based cathode materials exist for LIBs, such as the crystalline 2D-polyarylimide integrated with CNTs reported by Wang et al.[180] (Figure 86). High rate capability and ultra-stable cycle stability (100% capacity retention after 8000 cycles) are achieved for these materials, far exceeding the performance of the state-of-the-art polyimide electrodes.

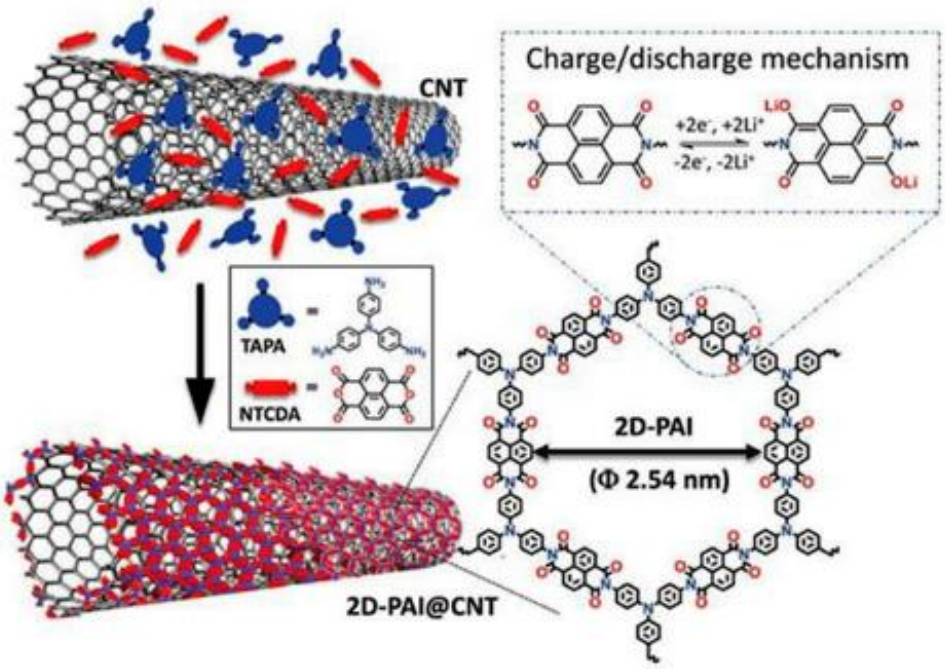

Figure 86: *Schematic illustration of synthesis of crystalline 2D-PAI@CNT and energy storage process.*[158]

COFs have already been proposed as promising redox-active substrates for multi-electron reaction, so the state of art can be used as inspiration for innovative Ca-COFs batteries.

In order to compete with the inorganic-based cathodes in terms of energy density, the operational potential of metal-organic batteries must be increased. According to Clar's theory, the electrons transferred to the carbonyl groups of quinones upon cation intercalation are delocalized over the aromatic carbon skeleton of the whole molecule.[181] Density functional theory (DFT) computations give us the correlation between the electron delocalization (aromaticity) and the metalation voltage of the carbonyl-containing polycyclic aromatic hydrocarbons. The results are illustrated in Figure 87:

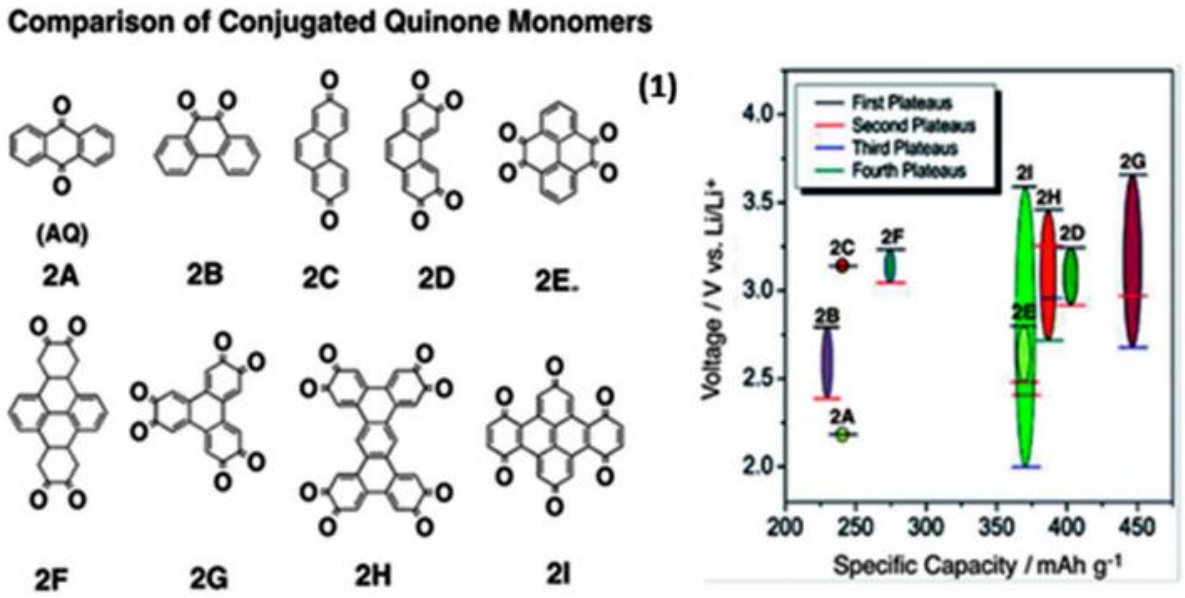

Figure 87: *Structures and electrochemical properties of AQ derivatives with varying degrees of aromatic conjugation.*[156]

The increase of the amount of carbonyl functional groups at optimal positions on the polycyclic aromatic hydrocarbons infrastructures increases the aromaticity difference between the products and the reactants of metalation, which subsequently increases the voltage. Moreover, employing full Clar polycyclic aromatic hydrocarbons (largest number of disjoint aromatic π-sextets or their derived structures as parent molecules) ensures high specific capacity. The redox potential is also improved by the introduction of electron-withdrawing groups.

Another strategy to improve the electrochemical performances of PAQS polymer is the incorporation of polysulfide linkages between AQ backbones. Gomez et al[182], showed the synthesis and characterization of new poly(anthraquinonyl sulfides) PAQxS in an attempt to improve the specific capacity of PAQS. The purpose was to combine the high performance of PAQS with the high capacity of sulfur built into new hybrid polymers. These polymers were synthesized with high yields by reacting sodium polysulfides formed *in situ* with 1,5-

dicholoroanthraquinone. By tuning the equivalent of sulfur, it is possible to modulate the length the sulfur chain between the polymers (figure 88)

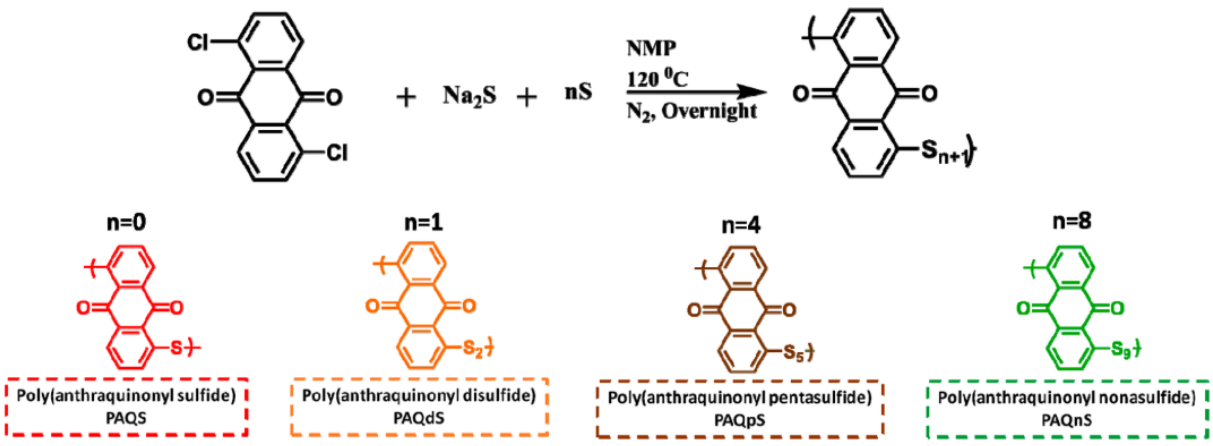

Figure 88: *Top) Synthesis of Poly(anthraquinonyl sulfides); bottom) Proposed structures for the synthesized polymers with different sulfur equivalents.*[182]

PAQxS cycled in LIBs batteries showed very high experimental initial capacities above 600 mAh/g, thanks to the breaking of the polysulfide chains, at high C-rate and good cyclability. The further application of these poly(anthraquinonyl sulfides) is high capacity redox polymers for energy storage in different multivalent metal batteries, such as calcium-based batteries.

IV. An innovative calcium/sulfur battery

1. State of art of metal/sulfur systems

Sulfur as a positive electrode material in batteries was introduced for the first time in 1960s by Herbert and Ulam[183] and since that time, quite many attempts have been undertaken to develop metal-sulfur batteries.[184] In fact, sulfur possesses several interesting properties: it offers one of the highest theoretical specific capacities (1675 mA h g^{-1}) among all existing positive electrode materials, and at the same time, it is abundant, non-toxic and extremely cheap (30 US$/ton), in principle allowing the realization of low-cost high-energy batteries.[185] A realistic target of practical energy density is in the range of 400–600 Wh kg^{-1}, which is higher as compared with the classical Li-ion cells. Significant advances have been realized in the past few years, and Li/S batteries can now be considered as realistic candidates for the next-generation energy storage systems.[186]

However, there is still a long way to go and many challenges to overcome, since metal-sulfur systems suffer from several yet unresolved drawbacks. The system limitations arise from different cell components: positive electrode, electrolyte and negative electrode. First, sulfur is known as a poor electronic conductor for its insulating nature ($\sigma = 5 \cdot 10^{-30}$ S cm^{-1})[187] and requires addition of high amounts of carbon additives.[188] Second, sulfur is partially soluble in most of the organic solvents used in the electrolyte, thus self-discharge can occur.[189] The morphology of the sulfur electrode changes upon cycling, and the final solid M_xS produced at the end of the discharge is also electronic insulator, as in the case of Li_2S for Li/S systems. Sulfur reduction produces polysulfide species, which are even more soluble than sulfur in the electrolyte, leading to the loss of active material and the diffusion of sulfur in the whole cell.

This process is commonly known as the "polysulfide shuttle" phenomenon, and limits the reversible capacity of the sulfur electrode high-order polysulfides formed at the positive electrode diffuse through the electrolyte to the Li metal anode, where they are reduced to form low-order polysulfides.[190] These short chain polysulfides can then diffuse back to the positive electrode, where they can be oxidized back to high-order species. The process is continuously repeated, resulting in prolonged charge process and low energy efficiency. Hence, a great effort was provided for developing an adapted electrode formulation, increasing both electronic conductivity and limiting polysulfide shuttle at the same time. All these phenomena are observed also for multivalent metal-sulfur systems such as Mg/S, Ca/S and Al/S batteries.[191]

To overcome this problem, several progressive strategies dealing with polysulfide shuttle may be adopted in the future, such as 1) development of a proper sulfur cathode able to encapsulate polysulfides, 2) application of an interlayer between the sulfur cathode and the separator or coating of the separator with another material, and 3) use of alternative nonporous ion conductive separator materials (polymer or ceramic) like those developed for Na/S batteries.[192] Moreover, in the case of Li/S batteries, other issues come from lithium dendrite growth and may cause short-circuits during battery charging. Moving towards new metal anodes, less plagued by dendrite growth, such as Mg and Ca, is essential to improve the safety of new metal-sulfur energy systems. Nevertheless, most of the proposed architectures are very sophisticated, relatively difficult to scale up, and mostly imply low active material loadings not suitable for designing high-energy Li/S cells. Most of the proposed strategies to overcome the issues are coming out logically through the investigations of Li/S batteries.[193]

The storyboard appears more complicated for Mg and Ca metal batteries, which are considered as promising electrochemical systems given the abundance of the elements and their physical and chemical features that could lead to very high energy-density cells. In brief, the formation

of a passive film with sluggish ion conductivity at the surface of a metal anode, the lack of electrolytes with high voltage stability, together with the problem of structure stability during the insertion of double-charge cations into crystalline hosts, dramatically narrows the choice of positive electrode materials.

In 2011, Kim et coworkers[194] made a rechargeable Mg/S battery using hexamethyldisilazide magnesium chloride (HMDSMgCl) and $AlCl_3$ Lewis acid in THF as the electrolyte. A mixture of sulfur, carbon, and binder was applied onto a porous carbon substrate for the cathode. The cell showed a fast capacity fade from 1200 to 395 mA h g^{-1} in two cycles. The high theoretical charge-storage capacity results from a 2-electron electrochemical conversion, with the anode reaction as:

$$Mg \rightleftarrows Mg^{2+} + 2e^-$$

and the cathode reaction as:

$$S + 2e^- \rightleftarrows S^{2-}$$

resulting in a reversible reaction of

$$S + Mg \rightleftarrows MgS$$

Despite these considerations, the mechanistic role of the electrolyte on the redox mechanisms remains unknown. Since that, significant improvements have been obtained in the design of electrolytes being both non-nucleophilic to accommodate the sulfur chemistry and compatible with magnesium electrode. In 2017, a binary mixture of $MgCl_2$ and $Mg(TFSI)_2$ salts dissolved in ether based solvents was used for the preparation of a Mg/S battery, characterized by a carbon/sulfur composite as cathode.[195] A detailed investigation of discharge mechanism was conducted by *operando* XRD. In this way, it was possible to show the disappearance of sulfur during the 1° high-voltage plateau, while the 2° low-voltage plateau corresponds to the

equilibrium between polysulfides and precipitated MgS. It was shown that the electrochemically precipitated MgS ($MgS_{electrochem}$) has a different crystal structure from that of synthesized MgS_{chem}.

In 2018, the group of Zhao-Karger and Fichtner[196] proposed a rechargeable Mg/S battery, with a $Mg[B(hfip)_4]_2$ based electrolyte and activated carbon cloth (ACC) as a support to immobilize sulfur as the cathode. The system showed excellent long-term Mg cycling stability with a low polarization. This electrolyte made it possible for the first time to investigate electrochemical processes by combining a wide range of characterization techniques, as it was done before for the Li/S batteries. These investigations showed that high capacity sulfur is electrochemically reduced to polysulfides first and then resulting in MgS at the end.

Mg/S cells were prepared with the magnesium aluminum chloride complex (MACC) electrolyte, to understand how the solvent affects the reduction of S_8. The electrodeposition overpotentials and current densities were found to vary with the different solvents used, suggesting that the nature of solvent plays a crucial role in the electrochemical processes at the Mg interface. Although the redox mechanisms for Mg/S batteries is still a matter of debate, there are presumably two possible pathways: a solid-state conversion pathway and a solution-mediated pathway. In a solid-state conversion mechanism, Mg^{2+} and S_8 form MgS directly. In a solvent-mediated mechanism, solubilized magnesium polysulfides (Mg_xS_y) are formed as intermediates and subsequently reduced to solid-state discharge products like MgS (figure 89). Solvent-mediated mechanisms are likely the only route to achieve high active material utilization because of the poor diffusion of Mg^{2+} in MgS and S_8. Therefore, we expect that the best Mg/S electrochemistry is achieved in solvent systems that support dissolution of Mg_xS_y species.[197]

$$x\mathrm{Mg}^{2+} + \frac{y}{8}\mathrm{S}_8 + 2x\mathrm{e}^- \rightarrow \mathrm{Mg}_x\mathrm{S}_{y(\mathrm{soln})}$$

$$(y-x)\mathrm{Mg}^{2+} + \mathrm{Mg}_x\mathrm{S}_{y(\mathrm{soln})} + 2(y-x)\mathrm{e}^- \rightarrow y\mathrm{MgS}_{(\mathrm{s})}$$

Figure 89: *Scheme of solvent-mediated mechanism occurring in Mg/S batteries.*[197]

In comparison to Mg/S battery chemistry that has entered its early research stage, Ca/S batteries show an even shorter history and have just been proposed as a new member of the family of alkaline-earth metal/sulfur batteries, with specific volumetric and specific capacities of the order of 1000 Wh/L and 570 Wh/kg.[40] The first limitation is the lack of a suitable electrolyte available to make Ca^{2+} to be electrochemically reduced, which obviously limits the understanding of the fundamental mechanistic details of Ca/S systems. Only in 2013, See and Seshadri[198] presented a first example of a high capacity primary Ca/S system, which showed a unique discharge process due to an electrolyte that doesn't allow Ca plating. Other electrolytes based on calcium borofluoride or borohydride enable reversible calcium deposition and stripping but are unfortunately not suitable for sulfur-based composite electrodes. The discharge of Ca/S battery is a non-reversible process when using a $Ca(ClO_4)_2$-based electrolyte, the oxidation of Ca only occurs partially during the first discharge in PC, EMS, and ACN/DME (1:1, w/w) since the growing SEI rapidly deactivates the negative electrode and prevents full discharge. Conversely, in ACN, Ca oxidation persists indicating a breakdown of the SEI layer under anodic bias.. Due to the difference in behavior of the SEI, the Ca/S system was evaluated in these electrolytes vs. S@CMK-3 (sulfur infiltrated hexagonally ordered mesoporous carbon). The galvanostatic discharge exhibits only one well-defined plateau. Additionally, after full galvanostatic discharge, the expected discharge product CaS is not observed by *ex situ* X-

ray diffraction, in contrast with Li/S systems, where Li_2S discharge product can be observed by *ex situ* XRD.

Recently several papers on Ca/S batteries have been published, showing the strong interest of the research community in this specific topic. These works will be carefully discussed hereafter in detail, as they will act as reference work for our experimental results.

In 2019, Manthiram et al.[199] proposed a reversible Ca/S battery through a Li-ion mediation concept with an electrolyte combining calcium and lithium triflate salts in tetraglyme solvent. The cathode was prepared with a carbon-sulfur composite on a freestanding carbon nanofiber (CNF) sheet. The addition of lithium triflate enables a better first discharge capacity and more importantly, seems to trigger the reversibility of the overall process in the subsequent cycles. After 20 cycles at C/10 current rate, a promising capacity of around 300 mAh/g is achieved. Nevertheless, despite its certain fundamental interest, such a dual-ion concept still depends on the use of lithium and have thus only limited application perspectives.

In 2020, Ponrouch et al.[100] combined experimental XPS and theoretical approach to unveil SEI components and rationalize the complex composition of the passivation layer formed on the Ca metal electrode in different electrolyte formulations. Borates are regarded as key component in the SEI layer and tri-coordinated boron (BO_3) was identified that might play a role in stabilizing the electrode/electrolyte interface, thus contributing to the electrochemical efficiency.

Only a few months ago, Zhao-Karger et al.[200] presented a room temperature Ca/S rechargeable battery, by employing a $Ca[B(hfip)_4]_2$ based electrolyte and a sulfur/carbon slurry casted on Al foil collector as a cathode. The cell have shown good reversibility and electrochemical activity, with a capacity retention of 200 mA h g^{-1} for 15 cycles. The mechanistic study by XPS verifies the chemical reversibility of the redox chemistry of the system.

In this chapter, we will show electrochemical activity of Ca/S battery at room temperature using the above-mentioned alkoxyborate-based electrolyte $Ca[B(hfip)_4]_2$/DME also employed by Zhao-Karger et al., and a composite positive electrode made from sulfur-impregnated ACC. By using a combination of *in situ* and *ex situ* spectroscopic techniques including X-ray absorption (XAS) and X-ray photoemission (XPS) spectroscopy, we propose the first study of the electrochemical mechanism of a Ca/S battery, which proceeds through the formation of several calcium polysulfide species to calcium sulfide as end of discharge product.

ACC (activated carbon clothes) composites have been used in several studies on metal/sulfur batteries.[201-202] The cloth has a microporous structure which results in rapid adsorption kinetics and the capability to adsorb sulfur with high efficiency, thanks to an extremely large surface area (more than 1000 $m^2\ g^{-1}$)[203], allowing a more effective adsorption capability compared to other carbon-based materials. Several porous, high surface area and conductive carbon materials, including mesoporous carbon, activated carbon, and carbon nanotubes were suggested as hosting substrates for sulfur cathodes for metal-S systems. It is believed that encapsulating sulfur in a carbon host improves its activity and limits the diffusion of polysulfides in the electrolyte, thus reducing the shuttle phenomena. The ACC composite is characterized by a highly porous carbon cloth, which results in rapid adsorption kinetics and the capability to adsorb to a higher level of active material. The former acts as a cathode current collector and a reservoir of the sulfur discharge products (polysulfides and metal sulfides) while encapsulation of sulfur in carbon improves its utility as an active mass and prevents diffusion of polysulfides to the electrolyte solution. In 2015, Rudnicka et al.[37] obtained a Li/S battery by impregnating microporous ACC with melted elemental sulfur. The electrochemical properties of the ACC/S composite cathode were tested in an ionic liquid electrolyte: reversible capacity, cyclic stability and Coulombic efficiency of the ACC/S cathode were better than sulfur

cathodes constituted by a mixture of sulfur with graphene nanoplatelets and carbon black, tested in the same ionic liquid electrolyte.

As we have seen in the previous paragraph, sulfurized ACC/S based cathodes have just found an application for Mg/S and Ca/S systems, marking the feasibility of this type of electrode with alkoxyborate based electrolytes.

In our work, the ACC/S electrodes were prepared using a modified melt-diffusion method already described in the literature[204] (Figure 90), starting from ACC 507-20 from Kynol Europa GmBH. 8 mm diameter discs were first punched out and dried at 120 °C for 4 hours under dynamic vacuum. Sublimed sulfur powder was then homogeneously dispersed on top of the disks, which were then heated in a stainless steel container at 155 °C for 16 hours, with a heating rate of 0.2 $C.min^{-1}$. After cooling, the electrodes were heated under argon flow at 200 °C for 50 minutes to evacuate the non-adsorbed sulfur. The sulfur content was estimated at around 10 wt. % by thermogravimetric analysis, giving a corresponding S loading of 0.8 – 1.0 mg cm^{-2}.

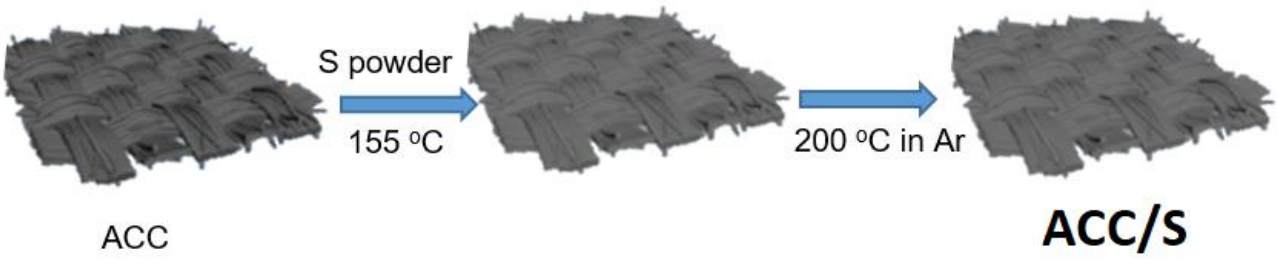

Figure 90: Scheme of preparation of ACC/S electrode.[204]

2. Electrochemical performance of ACC/S electrodes with $Ca[B(hfip)_4]_2$ based electrolyte

2.1. Materials and methods

SS coin cells (CR2032, 316L) were assembled in an argon-filled glovebox (H_2O and O_2 contents <0.5 ppm). Different types of Ca anodes were used: Ca shot (99.5%, Alfa Aesar) and Ca foil electrodes, scissor-cutted from 0.5 mm thick foil (ACI Alloys, U.S.A.) and then surface-scratched with scalpel. The ACC/S cathode (Ø: 8mm) was separated from the calcium foil anode with two glassy fiber membrane (Whatman, GF/A). The separators were wetted with 120 µl $Ca[B(hfip)_4]_2$ in DME (0,5 M) electrolyte solution. Galvanostatic tests were carried out at room temperature, in the potential range between +0.5 V and +3.5 V vs. Ca/Ca^{2+}, with current densities of C/10 (168 mA g^{-1}), C/20 (84 mA g^{-1}) and C/50 (33.5 mA g^{-1}). Cycling voltammetry tests were carried out at room temperature, in the potential range between +0.5 V and +3.5 V vs. Ca/Ca^{2+}, with a scan rate of 0.05 mV/s (approx. C/17). Electrochemical tests were performed by using a Maccor 4200 or Biologic VMP3 galvanostatic/potentiostat.

3.2 Results and discussions

The effect of the Ca anode on the electrochemical performance of the Ca/S system was tested by comparing two different Ca anodes (shot and foil) and cycled in the same potential windows and C/20 current rate. The galvanostatic profile and cycling performance are shown in Figure 91:

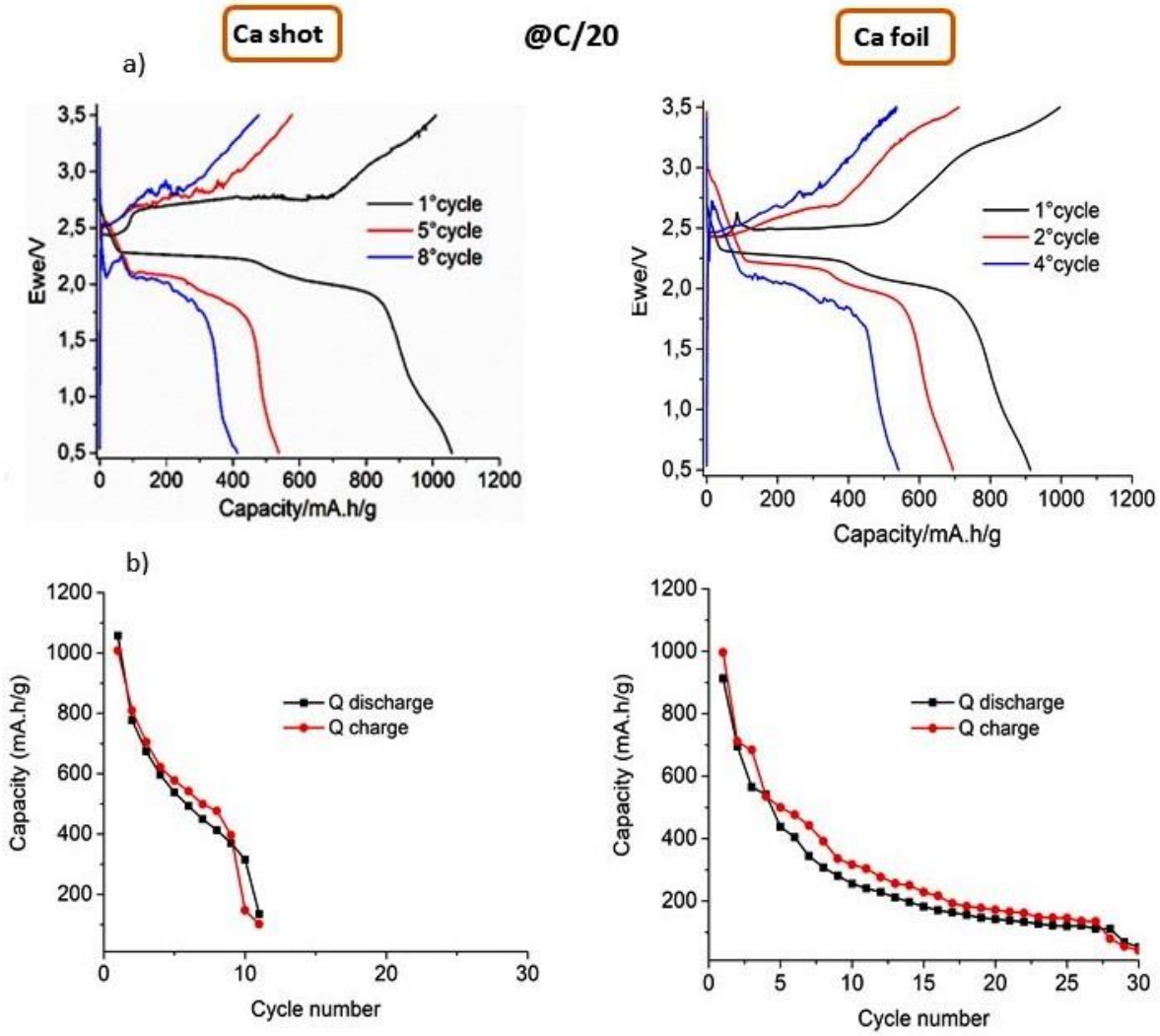

Figure 91: *Galvanostatic profiles (a) and cycling performances (b) of Ca/ S batteries using two different Ca anodes: shot and foil. $Ca[B(hfip)_4]_2$ in DME (0.5M) was used as an electrolyte and current rate C/20.*[205]

Spikes appear since the first charge for the Ca shot anode, and their intensity increases along further cycling, probably due to the irregular surface of the anodes and thus to the more pronounced phenomena of shortscuts or formation of passivation layer. On the other hand, spikes are absent until 4th cycle with Ca foil with a more regular surface. System with the Ca foil anode is characterized by a lower degree of polarization during cycling. The reasons can be sought in the different morphology of the Ca anodes: the more homogeneous and flat surface of the foil probably allows a better contact between electrolyte and scratched fresch Ca metal,

enhancing a better Ca mobility on the whole anode surface. On other hand, Ca shot is characterized by an irregular surface, just obtained by hammering, so holes could be present, in which the native surface oxidation layer cannot be removed totally after scratching. The result is a decreased area of fresh reactive Ca, with limitated Ca ion mobility; moreover, the presence of holes enhances the deposition of decomposition products on the irregular surface. These assumptions are confirmed by the capacity fade, definitely more pronounced with Ca shot anodes, with a rapid decay of the specific capacity and a battery life limited to the 11^{th} cycle.

These results show that the nature of the calcium anode strongly influences the electrochemical performance; the best results were obtained with calcium foils from ACI Alloys (0.5 mm thickness, 99.8 % purity), which native surface oxidation layer was however removed with a scalpel before use in order to obtain a shiny metal surface. These negative electrodes were thus used for all electrochemical experiments and the mechanistic studies by XPS and XAS spectroscopies reported in the following of this chapter.

To study the effect of the current rate on the electrochemistry, three Ca/S coin cells were cycled at different current rates (C/50, C/20 and C/10) in the same potential window (Figure 92).

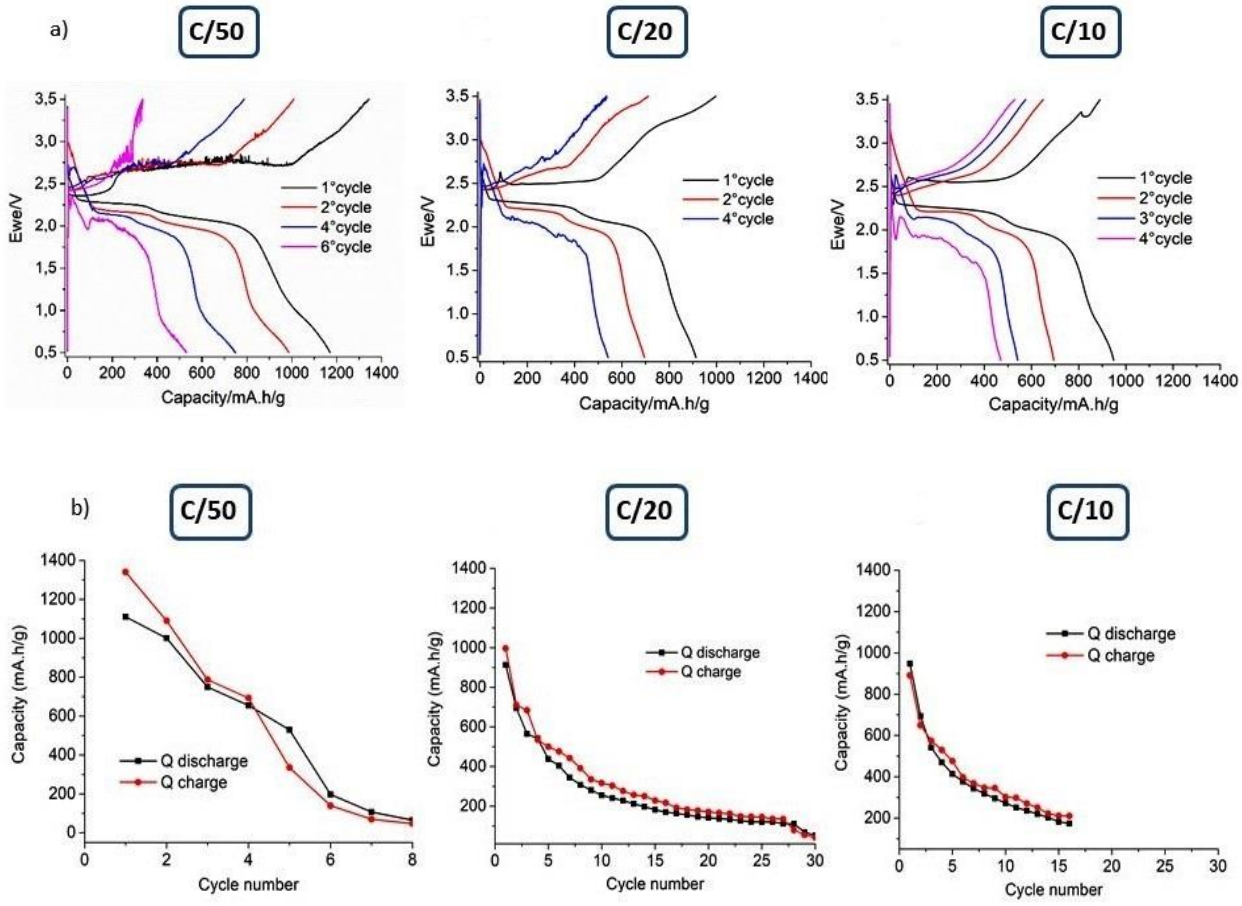

Figure 92: *Galvanostatic profiles (a) and cycling performances (b) of Ca/ S batteries obtained in $Ca[B(hfip)_4]_2$ in DME (0.5M) electrolyte and Ca foil as anode.*[205]

At C/50, discharge and charge capacity in the first cycle were 1171 and 1334 mA h g^{-1}, respectively, resulting in a Coulumbic efficiency of 88%. Spikes appear since the first charge, while their intensity increase as cycling goes on. This result has been even obserbed for Li/S batteries: with low discharge rates, the portion of CaS in the newly formed discharge product at each cycle increases with cycling, and capacity saturation is resulted in due to an increased reversibility of the discharge product.[206] The polarization increases regularly in the following cycles until cycle 8, when the cell stops working, probably due to the formation of a passive layer on the Ca anode.

The first discharge capacity 1170 mA h g^{-1} at C/50 is higher than those at C/10 and C/20, indicating a higher conversion of the sulfur to CaS, which reaches about 70%. Nevertheless, the capacity fade at C/50 is faster than at C/10 and C/20: only half of the initial capacity is retained after four cycles, and electrochemical activity is detected until cycle 8. At C/20 it worked until cycle 37 and at C/10 until 16 cycle. These results agree with those obtained with Mg/S batteries cycled at C/60, in which a rapidly Coulumbic efficiency and capacity retention fade was detected after a few cycles.[195] Problems of capacity retention related to self-discharge are observed also in Li/S systems.[207] Surprisingly, the polarization at C/50 is more pronounced than at C/20 and C/10. Considering these observations, the reason for this rapid decrease of the capacity at low current density can be connected to a more pronounced self-discharge and shuttle effect, but also the stability of the calcium anode towards the electrolyte.[208]

The cell cycled at C/20 shows an excellent reversible electrochemical activity at room temperature and a reasonably good cyclability, with discharge capacity retention of around 150 mA h g^{-1} after 28 cycles. During the first discharge, two well-defined plateaus are observed at 2.25 and 2.10 V vs. Ca/Ca^{2+}, followed by a slope region until the cut-off voltage of 0.5 V vs. Ca/Ca^{2+}. About 55% of sulfur is converted to CaS at the end of the process, possibly obtained via the formation of intermediate polysulfide species. The slope region could come from the process of nucleation and precipitation on insoluble CaS on the electrode, as already supposed for MgS deposition in Mg/S batteries.[195] The Coulombic efficiency is improved to 92% for the first cycle, compared to the system cycled at C/50 with 81% efficiency, indicating that a faster current rate limits the shuttle effects as sulfur species diffuse less into the electrolyte. Spikes are less marked than at C/50, probably due to less parasitic interactions between at the Ca anode. The latter observation is confirmed by the lower polarization of the cell.

A very similar discharge profile was observed also for Mg/S[196] and Li/S[37] systems using ACC/S cathodes. In both cases, the interconversion of sulfur to the final metal sulfide occurs via the formation of intermediate polysulfide species, indicating that the same reaction pathway is most probably followed by all metal sulfur systems.

The cell cycled at C/10 exhibits lower electrochemical activity, since only 57% of sulfur is converted during the first discharge, corresponding to a capacity of 948 mA h g^{-1}. After 16 cycles 180 mA h g^{-1} is retained, resulting in a Coulombic efficiency of 85%. The oxidation process during charge proceeds through a single voltage plateau followed by a sloppy region until the cut-off potential at 3.50 V vs. Ca/Ca^{2+}. Due to passivization of Ca anode, polarization is increasing with cycling and is probably connected with soluble sulfur species. XAS studies, carried out by Gao and coworker,[209] revealed that reduction of sulfur in the ether-based solvents involves distinct radical anion intermediates that persisted in solution even in the discharged and charged states.

The discharge and charge profiles at C/50, C/10 and C/20 are comparable, suggesting that the reaction mechanism from sulfur to CaS follows the same intermediate path in all three cases. The overall reduction reaction of sulfur to CaS can be resumed as:

$$S_8 + 16e^- + 8Ca^{+2} \longrightarrow 8CaS$$

Post-mortem characterization reveals the appearance of a yellowish color on the separators after disassembling the cycled cells, as shown in Figure 93:

Figure 93: *Separator recovered from the cycled Ca/S cell. The yellow color is indicator of polysulfide dissolution and diffusion in the electrolyte during cycling.*[205]

The yellowish color corresponds to polysulfides diffused out from the cathode structure, confirming that the electrochemical reduction of sulfur with calcium induces the formation of intermediate polysulfide species. In Li/S batteries, it is well-known that the design of the carbon-sulfur positive electrode plays a fundamental role in the voltage profile, in the capacity of retaining polysulfides and in the performance of the cell,[210] and the ACC/S positive electrode proposed in this proof-of-concept cell is not adapted for obtaining the best cycling performance. In fact, in such a basic system the sulfur is not expected to be retained at the cathode side, especially when soluble polysulfide intermediates are formed. Moreover, in this type of positive electrodes, the sulfur content is relatively low (around 10 wt.%)[202], and such a low value is not adapted to practical applications. Though many different carbon/sulfur composites were tested in Ca/S battery, the best results until now have been obtained with such ACC/S composite.

Figure 94 shows a cyclic voltammogram in 2–electrodes cell of the ACC/S electrode in $Ca[B(hfip)_4]_2$ in DME (0.5M), at a scan rate of 0.05 mV/s. During the reduction, two main

peaks at 2.09 and 1.89 V are followed by a minor event at 0.62 V vs. Ca/Ca^{2+}. During the following anodic scan, two broad peaks are observed at 2.57 and 3.29 V vs. Ca/Ca^{2+}. Two cathodic peaks correspond to the two plateaus observed in the galvanostatic discharge, and can be associated with the two-step reduction of sulfur.

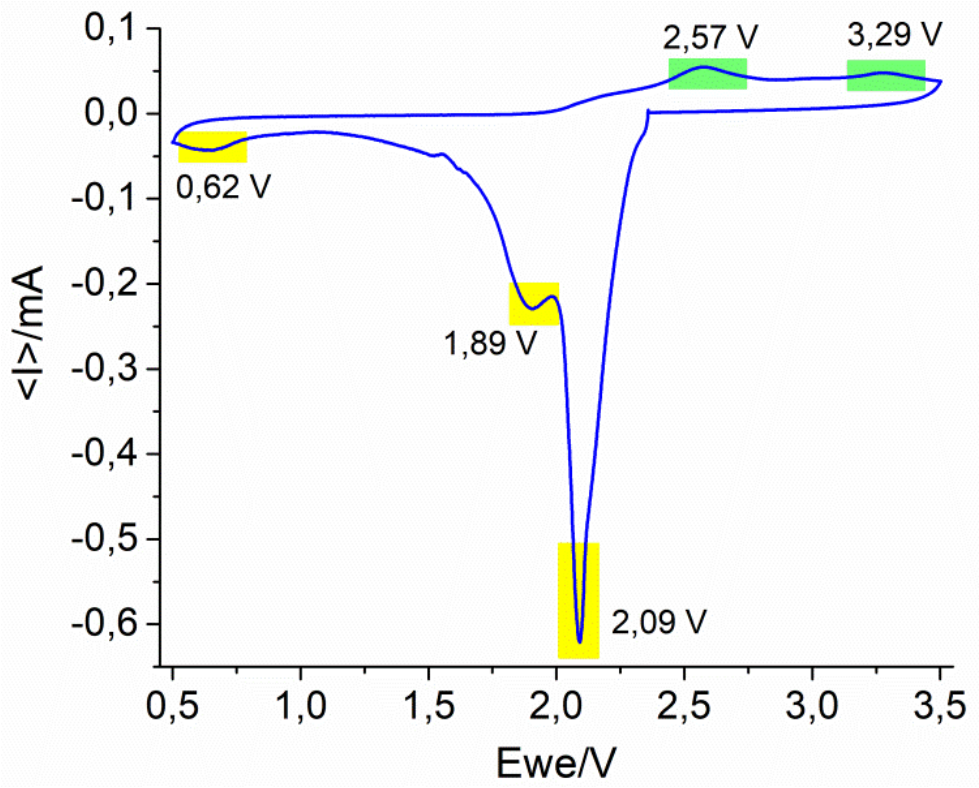

Figure 94: *Cyclic voltammogram of ACC/S cathode with $Ca[B(hfip)_4]_2$ in DME (0.5M) electrolyte vs. Ca/Ca^{2+}. Scan rate: 0.05 mV/s (approx. C/17).*[205]

Our Ca/S system shows interesting electrochemical performance, and it is competitive with the recently published Ca/S systems resumed in Figure 95:

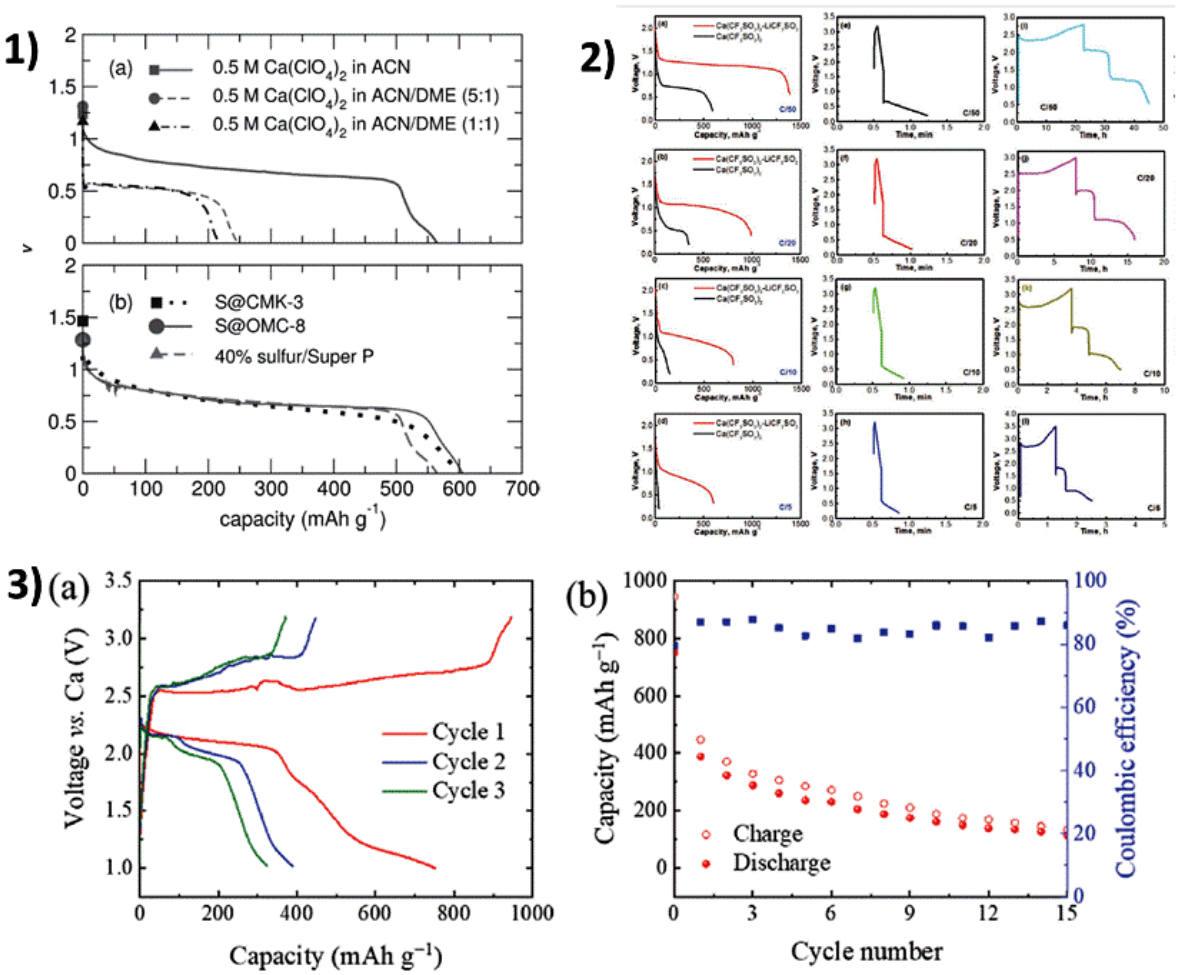

Figure 95: *References papers for comparison with our Ca/S cells performance (1: Seshadri[198]; 2: Manthiram[199]; 3: Fichtner[200]).*

1) In the work of Seshdari[198], the Ca/S primary cell exhibits a capacity of 600 $mA{\cdot}h{\cdot}g^{-1}$ in a single discharge step, due to not suitable $Ca(ClO_4)_2$/CAN electrolyte with sulfurized porous structured carbon host as the cathode. The advent of the alkoxyborate based salt has started the era of the reversible room temperature Ca/S batteries, thanks to the stable SEI formed and lower formation of decomposition products during cycling.

2) In the work of Manthiram[199], already discussed in the introduction, the Ca/S battery is developed with a hybrid electrolyte, comprised of a mixture of lithium and calcium ions. The cell cycled at C/10 delivers a first discharge capacity of about 800 $mA{\cdot}h{\cdot}g^{-1}$, then the capacity declines continuously in the following cycles and about 250 $mA{\cdot}h{\cdot}g^{-1}$

remain after 25 cycles. In comparison, we showed that our Ca/S system produces better performance, with better capacity retention, by using a single phase electrolyte, with a single salt system.

3) In the work of Fichtner[200], the sulfur/carbon composite cathode was employed with fluorinated alkoxyborate Ca based electrolyte. The first discharge/charge curve obtained at C/20 is characterized by three stages: a flat plateau at 2.2 V vs. Ca/Ca^{2+}, a slope at 1.5 V and another slope in the voltage range at 1.0 V vs. Ca/Ca^{2+}. Capacity fading is more pronunced than in our system at C/20, most probably because of the better accessibility of sulfur in ACC/S cathodes. Indeed, the sulfur/carbon composite of Fitchner has a higher sulfur loading than our ACC/S electrode, thus allowing a lower adsorbiotn sites for sulfur/polysulfides species, thus faster dissolution and a lower reversible cycling.

3. Mechanistic insights on the redox process of a Ca/S cell

The knowledge of the electrochemical mechanism of a battery system is necessary to improve the battery performance, and thus enhance its cycle life. However, despite the interesting results presented in the previous paragraphs, the electrochemical mechanism of Ca/S battery was still unknown. Such mechanism cannot be derived directly from that of Li/S systems, since the Ca electrolyte is different from the typical ones used in Li/S batteries, rather based on the LiTFSI salt.[211-212] Such a difference may lead, in principle, to different mechanisms of sulfur conversion. For this reason, we applied a combined spectroscopic approach, including *in situ* XAS and *ex situ* XPS, for unraveling the electrochemical mechanism in this new exciting battery system.

3.1. X-ray photoelectron spectroscopy (XPS)

XPS allows to follow the electrochemical activity of sulfur by pointing out the formation of intermediate polysulfide species and to identify the end-product of sulfur reduction as well as possible side reaction products at the electrode/electrolyte interface. It has been recently successfully carried out to determine the electrochemical mechanism in Li/S or Mg/S.[213-214-215] Fichtner and coworkers demonstrated the mechanistic study on the chemical reversibility of the S/CaS_x redox chemistry in the Ca/S batteries with the fluorinated alkoxyborate Ca based electrolyte.[200] Unfortunately, due to the low penetrating depth of photoelectrons, XPS can only be applied *ex situ* and probes only the extreme surface of the studied sample (a few nm).

In this work, we got the collaboration with IPREM (Université Pau Pays de l'Adour, CNRS, France). Several cells were cycled and stopped at selected points to be then studied by XPS (Figure 96).

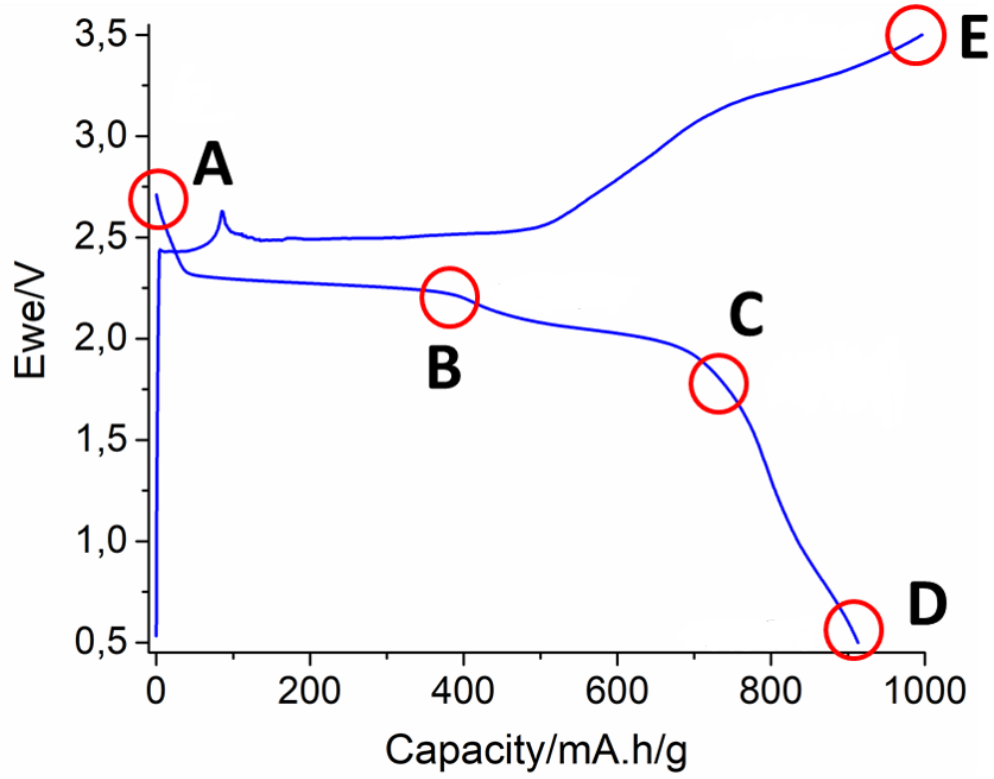

Figure 96: First discharge/charge cycle of the Ca/S cell (C/10 as current rate) and the different points selected for the XPS study (unwashed ex-situ samples).[205]

The S 2p, Ca 2p and F 1s XPS spectra of the ACC/S electrodes stopped at different points of the first discharge/charge cycle are shown in Figure 97. The corresponding quantitative analysis is reported in Table 8.

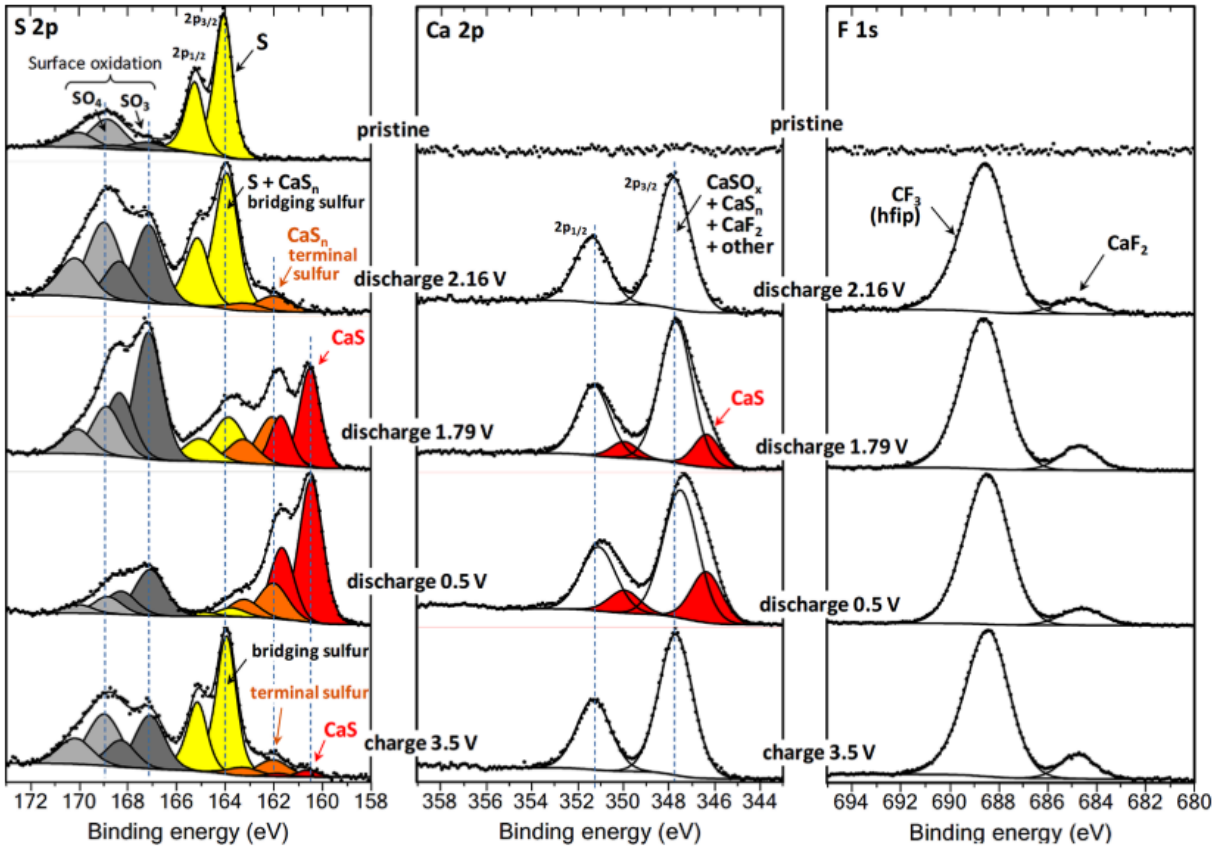

Figure 97: XPS S 2p, Ca 2p and F 1s spectra of the ACC/S composite electrodes stopped at different points of the first discharge/charge cycle of a Ca/S battery (unwashed ex-situ samples).[205]

Usually, samples are analyzed after extraction from the battery in an inert atmosphere, after a washing step to remove electrolyte and other soluble species. But in a case of Ca/S battery important electrochemically active species are soluble in the electrolyte, such as calcium polysulfides CaS_n. Thus unwashed samples were directly analyzed, such as in the case of Li/S batteries.[216] This means that a rather high amount of salt may remain at the surface of the electrodes, but also all the information about dissolved species and insoluble products, formed at the surface of the electrode as well. The S 2p spectrum of the pristine electrode shows the signature of elemental sulfur ($2p_{3/2}$-$2p_{1/2}$ doublet with $2p_{3/2}$ component at 164.0 eV), together with surface oxidation products (sulfite and sulfate), which cannot be avoided during the impregnation process. Let's recall that the XPS probe depth is only about 5 nm, which enhances

dramatically the signal of surface species. For the same reason, the measured amount of elemental sulfur is less than expected in the bulk (only 1.3 at. %). The signals of sulfite and sulfate are also observed after the electrochemical discharge/charge.

Peak	Pristine		Discharge 2.16 V		Discharge 1.79 V		Discharge 0.5 V		Charge 3.5 V		Chemical attribution
	BE (eV)	%	BE (eV)	%	BE (eV)	%	BE (eV)	%	BE (eV)	%	
C 1s	284.5	92.9	284.4	60.1	284.6	51.5	284.6	26.1	284.4	48.7	Activated carbon cloth
	---	---	286.8	2.9	286.8	1.3	286.8	3.0	286.8	2.6	C-O
	---	---	288.4	0.8	288.4	1.1	288.4	3.0	288.4	1.9	COO
	290.3	1.0	290.3	1.5	---	---	---	---	290.3	1.3	CO_3
	---	---	292.9	3.1	293.0	3.2	293.0	5.4	292.9	4.5	CF_3 (hfip)
O 1s	530.5	0.2	530.5	0.3	530.2	0.4	530.4	2.8	530.8	2.3	Mixed oxygen species
	531.7	2.5	531.8	9.7	531.7	13.9	531.7	18.0	531.9	9.5	
	533.1	1.6	533.4	3.6	533.3	4.4	533.3	3.8	533.3	3.6	
Ca $2p_{3/2}$	---	---	---	---	346.3	0.9	346.4	2.2	---	---	CaS
	---	---	347.8	3.1	347.7	4.7	347.5	6.4	347.7	3.8	All other Ca species
S $2p_{3/2}$	---	---	---	---	160.5	1.0	160.5	2.1	160.6	0.05	CaS
	---	---	162.0	0.2	162.0	0.7	162.0	0.6	162.0	0.15	Terminal sulfur (CaS_n)
	164.0	1.3	163.9	1.3	163.8	0.7	163.7	0.2	163.9	0.9	Elemental sulfur / bridging
	167.2	0.1	167.1	0.8	167.1	1.6	167.1	0.9	167.1	0.5	sulfur (CaS_n)
	168.8	0.4	168.9	0.9	168.9	0.7	168.8	0.3	169.0	0.5	Sulfite SO_3
											Sulfate SO_4
F 1s	---	---	684.9	0.8	684.7	1.3	684.6	1.7	684.7	1.7	CaF_2
	---	---	688.5	9.0	688.6	9.9	688.4	16.9	688.4	13.3	CF_3 (hfip)
B 1s	---	---	192.4	1.9	192.5	2.7	192.2	6.6	192.5	4.7	borate environment

Table 8: *Binding energy (eV) and atomic percent (%) of the XPS components of ACC/S composite electrodes stopped at different points of the first discharge/charge cycle (cf. Figure 96 and Figure 97).*[205]

During the discharge process, the S 2p signal of elemental sulfur is gradually and almost completely replaced by two new signals at 162 and 160.5 eV, attributed to terminal sulfur atoms in polysulfides CaS_n and to calcium sulfide CaS, respectively. It must be underlined that the signal of elemental sulfur cannot be distinguished from the signature of bridging sulfur atoms in polysulfides. Then, upon charge, CaS and short-chain polysulfides are gradually converted into elemental sulfur and long-chain polysulfides. The observed polysulfides formed at the different electrochemical steps are certainly a mixture of different CaS_n compounds with various chain lengths. Based on XPS data shown in Table 8, it is possible to estimate the average chain length $n_{av.}$ from the intensity ratio $R_{b/t}$ of the component assigned to bridging

sulfur atoms (S_b) to the component assigned to terminal sulfur atoms (S_t): S_t - S_b - S_b - … - S_b - S_t using the equation:

$$n_{av.} = 2\times(R_{b/t} + 1)$$

If CaS_2 is the only polysulfide present, no bridging S atoms are observed, so $R_{b/t} = 0$ and $n_{av.} = 2$. Opposite to this, if elemental sulfur is still present in the system together with long-chain polysulfides (at the beginning of discharge, for example) $R_{b/t}$ can be very high and $n_{av.} > 8$. Using this method, after discharge at 2.16 V vs. Ca/Ca^{2+}, a mixture of elemental sulfur and long-chain polysulfides are present since the calculated average chain length is $n_{av.} = 2\times(1.3/0.2 + 1) \approx 15$. After discharge at 1.79 V, there is $R_{b/t} = 1$ resulting in $n_{av.} \approx 4$. At the end of discharge (0.5 V) the electrochemically active species are composed of ~72 at. % CaS and ~28 at. % short-chain polysulfides CaS_n with $n_{av.} \approx 2.7$ (therefore, mostly CaS_2 and CaS_3). Finally, after charge at 3.5 V vs. Ca/Ca^{2+} a mixture of ~5 at. % CaS and ~95 at. % elemental sulfur and long-chain polysulfides are recovered with $n_{av.} \approx 14$. It is important to underline once more that the above mentioned compositions are representative of the extreme surface (~5 nm) and not of the bulk of the electrode.

In parallel, the Ca 2p XPS spectrum provides complementary information on the formation of CaS. Actually, Ca 2p peak is a poorly resolved signature for Ca species and gathers several species in an unresolved component (Ca $2p_{3/2}$ component at 347.7 eV). But fortunately the signature of CaS is well separated from all other Ca-containing species present in the system. Indeed, an additional component appears after discharge at 1.79 V vs. Ca/Ca^{2+} and after full-discharge at 0.5 V (Ca $2p_{3/2}$ at 346.4 eV) with a very well respected intensity ratio Ca/S = 1 to the S 2p component of CaS (Table 106). This attribution is comforted by the literature data on CaS, which indicate that the Ca $2p_{3/2}$ peak of this compound is expected at 346.45 eV.[217] Moreover, this Ca 2p component of CaS disappears upon charge (the remaining amount of CaS

is too low). Consequently, this study shows almost complete and reversible conversion of elemental sulfur contained in the pristine electrode into polysulfides CaS_n and CaS upon discharge and charge. These results can be positively compared to those obtained by Manthiram and co-workers for a mixed Li-Ca/S battery,[218] and are also comparable to those of Zhao-Karger et al. on a Mg/S system using a salt with the same anion.[219]

This XPS study also allows the identification of the side reaction products, by additional spectra (B 1s, O 1s and C 1s). From the F 1s spectra plotted in Figure 98, one can observe, besides the peak attributed to the salt $Ca[B(hfip)_4]_2$, a small peak assigned to CaF_2. This insoluble species formed at the surface of the electrode accounts for 1-3 at.% of the surface composition. Moreover, by comparing the intensity ratio of the CF_3 component (F 1s or C 1s) of the salt to the B 1s component, it appears that this ratio is much lower than expected: C 1s (CF_3)/B 1s ~ 1-2 instead of 8 for $[B(hfip)_4]$, and decreases gradually along the first cycle (Table 106). This means that most of the observed boron is not attributed to the salt but to a decomposition product of it, deposited at the surface of the electrodes. Moreover, looking at the quantitative data of calcium (Table 8), all identified calcium species at the surface, namely the salt $Ca[B(hfip)_4]_2$, CaS, CaS_n, CaF_2, and even $CaSO_3$ and $CaSO_4$ (assuming sulfite and sulfate are also associated to calcium) are not sufficient to explain the measured amount of calcium. Indeed, from 30 to 50% of the total observed calcium cannot be explained by the above species. Therefore, it is possible that part of the salt decomposes at the surface of the electrode to form mixed calcium boron oxide species, $(CaO)_x(B_2O_3)_y$, that might play a role in stabilizing the electrode/electrolyte interface thus contributing to the electrochemical efficiency.[100] Nonetheless, it should be again remembered that XPS is a surface-sensitive technique and that the amount of this decomposition product is significant in a 5 nm-thick layer at the surface, thus contributing only to a very negligible part of the mass of the electrode. On the basis of that, we can deduce that the thickness of decomposition product layer is lower than 5 nm.

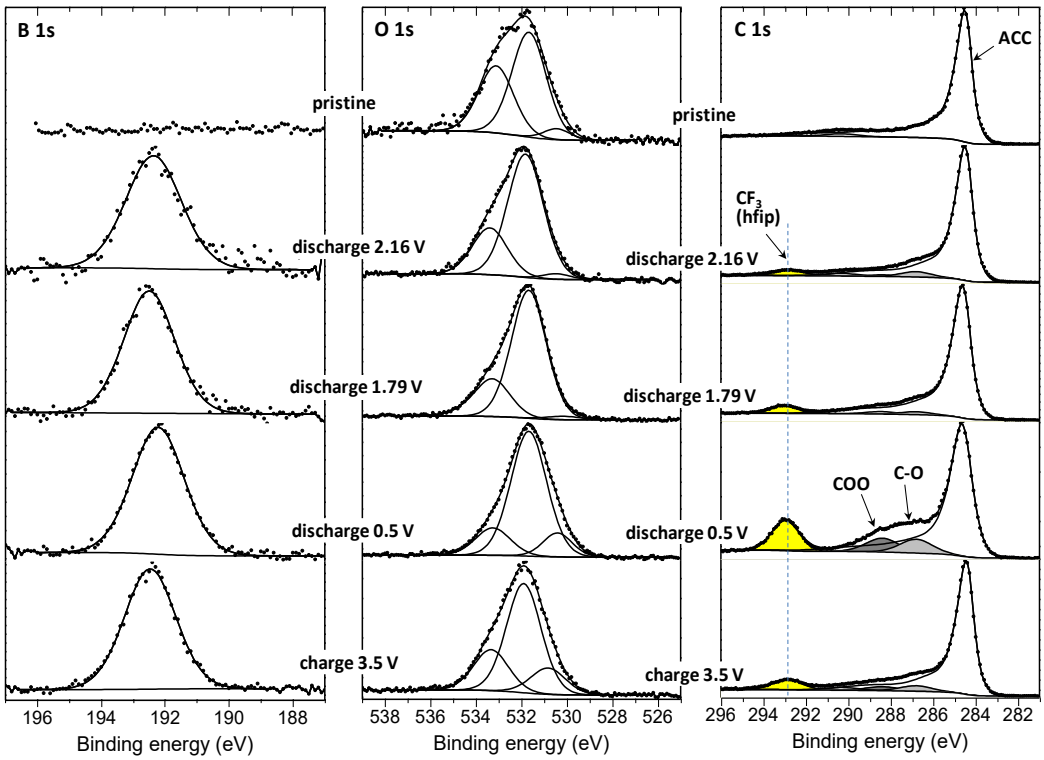

Figure 98: XPS B 1s, O 1s and C 1s spectra of the ACC/S composite electrodes stopped at different points of the first discharge/charge cycle of a Ca/S battery (unwashed ex-situ samples).[205]

These results match with the XPS data obtained by Fichtner and Zhao-Karger for the room-temperature Ca/S battery[200]. For these measurements, the cell was discharged and charged at C/20 in a voltage window between 0.5 and 3.4 V. The spectra of the pristine ACC/S cathode display the characteristic doublet of elemental sulfur at 164.1/165.3 eV; after discharge to 0.5 V, the S 2p signal could be deconvoluted into three doublet peaks. Signals at 161.0/162.2 eV can be assigned to CaS and the doublet at 162.4/163.6 eV to the terminal S atoms of polysulfides CaS_x, reflecting the effective conversion of sulfur to sulfides. Upon recharging to 3.4 V, the peaks for S_8 were restored while the signals for the sulfides (CaS/CaS_x) diminished.

The same XPS match can be observed for the rechargeable Mg/S battery developed by Fichtner and Zhao-Karger.[196] The S 2p spectra for the as-prepared ACC/S composite display the characteristic spin−orbit-splitting doublet for elemental sulfur with the S 2p3/2 and S 2p1/2

peaks at 164.0 and 165.2 eV, respectively. After discharging to 0.5 V, the intensities of the signals for S8 and MgSx decreased, whereas the intensities of the peak at 162.7 eV corresponding to MgS increased, reflecting the effective conversion of sulfur. Upon charging the cathode to 2.5 V, the S 2p peaks for MgS substantially shrank, while the signals for S_8 were restored.

3.2. X-ray absorption spectroscopy (XAS)

Operando sulfur K-edge X-ray absorption spectroscopy (XAS) is the technique of choice for monitoring electrochemical processes in working sulfur-based batteries, providing information on the chemical environment and on the electronic state of sulfur during the electrochemical reaction both in the electrode and in the electrolyte. In the case of metal-S batteries, issues arise through the unavoidable formation of various intermediate polysulfides during the reversible conversion of elemental sulfur into metal sulfides).[220] Poor confinement of the sulfur/polysulfides leads to large losses in active material, resulting in continuous capacity fading. In this context, it is essential to comprehend aspects such as the interactions among sulfur, the host matrix, polysulfides and the electrolyte in order to develop usable and marketable batteries. Sulfur is a reactive, heterovalent element that occurs in a wide range of formal oxidation states, ranging from −2 in some sulfides to +6 in sulphates. K-edge XAS spectra are sensitive to the oxidation state, chemical environment, type of bonding and group symmetry, and can be used as a fingerprint to identify individual sulfur compounds.[221]

Indeed, all expected sulfur species (*i.e.*, elemental sulfur, short and long chain polysulfides and solid sulfides such as CaS) can be easily discriminated using a combination of both the near-

edge (XANES) and the extended fine structure (EXAFS) portions of the XAS spectra.[222] Moreover, data analysis performed either using linear combinations of reference compounds or a multivariate chemometric approach allows one to follow the transformation of the sulfur compounds through the electrochemical cycle and to determine the relative amounts of different components in the working battery.[223] The same approach will be used to study our Ca/S battery system by using the dedicated experimental set-up initially developed in the framework of the European project EUROLIS for the study of Li/S[224], and nowadays readily available at the XAFS beamline to investigate sulfur-based batteries.[225] In addition to sulfur, also Ca K-edge XAS spectra can be measured in this case; this additional technique will help identifying possible soluble and solid-state Ca/S species formed during cycling. Moreover, the parallel analysis of Ca and S K-edge spectra will provide more reliable structural information on Ca-S species.

XAS is a synchrotron radiation based technique able to provide information on both local structure and electronic properties in a chemically selective manner. It can be used to characterize the dynamic processes that govern the electrochemical energy storage in batteries, and to shed light on the redox chemistry and changes in structure during galvanostatic cycling to design cathode materials with improved properties.[226-225] The XAFS beamline at Elettra Synchrotron (Basovizza, Italy)[227] has already in its present setup excellent characteristics essential for the success of *in situ* studies of sulfur-based batteries; operando XAS studies have been performed at beamline XAFS at Elettra on different systems as Li/S batteries. The beamline offers high energy resolution, high signal-to-noise ratio, a high monochromator stability and reproducibility, indispensable for high quality XANES and EXAFS spectra, necessary for the high precision determination of small changes in valence state, local symmetry and nearest coordination spheres of sulfur incorporated in cathode materials, during battery operation.[228]

The beamline XAFS can perform XAS in transmission and fluorescence. Its assets are to perform XAS with an excellent signal-to-noise ratio, stability, versatility and reliability, and a high automation level. The optical scheme (Figure 99) includes the mask, collimating mirror and double crystal monochromator; their aim is to suppress the contribution of higher harmonics when working at energies below 4 keV and therefore to enhance the performance of the beamline in the lower range of operation energies.[225]

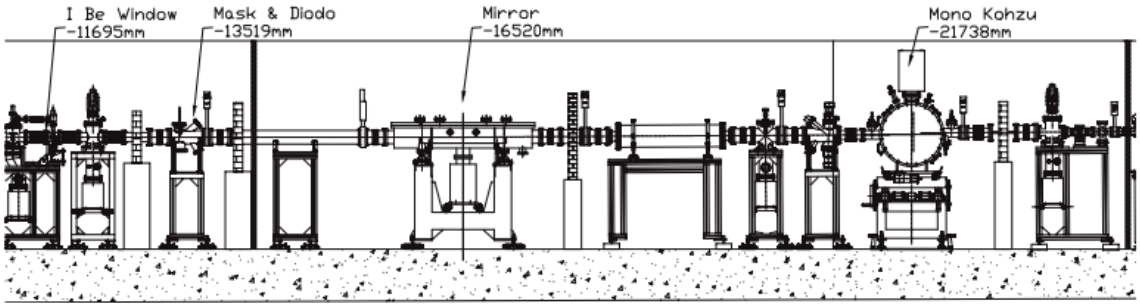

Figure 99: *Optical layout of the beamline XAFS.*[225]

A different type of electrochemical cell we used for *operando* studies of batteries; it is a Swagelok cell that was designed for *operando* experiments at synchrotron facilities for both X-ray diffraction and X-ray absorption, but which was recently also used for Raman spectroscopy. This specific Swagelok *in situ* cell adapted to the particularly low energy of the absorption K-edge of sulfur (and perfectly suited also for parallel Ca K-edge XAS measurements), enabling the measurement of XANES and EXAFS spectra in *operando* mode of Ca/S cells. For XAS, this cell can be used in the transmission and fluorescence modes. The main difference between this setup and the typical Swagelok configuration is the presence of a beryllium window (100 μm thickness) in contact with the working electrode, instead of the SS plunger (Figure 100). Despite its toxicity, Be is employed since it is electrochemically inert at the potentials experienced by a typical sulfur cathode, is an electrical conductor and especially because it is almost transparent to X-rays.[229]

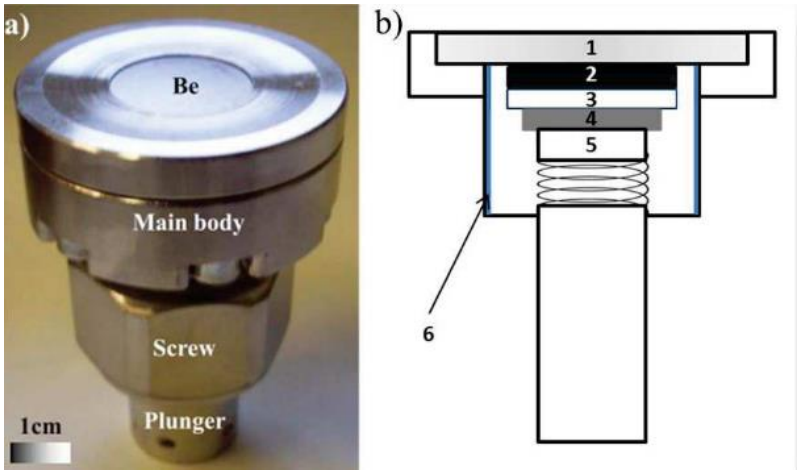

Figure 100: a): picture of the operando cell and b): schematic representation of the setup: 1 – Be window; 2 – working electrode; 3 – separator; 4 – Ca foil; 5 – stainless-steel plunger; 6 – Mylar foil[229]

In order to perform measurements at energies below 4 keV, the electrochemical cell can be placed inside a chamber connected directly to the beamline and equipped with electrical connections. The fluorescence detector can be placed inside, as shown in figure 101. The whole system can operate *in vacuo* or in a gas overpressure. For *in situ* studies of batteries, the chamber is usually filled with He at 10% above atmospheric pressure to avoid absorption of the air while at the same time avoiding a possible cell failure induced by vacuum conditions (for instance, evaporation of the electrolyte due to leaks induced by the external vacuum).[230]

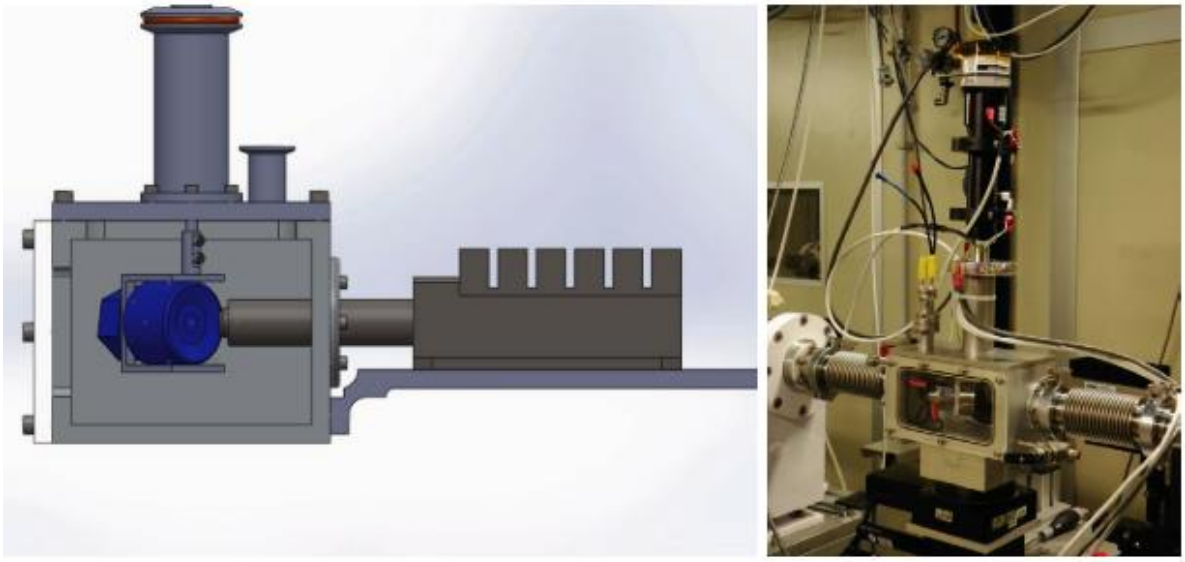

Figure 101: *Chamber for measurements at low energy.*[225]

96 hours of measuring time were needed at the XAFS beamline in order to perform alternate *operando* S and Ca K-edge XANES and EXAFS experiments on a Ca/S cathode material, electrochemically tested in our novel borate-based electrolyte formulation. With the beam focused on the back-surface of the sulfur electrode, the *operando* experiment allowed us to follow the evolution of sulfur and calcium species during a full discharge/charge cycle. Calcium sulfide and other calcium salts (the pure electrolyte salt $Ca[B(hfip)_4]_2$, calcium carbonate $CaCO_3$) were also measured as references. Our aim was to concentrate on the XANES portion of the spectra, which can provide quantitative information on the ratio between sulfur, Ca polysulfides, dissolved Ca species and CaS. Particular attention has been payed to data analysis: both Ca and S K-edge XANES spectra are typically measured in fluorescence detection mode due to the small penetration depth of the low energy X-rays in the material that hampers the measurement of spectra in the transmission mode. Such measurements are therefore affected by self-absorption of the fluorescence radiation, which may introduce systematic errors in the XANES analysis if not properly taken into account.

3.2.1. *operando* S K-edge XANES data analysis

The operando XAS analysis was conducted on an ACC/S (10% of sulfur load, 12 mm diameter) electrode during galvanostatic cycling versus Ca metal. The anode comprised a Ca foil (the size of foil was slightly larger than in coin cells, to allow a better fitting into *operando* cell) and 0.5 M $Ca[B(hfip)_4]_2$ in DME (250 µL) was used as the electrolyte. The electrochemical signature obtained in the *in situ* cell is much more polarized (probably for the special Swagelok cell used) than the signal in the coin cell, as shown in Figure 102. For this reason, the cell was cycled at C/25 current rate, in a large potential range from 0.5 to 4 V *vs.* Ca^{2+}/Ca, and a floating process at the constant potential of 0.5 V for 3 hours was added at the end of the discharge to push further the electrochemical reaction. Under these conditions, the reaction of almost 0.6 mole of Ca per mole of S was obtained during the first discharge, while 0.4 mole of Ca^{2+} were extracted during the subsequent charge. It must be noted that about the same fraction of sulfur reacted in the coin cell experiment. The battery delivered 1160 and 803 mA h g^{-1} during discharge and charge, respectively.

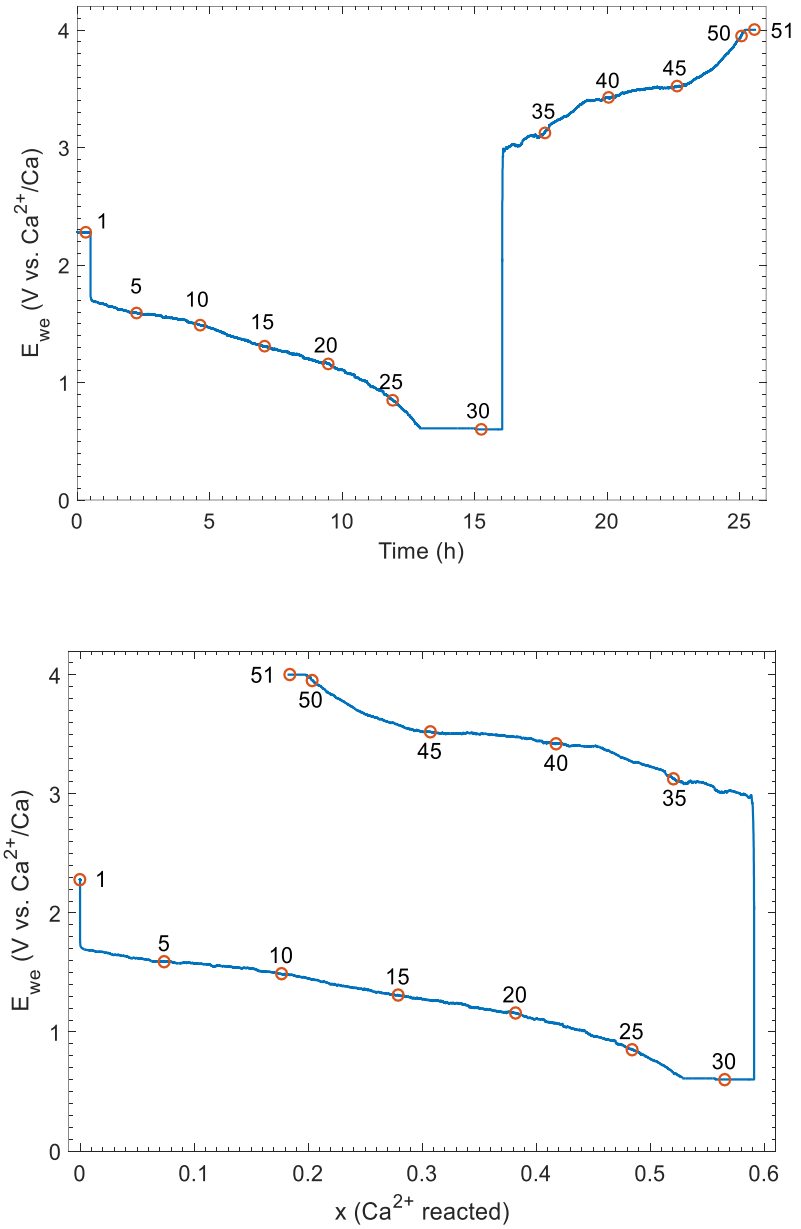

Figure 102: First discharge-charge cycle at C/25 of the Ca/S battery built in the in situ cell (described in ref. [231]) for the operando S K-edge XAS analysis plotted vs. time (up) and vs. mole of reacted Ca. (down). The red circles represent the positions of the measured spectra (30 for the first discharge, 51 for the following charge).[205]

The operando S K-edge XANES spectra collected on the back of the positive electrode through a full discharge-charge cycle are shown in Figure 103:

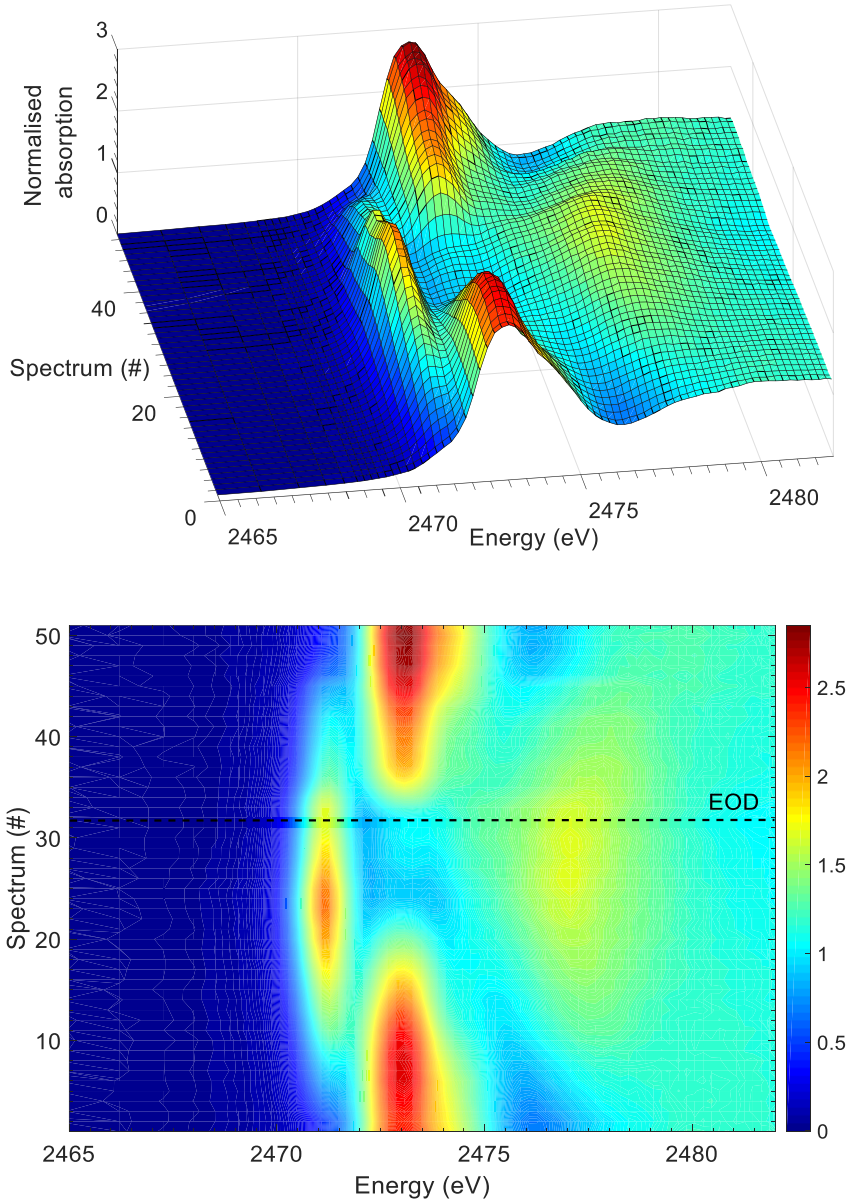

Figure 103: 3D (up) and topographic (down) view of the operando S K-edge XANES spectra measured during a full discharge/charge cycle of a Ca/S battery. The dashed line in the topographic view indicates the end of discharge (EOD), whereas the last spectrum is measured at the end of charge (EOC). The correspondence between electrochemistry and spectrum # is marked in Figure 102.[205]

Data analysis was performed on the full set of normalized XANES spectra *via* a chemometric approach, using a statistical tool named Principal Component Analysis (PCA) inside the Matlab environment. PCA is a factor analysis tool, and is generally used to discover the minimal

particular structures in multivariate spectral data sets.[232] PCA, together with Independent Component Analysis (ICA) and Multivariate Curve Resolution (MCR) are the most common methods sharing the same global objective: the resolution of complex mixtures into pure-components contributions based on no or little available information. In particular, PCA provides a totally blind abstract decomposition of a matrix of experimental data by computing orthogonal components aligned to the directions that explain the maximum of the variance of the data matrix.[233] More precisely, it is used here to determine the number of independent components contributing to the whole series of collected spectra during electrochemical cycling. The number of principal components determined in this way can be used as the basis for Multivariate Curve Resolution-Alternating Least Squares (MCR-ALS) analysis. [232-234] This algorithm allows the stepwise reconstruction of the "pure" spectral components which are necessary for interpreting the whole multiset of *operando* spectra. Such a combined method permits the fast and reliable extraction of maximum amount of meaningful data from a large data set, often allowing the detection of elusive intermediates and transient phases and their evolution through the whole reaction mechanism.[223]

The results of PCA applied to the whole experimental XANES dataset, shown in Figure 104, indicated that at least 6 independent spectral components must be used to process it. The "pure" spectral components where then first determined by the separate analysis by MCR-ALS of the charge and discharge processes (where the unimodality constraint could be applied to all components), and then combined and used as starting points for the MCR-ALS analysis of the full cycle dataset. In this case, unimodality was applied only to three of the six components: the first component of the discharge, the last component of the charge and the component reaching its maximum at the end of the discharge. Apart from this, the same non-negativity and closures constraints were applied to the analysis of the whole discharge/charge cycle. The latter

analysis provided the 6 pure spectral components together with the evolution of their concentration during the electrochemical cycle.

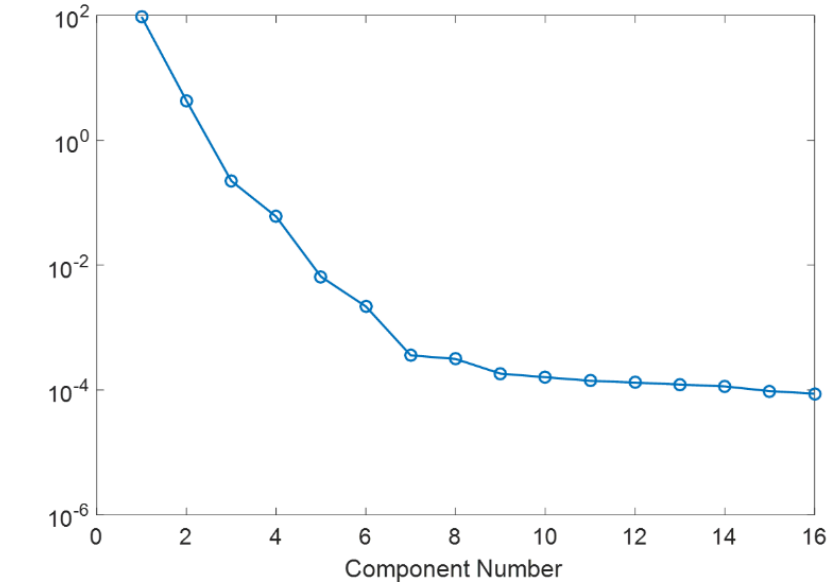

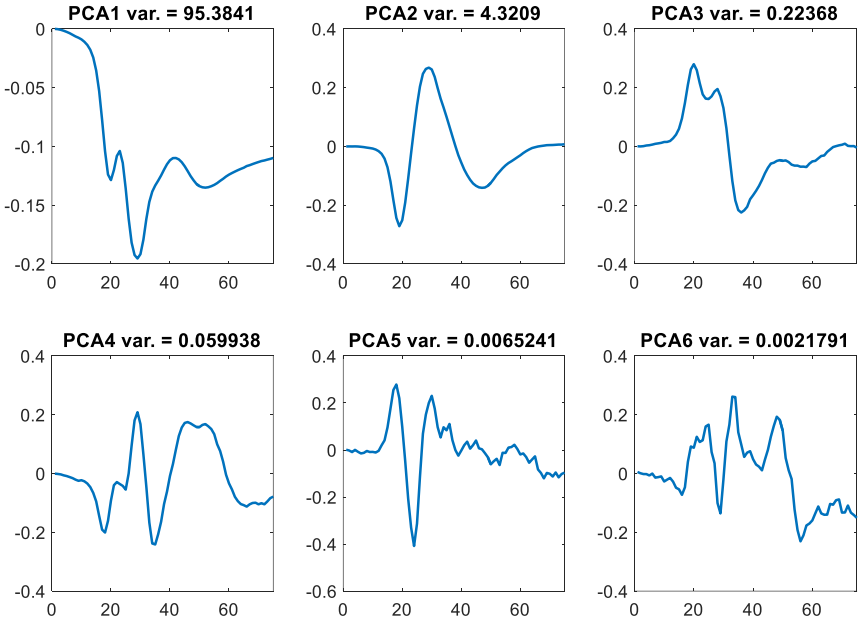

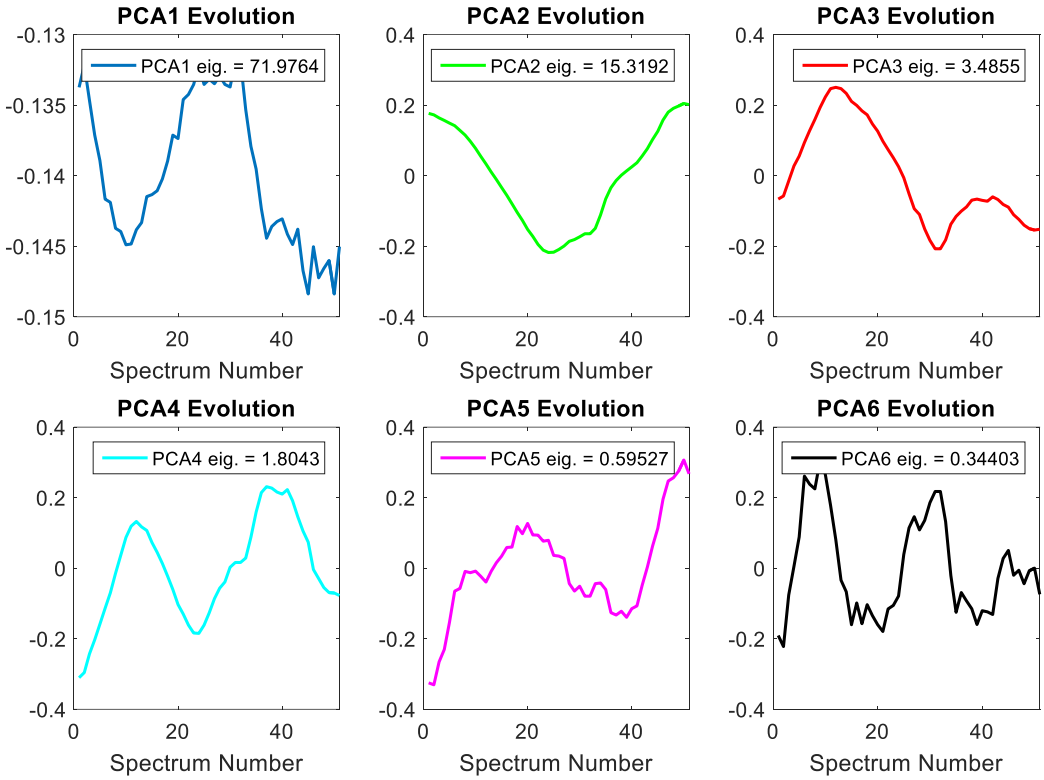

Figure 104: PCA analysis of the operando S K-edge XAS spectra measured during the whole discharge/charge cycle: Variance plot (top), principal components (middle) and their evolution (bottom) during the studied process.[205]

The pure spectral components obtained by MCR-ALS analysis are shown in Figure 105. On the basis of the previous XAS studies of the mechanism of Li/S and Mg/S systems,[195-235-236-237] their analysis is relatively straightforward, allowing a very clear description of the electrochemical mechanism.

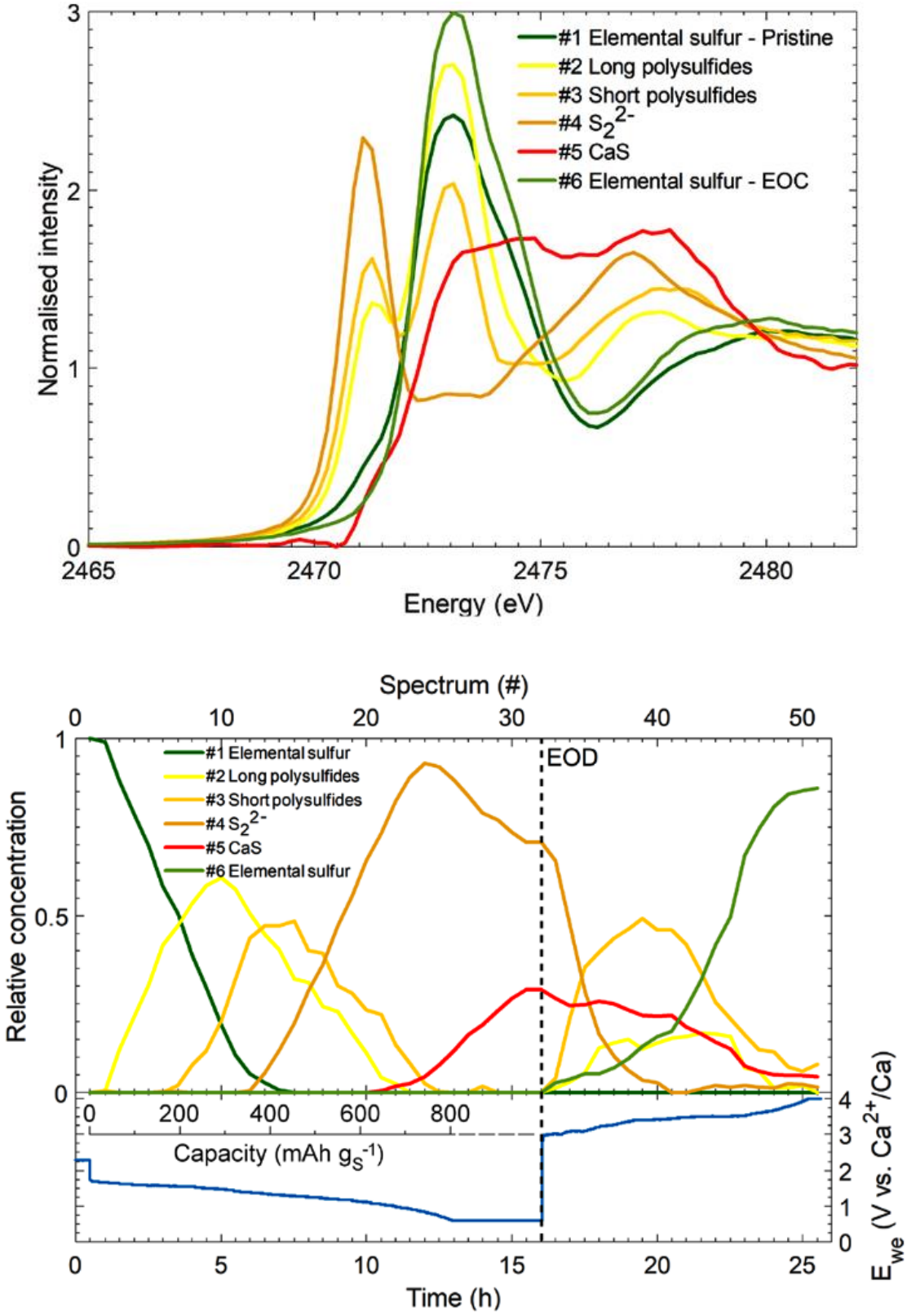

Figure 105: MCR-ALS components (top) and their relative contribution (bottom) to the operando S K-edge XANES spectra measured during a full discharge/charge cycle of a Ca/S battery. Electrochemical curve and the corresponding capacity in mAh g_S^{-1} are also reported.[205]

The first component (#1) shows a main peak at 2473 eV with a weak shoulder at 2474 eV, as usually observed for plain bulk sulfur (S_8), which indeed represents the pristine material (Figure 106). During the discharge, this component regularly decreases in intensity and is slowly replaced by two relatively similar components (#2 and #3) which do not show the shoulder at 2474 eV but present an additional feature at about 2471 eV. These two species represent calcium polysulfides, and the peaks at 2473 and 2471 eV are usually attributed to chain and terminal sulfur atoms of the polysulfide chain, respectively.[238–240] The ratio between the two signals increases with decreasing polysulfide chain length. For this reason, component #2 represents longer chain polysulfides than component #3. A very slight shift towards lower energies is also observed for the peak at 2471 eV with increasing polysulfide chain length. Thus, #2 must probably represents the first polysulfide formed after the opening of the S_8 cycle, *i.e.*, S_8^{2-}, while #3 corresponds to an intermediate composition or a mixture of different polysulfides between S_8^{2-} and S_2^{2-}. No additional feature is observed below 2471 eV, indicating that no significant amounts of radical polysulfides are formed in the studied Ca/S system.[241,242]

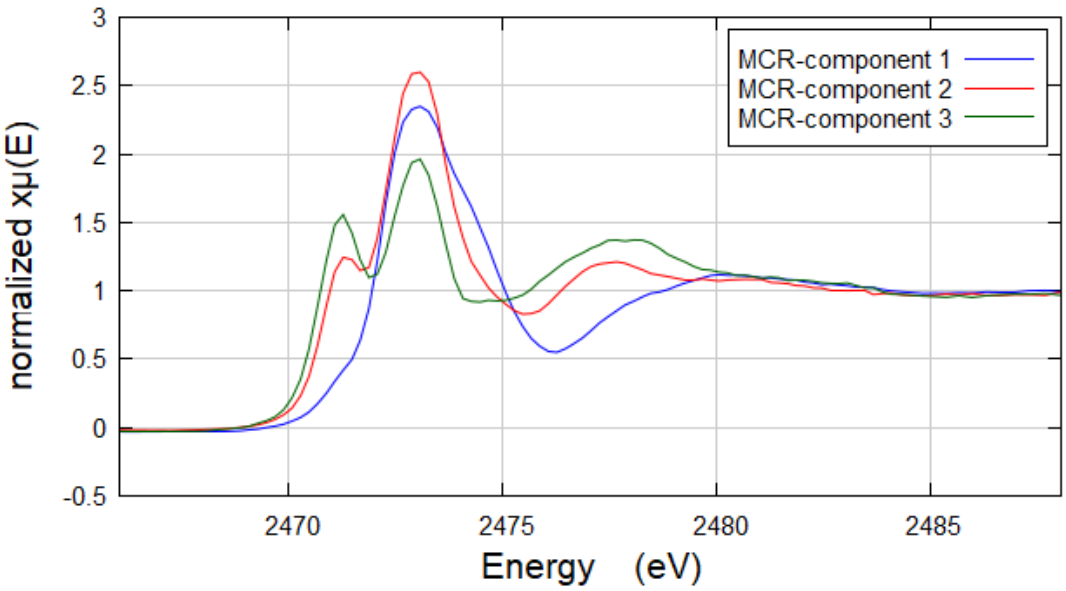

Figure 106: Comparison of the pure component MCR-ALS 2 and 3, representing polysulfides, with component MCR-ALS 1 representing elemental sulfur.[205]

The subsequent component #4 exhibits only a main feature at 2471 eV, while it has lost completely the signal at 2473 eV typical of sulfur in the polysulfide chains, indicating the formation of a polysulfide species containing only terminal sulfur atoms. This component can thus be attributed to the formation of sulfide anion S_2^{2-}, the shortest polysulfide. This component reaches its maximum intensity just before the precipitation of CaS, as expected.

It is interesting to notice that by performing appropriate linear combinations of #2, #3 and #4 it is possible to obtain the signature of all other possible polysulfide compositions between S_8^{2-} and S_2^{2-}, and that the observed trend clearly testifies the gradual formation of shorter and shorter polysulfides along the discharge.

The precipitation of CaS is testified by the appearance of component #5, which reaches its maximum intensity (about 25-30 % of the total sulfur) at the end of the discharge, and its attribution to CaS can be done by simply matching it with the spectrum of bulk CaS, which was also measured as a standard (Figure 107).

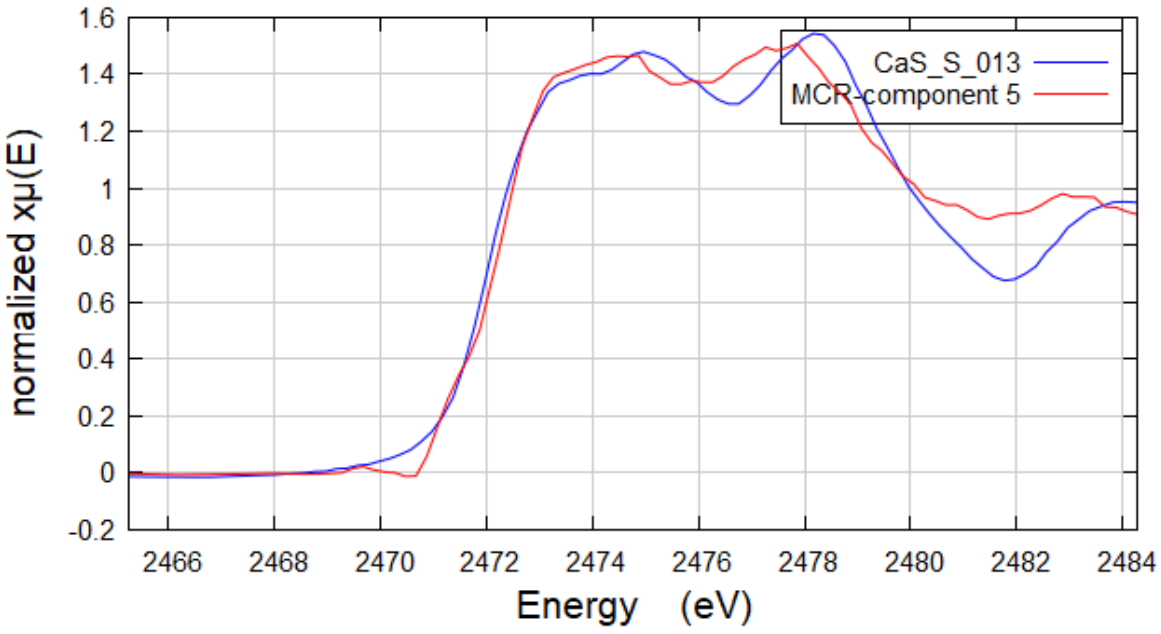

Figure 107: Comparison of the component #5 with the spectrum of bulk CaS.[205]

Interestingly, two different components representing elemental sulfur are found, *i.e.*, component #1 which represents sulfur in the pristine electrode and component #6 which testifies the reformation of elemental sulfur upon charge (Figure 108). It is interesting to notice that the main peak of the spectrum of elemental sulfur at 2473 eV in component #6 is more intense and thinner than that in component #1. This difference can be explained by the reduction of the amount of probed sulfur by XAS, which reduces the self-absorption and increases the definition of the XANES spectrum, and is not related to the precipitation of a different sulfur polymorph upon charge. This observation indicates a decrease of the amount of detected sulfur in the probed part of the sample, *i.e.*, in the back of the ACC/S electrode. The presence of a very weak shoulder at 2471 eV in component #1, might indicate that a very tiny amount of polysulfides are preset in the pristine sample, which might arise from a small short circuit or self-discharge of the cell during assembly and/or mounting on the beamline.

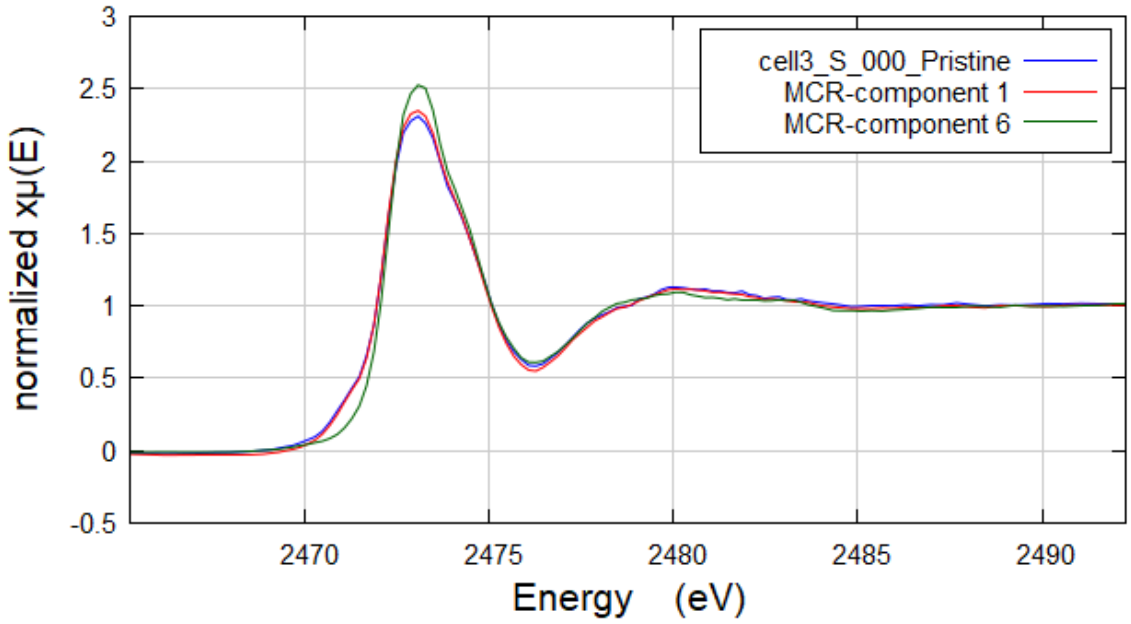

Figure 108: Comparison of the pure components #1 and #6 with pristine cell (sulfur).[205]

The decrease of the amount of sulfur probed by XAS between components #1 and #6 can be followed through the whole discharge and charge processes. In fact, the amount of sulfur in the

electrode part probed by XAS, i.e., its back side in contact with the Be window/current collector, can be evaluated by measuring the evolution of the integral of the K-Alfa lines of sulfur divided by the incident beam intensity in all measured spectra. As can be clearly seen in Figure 109, the amount of measured sulfur decreases with time during the discharge and the following charge, testifying the dissolution of the sulfur contained in the cathode and its slow diffusion in the electrolyte. This behavior is typical of this kind of cathode materials, where sulfur is not retained into a porous structure but is free to move in the electrolyte once transformed into solubilized polysulfide species.

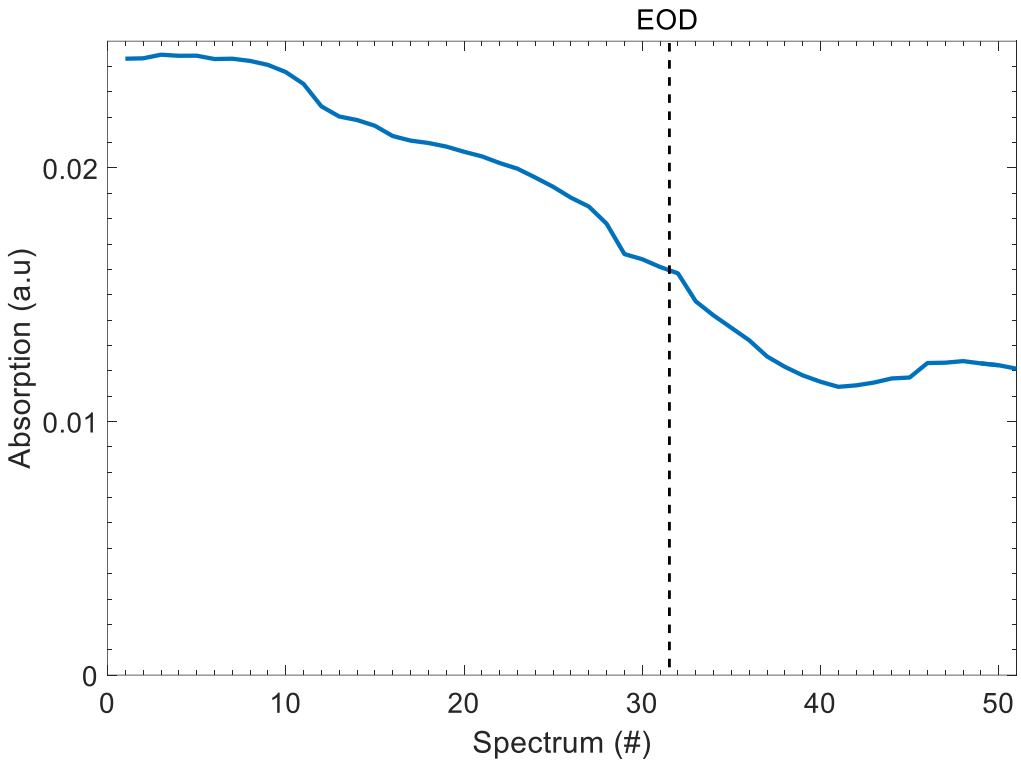

Figure 109: Evolution of the intensity of the total X-ray fluorescence emission of the probed region of the in situ cell (back of the electrode in contact with the Be window)[205].

The use of more sophisticated microporous carbon-based sulfur electrodes, or similar materials able to restrain the diffusion of polysulfides in the electrolyte and the consequent well-known polysulfide shuttle effect, will be necessary to produce a Ca/S viable cell.[243–245]

In spite of the very large polarization observed in the *in situ* experiment, one can try to correlate the different features of the electrochemical curve with the evolution of the sulfur species. Typically, in Li/S systems, the high voltage plateau is related to the equilibrium between sulfur and polysulfides, whereas the low voltage plateau is related to the equilibrium between polysulfides and solid Li_2S, the intermediate sloping region being governed by the equilibria between different polysulfide species.[246] In the case of the Ca/S system, during the *in situ* discharge (Figure 102), a discontinuity is observed after the reaction of ~0.24 mol of Ca per mole of S, which corresponds to a capacity of ~400 mA h g^{-1}. Such a capacity is not far from that measured at the end of the first plateau in coin cell. At this point of the discharge, the elemental sulfur content goes to 0 % (Figure 105 down, spectrum #13), thus comforting the idea that the first plateau corresponds well to the equilibrium between sulfur and polysulfides. CaS, on the other hand, appears only after the reaction of about 0.4 mol of Ca, corresponding to a capacity of 650 mA h g^{-1}, *i.e.*, towards the end of the second plateau (figure 104 down, spectrum #21). Even though these results are surprising, one should not forget that the XAS measurement is performed in the back of the electrode, and that some CaS might have formed before on a part of the electrode that is not probed. It is thus not unreasonable to transpose the same mechanism of Li/S and Mg/S systems to Ca/S batteries, with a similar "two plateaus" signature governed by the equilibria between polysulfides and the end-member solid phases, S and CaS.

To summarize the results, 6 components can be used to interpret the modification of the S K-edge spectra of the complete discharge/charge cycle:

- **Component #1 and #6** correspond to elemental sulfur.
- **Components #2 to #4** testify the gradual transformation of elemental sulfur in long and then short chain polysulfide along the discharge.

- **Component #5** indicates the (incomplete) formation of CaS at EOD.
- During the following charge, CaS is slowly transformed into the soluble polysulfides (**component #4**) which grow in length **(components #3 and #2**), and then precipitate as elemental sulfur (**component #6)** at EOD. The amount of sulfur detected by fluorescence decreases gradually during the discharge and following reactions, and only about half of the sulfur contained in the pristine electrode is detected at EOC.

By combining the results of both XPS and S K-edge XAS, it must be first noticed that the mechanism in Ca/S batteries strongly resembles that previously observed in Li/S and Mg/S systems: sulfur is gradually transformed into polysulfides in shorter and shorter chain lengths along the discharge, and finally precipitated as CaS at EOD. A total of about 25-30% of CaS is detected by S K-edge XAS at EOD under the in situ conditions (high polarisation, intrinsically dependent upon the in situ cell setup). The amount of sulfur in the back of the electrode decrease gradually during cycling, due to the formation of soluble polysulfide species. During charge, the reverse is observed, with the transformation of CaS in polysulfides and then in elemental sulfur EOD; no polysulfides are left at EOD and only pure sulfur is detected.

3.2.2. *in situ* and *ex situ* Ca K-edge XANES data analysis

Additional insight can be derived from the analysis of the Ca K-edge XANES spectra measured on the *in situ* cell in its pristine state, at the EOD and at EOC, together with those of selected references including bulk CaS, the pure electrolyte salt $Ca[B(hfip)_4]_2$ and $CaCO_3$, as a tentative representative decomposition product of the electrolyte. The results of the fits, performed using

the linear combination fitting (LCF) tool available in Athena[247], are shown in Figure 110 and the corresponding fit parameters are shown in Table 9.

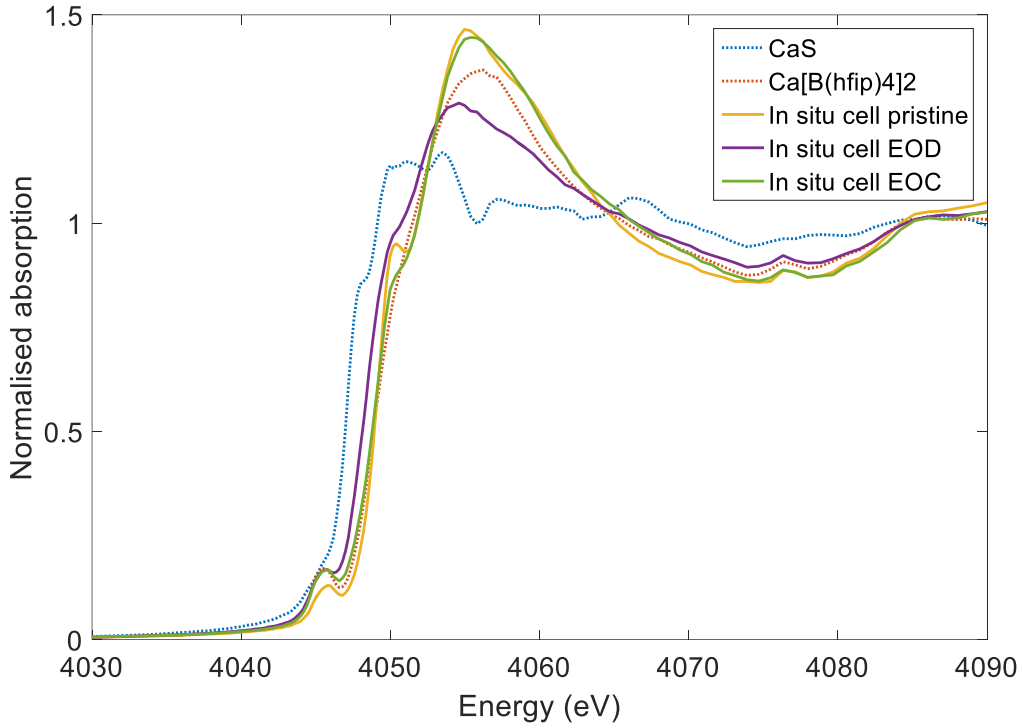

Figure 110: Ca K-edge XANES spectra of the in situ cell measured in the pristine state, at EOD and at EOC compared to selected reference compounds..[205]

The spectrum of the *in situ* Ca/S cell in the pristine state is quite similar to that of the bulk electrolyte salt, and in particular have the same edge position. Differences in the edge shape might come from the different configuration of calcium ions once the salt is dissolved in DME. The spectrum at EOD, however, is shifted towards lower energies, in agreement with the formation of CaS. At end of charge (EOC), the spectrum becomes very similar to that of the pristine state, indicating the disappearance of CaS. In order to quantify the amount of CaS in the measured spectrum, and to evaluate the possible presence of decomposition products, a linear combination fit (LCF) was performed using the LCF tool available in Athena[248] using some available reference compounds, namely CaS, the $Ca[B(hfip)_4]_2$ salt and $CaCO_3$ which was chosen among the available compounds to represent a possible Ca-containing

decomposition product of the electrolyte species formed in the cell during cycling. The XANES spectrum of $CaCO_3$, in fact, is very similar to that of $CaSO_4$, already detected by XPS. The results of the LCF fit are summarized in Table 9.

Sample	References			Goodness of fit (R-factor)
	$Ca[B(hfip)_4]_2$	CaS	$CaCO_3$	
Pristine	99 %	0 %	1 %	0.0076
EOD	67 %	29 %	4 %	0.0010
EOC	98 %	0 %	3 %	0.0038

Table 9: Results of the linear combination fit of the Ca K-edge XANES spectra of the in situ cell (calculated errors are below ±3 %).[205]

The spectra of the pristine cell and at EOC are very similar among them (Figure 111) and can be compared to those of the electrolyte and of a $CaCO_3$ reference:

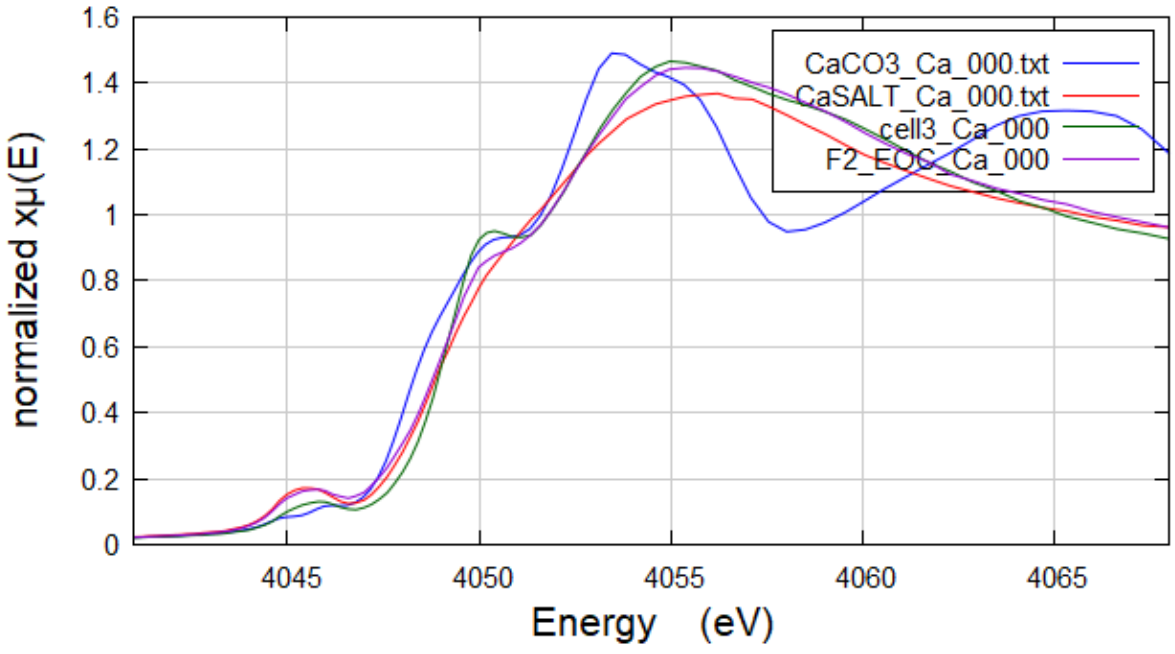

Figure 111: Ca K-edge XANES spectra of the in situ cell measured in the pristine state, EOC state, $CaCO_3$ and Ca salt compared to selected reference compounds.[205]

The main signal of the spectra corresponds well to that of the Ca electrolyte, with a shoulder at 4050 eV which resembles to that of $CaCO_3$, and which might come from a decomposition product of the reaction of the salt in the electrolyte. A linear combination fit of the spectra with those of the electrolyte salt and $CaCO_3$ confirms that both pristine and EOC spectra are practically identical to that of the electrolyte (cf. Table 9)

The spectrum at EOD, is shifted to lower energies compared to those of the pristine sample and of EOC, and can be rather compared with those of the electrolyte and that of CaS (Figure 112). The results of the LCF, shown in Table 9, indicate that about 29±3 % of the calcium in the spectrum at EOD is indeed CaS, and that the subtle evolution of the spectrum at EOD might indeed come from an evolution of the Ca species in the electrolyte, with the possible formation of decomposition products.

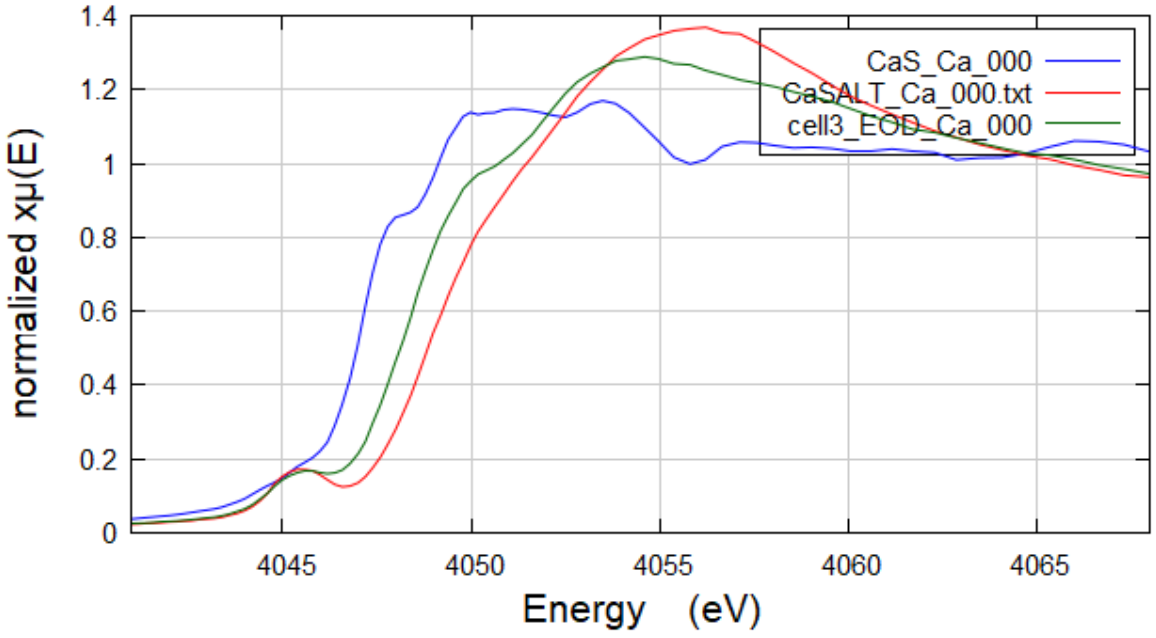

Figure 112: Ca K-edge XANES spectra of the in situ cell measured in the EOD state compared to selected reference compounds CaS and Ca salt.[205]

Based on data obtained by XPS and XAS spectroscopy, we are able to picture the entire mechanism of the redox process occurring into the Ca/S battery. The reduction of elemental sulfur to insoluble CaS, during discharge, passes through the formation of intermediate polysulfides, as resumed in Figure 113:

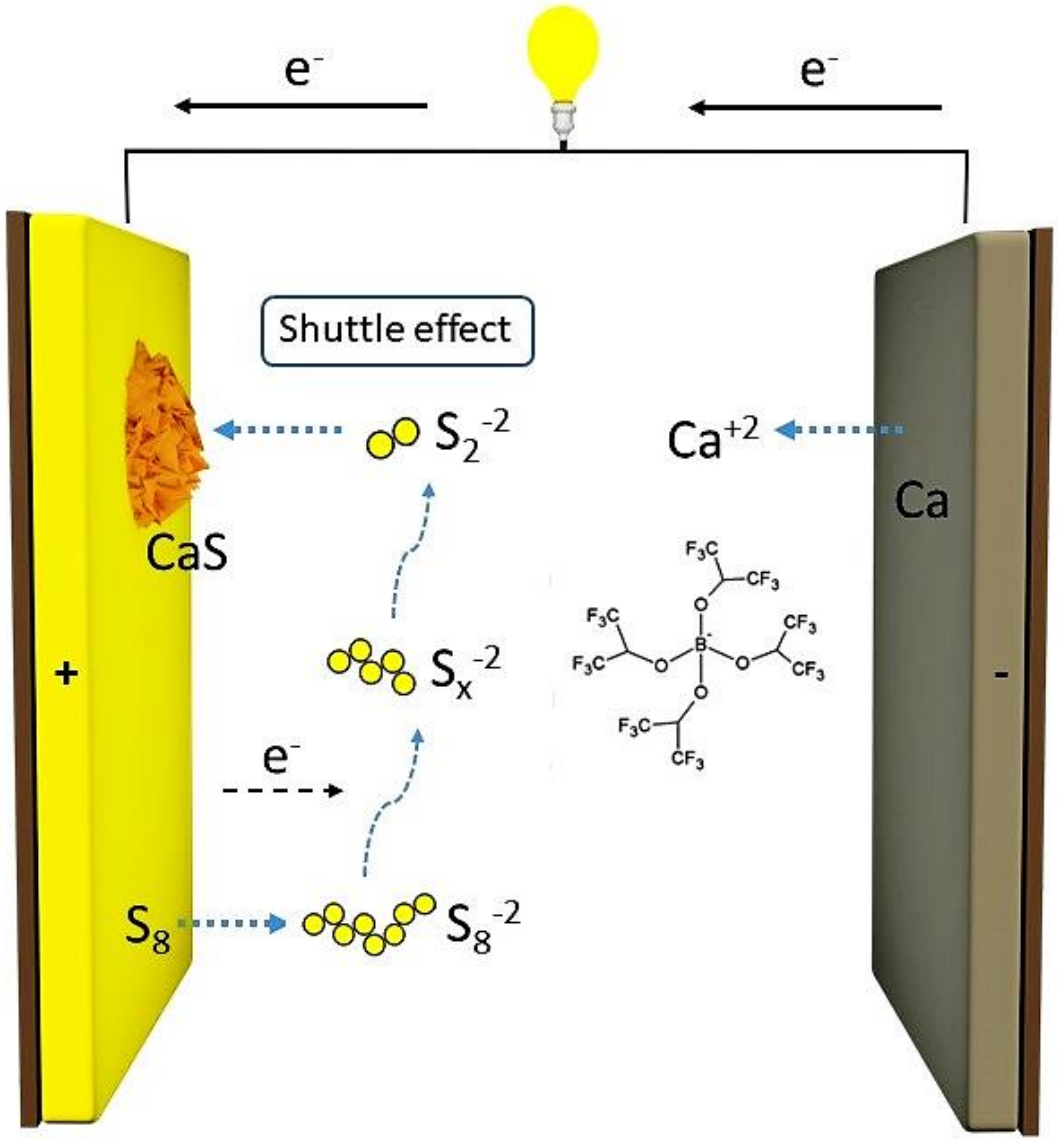

Figure 113: *Illustration of the discharge process occurring in the Ca/S cell.*[205]

The expected pathway of reduction and oxidation of elemental sulfur to insoluble CaS, passing by formation of intermediate soluble polysulfides species, can be resumed in Figure 114. The entire discharge/charge process proposed is the same occurring in Li/S and Mg/S systems.

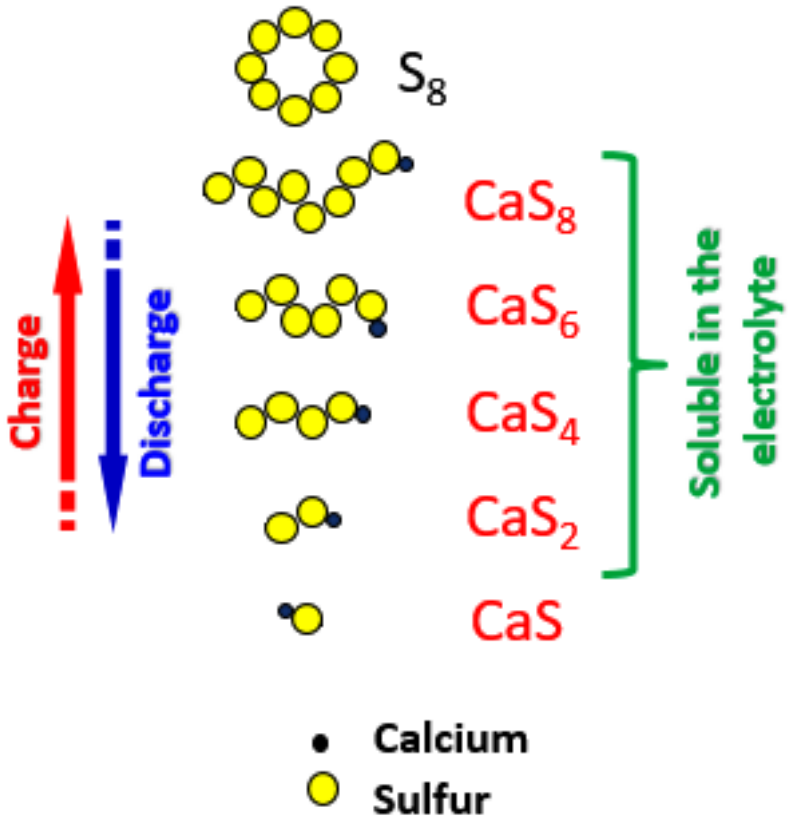

Figure 114: *A schematic illustration of the shuttle mechanism occurring in the Ca/S cell.*[205]

4. Conclusions

In this chapter, we have proven the compatibility of $Ca[B(hfip)_4]_2$-based electrolyte with sulfur based cathodes, using a ACC/S positive electrode, demonstrating an innovative proof-of-concept rechargeable Ca/S battery at room temperature. The electrochemical systems cycled with a current density between C/10 and C/20 possess the right ratio between the capacity delivered and capacity retention. C/50 current density systems are characterized by higher specific capacity delivered during discharge during first cycles, since the slowly kinetic of conversion of elemental sulfur to polysulfides based species and further formation of CaS promotes the better consumption of sulfur. On other hand, shuttle effect phenomena results more pronounced, by higher resting-time of cell, so the capacity fade is more pronounced than C/10 and C/20 systems. A faster current density as C/10 limits the system to lower capacity, since the faster kinetic of conversion of sulfur to final CaS is not suitable for the intermediates polysulfides species formation.

We clearly evidenced that the choice of calcium anode is crucial for the electrochemical performances. By using Ca foil, the spikes intensity during cycling is reduced, as well as the electrochemical performance is increased, since the regular surface of Ca foil compared to Ca shot ensures a better and more homogeneous interphase formation between anode and electrolyte, allowing an enhanced Ca ions mobility.

The detailed investigation of the electrochemical mechanism carried out by XAS and XPS shows that the reversible conversion of sulfur into polysulfide species and finally to CaS proceeds through the two well-defined plateaus, with the majority of the sulfur converted into CaS at the end of the first discharge. These reduced sulfur species are then gradually converted back to elemental sulfur during the following charge process, which proceeds through a single

plateau followed by a sloping region. Moreover, additional information provided by XPS reveals the deposition of a calcium-boron (probably oxide) decomposition product at the surface, which may play a role in the stability of the electrode/electrolyte interface.

As in Li/S systems, sulfur is gradually transformed into polysulfides in shorter and shorter chain lengths along the discharge, and finally precipitated as CaS at EOD. A total of about 30% of CaS is detected by S K-edge XAS at EOD under the in situ conditions (high polarisation, intrinsically dependent upon the in situ cell setup). The formation of CaS at EOD is confirmed also by in situ Ca K-edge XAS. The amount of sulfur in the back of the electrode decrease gradually during cycling, due to the formation of soluble polysulfide species.

During charge, the reverse is observed, with the transformation of CaS in polysulfides and then in elemental sulfur at EOC. No polysulfides are left at EOC, only pure sulfur is detected.

In spite of these promising results, the observed capacity fading of our Ca/S system is still very pronounced. The use of more sophisticated microporous carbon-based sulfur electrodes to restrain the diffusion of polysulfides in the electrolyte, will be necessary to produce a Ca/S viable cell. Another factors for low cycling stability are stability of the calcium metal/electrolyte interface (passivation), but might also be connected to specific issues of metal-sulfur systems, such as the physical-chemical properties (*e.g.*, solubility) of calcium polysulfides, to the ability of polysulfides anions to coordinate reversibly divalent cations, as well as to the possible difficult activation of sulfur and of the discharge products during cycling. A better understanding of such mechanisms is therefore necessary if one wants to move this battery system closer to commercialization. In spite of these negative notes, it must be underlined that the results shown here confirm that it is possible to activate sulfur cathodes in

pure-calcium batteries. Such results, even though very preliminary, are thus promising if one considers the potential application of an efficient Ca/S battery.

5. Perspectives

To further improve the performances of our Ca/S system, we have to focus in efforts in cathode and cell design as well as optimization of the electrolyte solvent or solvent blend to restrain the dissolution of polysulfide based species.

The formation of the passivation layer after few cycles plays a crucial role in the cycling life of the battery. The investigation of physical-chemical properties of electrolyte formulation can lead us to the improvement of batteries performance by elucidaning the degree of decomposition of salt(s) and solvent(s). Although the study of the formation of passivation layer in Ca systems has been started only sice few years, by XPS and XAS approaches, we are able to indentify some oxidation Ca-based byproducts on electrode surface, after cycling.The O 1s and C 1s XPS spectra reveals the formation of CO and COO based species on cathode surface after the first discharge. Moreover, the intentification of $CaCO_3$ by XAS approach might make guess at decomposition reaction of the salt in the electrolyte. All these species have been identified on cathode surface and we can only hypothesize that they can have an important role on the interface between the Ca metal anode and the electrolyte. In the paper of Ponrouch et al.[100] in 2020, experimental and computational studies have been employed to indentify the passivation layer composition of two different systems: $Ca(TFSI)_2$ and $Ca(BF_4)_2$ in a mixture of EC:PC solvents. While borate-based species and CaF_2 can acts as SEI, the formation of $CaCO_3$ and oxygenated Ca compounds can play as Ca^{2+} blocking passivation layer. As we have

discussed before, the Ellingham diagram[62] justifies the high reactivity of Ca towards oxygenated species (in this case, salt and/or solvent), allowing the formation of thermodynamically stable Ca oxides. A possible strategy was developed by Ponrocuh et al.[95] in 2021; the addition of borontrifluoride diethyletherate to $Ca(TFSI)_2$/EC:PC electrolyte allows for Ca plating and stripping, confirming the borate-based SEI compounds as protective species for the electrode-electrolyte interface and preventing the decomposition of the components of the electrolyte solution.

Electrochemical impedance spectroscopy (EIS) tool will give us important information about the electrochemical behavior of Ca/S batteries, by monitoring the evolution of impedance during the cycling process, so to investigate the capacity fading mechanism of the cells. As well studied for Li/S[249] and Mg/S[250] batteries, the charge-transfer resistance parameter R_{ct} plays a crucial role in the capacity fading of the Li/S cell. It reflects the charge-transfer process at the interface between the conductive agent and the electrolyte. The increase of R_{ct}, recorded as the middle frequency semicircle, may be closely related to the cumulative agglomerates, which decrease the electrically conductive area on the cathode surface and hinder the transportation of ions toward the inside of the cathode. It results in slow transfer reaction kinetic and capacity fading.[251]

Known from Li/S and Mg/S batteries, the design of the carbon-sulfur positive electrode plays a fundamental role in the voltage profile and in the performance of the cell. The ACC/S cathode proposed in this work is not adapted for obtaining the best cycling performance, as required for further practical applications. In fact, in such a simple system the sulfur is not expected to be retained at the cathode side, especially when soluble polysulfide intermediates are formed, allowed a significant fraction of active material lost in electrolyte bulk by dissolution.[195] Moreover, in this type of positive electrode, the sulfur content is relatively low (around 10

wt.%), and such a low value is not adapted to practical applications. Several preliminary tests have been performed with other microporous carbon hosts, allowing practical sulfur loadings of the order of 50 %. Nevertheless, the cycling performances were not satisfying, resulting in the activation of only a very small fraction of the total sulfur. The compatibility of our fluorinated alkoxyborate Ca based salt could be tested with a new type of graphene based sulfur composite cathode, as just developed by Fichtner for Mg/S batteries.[252] The reduced graphene oxide/sulfur nanocomposite material can be prepared by a combination of thermal and chemical precipitation methods. The system gives improved electrochemical performances compared to Mg/S systems with conventional sulfur based cathodes (composite and ACC), resulting in a discharge capacity of 236 $mA{\cdot}h{\cdot}g^{-1}$ after 50 cycles. Better cycling stability was explained by oxygen functional groups on graphene surface, which enable an uniform dispersion and higher surface area of sulfur on electrode. Additionally, it acts as a buffer layer to accommodate the volume changes upon electrochemical cycling between sulfur and MgS.

One of their major technical issues of our Ca/S system is shuttling of soluble polysulfides between electrodes, as we reported during the self-discharge analysis and galvanostatic tests, resulting in rapid capacity fading of electrochemical system. Metal–organic framework (MOF) can be tested as separator to mitigate the shuttling effect issues. In the work of Zhou et coworkers[253] is reported that the MOF-based separator acts as an ionic sieve in Li/S batteries, which selectively sieves Li^+ ions, while efficiently suppressing polysulfides migration to the anode side. They used cathodes with 70 % sulfur loading and the cell exhibited a low capacity decay rate over 1500 cycles. The potential for MOF-based materials as separator can be applied also for Ca/S batteries, since Ca-based MOF can be easily prepared starting by inexpensive precursors, as $CaCO_3$.

Another strategy to improve the electrochemical performances of our Ca/S cells can be the develop of an artificial SEI between the Ca anode and separator that reduces side reactions on the metal surface with polysulfides species. In the work of Dominko et al.[254], nano-fibrillated cellulose was used for fabrication of porous separator membranes. These separators are characterized by tunable thickness and porosity, biodegradability, good mechanical properties and chemical durability. They hinder the formation of high surface area lithium and reduces the degradation of lithium metal anode. This innovative approach can be translated even for Ca/S batteries.

V. References

(1) Brown, R. J. C.; Milton, M. J. T. Analytical Techniques for Trace Element Analysis: An Overview. *TrAC Trends Anal. Chem.* **2005**, *24* (3), 266–274. https://doi.org/10.1016/j.trac.2004.11.010.

(2) https://ourworldindata.org/energy.

(3) https://www.bp.com/en/global/corporate/energy-economics/statistical-review-of-world-energy/chief-economist-analysis.html.html#analysis-carbon-emissions.

(4) https://www.Batteries.included.how.better.storage.can.transform.renewable.energy.

(5) https://www.thebalancesmb.com/importance-of-battery-storage-for-sustainable-energy-.

(6) https://www.activesustainability.com/climate-change/link-between-climate-change-air-pollution/.

(7) https://www.climatecentral.org/news/climate-central-solutions-brief-battery-energy-storage.

(8) Mansour, D.-E. A. Energy Storage Technologies in MVDC Microgrids. In *Medium Voltage Direct Current Grid*; Elsevier, 2019; pp 189–207. https://doi.org/10.1016/B978-0-12-814560-9.00010-0.

(9) https://about.bnef.com/blog/behind-scenes-take-lithium-ion-battery-prices/.

(10) Https://Energysystemsnetwork.Com/Projects/Energy-Storage-Roadmap-Report. **2017**.

(11) Edström, K.; Dominko, R.; Fichtner, M.; Otuszewski, T.; Perraud, S.; Punckt, C.; Tarascon, J.; Vegge, T.; Martin, W. BATTERY 2030+. Inventing the Sustainable Batteries of the Future. Research Needs and Future Actions. *Book* **2020**, 83.

(12) *Lithium-Ion Batteries*; Kato, Y., Ogumi, Z., Martín, J. M. P., Eds.; Jenny Stanford Publishing, 2019. https://doi.org/10.1201/9780429259340.

(13) https://www.infineon.com/cms/en/discoveries/renewable-energies/.

(14) Van Noorden, R. The Rechargeable Revolution: A Better Battery. *Nature* **2014**, *507* (7490), 26–28. https://doi.org/10.1038/507026a.

(15) Sarma, D. D.; Shukla, A. K. Building Better Batteries: A Travel Back in Time. *ACS Energy Lett.* **2018**, *3* (11), 2841–2845. https://doi.org/10.1021/acsenergylett.8b01966.

(16) Heilig, M. L. United States Patent Office. *ACM SIGGRAPH Comput. Graph.* **1994**, *28* (2), 131–134. https://doi.org/10.1145/178951.178972.

(17) Tang, X.; Zou, C.; Wik, T.; Yao, K.; Xia, Y.; Wang, Y.; Yang, D.; Gao, F. Run-to-Run Control for Active Balancing of Lithium Iron Phosphate Battery Packs. *IEEE Trans. Power Electron.* **2020**, *35* (2), 1499–1512. https://doi.org/10.1109/TPEL.2019.2919709.

(18) Cho, S.; Chiu, T.-M.; Castaneda, H. Electrical and Electrochemical Behavior of a Zinc-Rich Epoxy Coating System with Carbon Nanotubes as a Diode-like Material. *Electrochim. Acta* **2019**, *316*, 189–201. https://doi.org/10.1016/j.electacta.2019.05.116.

(19) Yazami, R.; Touzain, P. A Reversible Graphite-Lithium Negative Electrode for

Electrochemical Generators. *J. Power Sources* **1983**, *9* (3), 365–371. https://doi.org/10.1016/0378-7753(83)87040-2.

(20) Wang, Q.; Ping, P.; Zhao, X.; Chu, G.; Sun, J.; Chen, C. Thermal Runaway Caused Fire and Explosion of Lithium Ion Battery. *J. Power Sources* **2012**, *208*, 210–224. https://doi.org/10.1016/j.jpowsour.2012.02.038.

(21) Fujita, T.; Toda, K. Microdisplacement Measurement Using a Liquid-Delay-Line Oscillator. *Jpn. J. Appl. Phys.* **2003**, *42* (Part 1, No. 9B), 6131–6134. https://doi.org/10.1143/JJAP.42.6131.

(22) Dunn, B.; Kamath, H.; Tarascon, J.-M. Electrical Energy Storage for the Grid: A Battery of Choices. *Science (80-.).* **2011**, *334* (6058), 928–935. https://doi.org/10.1126/science.1212741.

(23) https://www.cars.com/electric-cars/.

(24) https://www.greentechmedia.com/articles/read/tesla-battery-day-cost-reduction-three-years.

(25) https://greentransportation.info/ev-ownership/safer/tesla-model-s-2013.html.

(26) https://www.androidauthority.com/lithium-industry-overview-651670/.

(27) Martin, G.; Rentsch, L.; Höck, M.; Bertau, M. Lithium Market Research – Global Supply, Future Demand and Price Development. *Energy Storage Mater.* **2017**, *6* (November 2016), 171–179. https://doi.org/10.1016/j.ensm.2016.11.004.

(28) Http://Ugspace.Ug.Edu.Gh/Handle/123456789/31184. **2016**, No. 10507195.

(29) https://www.theverge.com/2020/9/22/21450916/tesla-battery-pack-elon-musk-price-kilowatt-hour-ev-cost-tabless.

(30) https://seekingalpha.com/article/4289626-look-top-5-lithium-ion-battery-manufacturers-in-2019.

(31) https://www.androidauthority.com/lithium-ion-batteries-overheating-605704/.

(32) Feng, X.; Ouyang, M.; Liu, X.; Lu, L.; Xia, Y.; He, X. Thermal Runaway Mechanism of Lithium Ion Battery for Electric Vehicles: A Review. *Energy Storage Mater.* **2018**, *10* (May 2017), 246–267. https://doi.org/10.1016/j.ensm.2017.05.013.

(33) https://www.msesupplies.com/blogs/news/source-of-detrimental-dendrite-growth-in-lithium-batteries-discovered https://www.msesupplies.com/blogs/news/source-of-detrimental-dendrite-growth-in-lithium-batteries-discovered.

(34) https://www6.slac.stanford.edu/news/2015-06-17-study-finds-way-prevent-fires-next-generation-lithium-batteries.aspx.

(35) Liu, X.; Ren, D.; Hsu, H.; Feng, X.; Xu, G.-L.; Zhuang, M.; Gao, H.; Lu, L.; Han, X.; Chu, Z.; Li, J.; He, X.; Amine, K.; Ouyang, M. Thermal Runaway of Lithium-Ion Batteries without Internal Short Circuit. *Joule* **2018**, *2* (10), 2047–2064. https://doi.org/10.1016/j.joule.2018.06.015.

(36) Wang, S.; Rafiz, K.; Liu, J.; Jin, Y.; Lin, J. Y. S. Effects of Lithium Dendrites on Thermal Runaway and Gassing of LiFePO 4 Batteries. *Sustain. Energy Fuels* **2020**, *4* (5), 2342–2351. https://doi.org/10.1039/D0SE00027B.

(37) Swiderska-Mocek, A.; Rudnicka, E. Lithium–Sulphur Battery with Activated Carbon Cloth-Sulphur Cathode and Ionic Liquid as Electrolyte. *J. Power Sources* **2015**, *273*, 162–167. https://doi.org/10.1016/j.jpowsour.2014.09.020.

(38) Peng, Z.; Freunberger, S. A.; Chen, Y.; Bruce, P. G. A Reversible and Higher-Rate Li-O2 Battery. *Science (80-.).* **2012**, *337* (6094), 563–566. https://doi.org/10.1126/science.1223985.

(39) Muldoon, J.; Bucur, C. B.; Gregory, T. Quest for Nonaqueous Multivalent Secondary Batteries: Magnesium and Beyond. *Chem. Rev.* **2014**, *114* (23), 11683–11720. https://doi.org/10.1021/cr500049y.

(40) Monti, D.; Ponrouch, A.; Araujo, R. B.; Barde, F.; Johansson, P.; Palacín, M. R. Multivalent Batteries—Prospects for High Energy Density: Ca Batteries. *Front. Chem.* **2019**, *7* (FEB), 1–6. https://doi.org/10.3389/fchem.2019.00079.

(41) Bitenc, J.; Ponrouch, A.; Dominko, R.; Johansson, P.; Palacin, M. R. Multivalent Charge Carriers. In *Encyclopedia of Electrochemistry*; Bard, A. J., Ed.; Wiley, 2020; p 110020. https://doi.org/10.1002/9783527610426.bard110020.

(42) Jäckle, M.; Groß, A. Microscopic Properties of Lithium, Sodium, and Magnesium Battery Anode Materials Related to Possible Dendrite Growth. *J. Chem. Phys.* **2014**, *141* (17), 174710. https://doi.org/10.1063/1.4901055.

(43) Jäckle, M.; Helmbrecht, K.; Smits, M.; Stottmeister, D.; Groß, A. Self-Diffusion Barriers: Possible Descriptors for Dendrite Growth in Batteries? *Energy Environ. Sci.* **2018**, *11* (12), 3400–3407. https://doi.org/10.1039/C8EE01448E.

(44) Davidson, R.; Verma, A.; Santos, D.; Hao, F.; Fincher, C.; Xiang, S.; Van Buskirk, J.; Xie, K.; Pharr, M.; Mukherjee, P. P.; Banerjee, S. Formation of Magnesium Dendrites during Electrodeposition. *ACS Energy Lett.* **2019**, *4* (2), 375–376. https://doi.org/10.1021/acsenergylett.8b02470.

(45) Pu, S. D.; Gong, C.; Gao, X.; Ning, Z.; Yang, S.; Marie, J.-J.; Liu, B.; House, R. A.; Hartley, G. O.; Luo, J.; Bruce, P. G.; Robertson, A. W. Current-Density-Dependent Electroplating in Ca Electrolytes: From Globules to Dendrites. *ACS Energy Lett.* **2020**, *5* (7), 2283–2290. https://doi.org/10.1021/acsenergylett.0c01153.

(46) Tchitchekova, D. S.; Monti, D.; Johansson, P.; Bardé, F.; Randon-Vitanova, A.; Palacín, M. R.; Ponrouch, A. On the Reliability of Half-Cell Tests for Monovalent (Li + , Na +) and Divalent (Mg 2+ , Ca 2+) Cation Based Batteries. *J. Electrochem. Soc.* **2017**, *164* (7), A1384–A1392. https://doi.org/10.1149/2.0411707jes.

(47) Saha, P.; Datta, M. K.; Velikokhatnyi, O. I.; Manivannan, A.; Alman, D.; Kumta, P. N. Rechargeable Magnesium Battery: Current Status and Key Challenges for the Future. *Prog. Mater. Sci.* **2014**, *66*, 1–86. https://doi.org/10.1016/j.pmatsci.2014.04.001.

(48) Shterenberg, I.; Salama, M.; Gofer, Y.; Levi, E.; Aurbach, D. The Challenge of Developing Rechargeable Magnesium Batteries. *MRS Bull.* **2014**, *39* (05), 453–460. https://doi.org/10.1557/mrs.2014.61.

(49) Ashby, E. C.; Yu, S. H.; Beach, R. G. The Preparation of Alkylmagnesium Fluroindes. *J. Am. Chem. Soc.* **1970**, *92* (2), 433–435. https://doi.org/10.1021/ja00705a634.

(50) Vestfried, Y.; Chusid, O.; Goffer, Y.; Aped, P.; Aurbach, D. Structural Analysis of Electrolyte Solutions Comprising Magnesium−Aluminate Chloro−Organic Complexes by Raman Spectroscopy. *Organometallics* **2007**, *26* (13), 3130–3137. https://doi.org/10.1021/om061076s.

(51) Kim, H. S.; Arthur, T. S.; Allred, G. D.; Zajicek, J.; Newman, J. G.; Rodnyansky, A. E.; Oliver, A. G.; Boggess, W. C.; Muldoon, J. Structure and Compatibility of a Magnesium Electrolyte with a Sulphur Cathode. *Nat. Commun.* **2011**, *2* (1), 427.

https://doi.org/10.1038/ncomms1435.

(52) Liebenow, C.; Yang, Z.; Lobitz, P. The Electrodeposition of Magnesium Using Solutions of Organomagnesium Halides, Amidomagnesium Halides and Magnesium Organoborates. *Electrochem. commun.* **2000**, *2* (9), 641–645. https://doi.org/10.1016/S1388-2481(00)00094-1.

(53) Zhao-Karger, Z.; Zhao, X.; Fuhr, O.; Fichtner, M. Bisamide Based Non-Nucleophilic Electrolytes for Rechargeable Magnesium Batteries. *RSC Adv.* **2013**, *3* (37), 16330. https://doi.org/10.1039/c3ra43206h.

(54) Chen, Z.; Liu, T.; Zhao, Z.; Zhang, Z.; Han, X.; Han, P.; Li, J.; Wang, J.; Li, J.; Huang, S.; Zhou, X.; Zhao, J.; Cui, G. Fast Anion Intercalation into Graphite Cathode Enabling High-Rate Rechargeable Zinc Batteries. *J. Power Sources* **2020**, *457* (November 2019), 227994. https://doi.org/10.1016/j.jpowsour.2020.227994.

(55) Heckmann, A.; Meister, P.; Kuo, L.-Y.; Winter, M.; Kaghazchi, P.; Placke, T. A Route towards Understanding the Kinetic Processes of Bis(Trifluoromethanesulfonyl) Imide Anion Intercalation into Graphite for Dual-Ion Batteries. *Electrochim. Acta* **2018**, *284*, 669–680. https://doi.org/10.1016/j.electacta.2018.07.181.

(56) Das, S. K.; Mahapatra, S.; Lahan, H. Aluminium-Ion Batteries: Developments and Challenges. *J. Mater. Chem. A* **2017**, *5* (14), 6347–6367. https://doi.org/10.1039/C7TA00228A.

(57) Møller, K. T.; Sargent, A.-L.; Remhof, A.; Heere, M. Beyond Hydrogen Storage—Metal Hydrides as Multifunctional Materials for Energy Storage and Conversion. *Inorganics* **2020**, *8* (11), 58. https://doi.org/10.3390/inorganics8110058.

(58) Li, Q.; Bjerrum, N. J. Aluminum as Anode for Energy Storage and Conversion: A Review. *J. Power Sources* **2002**, *110* (1), 1–10. https://doi.org/10.1016/S0378-7753(01)01014-X.

(59) Yang, K.; Zhao, Z.; Xin, X.; Tian, Z.; Peng, K.; Lai, Y. Graphitic Carbon Materials Extracted from Spent Carbon Cathode of Aluminium Reduction Cell as Anodes for Lithium Ion Batteries: Converting the Hazardous Wastes into Value-Added Materials. *J. Taiwan Inst. Chem. Eng.* **2019**, *104*, 201–209. https://doi.org/10.1016/j.jtice.2019.09.012.

(60) https://chemistrygod.com/the-most-abundant-elements.

(61) Arroyo-De-Dompablo, M. E.; Ponrouch, A.; Johansson, P.; Palacín, M. R. Achievements, Challenges, and Prospects of Calcium Batteries. *Chem. Rev.* **2019**, acs.chemrev.9b00339. https://doi.org/10.1021/acs.chemrev.9b00339.

(62) https://www.doitpoms.ac.uk/tlplib/recycling-metals/ellingham.php.

(63) Thomas, U. B.; Forster, F. T.; Haring, H. E. Corrosion and Growth of Lead-Calcium Alloy Storage Battery Grids as a Function of Calcium Content. *Trans. Electrochem. Soc.* **1947**, *92* (1), 313. https://doi.org/10.1149/1.3071822.

(64) Salkind, A. J.; Singh, P.; Cannone, A.; Atwater, T.; Wang, X.; Reisner, D. Impedance Modeling of Intermediate Size Lead–Acid Batteries. *J. Power Sources* **2003**, *116* (1–2), 174–184. https://doi.org/10.1016/S0378-7753(02)00690-0.

(65) Nissen, D. A. A Study of the Anode-Electrolyte Interface in a Thermal Battery. *J. Electrochem. Soc.* **1979**, *126* (2), 176. https://doi.org/10.1149/1.2129001.

(66) Arroyo-de Dompablo, M. E.; Ponrouch, A.; Johansson, P.; Palacín, M. R. Achievements, Challenges, and Prospects of Calcium Batteries. *Chem. Rev.* **2020**, *120*

(14), 6331–6357. https://doi.org/10.1021/acs.chemrev.9b00339.

(67) Pujare, N. U. A Calcium Oxygen Secondary Battery. *J. Electrochem. Soc.* **1988**, *135* (1), 260. https://doi.org/10.1149/1.2095574.

(68) Peled, E. Calcium Thionyl Chloride High-Rate Reserve Cell. *J. Electrochem. Soc.* **1981**, *128* (9), 1936. https://doi.org/10.1149/1.2127768.

(69) Aurbach, D.; Skaletsky, R.; Gofer, Y. The Electrochemical Behavior of Calcium Electrodes in a Few Organic Electrolytes. *J. Electrochem. Soc.* **1991**, *138* (12), 3536–3545. https://doi.org/10.1149/1.2085455.

(70) Haring, H. . E.; Thomas, U. B. The Electrochemical Behavior of Lead, Lead-Antimony and Lead-Calcium Alloys in Storage Cells. *Trans. Electrochem. Soc.* **1935**, *68* (1), 293. https://doi.org/10.1149/1.3493875.

(71) Ponrouch, A.; Frontera, C.; Bardé, F.; Palacín, M. R. Towards a Calcium-Based Rechargeable Battery. *Nat. Mater.* **2016**, *15* (2), 169–172. https://doi.org/10.1038/nmat4462.

(72) Wang, D.; Gao, X.; Chen, Y.; Jin, L.; Kuss, C.; Bruce, P. G. Plating and Stripping Calcium in an Organic Electrolyte. *Nat. Mater.* **2018**, *17* (1), 16–20. https://doi.org/10.1038/nmat5036.

(73) Li, Z.; Fuhr, O.; Fichtner, M.; Zhao-Karger, Z. Towards Stable and Efficient Electrolytes for Room-Temperature Rechargeable Calcium Batteries. *Energy Environ. Sci.* **2019**, *12* (12), 3496–3501. https://doi.org/10.1039/C9EE01699F.

(74) Shyamsunder, A.; Blanc, L. E.; Assoud, A.; Nazar, L. F. Reversible Calcium Plating and Stripping at Room Temperature Using a Borate Salt. *ACS Energy Lett.* **2019**, *4* (9), 2271–2276. https://doi.org/10.1021/acsenergylett.9b01550.

(75) Ponrouch, A.; Palacin, M. R. On the Road toward Calcium-Based Batteries. *Curr. Opin. Electrochem.* **2018**, *9*, 1–7. https://doi.org/10.1016/j.coelec.2018.02.001.

(76) Peled, E.; Tulman, R.; Meitav, A. Solid Electrolyte Interphase (SEI) Electrodes Part VI: Calcium-Ca(AlCl4)2-Sulfuryl Chloride System. *J. Power Sources* **1983**, *10* (2), 125–135. https://doi.org/10.1016/0378-7753(83)87002-5.

(77) Melemed, A.; Khurram, A.; Gallant, B. M. Current Understanding of Nonaqueous Electrolytes for Calcium-Based Batteries. *Batter. Supercaps* **2020**, DOI: batt.201900219. https://doi.org/10.1002/batt.201900219.

(78) Biria, S.; Pathreeker, S.; Li, H.; Hosein, I. D. Plating and Stripping of Calcium in an Alkyl Carbonate Electrolyte at Room Temperature. *ACS Appl. Energy Mater.* **2019**, *2* (11), 7738–7743. https://doi.org/10.1021/acsaem.9b01670.

(79) Ta, K.; Zhang, R.; Shin, M.; Rooney, R. T.; Neumann, E. K.; Gewirth, A. A. Understanding Ca Electrodeposition and Speciation Processes in Nonaqueous Electrolytes for Next-Generation Ca-Ion Batteries. *ACS Appl. Mater. Interfaces* **2019**, *11* (24), 21536–21542. https://doi.org/10.1021/acsami.9b04926.

(80) Nielson, K. V.; Liu, T. L. Dawn of Calcium Batteries. *Angew. Chem. Int. Ed.* **2020**, *59* (9), 3368–3370. https://doi.org/10.1002/anie.201913465.

(81) Tojo, T.; Sugiura, Y.; Inada, R.; Sakurai, Y. Reversible Calcium Ion Batteries Using a Dehydrated Prussian Blue Analogue Cathode. *Electrochim. Acta* **2016**, *207*, 22–27. https://doi.org/10.1016/j.electacta.2016.04.159.

(82) Tchitchekova, D. S.; Ponrouch, A.; Verrelli, R.; Broux, T.; Frontera, C.; Sorrentino,

A.; Bardé, F.; Biskup, N.; Arroyo-de-Dompablo, M. E.; Palacín, M. R. Electrochemical Intercalation of Calcium and Magnesium in TiS2: Fundamental Studies Related to Multivalent Battery Applications. *Chem. Mater.* **2018**, *30* (3), 847–856. https://doi.org/10.1021/acs.chemmater.7b04406.

(83) Tchitchekova, D. S.; Frontera, C.; Ponrouch, A.; Krich, C.; Bardé, F.; Palacín, M. R. Electrochemical Calcium Extraction from 1D-Ca 3 Co 2 O 6. *Dalt. Trans.* **2018**, *47* (33), 11298–11302. https://doi.org/10.1039/C8DT01754A.

(84) Yu, X.; Manthiram, A. Ambient-Temperature Energy Storage with Polyvalent Metal-Sulfur Chemistry. *Small Methods* **2017**, *1* (11), 1700217. https://doi.org/10.1002/smtd.201700217.

(85) https://www.chemicalbook.com/ChemicalProductProperty_EN_CB6854193.htm.

(86) Park, J.; Xu, Z.; Yoon, G.; Park, S. K.; Wang, J.; Hyun, H.; Park, H.; Lim, J.; Ko, Y.; Yun, Y. S.; Kang, K. Stable and High-Power Calcium-Ion Batteries Enabled by Calcium Intercalation into Graphite. *Adv. Mater.* **2020**, *32* (4), 1904411. https://doi.org/10.1002/adma.201904411.

(87) Adil, M.; Sarkar, A.; Roy, A.; Panda, M. R.; Nagendra, A.; Mitra, S. Practical Aqueous Calcium-Ion Battery Full-Cells for Future Stationary Storage. *ACS Appl. Mater. Interfaces* **2020**, *12* (10), 11489–11503. https://doi.org/10.1021/acsami.9b20129.

(88) Tran, T. T.; Obrovac, M. N. Alloy Negative Electrodes for High Energy Density Metal-Ion Cells. *J. Electrochem. Soc.* **2011**, *158* (12), A1411–A1416. https://doi.org/10.1149/2.083112jes.

(89) Yao, Z.; Hegde, V. I.; Aspuru-Guzik, A.; Wolverton, C. Discovery of Calcium-Metal Alloy Anodes for Reversible Ca-Ion Batteries. *Adv. Energy Mater.* **2019**, *9* (9), 1802994. https://doi.org/10.1002/aenm.201802994.

(90) Park, J.; Xu, Z.; Yoon, G.; Park, S. K.; Wang, J.; Hyun, H.; Park, H.; Lim, J.; Ko, Y.; Yun, Y. S.; Kang, K. Stable and High-Power Calcium-Ion Batteries Enabled by Calcium Intercalation into Graphite. *Adv. Mater.* **2020**, *32* (4), 1904411. https://doi.org/10.1002/adma.201904411.

(91) Zhao-Karger, Z.; Gil Bardaji, M. E.; Fuhr, O.; Fichtner, M. A New Class of Non-Corrosive, Highly Efficient Electrolytes for Rechargeable Magnesium Batteries. *J. Mater. Chem. A* **2017**, *5* (22), 10815–10820. https://doi.org/10.1039/C7TA02237A.

(92) Larush-Asraf, L.; Biton, M.; Teller, H.; Zinigrad, E.; Aurbach, D. On the Electrochemical and Thermal Behavior of Lithium Bis(Oxalato)Borate (LiBOB) Solutions. *J. Power Sources* **2007**, *174* (2), 400–407. https://doi.org/10.1016/j.jpowsour.2007.06.171.

(93) Lipson, A. L.; Pan, B.; Lapidus, S. H.; Liao, C.; Vaughey, J. T.; Ingram, B. J. Rechargeable Ca-Ion Batteries: A New Energy Storage System. *Chem. Mater.* **2015**, *27* (24), 8442–8447. https://doi.org/10.1021/acs.chemmater.5b04027.

(94) Lee, C. H.; Kim, C. S.; Jeong, S. K. Electrochemical Properties of $Li_4Ti_5O_{12}$ as a Negative Electrode for Calcium Secondary Batteries in $Ca(TFSI)_2$/THF Electrolyte. *Key Eng. Mater.* **2016**, *724*, 97–101. https://doi.org/10.4028/www.scientific.net/KEM.724.97.

(95) Forero-Saboya, J.; Bodin, C.; Ponrouch, A. A Boron-Based Electrolyte Additive for Calcium Electrodeposition. *Electrochem. commun.* **2021**, *124*, 106936.

https://doi.org/10.1016/j.elecom.2021.106936.

(96) Cang, R.; Zhao, C.; Ye, K.; Yin, J.; Zhu, K.; Yan, J.; Wang, G.; Cao, D. Aqueous Calcium-Ion Battery Based on a Mesoporous Organic Anode and a Manganite Cathode with Long Cycling Performance. *ChemSusChem* **2020**, *13* (15), 3911–3918. https://doi.org/10.1002/cssc.202000812.

(97) Ott, L. S.; Finke, R. G. Nanocluster Formation and Stabilization Fundamental Studies: † Investigating "Solvent-Only" Stabilization En Route to Discovering Stabilization by the Traditionally Weakly Coordinating Anion BF 4 - Plus High Dielectric Constant Solvents. *Inorg. Chem.* **2006**, *45* (20), 8382–8393. https://doi.org/10.1021/ic060876s.

(98) Zachara, J.; Wišniewski, W. Electronegativity Force of Cations and Thermal Decomposition of Complex Fluorides. *J. Therm. Anal.* **1995**, *44* (4), 929–935. https://doi.org/10.1007/BF02547276.

(99) Xu, K. Nonaqueous Liquid Electrolytes for Lithium-Based Rechargeable Batteries. *Chem. Rev.* **2004**, *104* (10), 4303–4418. https://doi.org/10.1021/cr030203g.

(100) Forero-Saboya, J.; Davoisne, C.; Dedryvère, R.; Yousef, I.; Canepa, P.; Ponrouch, A. Understanding the Nature of the Passivation Layer Enabling Reversible Calcium Plating. *Energy Environ. Sci.* **2020**, *13* (10), 3423–3431. https://doi.org/10.1039/D0EE02347G.

(101) Mohtadi, R.; Matsui, M.; Arthur, T. S.; Hwang, S.-J. Magnesium Borohydride: From Hydrogen Storage to Magnesium Battery. *Angew. Chemie Int. Ed.* **2012**, *51* (39), 9780–9783. https://doi.org/10.1002/anie.201204913.

(102) SOLOVEICHIK, G.; GAO, Y.; RIJSSENBEEK, J.; ANDRUS, M.; KNIAJANSKI, S.; BOWMANJR, R.; HWANG, S.; ZHAO, J. Magnesium Borohydride as a Hydrogen Storage Material: Properties and Dehydrogenation Pathway of Unsolvated Mg(BH4)2. *Int. J. Hydrogen Energy* **2009**, *34* (2), 916–928. https://doi.org/10.1016/j.ijhydene.2008.11.016.

(103) Lu, Z.; Ciucci, F. Metal Borohydrides as Electrolytes for Solid-State Li, Na, Mg, and Ca Batteries: A First-Principles Study. *Chem. Mater.* **2017**, *29* (21), 9308–9319. https://doi.org/10.1021/acs.chemmater.7b03284.

(104) Shao, Y.; Liu, T.; Li, G.; Gu, M.; Nie, Z.; Engelhard, M.; Xiao, J.; Lv, D.; Wang, C.; Zhang, J.-G.; Liu, J. Coordination Chemistry in Magnesium Battery Electrolytes: How Ligands Affect Their Performance. *Sci. Rep.* **2013**, *3* (1), 3130. https://doi.org/10.1038/srep03130.

(105) Tang, S.; Zhao, H. Glymes as Versatile Solvents for Chemical Reactions and Processes: From the Laboratory to Industry. *RSC Adv.* **2014**, *4* (22), 11251. https://doi.org/10.1039/c3ra47191h.

(106) Tobishima, S.; Morimoto, H.; Aoki, M.; Saito, Y.; Inose, T.; Fukumoto, T.; Kuryu, T. Glyme-Based Nonaqueous Electrolytes for Rechargeable Lithium Cells. *Electrochim. Acta* **2004**, *49* (6), 979–987. https://doi.org/10.1016/j.electacta.2003.10.009.

(107) Krossing, I.; Raabe, I. Noncoordinating Anions—Fact or Fiction? A Survey of Likely Candidates. *Angew. Chemie Int. Ed.* **2004**, *43* (16), 2066–2090. https://doi.org/10.1002/anie.200300620.

(108) Strauss, S. H. The Search for Larger and More Weakly Coordinating Anions. *Chem. Rev.* **1993**, *93* (3), 927–942. https://doi.org/10.1021/cr00019a005.

(109) Jelinek, T.; Baldwin, P.; Scheidt, W. R.; Reed, C. A. New Weakly Coordinating

Anions. 2. Derivatization of the Carborane Anion CB11H12-. *Inorg. Chem.* **1993**, *32* (10), 1982–1990. https://doi.org/10.1021/ic00062a018.

(110) Vidovic, D.; Moore, J. A.; Jones, J. N.; Cowley, A. H. Synthesis and Characterization of a Coordinated Oxoborane: Lewis Acid Stabilization of a Boron−Oxygen Double Bond. *J. Am. Chem. Soc.* **2005**, *127* (13), 4566–4567. https://doi.org/10.1021/ja0507564.

(111) Salem, H.; Shimon, L. J. W.; Leitus, G.; Weiner, L.; Milstein, D. B−C Bond Cleavage of BAr F Anion Upon Oxidation of Rhodium(I) with AgBAr F . Phosphinite Rhodium(I), Rhodium(II), and Rhodium(III) Pincer Complexes. *Organometallics* **2008**, *27* (10), 2293–2299. https://doi.org/10.1021/om800034t.

(112) Stang, P. J. Vinyl Triflate Chemistry: Unsaturated Cations and Carbenes. *Acc. Chem. Res.* **1978**, *11* (3), 107–114. https://doi.org/10.1021/ar50123a005.

(113) Strauss, S. H. The Search for Larger and More Weakly Coordinating Anions. *Chem. Rev.* **1993**, *93* (3), 927–942. https://doi.org/10.1021/cr00019a005.

(114) LaPointe, R. E.; Roof, G. R.; Abboud, K. A.; Klosin, J. New Family of Weakly Coordinating Anions. *J. Am. Chem. Soc.* **2000**, *122* (39), 9560–9561. https://doi.org/10.1021/ja002664e.

(115) Engesser, T. A.; Lichtenthaler, M. R.; Schleep, M.; Krossing, I. Reactive P-Block Cations Stabilized by Weakly Coordinating Anions. *Chem. Soc. Rev.* **2016**, *45* (4), 789–899. https://doi.org/10.1039/C5CS00672D.

(116) Macdonald, C. A. Complexes With Polyfluorinated Ligands Part I--Tetrafluorocatechol Partii--2-Amido- Hexafluoro-2-Propanol. **1972**.

(117) Xu, W.; Angell, C. A. Weakly Coordinating Anions, and the Exceptional Conductivity of Their Nonaqueous Solutions. *Electrochem. Solid-State Lett.* **2001**, *4* (1), E1. https://doi.org/10.1149/1.1344281.

(118) Beck, W.; Suenkel, K. Metal Complexes of Weakly Coordinating Anions. Precursors of Strong Cationic Organometallic Lewis Acids. *Chem. Rev.* **1988**, *88* (7), 1405–1421. https://doi.org/10.1021/cr00089a017.

(119) DeFrancesco, H.; Dudley, J.; Coca, A. Boron Chemistry: An Overview. In *ACS Symposium Series*; 2016; Vol. 1236, pp 1–25. https://doi.org/10.1021/bk-2016-1236.ch001.

(120) Huang, Z.; Wang, S.; Dewhurst, R. D.; Ignat'ev, N. V.; Finze, M.; Braunschweig, H. Boron: Its Role in Energy-Related Processes and Applications. *Angew. Chemie Int. Ed.* **2020**, *59* (23), 8800–8816. https://doi.org/10.1002/anie.201911108.

(121) Herb, J. T.; Nist-Lund, C. A.; Arnold, C. B. A Fluorinated Alkoxyaluminate Electrolyte for Magnesium-Ion Batteries. *ACS Energy Lett.* **2016**, *1* (6), 1227–1232. https://doi.org/10.1021/acsenergylett.6b00356.

(122) Herb, J. T.; Nist-Lund, C. A.; Arnold, C. B. A Fluorinated Alkoxyaluminate Electrolyte for Magnesium-Ion Batteries. *ACS Energy Lett.* **2016**, *1* (6), 1227–1232. https://doi.org/10.1021/acsenergylett.6b00356.

(123) Zhou, J.; Lancaster, S. J.; Walker, D. A.; Beck, S.; Thornton-Pett, M.; Bochmann, M. Synthesis, Structures, and Reactivity of Weakly Coordinating Anions with Delocalized Borate Structure: The Assessment of Anion Effects in Metallocene Polymerization Catalysts. *J. Am. Chem. Soc.* **2001**, *123* (2), 223–237. https://doi.org/10.1021/ja002820h.

(124) Shyamsunder, A.; Blanc, L. E.; Assoud, A.; Nazar, L. F. Reversible Calcium Plating and Stripping at Room Temperature Using a Borate Salt. *ACS Energy Lett.* **2019**, *4* (9), 2271–2276. https://doi.org/10.1021/acsenergylett.9b01550.

(125) Bitenc, J.; Scafuri, A.; Pirnat, K.; Lozinšek, M.; Jerman, I.; Grdadolnik, J.; Fraisse, B.; Berthelot, R.; Stievano, L.; Dominko, R. Electrochemical Performance and Mechanism of Calcium Metal-Organic Battery. *Batter. Supercaps* **2021**, *4* (1), 214–220. https://doi.org/10.1002/batt.202000197.

(126) Jaroń, T.; Wegner, W.; Grochala, W. M[Y(BH4)4] and M2Li[Y(BH4)6−xClx] (M = Rb, Cs): New Borohydride Derivatives of Yttrium and Their Hydrogen Storage Properties. *Dalt. Trans.* **2013**, *42* (19), 6886. https://doi.org/10.1039/c3dt33048f.

(127) Babij, N. R.; McCusker, E. O.; Whiteker, G. T.; Canturk, B.; Choy, N.; Creemer, L. C.; Amicis, C. V. De; Hewlett, N. M.; Johnson, P. L.; Knobelsdorf, J. A.; Li, F.; Lorsbach, B. A.; Nugent, B. M.; Ryan, S. J.; Smith, M. R.; Yang, Q. NMR Chemical Shifts of Trace Impurities: Industrially Preferred Solvents Used in Process and Green Chemistry. *Org. Process Res. Dev.* **2016**, *20* (3), 661–667. https://doi.org/10.1021/acs.oprd.5b00417.

(128) Rosenau, C. P.; Jelier, B. J.; Gossert, A. D.; Togni, A. Exposing the Origins of Irreproducibility in Fluorine NMR Spectroscopy. *Angew. Chemie Int. Ed.* **2018**, *57* (30), 9528–9533. https://doi.org/10.1002/anie.201802620.

(129) Concha, B. M.; Chatenet, M.; Maillard, F.; Ticianelli, E. A.; Lima, F. H. B.; de Lima, R. B. In Situ Infrared (FTIR) Study of the Mechanism of the Borohydride Oxidation Reaction. *Phys. Chem. Chem. Phys.* **2010**, *12* (37), 11507. https://doi.org/10.1039/c003652h.

(130) Andersen, M. P. S.; Hurley, M. D.; Ball, J. C.; Schneider, W. F.; Wallington, T. J.; Nielsen, O. J. CF3CH(ONO)CF3: Synthesis, IR Spectrum, and Use as OH Radical Source for Kinetic and Mechanistic Studies. *Int. J. Chem. Kinet.* **2003**, *35* (4), 159–165. https://doi.org/10.1002/kin.10116.

(131) Yamada, C.; Hirota, E. Infrared Diode Laser Spectroscopy of the CF 3 ν 3 Band. *J. Chem. Phys.* **1983**, *78* (4), 1703–1711. https://doi.org/10.1063/1.444969.

(132) Fichtner, M.; Chlopek, K.; Longhini, M.; Hagemann, H. Vibrational Spectra of Ca(BH 4) 2. *J. Phys. Chem. C* **2008**, *112* (30), 11575–11579. https://doi.org/10.1021/jp801482b.

(133) Yamaki, J. Thermally Stable Fluoro-Organic Solvents for Lithium Ion Battery. In *Fluorinated Materials for Energy Conversion*; Elsevier, 2005; pp 267–284. https://doi.org/10.1016/B978-008044472-7/50040-0.

(134) Kamitsos, E. I.; Chryssikos, G. D. Borate Glass Structure by Raman and Infrared Spectroscopies. *J. Mol. Struct.* **1991**, *247* (C), 1–16. https://doi.org/10.1016/0022-2860(91)87058-P.

(135) Walrafen, G. E.; Samanta, S. R.; Krishnan, P. N. Raman Investigation of Vitreous and Molten Boric Oxide. *J. Chem. Phys.* **1980**, *72* (1), 113–120. https://doi.org/10.1063/1.438894.

(136) Marshall, C. P.; Olcott Marshall, A. The Potential of Raman Spectroscopy for the Analysis of Diagenetically Transformed Carotenoids. *Philos. Trans. R. Soc. A Math. Phys. Eng. Sci.* **2010**, *368* (1922), 3137–3144. https://doi.org/10.1098/rsta.2010.0016.

(137) Clark, R. C.; Reid, J. S. The Analytical Calculation of Absorption in Multifaceted

Crystals. *Acta Crystallogr. Sect. A* **1995**, *51* (6), 887–897. https://doi.org/10.1107/S0108767395007367.

(138) Palatinus, L.; Chapuis, G. SUPERFLIP - A Computer Program for the Solution of Crystal Structures by Charge Flipping in Arbitrary Dimensions. *J. Appl. Crystallogr.* **2007**, *40* (4), 786–790. https://doi.org/10.1107/S0021889807029238.

(139) Sheldrick, G. M. SHELXT - Integrated Space-Group and Crystal-Structure Determination. *Acta Crystallogr. Sect. A Found. Crystallogr.* **2015**, *71* (1), 3–8. https://doi.org/10.1107/S2053273314026370.

(140) Dolomanov, O. V.; Bourhis, L. J.; Gildea, R. J.; Howard, J. A. K.; Puschmann, H. OLEX2: A Complete Structure Solution, Refinement and Analysis Program. *J. Appl. Crystallogr.* **2009**, *42* (2), 339–341. https://doi.org/10.1107/S0021889808042726.

(141) Li, Z.; Fuhr, O.; Fichtner, M.; Zhao-Karger, Z. Towards Stable and Efficient Electrolytes for Room-Temperature Rechargeable Calcium Batteries. *Energy Environ. Sci.* **2019**, *12* (12), 3496–3501. https://doi.org/10.1039/c9ee01699f.

(142) Hahn, N. T.; Driscoll, D. M.; Yu, Z.; Sterbinsky, G. E.; Cheng, L.; Balasubramanian, M.; Zavadil, K. R. Influence of Ether Solvent and Anion Coordination on Electrochemical Behavior in Calcium Battery Electrolytes. *ACS Appl. Energy Mater.* **2020**, *3* (9), 8437–8447. https://doi.org/10.1021/acsaem.0c01070.

(143) Peschke, M.; Blades, A. T.; Kebarle, P. Binding Energies for Doubly-Charged Ions M 2+ = Mg 2+ , Ca 2+ and Zn 2+ with the Ligands L = H 2 O, Acetone and N - Methylacetamide in Complexes M for n = 1 to 7 from Gas Phase Equilibria Determinations and Theoretical Calculations. *J. Am. Chem. Soc.* **2000**, *122* (42), 10440–10449. https://doi.org/10.1021/ja002021z.

(144) Erfani, M.; Saion, E.; Soltani, N.; Hashim, M.; Abdullah, W.; Navasery, M. Facile Synthesis of Calcium Borate Nanoparticles and the Annealing Effect on Their Structure and Size. *Int. J. Mol. Sci.* **2012**, *13* (12), 14434–14445. https://doi.org/10.3390/ijms131114434.

(145) Wang, S.; Ishihara, T.; Takita, Y. Partial Oxidation of Dimethyl Ether over Various Supported Metal Catalysts. *Appl. Catal. A Gen.* **2002**, *228* (1–2), 167–176. https://doi.org/10.1016/S0926-860X(01)00985-1.

(146) Bernstein, B. T.; Smith, J. F. Coefficients of Thermal Expansion for Face-Centered Cubic and Body-Centered Cubic Calcium. *Acta Crystallogr.* **1959**, *12* (5), 419–420. https://doi.org/10.1107/S0365110X59001268.

(147) Bulut, S.; Klose, P.; Krossing, I. Na[B(Hfip)4] (Hfip = OC(H)(CF3)2): A Weakly Coordinating Anion Salt and Its First Application to Prepare Ionic Liquids. *Dalt. Trans.* **2011**, *40* (32), 8114. https://doi.org/10.1039/c1dt10722d.

(148) Bulut, S.; Ab Rani, M. A.; Welton, T.; Lickiss, P. D.; Krossing, I. Preparation of [Al(Hfip) 4] − -Based Ionic Liquids with Siloxane-Functionalized Cations and Their Physical Properties in Comparison with Their [Tf 2 N] − Analogues. *ChemPhysChem* **2012**, *13* (7), 1802–1805. https://doi.org/10.1002/cphc.201200028.

(149) https://www.industrialheating.com/articles/89702-the-ellingham-diagram.

(150) Khaksar, S. Fluorinated Alcohols: A Magic Medium for the Synthesis of Heterocyclic Compounds. *J. Fluor. Chem.* **2015**, *172*, 51–61. https://doi.org/10.1016/j.jfluchem.2015.01.008.

(151) Josef, E.; Yan, Y.; Stan, M. C.; Wellmann, J.; Vizintin, A.; Winter, M.; Johansson, P.;

Dominko, R.; Guterman, R. Ionic Liquids and Their Polymers in Lithium-Sulfur Batteries. *Isr. J. Chem.* **2019**, *59* (9), 832–842. https://doi.org/10.1002/ijch.201800159.

(152) Gao, X.; Liu, X.; Mariani, A.; Elia, G. A.; Lechner, M.; Streb, C.; Passerini, S. Alkoxy-Functionalized Ionic Liquid Electrolytes: Understanding Ionic Coordination of Calcium Ion Speciation for the Rational Design of Calcium Electrolytes. *Energy Environ. Sci.* **2020**, *13* (8), 2559–2569. https://doi.org/10.1039/D0EE00831A.

(153) Cho, C.-W.; Preiss, U.; Jungnickel, C.; Stolte, S.; Arning, J.; Ranke, J.; Klamt, A.; Krossing, I.; Thöming, J. Ionic Liquids: Predictions of Physicochemical Properties with Experimental and/or DFT-Calculated LFER Parameters To Understand Molecular Interactions in Solution. *J. Phys. Chem. B* **2011**, *115* (19), 6040–6050. https://doi.org/10.1021/jp200042f.

(154) Zhao-Karger, Z.; Liu, R.; Dai, W.; Li, Z.; Diemant, T.; Vinayan, B. P.; Bonatto Minella, C.; Yu, X.; Manthiram, A.; Behm, R. J.; Ruben, M.; Fichtner, M. Toward Highly Reversible Magnesium–Sulfur Batteries with Efficient and Practical Mg[B(Hfip) 4] 2 Electrolyte. *ACS Energy Lett.* **2018**, *3* (8), 2005–2013. https://doi.org/10.1021/acsenergylett.8b01061.

(155) Muench, S.; Wild, A.; Friebe, C.; Häupler, B.; Janoschka, T.; Schubert, U. S. Polymer-Based Organic Batteries. *Chem. Rev.* **2016**, *116* (16), 9438–9484. https://doi.org/10.1021/acs.chemrev.6b00070.

(156) Mauger, A.; Julien, C.; Paolella, A.; Armand, M.; Zaghib, K. Recent Progress on Organic Electrodes Materials for Rechargeable Batteries and Supercapacitors. *Materials (Basel).* **2019**, *12* (11), 1770. https://doi.org/10.3390/ma12111770.

(157) Heiska, J.; Nisula, M.; Karppinen, M. Organic Electrode Materials with Solid-State Battery Technology. *J. Mater. Chem. A* **2019**, *7* (32), 18735–18758. https://doi.org/10.1039/C9TA04328D.

(158) Lu, Y.; Chen, J. Prospects of Organic Electrode Materials for Practical Lithium Batteries. *Nat. Rev. Chem.* **2020**, *4* (3), 127–142. https://doi.org/10.1038/s41570-020-0160-9.

(159) Wu, H.; Wang, K.; Meng, Y.; Lu, K.; Wei, Z. An Organic Cathode Material Based on a Polyimide/CNT Nanocomposite for Lithium Ion Batteries. *J. Mater. Chem. A* **2013**, *1* (21), 6366. https://doi.org/10.1039/c3ta10473g.

(160) Ponrouch, A.; Palacin, M. R. On the Road toward Calcium-Based Batteries. *Curr. Opin. Electrochem.* **2018**, *9*, 1–7. https://doi.org/10.1016/j.coelec.2018.02.001.

(161) Song, Z.; Zhou, H. Towards Sustainable and Versatile Energy Storage Devices: An Overview of Organic Electrode Materials. *Energy Environ. Sci.* **2013**, *6* (8), 2280. https://doi.org/10.1039/c3ee40709h.

(162) Lu, Y.; Zhang, Q.; Li, L.; Niu, Z.; Chen, J. Design Strategies toward Enhancing the Performance of Organic Electrode Materials in Metal-Ion Batteries. *Chem* **2018**, *4* (12), 2786–2813. https://doi.org/10.1016/j.chempr.2018.09.005.

(163) Alt, H.; Binder, H.; Köhling, A.; Sandstede, G. Investigation into the Use of Quinone Compounds-for Battery Cathodes. *Electrochim. Acta* **1972**, *17* (5), 873–887. https://doi.org/10.1016/0013-4686(72)90010-2.

(164) Ohzuku, T.; Wakamatsu, H.; Takehara, Z.; Yoshizawa, S. Nonaqueous Lithium/Pyromellitic Dianhydride Cell. *Electrochim. Acta* **1979**, *24* (6), 723–726. https://doi.org/10.1016/0013-4686(79)87057-7.

(165) Zhao, Q.; Lu, Y.; Chen, J. Advanced Organic Electrode Materials for Rechargeable Sodium-Ion Batteries. *Adv. Energy Mater.* **2017**, *7* (8), 1601792. https://doi.org/10.1002/aenm.201601792.

(166) Wang, H.; Yao, C.-J.; Nie, H.-J.; Wang, K.-Z.; Zhong, Y.-W.; Chen, P.; Mei, S.; Zhang, Q. Recent Progress in Carbonyl-Based Organic Polymers as Promising Electrode Materials for Lithium-Ion Batteries (LIBs). *J. Mater. Chem. A* **2020**, *8* (24), 11906–11922. https://doi.org/10.1039/D0TA03321A.

(167) Yang, J.; Shi, Y.; Sun, P.; Xiong, P.; Xu, Y. Optimization of Molecular Structure and Electrode Architecture of Anthraquinone-Containing Polymer Cathode for High-Performance Lithium-Ion Batteries. *ACS Appl. Mater. Interfaces* **2019**, *11* (45), 42305–42312. https://doi.org/10.1021/acsami.9b16678.

(168) Song, Z.; Zhan, H.; Zhou, Y. Anthraquinone Based Polymer as High Performance Cathode Material for Rechargeable Lithium Batteries. *Chem. Commun.* **2009**, No. 4, 448–450. https://doi.org/10.1039/B814515F.

(169) Bitenc, J.; Lindahl, N.; Vizintin, A.; Abdelhamid, M. E.; Dominko, R.; Johansson, P. Concept and Electrochemical Mechanism of an Al Metal Anode – Organic Cathode Battery. *Energy Storage Mater.* **2020**, *24* (June), 379–383. https://doi.org/10.1016/j.ensm.2019.07.033.

(170) Bitenc, J.; Pirnat, K.; Mali, G.; Novosel, B.; Randon Vitanova, A.; Dominko, R. Poly(Hydroquinoyl-Benzoquinonyl Sulfide) as an Active Material in Mg and Li Organic Batteries. *Electrochem. commun.* **2016**, *69*, 1–5. https://doi.org/10.1016/j.elecom.2016.05.009.

(171) Bitenc, J.; Pirnat, K.; Bančič, T.; Gaberšček, M.; Genorio, B.; Randon-Vitanova, A.; Dominko, R. Anthraquinone-Based Polymer as Cathode in Rechargeable Magnesium Batteries. *ChemSusChem* **2015**, *8* (24), 4128–4132. https://doi.org/10.1002/cssc.201500910.

(172) Bitenc, J.; Vizintin, A.; Grdadolnik, J.; Dominko, R. Tracking Electrochemical Reactions inside Organic Electrodes by Operando IR Spectroscopy. *Energy Storage Mater.* **2019**, *21* (May), 347–353. https://doi.org/10.1016/j.ensm.2019.05.038.

(173) Doe, R. E.; Han, R.; Hwang, J.; Gmitter, A. J.; Shterenberg, I.; Yoo, H. D.; Pour, N.; Aurbach, D. Novel, Electrolyte Solutions Comprising Fully Inorganic Salts with High Anodic Stability for Rechargeable Magnesium Batteries. *Chem. Commun.* **2014**, *50* (2), 243–245. https://doi.org/10.1039/C3CC47896C.

(174) Vizintin, A.; Bitenc, J.; Kopač Lautar, A.; Pirnat, K.; Grdadolnik, J.; Stare, J.; Randon-Vitanova, A.; Dominko, R. Probing Electrochemical Reactions in Organic Cathode Materials via in Operando Infrared Spectroscopy. *Nat. Commun.* **2018**, *9* (1), 661. https://doi.org/10.1038/s41467-018-03114-1.

(175) Rodríguez-Pérez, I. A.; Yuan, Y.; Bommier, C.; Wang, X.; Ma, L.; Leonard, D. P.; Lerner, M. M.; Carter, R. G.; Wu, T.; Greaney, P. A.; Lu, J.; Ji, X. Mg-Ion Battery Electrode: An Organic Solid's Herringbone Structure Squeezed upon Mg-Ion Insertion. *J. Am. Chem. Soc.* **2017**, *139* (37), 13031–13037. https://doi.org/10.1021/jacs.7b06313.

(176) Li, Z.; Fuhr, O.; Fichtner, M.; Zhao-Karger, Z. Towards Stable and Efficient Electrolytes for Room-Temperature Rechargeable Calcium Batteries. *Energy Environ. Sci.* **2019**, *12* (12), 3496–3501. https://doi.org/10.1039/C9EE01699F.

(177) Bitenc, J.; Pavčnik, T.; Košir, U.; Pirnat, K. Quinone Based Materials as Renewable High Energy Density Cathode Materials for Rechargeable Magnesium Batteries. *Materials (Basel).* **2020**, *13* (3), 506. https://doi.org/10.3390/ma13030506.

(178) Balogun, M.-S.; Yang, H.; Luo, Y.; Qiu, W.; Huang, Y.; Liu, Z.-Q.; Tong, Y. Achieving High Gravimetric Energy Density for Flexible Lithium-Ion Batteries Facilitated by Core–Double-Shell Electrodes. *Energy Environ. Sci.* **2018**, *11* (7), 1859–1869. https://doi.org/10.1039/C8EE00522B.

(179) Geng, K.; He, T.; Liu, R.; Dalapati, S.; Tan, K. T.; Li, Z.; Tao, S.; Gong, Y.; Jiang, Q.; Jiang, D. Covalent Organic Frameworks: Design, Synthesis, and Functions. *Chem. Rev.* **2020**, *120* (16), 8814–8933. https://doi.org/10.1021/acs.chemrev.9b00550.

(180) Wang, Z.; Jin, W.; Huang, X.; Lu, G.; Li, Y. Covalent Organic Frameworks as Electrode Materials for Metal Ion Batteries: A Current Review. *Chem. Rec.* **2020**, tcr.202000074. https://doi.org/10.1002/tcr.202000074.

(181) Wu, D.; Xie, Z.; Zhou, Z.; Shen, P.; Chen, Z. Designing High-Voltage Carbonyl-Containing Polycyclic Aromatic Hydrocarbon Cathode Materials for Li-Ion Batteries Guided by Clar's Theory. *J. Mater. Chem. A* **2015**, *3* (37), 19137–19143. https://doi.org/10.1039/C5TA05437K.

(182) Gomez, I.; Leonet, O.; Alberto Blazquez, J.; Grande, H.-J.; Mecerreyes, D. Poly(Anthraquinonyl Sulfides): High Capacity Redox Polymers for Energy Storage. *ACS Macro Lett.* **2018**, *7* (4), 419–424. https://doi.org/10.1021/acsmacrolett.8b00154.

(183) D., H.; J., U. Electric Dry Cells and Storage Batteries - US Patent 3043896. **1962**, 3043896.

(184) Yu, X.; Manthiram, A. A Progress Report on Metal–Sulfur Batteries. *Adv. Funct. Mater.* **2020**, *30* (39), 2004084. https://doi.org/10.1002/adfm.202004084.

(185) Hoffman, D. C.; Seaborg, G. T. Chemistry of the Heaviest Elements. *Radiochim. Acta* **1996**, *72* (1), 1–6. https://doi.org/10.1524/ract.1996.72.1.1.

(186) Manthiram, A.; Fu, Y.; Chung, S.-H.; Zu, C.; Su, Y.-S. Rechargeable Lithium–Sulfur Batteries. *Chem. Rev.* **2014**, *114* (23), 11751–11787. https://doi.org/10.1021/cr500062v.

(187) Choi, Y.-J.; Chung, Y.-D.; Baek, C.-Y.; Kim, K.-W.; Ahn, H.-J.; Ahn, J.-H. Effects of Carbon Coating on the Electrochemical Properties of Sulfur Cathode for Lithium/Sulfur Cell. *J. Power Sources* **2008**, *184* (2), 548–552. https://doi.org/10.1016/j.jpowsour.2008.02.053.

(188) Ryu, H. S.; Ahn, H. J.; Kim, K. W.; Ahn, J. H.; Cho, K. K.; Nam, T. H. Self-Discharge Characteristics of Lithium/Sulfur Batteries Using TEGDME Liquid Electrolyte. *Electrochim. Acta* **2006**, *52* (4), 1563–1566. https://doi.org/10.1016/j.electacta.2006.01.086.

(189) RYU, H.; AHN, H.; KIM, K.; AHN, J.; LEE, J.; CAIRNS, E. Self-Discharge of Lithium–Sulfur Cells Using Stainless-Steel Current-Collectors. *J. Power Sources* **2005**, *140* (2), 365–369. https://doi.org/10.1016/j.jpowsour.2004.08.039.

(190) Mikhaylik, Y. V.; Akridge, J. R. Polysulfide Shuttle Study in the Li/S Battery System. *J. Electrochem. Soc.* **2004**, *151* (11), A1969. https://doi.org/10.1149/1.1806394.

(191) Medenbach, L.; Adelhelm, P. Cell Concepts of Metal–Sulfur Batteries (Metal = Li, Na, K, Mg): Strategies for Using Sulfur in Energy Storage Applications. *Top. Curr. Chem.* **2017**, *375* (5), 81. https://doi.org/10.1007/s41061-017-0168-x.

(192) Yu, X.; Manthiram, A. Ambient-Temperature Energy Storage with Polyvalent Metal-Sulfur Chemistry. *Small Methods* **2017**, *1* (11), 1700217. https://doi.org/10.1002/smtd.201700217.

(193) Scheers, J.; Fantini, S.; Johansson, P. A Review of Electrolytes for Lithium–Sulphur Batteries. *J. Power Sources* **2014**, *255*, 204–218. https://doi.org/10.1016/j.jpowsour.2014.01.023.

(194) Kim, H. S.; Arthur, T. S.; Allred, G. D.; Zajicek, J.; Newman, J. G.; Rodnyansky, A. E.; Oliver, A. G.; Boggess, W. C.; Muldoon, J. Structure and Compatibility of a Magnesium Electrolyte with a Sulphur Cathode. *Nat. Commun.* **2011**, *2* (1), 427. https://doi.org/10.1038/ncomms1435.

(195) Robba, A.; Vizintin, A.; Bitenc, J.; Mali, G.; Arčon, I.; Kavčič, M.; Žitnik, M.; Bučar, K.; Aquilanti, G.; Martineau-Corcos, C.; Randon-Vitanova, A.; Dominko, R. Mechanistic Study of Magnesium–Sulfur Batteries. *Chem. Mater.* **2017**, *29* (21), 9555–9564. https://doi.org/10.1021/acs.chemmater.7b03956.

(196) Zhao-Karger, Z.; Liu, R.; Dai, W.; Li, Z.; Diemant, T.; Vinayan, B. P.; Bonatto Minella, C.; Yu, X.; Manthiram, A.; Behm, R. J.; Ruben, M.; Fichtner, M. Toward Highly Reversible Magnesium–Sulfur Batteries with Efficient and Practical Mg[B(Hfip) 4] 2 Electrolyte. *ACS Energy Lett.* **2018**, *3* (8), 2005–2013. https://doi.org/10.1021/acsenergylett.8b01061.

(197) Bevilacqua, S. C.; Pham, K. H.; See, K. A. Effect of the Electrolyte Solvent on Redox Processes in Mg–S Batteries. *Inorg. Chem.* **2019**, *58* (16), 10472–10482. https://doi.org/10.1021/acs.inorgchem.9b00891.

(198) See, K. A.; Gerbec, J. A.; Jun, Y.; Wudl, F.; Stucky, G. D.; Seshadri, R. A High Capacity Calcium Primary Cell Based on the Ca-S System. *Adv. Energy Mater.* **2013**, *3* (8), 1056–1061. https://doi.org/10.1002/aenm.201300160.

(199) Yu, X.; Boyer, M. J.; Hwang, G. S.; Manthiram, A. Toward a Reversible Calcium-Sulfur Battery with a Lithium-Ion Mediation Approach. *Adv. Energy Mater.* **2019**, *9* (14), 1803794. https://doi.org/10.1002/aenm.201803794.

(200) Li, Z.; Vinayan, B. P.; Diemant, T.; Behm, R. J.; Fichtner, M.; Zhao-Karger, Z. Rechargeable Calcium–Sulfur Batteries Enabled by an Efficient Borate-Based Electrolyte. *Small* **2020**, *16* (39), 2001806. https://doi.org/10.1002/smll.202001806.

(201) Elazari, R.; Salitra, G.; Garsuch, A.; Panchenko, A.; Aurbach, D. Sulfur-Impregnated Activated Carbon Fiber Cloth as a Binder-Free Cathode for Rechargeable Li-S Batteries. *Adv. Mater.* **2011**, *23* (47), 5641–5644. https://doi.org/10.1002/adma.201103274.

(202) Meng, Z.; Foix, D.; Brun, N.; Dedryvère, R.; Stievano, L.; Morcrette, M.; Berthelot, R. Alloys to Replace Mg Anodes in Efficient and Practical Mg-Ion/Sulfur Batteries. *ACS Energy Lett.* **2019**, *4* (9), 2040–2044. https://doi.org/10.1021/acsenergylett.9b01389.

(203) https://www.chemviron.eu/products/activated-carbon/activated-carbon-cloth/.

(204) Gao, T.; Hou, S.; Wang, F.; Ma, Z.; Li, X.; Xu, K.; Wang, C. Reversible S 0 /MgS x Redox Chemistry in a MgTFSI 2 /MgCl 2 /DME Electrolyte for Rechargeable Mg/S Batteries. *Angew. Chemie* **2017**, *129* (43), 13711–13715. https://doi.org/10.1002/ange.201708241.

(205) Scafuri, A.; Berthelot, R.; Pirnat, K.; Vizintin, A.; Bitenc, J.; Aquilanti, G.; Foix, D.; Dedryvère, R.; Arčon, I.; Dominko, R.; Stievano, L. Spectroscopic Insights into the

Electrochemical Mechanism of Rechargeable Calcium/Sulfur Batteries. *Chem. Mater.* **2020**, *32* (19), 8266–8275. https://doi.org/10.1021/acs.chemmater.0c02074.

(206) Noh, H.; Song, J.; Park, J.-K.; Kim, H.-T. A New Insight on Capacity Fading of Lithium–Sulfur Batteries: The Effect of Li2S Phase Structure. *J. Power Sources* **2015**, *293*, 329–335. https://doi.org/10.1016/j.jpowsour.2015.05.072.

(207) Richter, R.; Häcker, J.; Zhao-Karger, Z.; Danner, T.; Wagner, N.; Fichtner, M.; Friedrich, K. A.; Latz, A. Insights into Self-Discharge of Lithium– and Magnesium–Sulfur Batteries. *ACS Appl. Energy Mater.* **2020**, *3* (9), 8457–8474. https://doi.org/10.1021/acsaem.0c01114.

(208) Busche, M. R.; Adelhelm, P.; Sommer, H.; Schneider, H.; Leitner, K.; Janek, J. Systematical Electrochemical Study on the Parasitic Shuttle-Effect in Lithium-Sulfur-Cells at Different Temperatures and Different Rates. *J. Power Sources* **2014**, *259*, 289–299. https://doi.org/10.1016/j.jpowsour.2014.02.075.

(209) Gao, J.; Lowe, M. A.; Kiya, Y.; Abruña, H. D. Effects of Liquid Electrolytes on the Charge–Discharge Performance of Rechargeable Lithium/Sulfur Batteries: Electrochemical and in-Situ X-Ray Absorption Spectroscopic Studies. *J. Phys. Chem. C* **2011**, *115* (50), 25132–25137. https://doi.org/10.1021/jp207714c.

(210) Barchasz, C.; Mesguich, F.; Dijon, J.; Leprêtre, J.-C.; Patoux, S.; Alloin, F. Novel Positive Electrode Architecture for Rechargeable Lithium/Sulfur Batteries. *J. Power Sources* **2012**, *211*, 19–26. https://doi.org/10.1016/j.jpowsour.2012.03.062.

(211) Jeschke, S.; Johansson, P. Predicting the Solubility of Sulfur: A COSMO-RS-Based Approach to Investigate Electrolytes for Li-S Batteries. *Chem. - A Eur. J.* **2017**, *23* (38), 9130–9136. https://doi.org/10.1002/chem.201701011.

(212) Yin, Y.-X.; Xin, S.; Guo, Y.-G.; Wan, L.-J. Lithium-Sulfur Batteries: Electrochemistry, Materials, and Prospects. *Angew. Chemie Int. Ed.* **2013**, *52* (50), 13186–13200. https://doi.org/10.1002/anie.201304762.

(213) Tutusaus, O.; Mohtadi, R.; Singh, N.; Arthur, T. S.; Mizuno, F. Study of Electrochemical Phenomena Observed at the Mg Metal/Electrolyte Interface. *ACS Energy Lett.* **2017**, *2* (1), 224–229. https://doi.org/10.1021/acsenergylett.6b00549.

(214) Dominko, R.; Vizintin, A.; Aquilanti, G.; Stievano, L.; Helen, M. J.; Munnangi, A. R.; Fichtner, M.; Arcon, I. Polysulfides Formation in Different Electrolytes from the Perspective of X-Ray Absorption Spectroscopy. *J. Electrochem. Soc.* **2018**, *165* (1), A5014–A5019. https://doi.org/10.1149/2.0151801jes.

(215) Smart, R. S. C.; Skinner, W. M.; Gerson, A. R. XPS of Sulphide Mineral Surfaces: Metal-Deficient, Polysulphides, Defects and Elemental Sulphur. *Surf. Interface Anal.* **1999**, *28* (1), 101–105. https://doi.org/10.1002/(SICI)1096-9918(199908)28:1<101::AID-SIA627>3.0.CO;2-0.

(216) Vizintin, A.; Lozinšek, M.; Chellappan, R. K.; Foix, D.; Krajnc, A.; Mali, G.; Drazic, G.; Genorio, B.; Dedryvère, R.; Dominko, R. Fluorinated Reduced Graphene Oxide as an Interlayer in Li–S Batteries. *Chem. Mater.* **2015**, *27* (20), 7070–7081. https://doi.org/10.1021/acs.chemmater.5b02906.

(217) Briggs, D.; Seah, M. P. *Practical Surface Analysis: Auger and X-Ray Photoelectron Spectroscopy*; Practical Surface Analysis; Wiley, 1990.

(218) Yu, X.; Boyer, M. J.; Hwang, G. S.; Manthiram, A. Toward a Reversible Calcium-Sulfur Battery with a Lithium-Ion Mediation Approach. *Adv. Energy Mater.* **2019**, *9*

(14), 1803794. https://doi.org/10.1002/aenm.201803794.

(219) Zhao-Karger, Z.; Liu, R.; Dai, W.; Li, Z.; Diemant, T.; Vinayan, B. P.; Bonatto Minella, C.; Yu, X.; Manthiram, A.; Behm, R. J.; Ruben, M.; Fichtner, M. Toward Highly Reversible Magnesium–Sulfur Batteries with Efficient and Practical Mg[B(Hfip)4]2 Electrolyte. *ACS Energy Lett.* **2018**, *3* (8), 2005–2013. https://doi.org/10.1021/acsenergylett.8b01061.

(220) Giorgetti, M. A Review on the Structural Studies of Batteries and Host Materials by X-Ray Absorption Spectroscopy. **2013**, *2013*.

(221) Dey, A.; Okamura, T.; Ueyama, N.; Hedman, B.; Hodgson, K. O.; Solomon, E. I. Sulfur K-Edge XAS and DFT Calculations on P450 Model Complexes: Effects of Hydrogen Bonding on Electronic Structure and Redox Potentials. *J. Am. Chem. Soc.* **2005**, *127* (34), 12046–12053. https://doi.org/10.1021/ja0519031.

(222) Martin-Diaconescu, V.; Kennepohl, P. Sulfur K-Edge XAS as a Probe of Sulfur-Centered Radical Intermediates. *J. Am. Chem. Soc.* **2007**, *129* (11), 3034–3035. https://doi.org/10.1021/ja0676760.

(223) Fehse, M.; Iadecola, A.; Sougrati, M. T.; Conti, P.; Giorgetti, M.; Stievano, L. Applying Chemometrics to Study Battery Materials: Towards the Comprehensive Analysis of Complex Operando Datasets. *Energy Storage Mater.* **2019**, *18*, 328–337. https://doi.org/10.1016/j.ensm.2019.02.002.

(224) Patel, M. U. M.; Arčon, I.; Aquilanti, G.; Stievano, L.; Mali, G.; Dominko, R. X-Ray Absorption Near-Edge Structure and Nuclear Magnetic Resonance Study of the Lithium-Sulfur Battery and Its Components. *ChemPhysChem* **2014**, *15* (5), 894–904. https://doi.org/10.1002/cphc.201300972.

(225) Aquilanti, G.; Giorgetti, M.; Dominko, R.; Stievano, L.; Arčon, I.; Novello, N.; Olivi, L. Operando Characterization of Batteries Using X-Ray Absorption Spectroscopy: Advances at the Beamline XAFS at Synchrotron Elettra. *J. Phys. D. Appl. Phys.* **2017**, *50* (7), 074001. https://doi.org/10.1088/1361-6463/aa519a.

(226) Vizintin, A.; Chabanne, L.; Tchernychova, E.; Arčon, I.; Stievano, L.; Aquilanti, G.; Antonietti, M.; Fellinger, T.-P.; Dominko, R. The Mechanism of Li2S Activation in Lithium-Sulfur Batteries: Can We Avoid the Polysulfide Formation? *J. Power Sources* **2017**, *344*, 208–217. https://doi.org/10.1016/j.jpowsour.2017.01.112.

(227) https://www.elettra.trieste.it/it/index.html.

(228) Fabiani, S.; Ahangarianabhari, M.; Baldazzi, G.; Bellutti, P.; Bertuccio, G.; Bruschi, M.; Bufon, J.; Carrato, S.; Castoldi, A.; Cautero, G.; Ciano, S.; Cicuttin, A.; Crespo, M. L.; Santos, M. Dos; Gandola, M.; Giacomini, G.; Giuressi, D.; Guazzoni, C.; Menk, R. H.; Niemela, J.; Olivi, L.; Picciotto, A.; Piemonte, C.; Rashevskaya, I.; Rachevski, A.; Rignanese, L. P.; Sbrizzi, A.; Schillani, S.; Vacchi, A.; Garcia, V. V.; Zampa, G.; Zampa, N.; Zorzi, N. Development and Tests of a New Prototype Detector for the XAFS Beamline at Elettra Synchrotron in Trieste. *J. Phys. Conf. Ser.* **2016**, *689* (1), 012017. https://doi.org/10.1088/1742-6596/689/1/012017.

(229) Leriche, J. B.; Hamelet, S.; Shu, J.; Morcrette, M.; Masquelier, C.; Ouvrard, G.; Zerrouki, M.; Soudan, P.; Belin, S.; Elkaïm, E.; Baudelet, F. An Electrochemical Cell for Operando Study of Lithium Batteries Using Synchrotron Radiation. *J. Electrochem. Soc.* **2010**, *157* (5), A606. https://doi.org/10.1149/1.3355977.

(230) Sainctavit, P.; Petiau, J.; Manceau, A.; Rivallant, R.; Belakhovsky, M.; Renaud, G.

Two-mirror Device for Harmonic Rejection. *Rev. Sci. Instrum.* **1989**, *60* (7), 2027–2029. https://doi.org/10.1063/1.1140867.

(231) Dominko, R.; Patel, M. U. M.; Lapornik, V.; Vizintin, A.; Koželj, M.; Novak Tušar, N.; Arčon, I.; Stievano, L.; Aquilanti, G. Analytical Detection of Polysulfides in the Presence of Adsorption Additives by Operando X-Ray Absorption Spectroscopy. *J. Phys. Chem. C* **2015**, *119* (33), 19001–19010. https://doi.org/10.1021/acs.jpcc.5b05609.

(232) Slutsky, B. Handbook of Chemometrics and Qualimetrics: Part A By D. L. Massart, B. G. M. Vandeginste, L. M. C. Buydens, S. De Jong, P. J. Lewi, and J. Smeyers-Verbeke. Data Handling in Science and Technology Volume 20A. Elsevier: Amsterdam. 1997. Xvii + 867 Pp. ISBN . *J. Chem. Inf. Comput. Sci.* **1998**, *38* (6), 1254–1254. https://doi.org/10.1021/ci980427d.

(233) Ku, W.; Storer, R. H.; Georgakis, C. Disturbance Detection and Isolation by Dynamic Principal Component Analysis. *Chemom. Intell. Lab. Syst.* **1995**, *30* (1), 179–196. https://doi.org/10.1016/0169-7439(95)00076-3.

(234) Kumar, N.; Bansal, A.; Sarma, G. S.; Rawal, R. K. Chemometrics Tools Used in Analytical Chemistry: An Overview. *Talanta* **2014**, *123*, 186–199. https://doi.org/10.1016/j.talanta.2014.02.003.

(235) Dominko, R.; Patel, M. U. M.; Lapornik, V.; Vizintin, A.; Koželj, M.; N. Tušar, N.; Arčon, I.; Stievano, L.; Aquilanti, G. Analytical Detection of Polysulfides in the Presence of Adsorption Additives by Operando X-Ray Absorption Spectroscopy. *J. Phys. Chem. C* **2015**, *119* (33), 19001–19010. https://doi.org/10.1021/acs.jpcc.5b05609.

(236) Zhao, E.; Wang, J.; Li, F.; Jiang, Z.; Yang, X.-Q.; Wang, F.; Li, H.; Yu, X. Exploring Reaction Dynamics in Lithium–Sulfur Batteries by Time-Resolved Operando Sulfur K-Edge X-Ray Absorption Spectroscopy. *Chem. Commun.* **2019**, *55* (34), 4993–4996. https://doi.org/10.1039/C9CC00485H.

(237) Cuisinier, M.; Cabelguen, P.-E.; Evers, S.; He, G.; Kolbeck, M.; Garsuch, A.; Bolin, T.; Balasubramanian, M.; Nazar, L. F. Sulfur Speciation in Li–S Batteries Determined by Operando X-Ray Absorption Spectroscopy. *J. Phys. Chem. Lett.* **2013**, *4* (19), 3227–3232. https://doi.org/10.1021/jz401763d.

(238) Pascal, T. A.; Wujcik, K. H.; Velasco-Velez, J.; Wu, C.; Teran, A. A.; Kapilashrami, M.; Cabana, J.; Guo, J.; Salmeron, M.; Balsara, N.; Prendergast, D. X-Ray Absorption Spectra of Dissolved Polysulfides in Lithium–Sulfur Batteries from First-Principles. *J. Phys. Chem. Lett.* **2014**, *5* (9), 1547–1551. https://doi.org/10.1021/jz500260s.

(239) Cuisinier, M.; Cabelguen, P.-E.; Evers, S.; He, G.; Kolbeck, M.; Garsuch, A.; Bolin, T.; Balasubramanian, M.; Nazar, L. F. Sulfur Speciation in Li–S Batteries Determined by Operando X-Ray Absorption Spectroscopy. *J. Phys. Chem. Lett.* **2013**, *4* (19), 3227–3232. https://doi.org/10.1021/jz401763d.

(240) Patel, M. U. M.; Arčon, I.; Aquilanti, G.; Stievano, L.; Mali, G.; Dominko, R. X-Ray Absorption Near-Edge Structure and Nuclear Magnetic Resonance Study of the Lithium-Sulfur Battery and Its Components. *ChemPhysChem* **2014**, *15* (5), 894–904. https://doi.org/10.1002/cphc.201300972.

(241) Cuisinier, M.; Hart, C.; Balasubramanian, M.; Garsuch, A.; Nazar, L. F. Radical or Not Radical : Revisiting Lithium – Sulfur Electrochemistry in Nonaqueous Electrolytes. *Adv. Energy Mater.* **2015**, *5*, 1401801. https://doi.org/10.1002/aenm.201401801.

(242) Wujcik, K. H.; Pascal, T. A.; Pemmaraju, C. D.; Devaux, D.; Stolte, W. C.; Balsara, N. P.; Prendergast, D. Characterization of Polysulfide Radicals Present in an Ether-Based Electrolyte of a Lithium-Sulfur Battery During Initial Discharge Using In Situ X-Ray Absorption Spectroscopy Experiments and First-Principles Calculations. *Adv. Energy Mater.* **2015**, *5* (16), 1500285. https://doi.org/10.1002/aenm.201500285.

(243) Ren, W.; Ma, W.; Zhang, S.; Tang, B. Recent Advances in Shuttle Effect Inhibition for Lithium Sulfur Batteries. *Energy Storage Mater.* **2019**, *23* (February), 707–732. https://doi.org/10.1016/j.ensm.2019.02.022.

(244) Rana, M.; Li, M.; Huang, X.; Luo, B.; Gentle, I.; Knibbe, R. Recent Advances in Separators to Mitigate Technical Challenges Associated with Re-Chargeable Lithium Sulfur Batteries. *J. Mater. Chem. A* **2019**, *7* (12), 6596–6615. https://doi.org/10.1039/C8TA12066H.

(245) Xu, J.; Ma, J.; Fan, Q.; Guo, S.; Dou, S. Recent Progress in the Design of Advanced Cathode Materials and Battery Models for High-Performance Lithium-X (X = O2, S, Se, Te, I2, Br2) Batteries. *Adv. Mater.* **2017**, *29* (28), 1606454. https://doi.org/10.1002/adma.201606454.

(246) Wild, M.; O'Neill, L.; Zhang, T.; Purkayastha, R.; Minton, G.; Marinescu, M.; Offer, G. J. Lithium Sulfur Batteries, A Mechanistic Review. *Energy Environ. Sci.* **2015**, *8* (12), 3477–3494. https://doi.org/10.1039/C5EE01388G.

(247) Ravel, B.; Newville, M. ATHENA , ARTEMIS , HEPHAESTUS : Data Analysis for X-Ray Absorption Spectroscopy Using IFEFFIT. *J. Synchrotron Radiat.* **2005**, *12* (4), 537–541. https://doi.org/10.1107/S0909049505012719.

(248) Ravel, B.; Newville, M. ATHENA, ARTEMIS, HEPHAESTUS: Data Analysis for X-Ray Absorption Spectroscopy Using IFEFFIT. *J. Synchrotron Rad.* **2005**, *12* (Pt 4), 537–541. https://doi.org/10.1107/S0909049505012719.

(249) Deng, Z.; Zhang, Z.; Lai, Y.; Liu, J.; Li, J.; Liu, Y. Electrochemical Impedance Spectroscopy Study of a Lithium/Sulfur Battery: Modeling and Analysis of Capacity Fading. *J. Electrochem. Soc.* **2013**, *160* (4), A553–A558. https://doi.org/10.1149/2.026304jes.

(250) Häcker, J.; Danner, C.; Sievert, B.; Biswas, I.; Zhao-Karger, Z.; Wagner, N.; Friedrich, K. A. Investigation of Magnesium–Sulfur Batteries Using Electrochemical Impedance Spectroscopy. *Electrochim. Acta* **2020**, *338*, 135787. https://doi.org/10.1016/j.electacta.2020.135787.

(251) Xiong, S.; Xie, K.; Diao, Y.; Hong, X. On the Role of Polysulfides for a Stable Solid Electrolyte Interphase on the Lithium Anode Cycled in Lithium–Sulfur Batteries. *J. Power Sources* **2013**, *236*, 181–187. https://doi.org/10.1016/j.jpowsour.2013.02.072.

(252) Vinayan, B. P.; Zhao-Karger, Z.; Diemant, T.; Chakravadhanula, V. S. K.; Schwarzburger, N. I.; Cambaz, M. A.; Behm, R. J.; Kübel, C.; Fichtner, M. Performance Study of Magnesium–Sulfur Battery Using a Graphene Based Sulfur Composite Cathode Electrode and a Non-Nucleophilic Mg Electrolyte. *Nanoscale* **2016**, *8* (6), 3296–3306. https://doi.org/10.1039/C5NR04383B.

(253) Bai, S.; Liu, X.; Zhu, K.; Wu, S.; Zhou, H. Metal–Organic Framework-Based Separator for Lithium–Sulfur Batteries. *Nat. Energy* **2016**, *1* (7), 16094. https://doi.org/10.1038/nenergy.2016.94.

(254) Pavlin, N.; Hribernik, S.; Kapun, G.; Talian, S. D.; Njel, C.; Dedryvère, R.; Dominko,

R. The Role of Cellulose Based Separator in Lithium Sulfur Batteries. *J. Electrochem. Soc.* **2019**, *166* (3), A5237–A5243. https://doi.org/10.1149/2.0401903jes.

VI. Scientific production

➢ Oral presentation:

"A non-nucleophilic fluorinated alkoxyborate based electrolyte for rechargeable Ca batteries" oral presentation, attended at ''Towards Futuristic Energy Storage; paving its way through Supercapacitors, Li-ion batteries and beyond '' conference ; Tours (France), 22/01/2020 - 24/01/2020

➢ Publications:

*Jan Bitenc, **Antonio Scafuri**, Klemen Pirnat, Matic Lozinšek, Ivo Jerman, Jože Grdadolnik, Bernard Fraisse, Romain Berthelot, Lorenzo Stievano, Robert Dominko*

"Electrochemical Performance and Mechanism of Calcium Metal–Organic Battery"

Batter. Supercaps , 2020, 3, 1-8

https://doi.org/10.1002/batt.202000197

***Antonio Scafuri**, Lorenzo Stievano, Giuliana Aquilanti, Iztok Arčon, Alen Vinzitin, Rémi Dedryvère, Dominique Foix, Romain Berthelot, Klemen Pirnat, Robert Dominko*

''Spectroscopic insights into rechargeable calcium/sulfur battery"

Chem. Mater., 2020, 32, 19, 8266-8275

https://doi.org/10.1021/acs.chemmater.0c02074

VII. Obširnejši povzetek doktorskega dela v slovenščini

1. Uvod

1.1 Tehnološki razvoj akumulatorjev in trenutno stanje

Elektrokemijska celica je naprava, ki omogoča pretvorbo kemijske energije direktno v električno. Sestavljena je iz negativne in pozitivne elektrode (ki ju nepravilno imenujemo tudi anoda oziroma katoda) in elektrolita. Vsaka elektroda ima svoj elektrokemijski potencial, ki je odvisen od njene fizikalno-kemijske narave.[1] Zaradi redoks reakcij na elektrodah nastane prebitek oz. primanjkljaj elektronov. Med elektrodama je elektrolit, ki je električni izolator. Šele ko sklenemo zunanji električni krog, pride do izmenjave elektronov med elektrodama in sistem spontano reagira vse dokler ne doseže ravnotežja, to je, dokler ne minimizira svoje proste energije.

Poznamo dva tipa elektrokemijskih celic: primarne in sekundarne. Primarne celice ali baterije lahko samo enkrat izpraznimo, nato niso več uporabne. Sekundarne celice ali akumulatorje lahko večkrat izpraznimo in napolnimo. Akumulatorje lahko uporabljamo kot električni izvir ali pa kot shranjevalnike energije in jih v principu lahko sestavimo v izpraznjenem stanju.[2] Moderna »energijska revolucija« se je začela leta 1991, ko je SONY komercializiral prvi litij ionski akumulator. To je povzročilo velike spremembe v komunikacijah, načinu dela, mobilnosti in življenskem slogu zahodne civilizacije v zadnjih 25 letih. Delovanje Li-ionskega delovanja je shematsko prikazano na Sliki 1. Negativna elektroda je sestavljena iz grafita. Le ta lahko shranjuje Li ione med posameznimi grafenskimi plastmi. Pozitivna elektroda je narejena iz materiala, ki lahko interkalira litijev ion – običajno gre za okside prehodnih kovin z visokim redoks potencialom. V primeru $LiCoO_2$ gre za plastovito strukturo, poznamo pa tudi drugačne strukture. Obe elektrodi lahko reverzibilno izmenjujeta Li ione. Pri polnjenju se Li ioni deinterkalirajo iz pozitivne elektrode in interkalirajo v negativno grafitno elektrodo. Pri

praznjenju se proces obrne. Elektrodi sta fizično ločeni in med njima je brezvodni elektrolit, ki prenaša Li ione med elektrodama.[3]

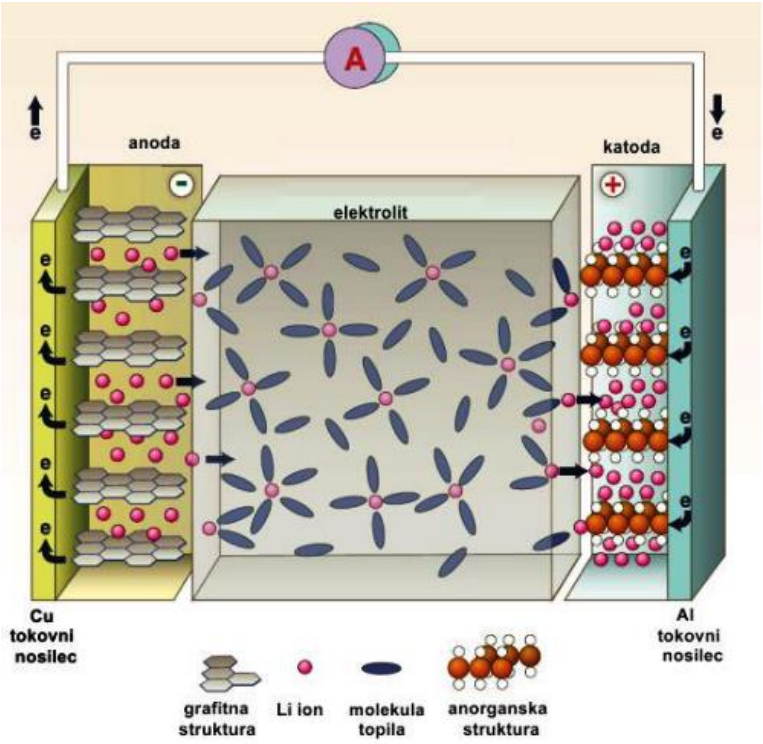

Slika 1: Shema litij ionskega akumulatorja.[3]

Svetovni trg li-ionskih akumulatorjev neprestano raste in cena sodobnih akumulatorjev je v zadnjem desetletju precej upadla. Razvoj novih Li-akumulatorjev je usmerjen v nove tehnologije z boljšimi karakteristikami, predvsem nižjo ceno in večjim dosegom električnih avtomobilov. Poleg tega je pomembno, da bodo akumulatorji nove generacije temeljili na trajnostnih virih in bodo elektrodni materiali narejeni iz elementov, ki so široko razširjeni v zemeljski skorji.

1.2 Kalcijevi akumulatorji

Kalcij je 5 najbolj razširjen element v zemeljski skorji in je s 41500 ppm kar 2000 krat bolj razširjen od litija. Elektrokemijski potencial Ca/Ca^{2+} je -2,87 V proti SHE in je le za 0,17 V višji od litijevega. Specifična kapaciteta Ca je 1,34 A h g^{-1}. Zaradi visoke gostote 1,54 g cm^{-3} ima Ca visoko volumsko specifično kapaciteto 2,06 A h cm^{-3}. Grafit, ki je uporabljen v

sedanjih Li-ionskih baterijah, ima le 0,97 A h cm^{-3}, kar je več kot 2 kratno izboljšanje. Ionski radij Ca^{2+} iona je 1.0 Å, kar je le za 34% več od Li^{+} iona.[4] Razvoj Ca akumulatorjev je počasen predvsem zaradi pomanjkanja ustreznih elektrolitov. Eden od začetnih problemov je pasivizacija Ca anode v stiku s konvencionalnimi Ca solmi, ki lahko popolnoma blokira delovanje transport Ca^{2+} ionov. Zaradi tega je potrebno razviti elektrolit, ki bi omogočal reverzibilno odlaganje/odtapljanje Ca pri sobni temperaturi, bil kompatibilen z Ca anodo, imel dovolj široko napetostno stabilnostno okno in hkrati imel visoko ionsko prevodnost. Na anodno stabilnost elektrolita bistveno vpliva kemijska struktura aniona.[5]

2. Namen Dela

Namen tega projekta je bil razviti in testirati nove elektrolite in elektrodne materiale za kalcijeve akumulatorje, ki bi kot negativno elektrodo uporabljali kovinski kalcij in omogočali delovanje pri sobni temperaturi. Doktorat je bil izveden na dveh lokacijah, v Univerzi v Ljubljani in Univerzi v Montpellierju. Ekipa iz Ljubljanske univerze je prispevala izkušnje o organskih katodah in razvoju elektrolitov, medtem ko je ekipa iz Montpellierja prispevala znanje iz kemije materialov. Doktorska disertacija je razdeljena po poglavjih, ki so kronološko in logično razvrščena. Cilj je bil razviti primeren elektrolit in ga nato uporabiti v Ca akumulatorju v kombinaciji z različnimi pozitivnimi elektrodnimi materiali. Pri tem smo uporabili organske katode, ki so jih v Ljubljani razvijali za Li-, Mg- in Al- akumulatorje. Kot drugi tip smo uporabili žveplove katode, s katerim imajo v Montpellierju bogate izkušnje iz Li-S in Mg-S akumulatorskih sistemov.

Prvi cilj doktorske disertacije , opisan v drugem poglavju, je bilo razviti in okarakterizirati novo Ca sol. Temu je sledila priprava elektrolita, ki bi imel vse zaželene lastnosti, naštete v prvem poglavju. Elektrokemijsko nalaganje kalcija je kontrolirano s površinskim filmom. To pomeni da sveži Ca depoziti reagirajo z elektrolitom in tvorijo pasivno plast, ki preprečuje nadaljnje reverzibilno odlaganje Ca ter s tem poslabšajo Coulombsko učinkovitost. Na začetku tega doktorskega dela, leta 2017, je skupina pod vodstvom Petra g. Brucea[6] objavila prvi primer reverzibilnega odlaganja Ca pri sobni temperaturi, pri čemer so kot elektrolit uporabili $Ca(BH_4)_2$ v THF. Ker je opisan elektrolit imel precej nizko anodno stabilnost 2.5 V proti Ca/Ca^{2+}, ni bil primeren za pozitivne elektrodne materiale z visoko napetostjo. Ker je BH_4^-

anion močan nukleofil in reducent, tudi ni primeren za uporabo skupaj z organskimi elektrodnimi materiali, ki vsebujejo elektrofilno karbonilno skupino. Naša ideja je bila razviti nov Ca elektrolit, ki bi bil primeren za praktično uporabo v Ca akumulatorjih. Tekom naših raziskav sta dve raziskovalni skupini pod vodstvom Fichtnerja[7] in Nazar[8] objavila dva članka, kjer so pripravili enako sol kot mi in jo uporabili v Ca akumulatorju. Ker smo s tem izgubili na inovativnosti naših raziskav, smo razvili sintezo $Ca[B(hfip)_4]_2$ soli pri sobni temperaturi, medtem ko sinteza po Fichtnerju poteka pod refluksom. Nato smo se lotili detajlne karakterizacije Ca soli z mnogimi analitskimi metodami da bi dokazali strukturo, čistost in kemijsko-fizikalne lastnosti ter kako te lastnosti vplivajo na delovanje Ca akumulatorja.

Drugi cilj je bil pripraviti Ca-organski akumulator, kar je opisano v tretjem poglavju. Razvoj Ca akumulatorjev je počasen tudi zaradi neustreznih katodnih materialov. Zaradi večje gostote naboja in večjega radija Ca^{2+} iona v primerjavi z Li^+ je interkalacija Ca^{2+} iona zelo problematična v anorganskih katodnih materialih. Ker organski materiali veljajo za bolj fleksibilne od anorganskih, smo testirali dva redoks aktivna organska polimera poli(antrakinon) (PAQ) in poli(antrakinonil sulfid) (PAQS). Ta dva polimera smo izbrali zaradi obetavnih rezultatov na sorodnih Mg akumulatorskih sistemih. S pomočjo IR spektroskopije smo na primeru Ca-PAQS akumulatorja potrdili redoks mehanizem karbonilne skupine in dokazali njeno kompatibilnost z $Ca[B(hfip)_4]_2$ soljo

Tretji cilj doktorske disertacije je bil razviti Ca-S akumulator, ki bi imel stabilno delovanje pri sobni temperaturi. Kot žveplovo katodo smo uporabili žveplo, nanešeno na nosilec iz ogljikove tkanine in elektrolit na osnovi fluiriranega alkoksiborata $Ca[B(hfip)_4]_2$.Redoks mehanizem med polnjenjem in praznjenjem Ca-S akumulatorja smo potrdili s pomočjo XPS in XAS spektroskopije. Pri praznjenju se žveplo najprej reducira do daljših topnih polisulfidov, ki postajajo krajši in na koncu dobimo netopen CaS. Pri polnjenju poteka reverzibilen proces v obratni smeri vse do nastanka žvepla. Ta mehanizem je zelo podoben kot pri Li-S in Mg-S akumulatorjih. Zaradi velike razširjenosti kalcija v zemeljski skorji in podobni specifični volumetrični gostoti kot litij, je Ca-S tehnologija zanimiva alternativa Li-S akumulatorjem v prihodnosti.

3. Rezultati in diskusija

3.1 Dizajniranje elektrolita

Da bi se čimbolj izognili sledovom vode, smo celotno pripravo elektrolita izvedli v inertni argonovi atmosferi znotraj suhe komore (vsebnost vode in kisika pod 0.1 ppm). $Ca[B(hfip)_4]_2$ sol smo sintetizirali iz $Ca(BH_4)_2$ x 2THF (1,07 gr. 5 mmol), ki smo ga najprej raztopili v 10 mL brezvodnega 1,2-dimetoksietana (DME). Tej suspenziji smo v roku 30 min počasi dodali 4,5 mL brezvodnega heksafluoroizopropanola (7,14 g, 42,5 mmol) ob intenzivnem mešanju. Motno suspenzijo smo nato mešali 20 ur pri sobni temperaturi, nato smo pod znižanim tlakom odpareli hlapne komponente in dobili $Ca(BH_4)_2 \times 2DME$ v obliki belega prahu, ki smo na nato sušili pri 50 °C v vakuumu čez noč (8,32 g, 94%).[9]

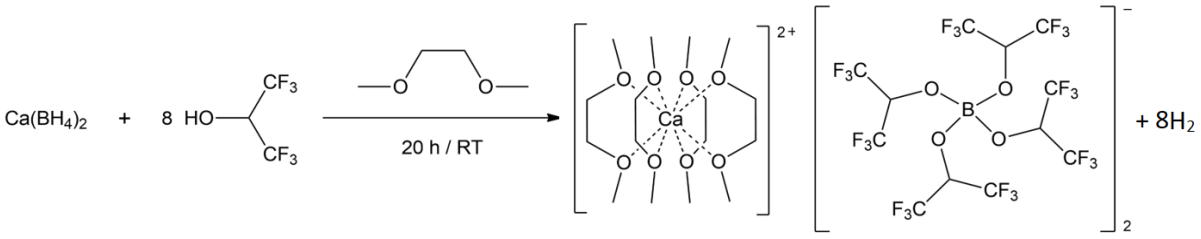

Slika 2: Shema sinteze $Ca[B(hfip)_4]_2 \times 4DME$ soli.[9]

Ker pri reakciji nastane plinast vodik kot stranski produkt, prebitni 1,1,1,3,3,3,-hexafluoroizopropanol (T_v=56 °C) in DME topilo (T_v=85 °C) pa sta zelo hlapna, je izolacija in čiščenje Ca soli zelo enostavna – samo odparimo hlapne komponente in dobimo čisti produkt.

Tako dobljeno $Ca[B(hfip)_4]_2 \times 4DME$ sol smo karakterizirali z raznimi tehnikami, kot so ^1H, ^{13}C and ^{19}F NMR, FTIR, Ramansko spektroskopijo, praškovno in monokristalno rentgensko spektroskopijo.

^1H NMR (600 MHz, MeCN–*d3*)**:** δ 4,72 (br m, 8H, –CH–$(CF_3)_2$); 3,49 (s, 16H, –OCH_2–); 3,32 (s, 24H, OMe) ppm. Singletna signala pri 3,49 in 3,32 ppm pripadata protonom CH_3– in –CH_2– skupinam iz topila DME, ki koordinira Ca sol in razmerje integralov ustreza koordinacijskemu razmerju Ca sol/DME = ¼. Širok multiplet signal pri 4,72 ppm ustreza protonom v CF_3–CH–

CF_3, ki so so sklopljeni s šestimi F atomi ($^3J_{H–F}$ = 2-15 Hz), vendar v izmerjenem NMR spektru ni možno razločiti septetne oblike (Slika 3a).

^{19}F NMR (565 MHz, MeCN–*d3*)**:** -75,7 (d, $^3J_{HF}$ = 6.5 Hz) ppm. Trifluoroocetna kislina je bila uporabljena kot interni standard s premikom -76.72 ppm. Ker pri snemanju nismo uporabili H–F razklopitve, imamo v spektru viden dublet z značilno sklopitvijo $^3J_{HF}$ = 6.5 Hz (Slika 3b).

^{13}C NMR (151 MHz, MeCN–*d3*)**:** 1^{2}3,9 (q, $^1J_{CF}$ = 285 Hz); 72,3; 70,5 (s, $^2J_{CF}$ = 32 Hz); 59,2 ppm. ^{13}C NMR spektre smo razklopili od ^{1}H, ne pa tudi od ^{19}F. Zaradi tega imajo –CF_3 ogljiki značilno kvartetno ($^1J_{CF}$ = 285 Hz) in CF_3–*CH*(–O–)–CF_3 septetno sklopitev ($^2J_{CF}$ = 32 Hz) (Slika 3c).

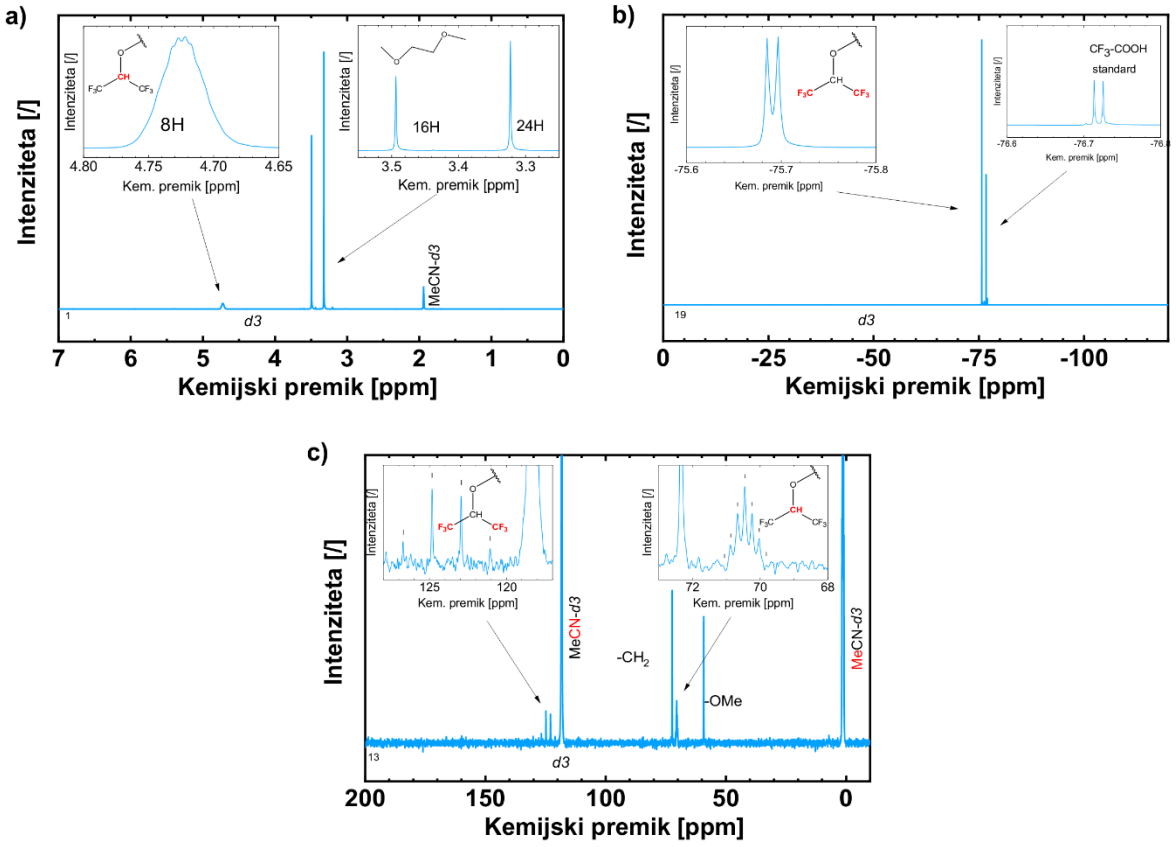

Slika 3: a) ^{1}H NMR b) ^{19}F NMR in c) ^{13}C NMR spektri $Ca[B(hfip)_4]_2$×4DME soli v MeCN-d3 topilu.[9]

FTIR spektre (Slika 4a) smo posneli znotraj suhe komore (Ar atmosfera) v ATR načinu (Ge kristal) v območju 4000–600 cm^{-1}. Najbolj intenziven vrh pri 1187 cm^{-1} lahko pripišemo

B−O−C vzdolžnemu nihanju in CF_3 sim/antisimetričnem nihanjem. Vrh pri 1381 cm^{-1} lahko pripišemo nihaju C−CF_3 skupin. Močan signal pri 686 cm^{-1} pripada deformaciji CF_3 skupine. Dva signala pri 1097 cm^{-1} in 1058 cm^{-1} pripadata C–O prečnim nihanjem iz koordiniranega DME in borovega kompleksa.

Ramanski spekter $Ca[B(hfip)_4]_2$×4DME soli je bolj kompleksen in manj informativen kot infrardeči spekter zaradi nizke intenzivnosti CF_3 in B–O–C skupin. Opazimo lahko prisotnost koordiniranega DME: signali 3000–2800 cm^{-1} pripradajo simetričnem in antisimetričnem vzdolžnim nihanjem ter 1483 in 1455 cm^{-1} deformaciji CH_3 in CH_2 skupin. Vrh pri 879 cm^{-1} pripada C–O deformaciji in 722 cm^{-1} pripada C–C deformaciji. Signal pri 805 cm^{-1} lahko pripišemo simetričnemu B–O–C nihanju.[9]

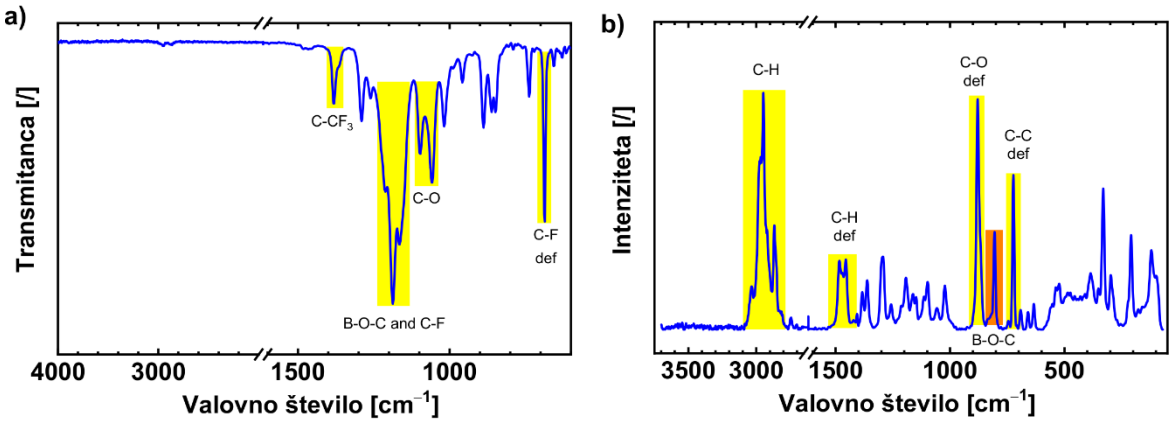

Slika 4: a) FTIR in b) Raman spektra $Ca[B(hfip)_4]_2$×4DME soli.[9]

Pripravili smo kalcijev elektrolit na osnovi 0,3 M $Ca[B(hfip)_4]_2$ v DME in ga elektrokemijsko testirali. Najprej smo preverili ali je z njim možno reverzibilno odlagati kalcij, pri čemer smo uporabili kovinski kalcij kot protielektrodo in nerjaveče jeklo kot delovno elektrodo. Kot lahko vidimo iz CV krivulje (Slika 5a) gre prvih nekaj ciklov za aktivacijo, kar je najbrž povezano s prenapetostjo na Ca protielektrodi. Na začetku je potrebna za odlaganje Ca napetost -0,2 V, za njegovo odstranjevanje pa +0,2 V proti Ca elektrodi. Coulombska učinkovitost tega procesa je na začetku 53%, nato zraste na 67%, kjer se ustali (Slika 5b). Razmeroma nizka Coulombska učinkovitost bi lahko bila posledica reakcije kalcijevih depozitov z elektrolitom ali zaradi izgube električnih kontaktov med kalcijevimi depoziti in protielektrodo iz nerjavečega jekla.[9]

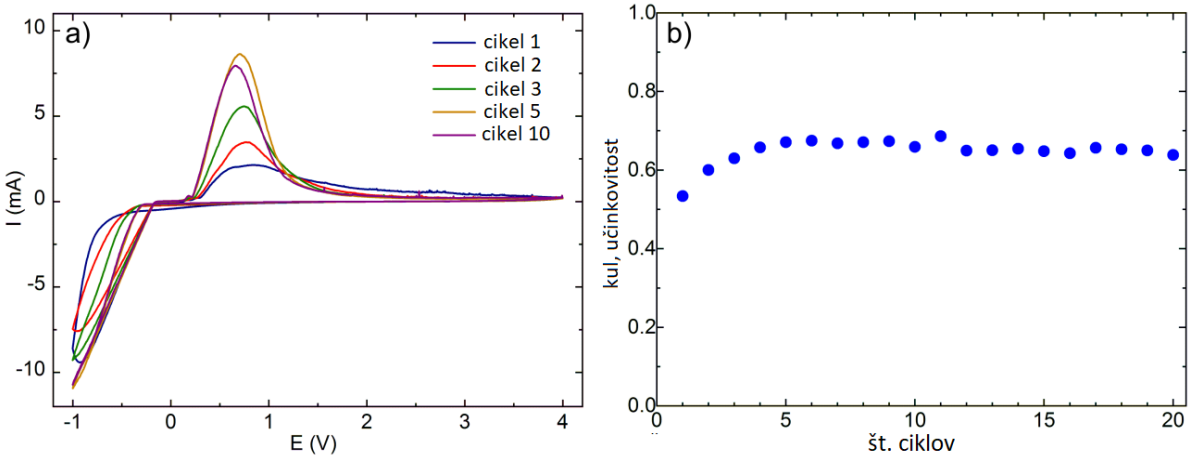

Slika 5: a) CV odlaganja/odstranjevanja kalcija na nerjavečem jeklu v 0.3 M $Ca[B(hfip)_4]_2$ v DME elektrolitu, napetostno okno -1.0 to 4.0 V proti Ca/Ca^{2+}, hitrost preleta 25 mV/s, sobna temperatura. b) Coulombska učinkovitost CV procesa.[9]

3.2 Kalcij-organski akumulator

3.2.1 Elektrokemijsko delovanje

Zaradi precejšnje velikosti Ca^{2+} iona in velike gostote naboja (2+) je zelo težavna interkalacija Ca^{2+} ionov v anorganske katodne materiale. Po drugi strani so organski katodni materiali zaradi svoje fleksibilnosti precej bolj perspektivni za uporabo v Ca akumulatorjih. Na Kemijskem inštitutu imajo precej izkušenj z Mg-organskimi akumulatorji.[10] Z uporabi katodnih materialov na osnovi poli(antrakinona) PAQ in poli(antrakinonil sulfida) PAQS so dobili precej dobro delovanje v Mg akumulatorskih sistemih,[11] zato smo se odločili ta dva materiala testirati tudi v Ca akumulatorskem sistemu. PAQS smo pripravili po recepturi in literature.[12] Za pripravo PAQS/MWCNT kompozita smo uporabili 0,30 g večstenskih ogljikovih nanocevk (MWCNT, NTL, C-grade), ki smo jih dispergirali v 50 mL *N*-metil pirolidona (NMP) z ultrazvočnim prstom (Sonics Vibra Cell CV 334) 2 krat po 20 min. Nato smo dodali 1,5-dikloroantrakinon (3,41 g) in ponovno dispergirali z ultrazvokom za 20 min. Zmes smo ohladili na 8 °C in dodali

brezvoden Na_2S (0,93 g) ter ponovno dispergirali z ultrazvokom za 30 min. Reakcijo smo nato izvajali pri 200 °C čez noč v inertni atmosferi. Po končani reakciji smo zmes ohladili, filtrirali in trden produkt spirali z vročo vodo (2×) in acetonom (2×). Produkta smo dodatno spirali z EtOH preko Soxhletove ekstrakcije čez noč in nato posušili pri 50 °C. Končni izkoristek reakcije je bil 95%.

Samostoječe elektrode smo napravili iz aktivnega materiala, Printex XE2 saj in teflona kot veziva v masnem razmerju 60:30:10. Zmes smo mleli v krogličnem mlinu Retsch PM100 pri 300 obratih na min ob dodatku 2-propanola kot topila. Po mletju smo kompozit ročno gnetli v ahatni terilnici dokler nismo dobili gumijast material. Tega smo razvaljali na stekleni plošči do ustrezne debeline (2-3 mg aktivnega materiala cm^{-2}), previdno odlepili s površine, sušili na 50 °C in iz tega izsekali elektrode s premerom 12 mm. Te smo nato dodatno sušili v suhi komori pri 50 °C.

Elektrokemijske meritve smo izvajali v dvo ali troelektrodnih Swagelok celicah, ki smo jih sestavljali v suhi komori. Za protielektrodo in referenčno elektrodo (3 elektrodna celica) smo uporabili kovinski kalcij (99,5% Alfa Aesar). Za separator smo uporabili papir na osnovi steklenih vlaken (Whatman GF/A). Za delovno elektrodo smo uporabili prej omenjene samostoječe elektrode na osnovi aktivnega materiala. Meritve smo izvajali v potencialnem oknu 1,3–3,3 V proti Ca/Ca^{2+} na napravah WMP3 ali MPG2 Biologic S. A.

Slika 6a prikazuje delovanje Ca-organskega akumulatorja na osnovi PAQS/MWCNT aktivnega materiala v 3 elektrodni celici. Pri praznjenju dobimo plato s povprečno napetostjo 2,2 V, kar je bolje razvidno iz diferenčnega grafa dQ/dE proti E (Slika 6b). Po 10 ciklih dobimo kapaciteto 114 mAh / g, kar potrjuje, da sta tako hitrost bledenja na katodi kot tudi povečanje prevelikega potenciala na Ca anodi odgovorni za hitro propadanje kapacitete v prejšnji 2-elektrodni celici večji prispevek slednjih (Slika 6c). Iz tega lahko sklepamo, da redukcija antrakinonskega polimera poteka v obliki enostopenjske dvoelektronske reakcije ali pa pa gre za dve stopnji z zelo podobnim potencialom. V trielektrodni celici opazimo tudi veliko povečanje prenapetosti med Ca referenčno in protielektrodo s cikli, kar tudi razloži dejstvo zakaj navadna 2 elektrodna celica po 6 ciklih neha delovati. Do tega pride zaradi pasivizacije Ca elektrode, ko le ta reagira z elektrolitom. Pri tem nastanejo na kalcijevi površini razni degradacijski produkti ter CaF_2, kar je opisano v literaturi.[7,8]

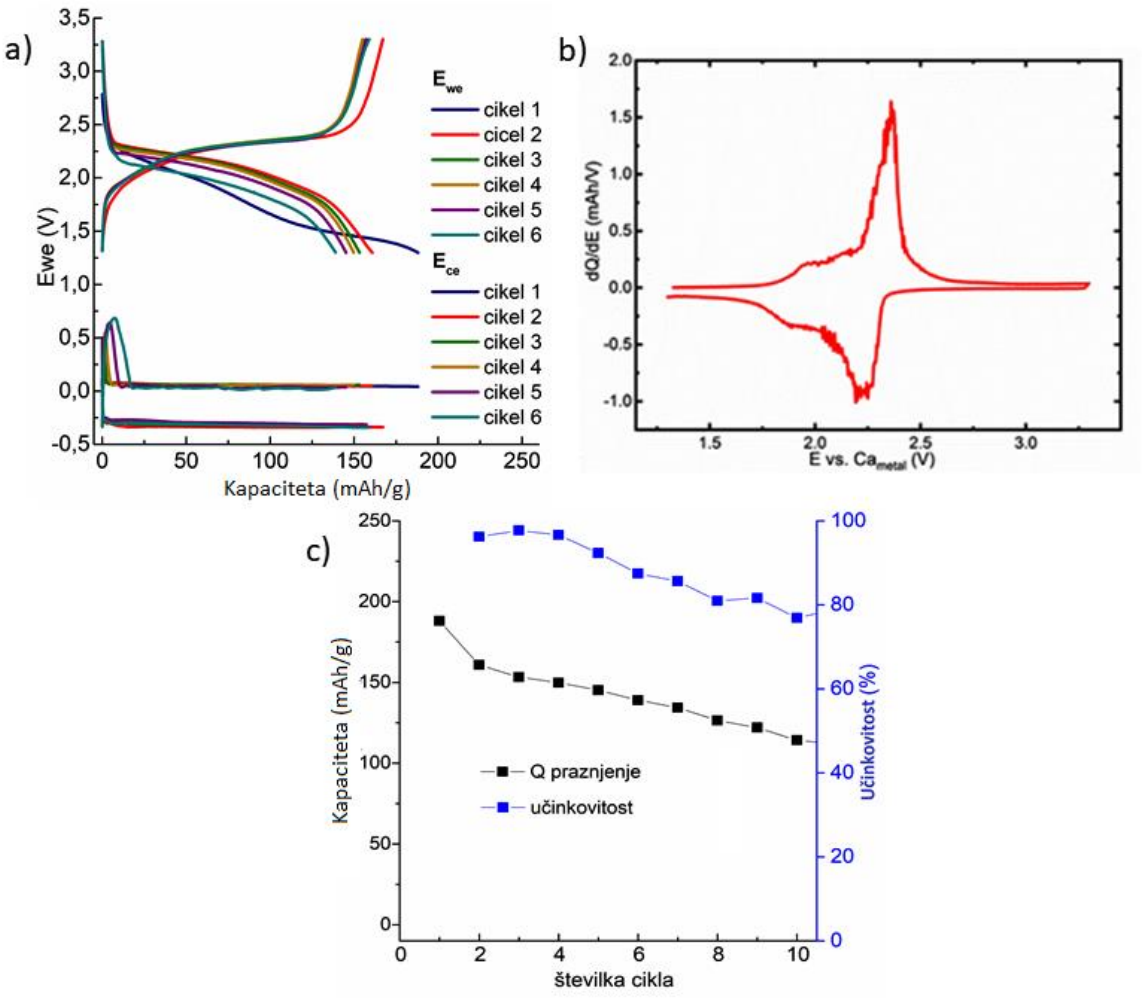

Slika 6: a) Galvanostatske meritve Ca-PAQS/MWCNT trielektrodne celice s Ca referenčno elektrodo, tok 0,5C oz. 122,5 mA/g. Gornje krivulje prikazujejo potencial PAQS/MWCNT delovne elektrode, medtem ko spodnje prikazujejo potencial Ca protielektrode proti referenčni elektrodi. Pozitivne vrednosti predstavljajo odtapljanje, negativne pa nalaganje Ca na protielektrodo. b) Diferenčni graf trielektrodne celice dE/dQ v odvisnosti od napetosti PAQS/MWCNT proti Ca/Ca^{2+}, tretji cikel. c) Izpustna zmogljivost in Coulombic učinkovitost med kolesarjenjem.[9]

3.2.2 *ex situ* FTIR spektroskopija

Za določitev redoks mehanizma med delovanjem Ca-PAQS/MWCNT akumulatorja smo uporabili IR spektroskopijo. Akumulatorske celice smo razdrli v suhi komori, previdno vzeli elektrode in jih trikrat spirali z DME, da smo odstranili elektrolit. Vse IR meritve elektrod smo izvedli s pomočjo spektrometra Bruker Alpha II v ATR tehniki na Ge kristalu, v inertni atmosferi (suha komora), da smo preprečili oksidacijo izpraznjene elektrode. S pomočjo IR spektrov smo pokazali, da se karbonilna skupina reverzibilno reducira do fenolata, pri čemer se porabi en elektron (Slika 7a).

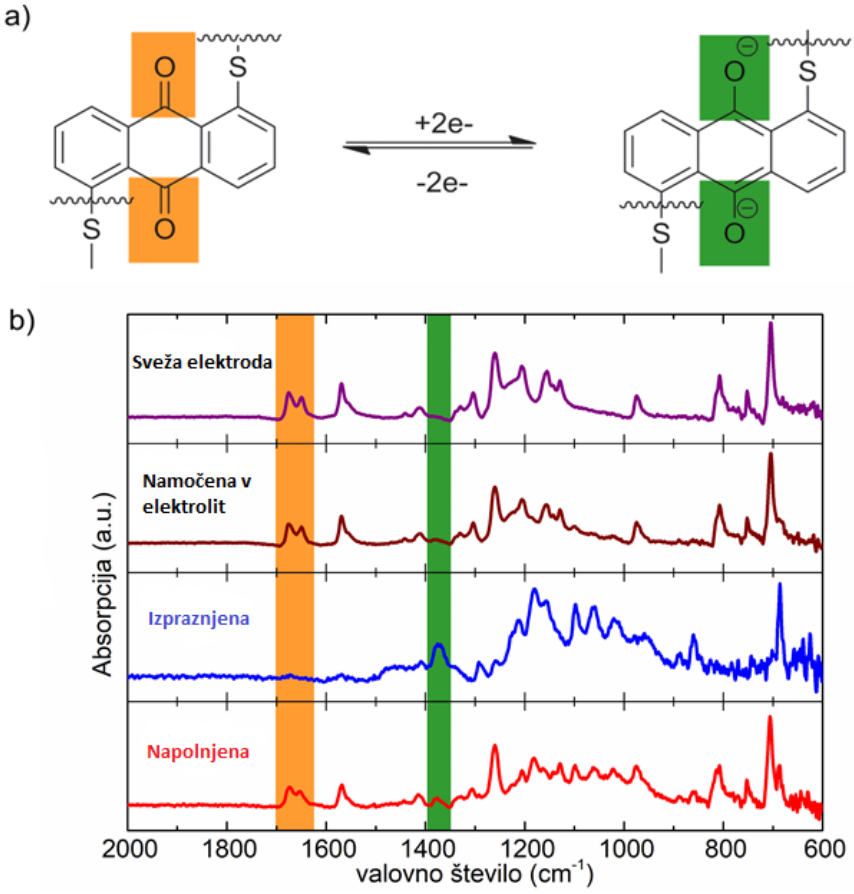

Slika 7: a) Elektrokemijska reakcija PAQS med praznjenjem in polnjenjem. b) ATR-IR spektri sveže PAQS/MWCNT elektrode (vijolična), namočene v elektrolit (rjava), izpraznjene (modra) in napolnjene elektrode (rdeča).[9]

Pomerili smo štiri IR spektre PAQS/MWCNT elektrod: svežo, namočeno v elektrolit in nato sprano, izpraznjeno in napolnjeno elektrodo. Elektroda namočena in v elektrolit in nato sprana je služila za kontrolo. S tem smo preverili ali aktivni material morda reagira z elektrolitom (Slika 7b). V IR spektrih lahko opazimo veliko razliko med izpraznjeno in napolnjeno elektrodo. Za PAQS so značilni sledeči vrhovi: Dva vrhova pri 1674 and 1650 cm^{-1} pripadata vzdolžnemu nihanju karbonilne C=O vezi, vrh pri 1570 cm^{-1} pripada vzdolžnem nihanju –C=C– vezi in vrh pri 704 cm^{-1} pripada deformaciji C–H vezi. Vsi ti vrhovi pri praznjenju izginejo, pri čemer se pojavi novi vrh pri 1374 cm^{-1}, ki pripada fenolatni skupini kar je v skladu z literaturnimi podatki na monovalentnih Li[13] in dvovalentnih Mg[13] akumulatorjih.

Pri napolnjeni elektrodi se ponovno pojavijo značilni vrhovi za C=O in –C=C– vez, kakor tudi deformacijo C–H vezi kar nakazuje na reverzibilnost te redoks reakcije. V območju med 1100 in 1000 cm^{-1} se pri izpraznjeni elektrodi pojavijo novi vrhovi. Te lahko razložimo s tem, da Ca^{2+} ni edini kation, ki se veže na fenolatni anion, ampak imamo tudi $Ca[B(hfip)_4]^+$ kation in ti vrhovi pripadajo $[B(hfip)_4]^-$ anionu. Tudi v napolnjenem stanju ti vrhovi ne izginejo popolnoma, kar je verjetno povezano z nepopolno oksidacijo med polnjenjem.

3.3 Inovativen Ca-Žveplov akumulator

3.3.1 Elektrokemija

Gumbne akumulatorske celice (CR2031, 316L) smo sestavljali v suhi komori pod inertno Ar atmosfero (vsebnost vode in kisika pod 0,5 ppm). Kalcijeve elektrode smo izrezali iz Ca folije (ACI alloys, ZDA) debeline 0,5 mm, nakar smo njihovo oksidirano površino očistili s praskanjem s skalpelom. Žveplove katode ACC/S smo pripravili iz ogljikove tkanine, prepojene z žveplom, kakor je opisano v literaturi.[14] Kot separator smo uporabili dva sloja papirja, narejenega iz steklenih vlaken (Whatman, GF/A). Kot elektrolit smo uporabili 120 µl *0,5 M* $Ca[B(hfip)_4]_2$ raztopljen v DME. Galvanostatske meritve smo izvajali pri sobni temperaturi v potencialem oknu 0.5–3.5 V proti Ca/Ca^{2+} pri treh različnih tokovnih gostotah C/10, C/20 in C/50. Elektrokemijske meritve smo izvajali na potenciostatu Maccor 4200 ali Biologic VMP3.

Delovanje Ca-S gumbnega akumulatorja smo testirali pri treh različnih tokovnih gostotah C/50, C/20 in C/10 v istem potencialnem oknu (Slika 8).

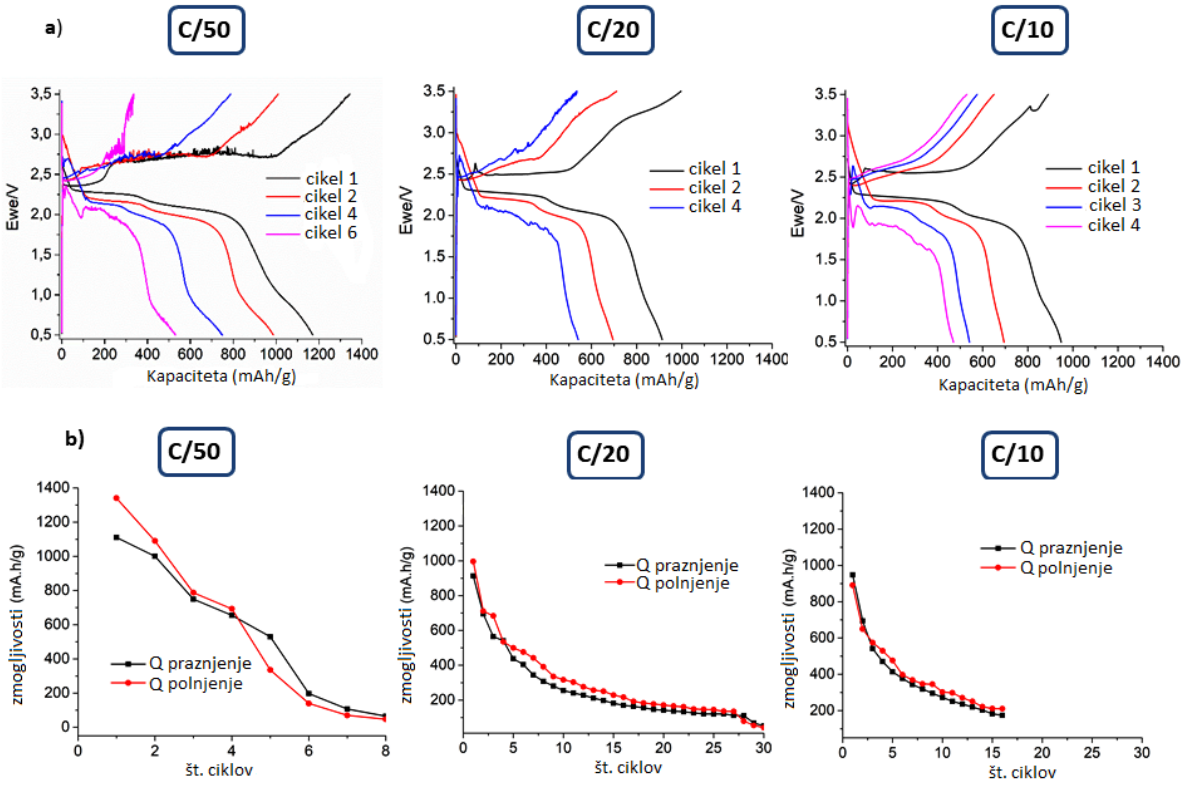

Slika 8: Galvanostatske krivulje (a) in stabilnost kapacitete s cikli (b) Ca/ S akumulatorja na osnovi 0,5M $Ca[B(hfip)_4]_2$ v DME elektrolita.[15]

Pri nizkem toku C/50 dobimo v prvem ciklu praznilno kapaciteto 1171 mA h g^{-1} in Coulombsko učinkovitost 81%. Nizko Coulombsko učinkovitost lahko razložimo z migracijo polisulfidov, ki je pri nizkih tokovih bolj opazna (polysufide shuttle effect). Že v prvih ciklih opazimo značilno žagasto obliko krivulje pri polnjenju in večanje polarizacije s cikli. Po 8 ciklih baterija neha delovati. To lahko razložimo s pasivizacijo Ca elektrode, ki po 8 ciklih popolnoma blokira površino Ca elektrode. Pasivizacija je pri nizkih tokovih bolj opazna, saj so Ca depoziti dalj časa v stiku z elektrolitom.

Akumulatorska celica pri toku C/20 sicer kaže precej boljše delovanje, saj ima po 28 ciklih še vedno kapaciteto 150 mA h g^{-1}. Med prvim praznjenjem dobimo dva platoja pri napetostih 2.25

V in 2.10 V proti Ca/Ca^{2+}. Glede na praznilno kapaciteto 920 mAh/g se 55% žvepla v akumulatorju pretvori v CaS.

Pri C/10 dobimo podobno začetno kapaciteto in podobno stabilnost delovanja kot pri C/20. Zaradi hitrega ponljenja in praznjenja dobimo visoko Coulombsko učinkovitost 95%. Pri polnjenje opazimo le en plato, polarizacija pa je zaradi višjih tokov bolj opazna kot pri C/20. V vseh treh primerih opazimo večanje polarizacije s cikli, kar je povezano z postopno pasivizacijo Ca anode.

3.3.2 Rentgenska fotoelektronska spektroskopija (XPS)

Rentgenska fotoelektronska spektroskopija (XPS) omogoča kemijsko analizo površin. Poleg elementne sestave nam omogoča tudi določitev oksidacijskega stanja in kemijskega okolja. V našem primeru smo XPS metodo uporabili za analizo žveplovih elektrod in tako določili vsebnost žvepla, polisulfidov, končnega produkta CaS. Izmerili smo S 2p, Ca 2p in F 1s XPS spektre ACC/S elektrod pri različnih stopnjah izpraznjenosti in napolnjenosti Ca-S akumulatorja kot je prikazano na Sliki 9. Pri tem smo zaradi topnosti polisulfidov uporabili nesprane elektrode.

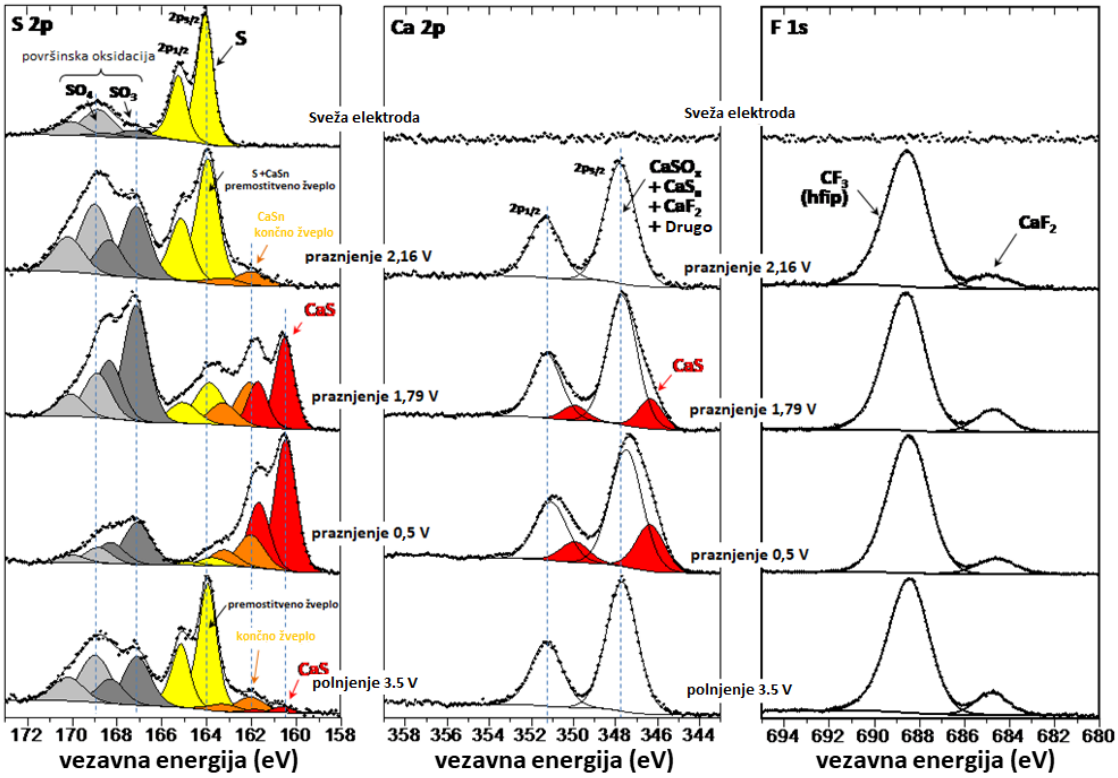

Slika 9: XPS S 2p, Ca 2p in F 1s spektri ACC/S kompozitne žveplove elektrode pri različnih stopnjah izpraznjenosti in napolnjenosti Ca-S akumulatorja.[15]

Med praznjenjem se S 2p signal za elementarno žveplo postopno zmanjšuje, pri čemer ga skoraj v celoti nadomestita dva nova signala: vrh pri 162 eV ustreza terminalnim žveplovim atomom v polisulfidih, vrh pri 160,5 eV pa žveplu v CaS. Pri tem je potrebno omeniti, da na ta način ne moremo ločiti med elementarnim žveplom in mostovnimi žveplovimi atomi v polisulfidih. Kljub temu lahko iz razmerja med mostovnimi in terminalnimi žveplovimi atomi določimo povprečno dolžino polisulfidov. V začetni fazi praznjenja akumulatorja imamo dolge polisulfide S_8^{2-}, ki se nato postopno krajšajo do S_2^{2-}. V končni fazi praznjenja pride do nastanka netopnega CaS produkta. Med polnjenjem se dogaja obraten proces. Netopen CaS se najprej pretvori v krajše polisulfide, ti se daljšajo in na koncu pretvorijo nazaj v elementarno žveplo.

Podobno informacijo lahko dobimo tudi iz Ca $2p_{3/2}$ XPS spektrov, čeprav je težje razločiti med posameznimi specijami. Ker je signal od CaS (346,3 eV) dovolj drugačen od ostalih Ca spojin (347,8 eV), lahko pri prazni elektrodi opazimo rahel premik Ca $2p_{3/2}$ vrha k nižji vrednosti.

Iz F1s XPS spektrov lahko sklepamo na prisotnost $Ca[B(hfip)_4]_2$ soli na površini elektrode, kar je pričakovano, ker smo uporabili nesprane elektrode. Poleg tega se pojavi manjši vrh pri 684,7 eV. Le ta vrh ustreza CaF_2 in nastane pri razgradnji kalcijeve soli ter sestavlja okoli 1-3 at. % površine elektrode.

3.3.3 *Operando* rentgenska absorpcijska spektroskopija na žveplovem K-robu

Operando rentgenska absorbcijska spektroskopija (XAS) na žveplovem K-robu je ena od tehnik, kjer lahko spremljamo oksidacijsko stanje in kemijsko okolje žvepla med samim delovanjem akumulatorja – tako na sami elektrodi, kakor tudi v elektrolitu. To je v primeri žveplovih akumulatorjev zelo koristna informacija, saj med polnjenjem in praznjenjem nastajajo razni polisulfidi, topni v elektrolitu.[16]

Operando XAS meritve smo izvajali na ACC/S žveplovi elektrodi, kjer je žveplo (10 wt. %) nanešeno na ogljikovo tkanino. Za anodo smo uporabili Ca folijo, za elektrolit pa raztopino 0,5 M $Ca[B(hfip)_4]_2$ v DME (250 µL). Galvanostatska krivulja v in situ akumulatorski celici kaže precej cečjo polarizacijo kot v gumbni celici. Zaradi tega smo celico praznili pri nizkem toku C/25 v širokem potencialnem oknu od 0,5 do 4,0 V proti Ca^{2+}/Ca. XAS spekter v popolnoma izpraznjenem stanju smo pomerili šele po 3 urnem držanju napetosti pri 0,5 V proti Ca/Ca^{2+}. Pod temi pogoji smo pri praznjenju uspeli porabiti 0,6 mola Ca na mol žvepla, pri sledečem polnjenju pa vrniti 0,4 mola Ca na mol žvepla – kar je podobno kot pri gumbni akumulatorski celici. Operando XAS meritve smo izvedli iz zadnje strani žveplove katode, rezultati so prikazani v bližini absorpcijskega roba (X-ray Absorption Near-Edge Structure, XANES) in so prikazani na Sliki 10.

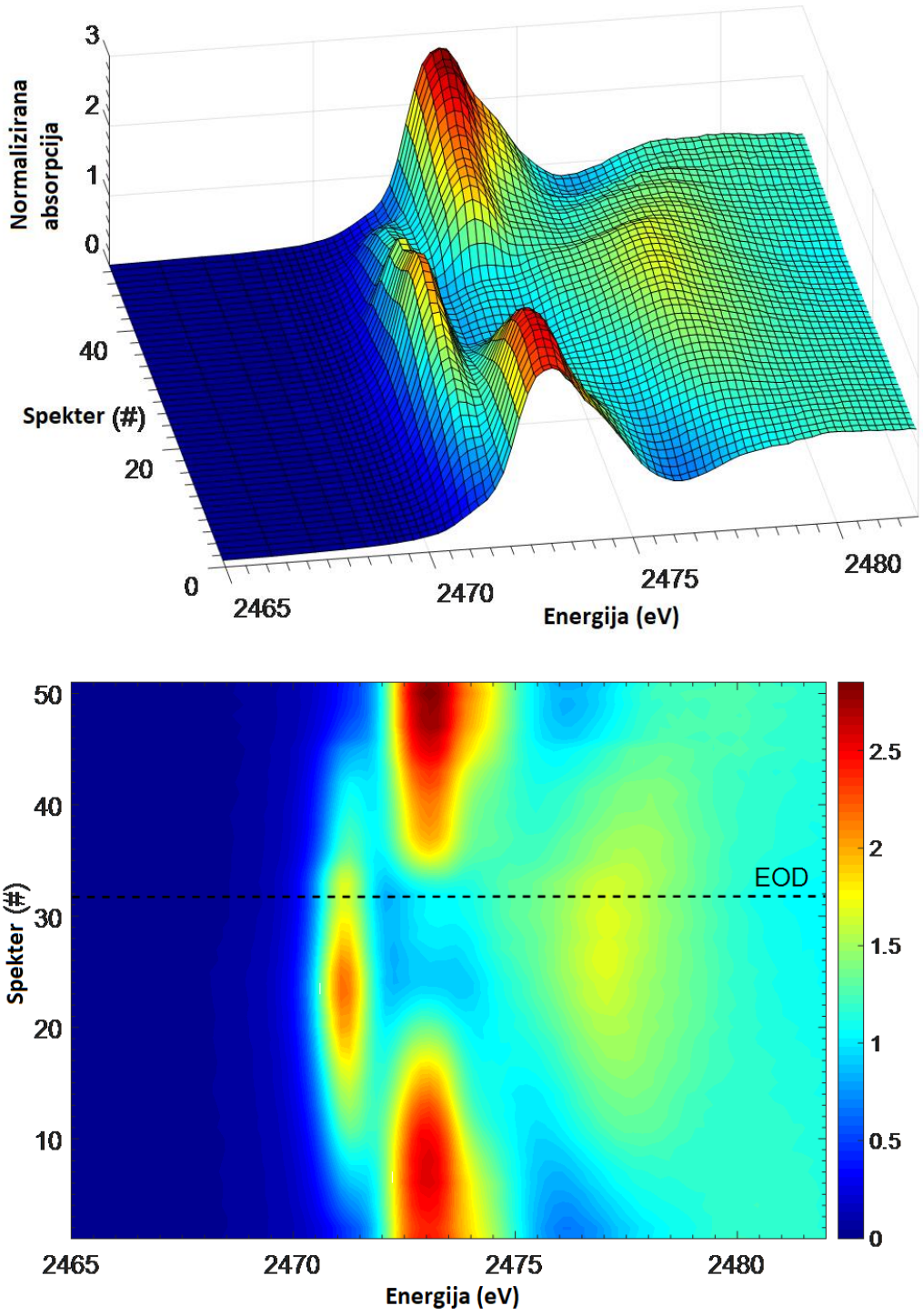

Slika 10: 3D (zgoraj) in topografski pogled (spodaj) na XANES žveplov K-robni spekter med polnjenjem in praznjenjem Ca-S akumulatorja pri C/25. Črtkana črta (EOD) predstavlja popolnoma izpraznjen akumulator.[15]

4. Zaključek

Prvi cilj doktorske disertacije je bil razviti novo kalcijevo sol na osnovi šibko koordinativnega heksafluoroizopropoksi boratnega aniona $Ca[B(hfip)_4]_2$ in jo okarakterizirati z raznimi analitskimi metodami. Elektrokemijski testi na elektrolitu 0,5 M $Ca[B(hfip)_4]_2$ v DME so pokazali obetavne rezultate, kot so visoka oksidativna stabilnost, visoka ionska prevodnost in visoka Coulombsko učinkovitost za elektrokemijsko odlaganje/odstranjevanje kalcija.

Nato smo testirali delovanje novega Ca elektrolita v Ca-organskem akumulatorju, kjer smo kot katode uporabili polimera poli(antrakinon) PAQ in poli(antrakinonil sulfid) PAQS. Dvoelektrodne akumulatorske celice po nekaj ciklih nehali delovati. S pomočjo trielektrodnih meritev smo odkrili, da je razlog velika polarizacija zaradi pasivizacije Kalcija. Reverzibilnost elektrokemijske reakcije PAQS med polnjenjem in praznjenjem akumulatorja smo dokazali s pomočjo ex situ IR spektroskopije, kjer smo lahko spremljali reverzibilno redukcijo karbonilne skupine do fenoksida.

Zadnji cilj je bil testiranje našega Ca elektrolita v Ca-S akumulatorju pri sobni temperaturi. Žveplova katoda je bila narejena iz ogljikove tkanine, impregnirane z žveplom (ACC/S). Elektrokemijsko reakcijo žvepla smo spremljali z rentgensko fotoelektronsko (XPS) in rentgensko absorpcijsko (XAS) spektroskopijo. Z obema metodama smo dokazali, da redukcija žvepla pri praznjenju akumulatorja poteka preko topnih polisulfidov, ki se na koncu pretvorijo v netopen CaS. S pomočjo XPS smo na površini elektrod zaznali razpadne produkte elektrolita, ki najverjetneje pripadajo Ca boratu. Ta pasiven sloj morda igra pomembno vlogo pri stabilizaciji elektrode v stiku z elektrolitom.

Literatura

(1) Van Noorden, R. The Rechargeable Revolution: A Better Battery. *Nature* **2014**, *507* (7490), 26–28. https://doi.org/10.1038/507026a.

(2) Sarma, D. D.; Shukla, A. K. Building Better Batteries: A Travel Back in Time. *ACS Energy Lett.* **2018**, *3* (11), 2841–2845. https://doi.org/10.1021/acsenergylett.8b01966.

(3) Dunn, B.; Kamath, H.; Tarascon, J.-M. Electrical Energy Storage for the Grid: A Battery of Choices. *Science (80-.).* **2011**, *334* (6058), 928–935. https://doi.org/10.1126/science.1212741.

(4) Saha, P.; Datta, M. K.; Velikokhatnyi, O. I.; Manivannan, A.; Alman, D.; Kumta, P. N. Rechargeable Magnesium Battery: Current Status and Key Challenges for the Future. *Prog. Mater. Sci.* **2014**, *66*, 1–86. https://doi.org/10.1016/j.pmatsci.2014.04.001.

(5) Ponrouch, A.; Palacin, M. R. On the Road toward Calcium-Based Batteries. *Curr. Opin. Electrochem.* **2018**, *9*, 1–7. https://doi.org/10.1016/j.coelec.2018.02.001.

(6) Wang, D.; Gao, X.; Chen, Y.; Jin, L.; Kuss, C.; Bruce, P. G. Plating and Stripping Calcium in an Organic Electrolyte. *Nat. Mater.* **2018**, *17* (1), 16–20. https://doi.org/10.1038/nmat5036.

(7) Li, Z.; Fuhr, O.; Fichtner, M.; Zhao-Karger, Z. Towards Stable and Efficient Electrolytes for Room-Temperature Rechargeable Calcium Batteries. *Energy Environ. Sci.* **2019**, *12* (12), 3496–3501. https://doi.org/10.1039/C9EE01699F.

(8) Shyamsunder, A.; Blanc, L. E.; Assoud, A.; Nazar, L. F. Reversible Calcium Plating and Stripping at Room Temperature Using a Borate Salt. *ACS Energy Lett.* **2019**, *4* (9), 2271–2276. https://doi.org/10.1021/acsenergylett.9b01550.

(9) Bitenc, J.; Scafuri, A.; Pirnat, K.; Lozinšek, M.; Jerman, I.; Grdadolnik, J.; Fraisse, B.; Berthelot, R.; Stievano, L.; Dominko, R. Electrochemical Performance and Mechanism of Calcium Metal-Organic Battery. *Batter. Supercaps* **2021**, *4* (1), 214–220. https://doi.org/10.1002/batt.202000197.

(10) Bitenc, J.; Pirnat, K.; Bančič, T.; Gaberšček, M.; Genorio, B.; Randon-Vitanova, A.; Dominko, R. Anthraquinone-Based Polymer as Cathode in Rechargeable Magnesium Batteries. *ChemSusChem* **2015**, *8* (24), 4128–4132. https://doi.org/10.1002/cssc.201500910.

(11) Bitenc, J.; Pavčnik, T.; Košir, U.; Pirnat, K. Quinone Based Materials as Renewable High Energy Density Cathode Materials for Rechargeable Magnesium Batteries. *Materials (Basel).* **2020**, *13* (3), 506. https://doi.org/10.3390/ma13030506.

(12) Song, Z.; Zhan, H.; Zhou, Y. Anthraquinone Based Polymer as High Performance Cathode Material for Rechargeable Lithium Batteries. *Chem. Commun.* **2009**, No. 4, 448–450. https://doi.org/10.1039/B814515F.

(13) Vizintin, A.; Bitenc, J.; Kopač Lautar, A.; Pirnat, K.; Grdadolnik, J.; Stare, J.; Randon-Vitanova, A.; Dominko, R. Probing Electrochemical Reactions in Organic Cathode Materials via in Operando Infrared Spectroscopy. *Nat. Commun.* **2018**, *9* (1), 661. https://doi.org/10.1038/s41467-018-03114-1.

(14) Swiderska-Mocek, A.; Rudnicka, E. Lithium–Sulphur Battery with Activated Carbon Cloth-Sulphur Cathode and Ionic Liquid as Electrolyte. *J. Power Sources* **2015**, *273*, 162–167. https://doi.org/10.1016/j.jpowsour.2014.09.020.

(15) Scafuri, A.; Berthelot, R.; Pirnat, K.; Vizintin, A.; Bitenc, J.; Aquilanti, G.; Foix, D.; Dedryvère, R.; Arčon, I.; Dominko, R.; Stievano, L. Spectroscopic Insights into the Electrochemical Mechanism of Rechargeable Calcium/Sulfur Batteries. *Chem. Mater.* **2020**, *32* (19), 8266–8275. https://doi.org/10.1021/acs.chemmater.0c02074.

(16) Giorgetti, M. A Review on the Structural Studies of Batteries and Host Materials by X-Ray

Absorption Spectroscopy. *ISRN Mater. Sci.* **2013**, *2013*, 1–22. https://doi.org/10.1155/2013/938625.